Probing Quark-Gluon Plasma with Beauty Quarks

by

Ta-Wei Wang

Submitted to the Department of Physics
in partial fulfillment of the requirements for the degree of

Doctor of Philosophy in Physics

at the

MASSACHUSETTS INSTITUTE OF TECHNOLOGY

June 2019

Author .....
Department of Physics
March 1, 2019

Certified by .....
Yen-Jie Lee
Professor of Physics
Thesis Supervisor

Accepted by .....
Nergis Mavalvala
Associate Department Head of Physics

Probing Quark-Gluon Plasma with Beauty Quarks

by

Ta-Wei Wang

Submitted to the Department of Physics
on March 1, 2019, in partial fulfillment of the
requirements for the degree of
Doctor of Philosophy in Physics

Abstract

This thesis presents the first ever attempts of direct measurements of B mesons in heavy ion collisions with the CMS experiment. The full decay chains of B mesons were reconstructed by identifying the corresponding decay vertices. Machine learning classification models were used extensively and an unprecedented signal to background ratio was reached. Both cross sections and nuclear modification factors which quantify the medium effect of the quark-gluon plasma were measured. This thesis will introduce the techniques that enabled these novel analyses and discuss the implications of the results.

Thesis Supervisor: Yen-Jie Lee
Title: Professor of Physics

Acknowledgments

This thesis is dedicated to all the professors, researchers, post-docs, and graduate students I worked with at MIT and at CERN. The analyses presented here would not have been possible without the help, guidance, and support from them.

I would like to express my sincerest gratitude to my advisor, Professor Yen-Jie Lee. I was a tardy and dull student of the lab and it was his patience that fostered what I have achieved now. None of my Ph.D. researches could ever have been done without his trust, support, and enlightenment. His presence behind the scenes has always given me the courage to present our experimental results proudly and confidently in front of the community. I want to thank Professor Wit Busza for his periodic physics challenges and brainstorming sessions. It has been the biggest incentive and a reminder for me to never forget my curiosity toward the magnificence of physics. I want to thank Professor Gunther Roland for his guidance, which made possible the success of the MIT heavy ion group. I feel so proud to claim that I have been a member of this amazing group. I want to thank Professor Bolek Wyslouch for taking care of our working environment and ensuring our needs were all satisfied. His efforts enabled us to concentrate on our researches without distractions. I want to thank Professor Krishna Rajagopal for his kind suggestions and help on my thesis. This thesis would not be consistent and readable without his incisive comments. I want to thank George Stephans, our senior research scientist. My success as a Monte Carlo contact is largely attributable to his careful management and detail-oriented instructions regarding the MC samples. I want to thank Anna Maria Convertino, our group secretary, for arranging all our administrative matters smoothly. I cannot imagine how disastrous our traveling would have been without her help!

To the post-docs I worked closely with over the past 5 years: Thank you, Camelia Mironov, you were always my mentor and life-saver. Without your help, none of my analyses could have been published. It was your support that made all these difficult measurements come true. I have learned so much from your focus and determination and your ways of approaching problems. I look up to you as my toughest teacher

and my most respected role model. Thank you, Gian Michele Innocenti. The spectra meetings became a pleasant experience because of your leadership. We may not be the most interesting PING, but we are having the most fun. Your help and organizing of the heavy flavor analyses made possible the success of this working group and built up the reputation of the CMS heavy flavor team.

To my fellow graduate students, Dragos Velicanu, Alex Barbieri, Doga Gulhan, Mukund Varma, Austin Baty, Christopher McGinn, Jing Wang, Kaya Tatar, and Ran Bi: It was my biggest honor to have worked with a group of people as brilliant, motivated, and light-hearted as you. It was your presence in the office that made my days. The conversations and the fun we had are the oases to get away from the heavy workloads. The movie nights and the after-work drinks we had during the most insane 2015 data-taking period I will never forget. I would like to express my special thanks to Jing Wang. There cannot be a better partner to work with in the world. Those crazy nights fighting for approval meetings and the late dinners we had after the exhausted days I can still vividly remember. The times we spent together will always be the most precious moments in my life. I want to thank Hyunchul Kim for helping me on various aspects of my analyses. Your initiatives and introductions inspired me to dive into the study of the beauty quark, which made up my thesis topic today. To my close friends Jian Feng Kong, Jun Yong Khoo, and Elton Yechao Zhu, the times we spent hunting for free food events and exchanging gaming ideas made up the most enjoyable part of my Ph.D. life.

My times as a graduate student have been a long journey and I am extremely lucky to have been a member of this amazing community, surrounded by the kindest colleagues I could ever hope for. My sincerest gratitude for your companionship. Finally, most of all, I want to thank my family. It was your supports all the way across the Pacific Ocean from Taiwan, my lovely homeland, that pushed me forward and gave me the courage to move on. I love you and I always will.

Contents

1 Introduction **27**

1.1 A brief history of nuclear physics 28

1.2 Quark Gluon Plasma 32

1.3 Hard probes 34

2 Heavy flavor **41**

2.1 A survey of the charm quark 43

2.1.1 Medium modifications of the charm spectra 44

2.1.2 Heavy quark diffusion in the medium 49

2.1.3 Heavy quark hadronization in the QGP 54

2.1.4 Cold nuclear matter effects and the surprise in pA collisions . 58

2.2 A beautiful probe 61

2.3 The knowns and the known unknowns 70

3 Common high energy/particle physics notions **75**

4 Experimental Apparatus **79**

4.1 The Large Hadron Collider 79

4.2 The Compact muon solenoid 80

4.2.1 Tracking System 82

4.2.2 Electromagnetic Calorimeter (ECAL) 86

4.2.3 Hadronic Calorimeter (HCAL) 87

4.2.4 Muon System 89

4.2.5 Relevant sub-detectors to this thesis . . . 92
4.3 Trigger System . . . 93
4.3.1 Level-1 Trigger (L1) . . . 93
4.3.2 High Level Trigger (HLT) . . . 94

5 Physics Objects **97**
5.1 Track . . . 97
5.1.1 Kalman filter . . . 99
5.2 Vertex . . . 103
5.2.1 Vertexing using Kalman filter . . . 104
5.3 Muons . . . 107
5.3.1 Regional Reconstruction . . . 108
5.3.2 Standalone Muon . . . 108
5.3.3 Global Muon . . . 109
5.3.4 Tracker Muon . . . 109

6 Machine learning **111**
6.1 Training and testing error . . . 114
6.2 Feature engineering . . . 116
6.2.1 Feature selection . . . 117
6.3 Decision tree . . . 119
6.4 Ensemble method . . . 121
6.4.1 Boosting (adaptive) . . . 122

7 Analysis **127**
7.1 Data samples . . . 129
7.2 Monte Carlo samples . . . 130
7.2.1 Signal samples . . . 130
7.2.2 J/ψ samples . . . 132
7.2.3 MC re-weighting . . . 132
7.3 B meson reconstruction . . . 136

7.3.1 Secondary vertex reconstruction . . . 136
7.4 Selection criteria . . . 138
7.4.1 Muon and J/ψ selection . . . 139
7.4.2 Track selection . . . 141
7.4.3 J/ψ meson selection . . . 141
7.4.4 $K^*(892)^0$, ϕ and B meson selection . . . 142
7.5 B meson selection optimization . . . 146
7.5.1 Feature engineering . . . 146
7.5.2 Machine learning selection criteria optimization . . . 148
7.6 Signal Extraction . . . 155
7.7 Peaking background . . . 165
7.8 Systematic uncertainties . . . 168
7.8.1 Luminosity . . . 168
7.8.2 Branching ratio . . . 168
7.8.3 B meson p_T shape . . . 169
7.8.4 Tracking efficiency . . . 169
7.8.5 Muon efficiency . . . 170
7.8.6 Selection efficiency . . . 171
7.8.7 Acceptance correction . . . 174
7.8.8 Yield extraction . . . 175
7.8.9 Summary table . . . 176
7.9 FONLL . . . 185
7.10 Cross section . . . 187
7.11 Nuclear modification factor . . . 191
7.11.1 Comparison with theoretical predictions and discussions . . . 192

8 Conclusions **197**

List of Figures

1-1 The decay of neutral kaons through the mixing between the invariant mass eigenstates and the weak interaction eigenstates of quarks [170]. The amplitudes of the two diagrams cancel with each other (ignoring the mass difference between up and charm quark), leading to a small decay rate observed in experiments. 29

1-2 An illustration of the evolution of the Quark-Gluon Plasma (QGP) in Minkowski diagram with time (y-axis) and longitudinal direction (x-axis) coordinates (left panel). Formation of the QGP viewd in different timestamps (right panel). Blue and grey spheres are hadrons. Red regions indicate the formation of the QGP [32]. 34

1-3 The two charged particle momentum correlations measured for different collision centralities (quantification of how "head-on" a collision is) in PbPb collisions at $\sqrt{s_{\mathrm{NN}}} = 2.76$ TeV recorded by the CMS experiment. Substantial ridge structures are observed around $\Delta\phi = 0$ across all $\Delta\eta$ values [100, 102] for more off-center collisions. $\Delta\phi$, $\Delta\eta$ are the differences in pseudo-rapidity and polar angle in the charged particle pairs respectively. 36

1-4 Fourier coefficients of the charged particle azimuthal distribution for different collision centralities in PbPb collisions at $\sqrt{s_{\mathrm{NN}}} = 2.76$ TeV recorded by the ALICE experiment [40, 41]. Positive values correspond to final state anisotropies. 37

1-5 Dijet asymmetry ratio, A_J, from pp and PbPb collisions at $\sqrt{s_{NN}} = 2.76$ TeV recorded by the CMS experiment [101]. The upper left panel shows the ratio as obtained in pp collisions. The lower right panel corresponds to the ratio obtained in the most central PbPb collision events. A significant transverse momentum imbalance is observed. . 39

1-6 Nuclear modification factor measurements of charged hadrons from SPS [191, 147], RHIC [134, 137], and LHC [42, 104]. A less than unity value indicates a suppressed production rate in PbPb collisions with respective to pp collisions. 40

2-1 The nuclear modification factor (R_{AA}) of heavy flavor electrons at mid-rapidity down to $p_T = 0.5$ GeV/c in two centrality intervals (left: 0–10%, right: 20–40%) measured in PbPb collisions at $\sqrt{s_{NN}} = 2.76$ TeV from the ALICE experiment [73]. The results are compared with various theoretical predictions with and without the inclusion of nuclear shadowing effects. 47

2-2 The nuclear modification factor (R_{AA}) of heavy flavor muons at mid-rapidity with different event centrality (from 10 to 60%) measured in PbPb collisions at $\sqrt{s_{NN}} = 2.76$ TeV from the ATLAS experiment [83]. 48

2-3 Nuclear modification factor ((R_{AA})) measurements of open charm mesons in PbPb collisions at $\sqrt{s_{NN}} = 5.02$ TeV from the ALICE [72] (upper) and the CMS [126] (lower left) experiment. A comparison between the results obtained by the two experiments is shown in the lower right panel. 50

2-4 Upper: nuclear modification factor ((R_{AA})) measurements in PbPb collisions at $\sqrt{s_{NN}} = 5.02$ TeV for inclusive charged particles [12] and non-strange D mesons [72] from the ALICE experiment. Lower: similar measurements for inclusive charged hadrons [39], D^0 mesons [126], non-prompt J/ψ mesons [123] (J/ψ mesons from b hadron decays), and B mesons [114]. 51

2-5 Prompt D^0 meson azimuthal anisotropy coefficients, v_2 and v_3, in PbPb collisions at $\sqrt{s_{\rm NN}} = 5.02$ TeV from the CMS experiment [124]. . . . 55

2-6 Non-strange D meson (D^0, D^+, and D^{*+}) azimuthal anisotropy coefficients, v_2, in PbPb collisions at $\sqrt{s_{\rm NN}} = 5.02$ TeV from the ALICE experiment [69, 68]. 56

2-7 Left: the Λ_c^+/D^0 yield ratios measured in pp collisions at $\sqrt{s} = 7$ TeV and in pPb and PbPb collisions at $\sqrt{s_{\rm NN}} = 5.02$ TeV by the ALICE experiment [71]. Right: Comparison of nuclear modification factors ($R_{\rm AA}$) between inclusive charged hadrons, Λ_c^+ baryons, non-strange D mesons (D^0, D^+, and D^{*+}), and D_s^+ mesons. 57

2-8 Comparison of nuclear modification factors ($R_{\rm AA}$) between non-strange D mesons (D^0, D^+, and D^{*+}) and strange-charm D_s^+ mesons from the ALICE experiment [72]. 57

2-9 Nuclear modification factors ($R_{\rm pA}$) of non-strange D mesons [59] (left) and heavy flavor muons [65] (right) measured in pPb collisions from the ALICE experiments. 59

2-10 Azimuthal anisotropy coefficient, v_2, of D^0 mesons [121] (left) and heavy flavor electrons [67] (right) measured in pPb collisions from the CMS and ALICE experiments. 59

2-11 Nuclear modification factors ($R_{\rm pA}$) of non-strange D mesons [59] compared with transport models that include the presence of a medium in the pPb collisions. 60

2-12 Nuclear modification factor (left panel) and elliptic flow (right panel) for heavy quarks in semi-central PbPb ($\sqrt{s_{\rm NN}} = 2.76$ TeV) collisions for different values of the heavy quark (HQ) mass, in a Boltzmann (solid lines) and in a Langevin approach (dashed lines) [22]. 63

2-13 Fractional energy loss, $\Delta E/E$, of charm quarks as a function of their path length in a fixed-temperature QGP for various model calculations at two temperatures T and three initial quark energies E [22]. 65

2-14 Fractional energy loss, $\Delta E/E$, of beauty quarks as a function of their path length in a fixed-temperature QGP for various model calculations at two temperatures T and three initial quark energies E [22]. 66

2-15 Nuclear modification factors (R_{AA}) of non-prompt J/ψ mesons as a function of $\mathrm{p_T}$ (upper left), rapidity (upper right), and centrality (lower left, larger $\mathrm{N_{part}}$ indicates more central collisions) in PbPb collisions at $\sqrt{s_{\mathrm{NN}}} = 2.76$ and 5.02 TeV measured by the the CMS [123] experiment. Similar results from the ATLAS experiment [84] (lower right) is also shown for comparison. 68

2-16 Azimuthal anisotropy coefficients v_2, of non-prompt J/ψ mesons as a function of $\mathrm{p_T}$ (upper left), rapidity (upper right), and centrality (lower) in PbPb collisions at $\sqrt{s_{\mathrm{NN}}} = 5.02$ TeV measured by the ATLAS experiment [85]. 69

2-17 Azimuthal anisotropy coefficients v_2, of heavy flavor muons [57] and electrons [56] in PbPb collisions at $\sqrt{s_{\mathrm{NN}}} = 2.76$ TeV measured by the ALICE experiment. 69

3-1 Distribution of the sum of HF E_T for a large minimum bias event sample divided into centrality classes [110]. 78

4-1 A schematics of the LHC with the beam injection sequence. 81

4-2 The integrated luminosity delivered by the LHC for proton-lead collisions during 2013. 81

4-3 The integrated luminosity delivered by the LHC for proton-proton (left) and lead-lead (right) collisions during 2015. 82

4-4 An overview of the CMS detector. 83

4-5 The CMS tracker layout. The outer radius is around 110 cm, and the total length in the z direction (along the beam pipe) is approximately 540 cm. 84

4-6 Layout of the pixel detector in the CMS tracker. 84

4-7 Resolutions of track p_{T} (left), d_0 (center), and z_0 (right) with muons p_{T} of 1, 10, 100 GeV/c [94]. 85

4-8 Layout of the CMS Electromagnetic Calorimeter system (ECAL). . . 87

4-9 ECAL energy resolution as a function of energy measured in an electron test beam [94]. The central value of the stochastic (S), noise (N), and constant (C) terms are shown in the legend. 88

4-10 Layout of the CMS Hadronic Calorimeter (HCAL). 89

4-11 Layout of the CMS muon system. 90

4-12 Layout of the Drift Tubes (DT). 91

4-13 Layout of the Cathode Strip Chambers (CSC). 91

4-14 Layout of the Resistive Plate Chambers (RPC). 92

4-15 Architecture of the Level-1 Trigger. 93

4-16 Trigger system [95]. 95

5-1 Primary vertex resolutions [99] in x (left), y (center), and z (right) as a function of the number of tracks used in the fitted vertices from simulation. 104

5-2 Muon reconstruction efficiencies in the barrel (left) and the endcap (right) with data compared to simulations [98]. 110

6-1 Exemplary phase space of track trajectory data with two features, fitting χ^2 (y-axis) and number of tracker hits (x-axis). Signal (true) data points are shown as red dots while background (false) data points are shown as blue dots. A rectangle is selected from the phase space, populated mostly by signal data points. 112

6-2 Exemplary phase space of track trajectory data with two features, fitting χ^2 (y-axis) and number of tracker hits (x-axis). Signal (true) data points are shown as red dots while background (false) data points are shown as blue dots. A straight line is drawn to separate the signal points from background points. 113

6-3 Exemplary error curve as a function of model complexity. Training and testing error are shown as blue and red curves. 116

6-4 Exemplary flowchart of a shallow decision tree. 119

6-5 Exemplary flowchart of a second shallow decision tree. The decision of this tree will be combined with the first tree in the boosting algorithm to make the final prediction. 123

7-1 A schematics of the B^+ meson decay. 128

7-2 B_s^0 meson p_T spectrum obtained in PbPb MC simulations (left) compared to FONLL calculations in PbPb collisions at 5.02 TeV (middle). The ratio between the two distributions was fitted with a 2nd order polynomial function (right). 133

7-3 Centrality distribution of MC simulations (red) and real data (black) in PbPb collisions at 5.02 TeV (left). The ratio between the centrality distributions of real data and MC simulations was fitted with a exponential-like function (right). 134

7-4 Primary vertex z position (PVz) spectrum obtained in PbPb collision simulations after the re-weighing procedure (red marker) compared to real PbPb collision data (black marker) at 5.02 TeV (left). The ratio between the MC simulations and real data distributions (right). . . . 135

7-5 A flowchart of the B meson reconstruction workflow 138

7-6 Single muon acceptance×efficiency using pp (left) and PbPb (right) reconstruction algorithms. The red line represents the 2015 single muon acceptance cuts [123]. 140

7-7 J/ψ meson invariant mass spectra from the selected B^+ (top left), B^0 (top right), and B_s^0 (bottom) meson candidates with $10 < p_T < 60$ GeV/c and $|y| < 2.4$ passing the selection criteria described above in pPb collision real data and MC simulations. 143

7-8 $K^*(892)^0$ (left) and ϕ meson (right) invariant mass spectra, from the selected B^0 and B_s^0 meson candidates respectively, with $10 < \mathrm{p_T} < 60$ GeV/c and $|y| < 2.4$ passing the selection criteria described above in pPb collision real data and MC simulations. 144

7-9 J/ψ meson invariant mass spectra from the selected B_s^0 meson candidates with $15 < \mathrm{p_T} < 50$ GeV/c and $|y| < 2.4$ passing the selection criteria described above in pp (left) and PbPb (right) collision real data and MC simulations. 144

7-10 ϕ meson invariant mass spectra from the selected B_s^0 meson candidates with $15 < \mathrm{p_T} < 50$ GeV/c and $|y| < 2.4$ passing the selection criteria described above in pp (left) and PbPb (right) collision real data and MC simulations. 145

7-11 A schematics of the B^+ meson decay and the definitions of features (variables) used in selection optimization. 148

7-12 Significance, i.e., $S/\sqrt{S+B}$, as a function of signal efficiency in PbPb collisions. The four panels correspond to B^+ $\mathrm{p_T}$ 10–15 (upper left), 15–20 (upper right), 20–30 (lower left), and 30–50 (lower right) GeV/c. 151

7-13 BDT discriminant distributions of signal and background from the testing and training sample (upper left and right). Efficiency as a function of BDT discriminant cut value for training and testing sample (lower left). $S/\sqrt{S+B}$ as a function of BDT discriminant cut value for B_s^0 mesons with $\mathrm{p_T}$ 7–15 GeV/c in PbPb collisions (lower right). The green dash line indicates the optimal BDT cut value used in the analyses 154

7-14 Invariant mass spectra of B^+ candidates in pPb collisions measured in $|y_{lab}| < 2.4$ and in the $\mathrm{p_T}$ range of 10–15 (upper left), 15–20 (upper right), 20–25 (middle left), 25–30 (middle right), and 30–60 GeV/c (bottom). 159

7-15 Invariant mass spectra of B^0 candidates in pPb collisions measured in $|y_{lab}| < 2.4$ and in the $\mathrm{p_T}$ range of 10–15 (upper left), 15–20 (upper right), and 20–60 GeV/c (bottom). 160

7-16 Invariant mass spectra of B_s^0 candidates in pPb collisions measured in $|y_{lab}| < 2.4$ and in the p_T range of 10–60 GeV/c. 161

7-17 Invariant mass spectra of B^+ candidates in pp collisions measured in $|y| < 2.4$ and in the p_T range of 7–10 (upper left), 10–15 (upper right), 15–20 (middle left), 20–30 (middle right), and 30–50 GeV/c (bottom). 162

7-18 Invariant mass spectra of B^+ candidates in PbPb collisions measured in $|y| < 2.4$ and in the p_T range of 7–10 (upper left), 10–15 (upper right), 15–20 (middle left), 20–30 (middle right), and 30–50 GeV/c (bottom). 163

7-19 Invariant mass spectra of B_s^0 candidates in pp collisions measured in $|y| < 2.4$ and in the p_T range of 7–15 (left) and 15–50 GeV/c (right). . 164

7-20 Invariant mass spectra of B_s^0 candidates in PbPb collisions measured in $|y| < 2.4$ and in the p_T range of 7–15 (left) and 15–50 GeV/c (right). 164

7-21 B^+ candidate invariant mass spectra obtained in non-prompt J/ψ MC simulations after vetoing the contribution of genuine $B^+ \to J/\psi\, K^+ \to \mu^+\, \mu^-\, K^+$ signal candidates for pp (left) and PbPb (right) collisions. 166

7-22 Comparison of signal (blue) and non-prompt (red) background contributions in B_s^0 channel in pp (top) and PbPb (bottom) collisions for B_s^0 mesons with p_T in 7–15 (left) and 15–50 GeV/c (right) intervals. . . 167

7-23 Double ratio of the cut variations for B meson vertex fitting probability (upper left), cosine(θ) angel (upper middle), decay length (upper right), track p_T (lower left), track η (lower middle), and BDT discriminant value (lower right) of B^+ channel in pp collisions. 173

7-24 Double ratio of the cut variations for B meson vertex fitting probability (upper left), cosine(θ) angel (upper middle), decay length (upper right), track p_T (lower left), track η (lower middle), and BDT discriminant value (lower right) of B^+ channel in PbPb collisions. 174

7-25 B_s^0 invariant mass spectra (top) and the corresponding cross sections (bottom) using a cut-base method in pp collisions. 178

7-26 B_s^0 invariant mass spectra (top) and the corresponding cross sections (bottom) using the PbPb trained BDT discriminant in pp data. . . . 179

7-27 Normalized and uncorrected yields between real data and MC simulations (left) and ratios (right) with p_T (top) and rapidity (bottom) binning of the B_s^0 channel in pp collisions. 180

7-28 Variated acceptance distributions from toys obtained by p_T (red) and rapidity (blue) yield ratios for the B_s^0 channel in pp collisions. B_s^0 mesons with p_T 7 to 15 GeV/c (left) and 15 to 50 GeV/c (right). The black line in the middle is the nominal acceptance value in the analysis. 181

7-29 Invariant mass fit of the B_s^0 channel for B_s^0 mesons with p_T $15 < p_T < 50$ GeV/c in 5.02 TeV pp collisions. The background function variations from left to right are default linear, 2nd-order polynomial, 3rd-order polynomial, and exponential function. 182

7-30 Invariant mass fit of the B_s^0 channel for B_s^0 mesons with p_T $15 < p_T < 50$ GeV/c in 5.02 TeV pp collisions. The signal function variations from left to right are default double Gaussian, single Gaussian, triple Gaussian, width decreased, width increased, and mean fixed by MC simulations. 183

7-31 FONLL calculation for the p_T-differential cross sections of the B^+ (left) and B_s^0 (right) mesons in pp collisions at $\sqrt{s} = 5.02$ TeV. The black points represent the rebinned FONLL results and the red points represent the rebinned results scaled by the corresponding fragmentation function value. 186

7-32 The p_T-differential cross sections of the B^+ (left) and B_s^0 (right) mesons in pp collisions at $\sqrt{s} = 5.02$ TeV in p_T intervals from 7 to 50 GeV/c. The vertical bars (boxes) correspond to statistical (systematic) uncertainties. The global systematic uncertainty, listed in the legend and not included in the point-to-point uncertainties, comprises the uncertainties in the integrated luminosity measurement and in the branching ratios. The pp cross section is compared to FONLL calculations [34] represented by the colored yellow boxes with the heights indicating the theoretical uncertainties. 188

7-33 The p_T-differential cross sections of the B^+ (left), B^0 (center), and B_s^0 (right) mesons measured in pPb collisions at $\sqrt{s_{NN}} = 5.02$ TeV. Vertical bars (boxes) correspond to statistical (systematic) uncertainties. The global systematic uncertainty, listed in each panel and not included in the data points, comprises the uncertainties in the integrated luminosity measurement and in the branching ratios. Results are compared to FONLL calculations [177, 178], scaled by the number of binary NN collisions, represented by a continuous histogram. The dashed histograms represent the theoretical uncertainties of the FONLL reference. 190

7-34 The p_T-differential corrected yields of the B^+ (left) and B_s^0 (right) mesons scaled by nuclear overlapping function (T_{AA}) in PbPb collisions at $\sqrt{s_{NN}} = 5.02$ TeV in B meson p_T intervals from 7 to 50 GeV/c. The vertical bars (boxes) correspond to statistical (systematic) uncertainties. The global systematic uncertainty comprises the uncertainties in T_{AA}, number of minimum-bias events, and branching ratios. . . . 190

7-35 The nuclear modification factors $R_{\rm pA}^{\rm FONLL}$ of the B (left), B^0 (center), B_s^0 (right) mesons measured in pPb collisions at $\sqrt{s_{\rm NN}} = 5.02$ TeV. The statistical and systematic uncertainties on the pPb data are shown as bars and yellow boxes around the data points respectively. The systematic uncertainties from the FONLL predictions are plotted separately as open blue boxes. The global systematic uncertainties are shown as full gray boxes at unity and are not included in the data points. . . . 191

7-36 The nuclear modification factor $R_{\rm AA}$ of the B^+ (left) and B_s^0 (right) mesons measured in PbPb collisions at $\sqrt{s_{\rm NN}} = 5.02$ TeV from 7 to 50 GeV/c. The vertical bars (boxes) correspond to statistical (systematic) uncertainties. The global systematic uncertainty, represented by colored boxes at $R_{\rm AA} = 1$, comprises the uncertainties in the integrated luminosity measurement and the $T_{\rm AA}$ value. 192

7-37 The $\rm p_T$ dependence of the nuclear modification factor $R_{\rm AA}$ of the B^+ mesons measured in PbPb collisions at $\sqrt{s_{\rm NN}} = 5.02$ TeV. Five theoretical calculations are shown for comparison: TAMU [165, 166], Djordjevic [150], CUJET3.0 [197, 196, 195], AdS/CFT HH [169, 163], and MC@sHQ+EPOS2 [181, 159]. The line width of the theoretical calculation from Ref. [165, 166] represents the size of its statistical uncertainty. 193

7-38 The $\rm p_T$ dependence of the nuclear modification factor $R_{\rm AA}$ of the B_s^0 mesons measured in PbPb collisions at $\sqrt{s_{\rm NN}} = 5.02$ TeV. Two theoretical calculations are also shown for comparison: TAMU [165, 166] and CUJET3.0 [197, 196, 195]. The line width of the theoretical calculation from Refs. [165, 166] represents the size of its statistical uncertainty. . 195

7-39 Nuclear modification factor $R_{\rm AA}$ ratio between the B_s^0 and B^+ mesons measured in PbPb collisions at $\sqrt{s_{\rm NN}} = 5.02$ TeV for B meson $\rm p_T$ between 7 to 50 GeV/c. Two theoretical calculations are also shown for comparison: TAMU [165, 166], and CUJET3.0 [197, 196, 195]. . . 196

8-1 Nuclear modification factors (R_{AA}) measured in PbPb collisions at $\sqrt{s_{\mathrm{NN}}} = 5.02$ TeV for inclusive charged hadrons [39], D mesons [126], non-prompt J/ψ mesons [123] (J/ψ mesons from B hadron decay), and B mesons [114] in different $\mathrm{p_T}$ intervals and rapidity ranges. 198

List of Tables

2.1 Summary of nuclear modification factor (R_{AA}) measurements on charm flavor (open and closed mesons) from the ALICE, ATLAS, and CMS experiment at LHC. 45

2.2 Summary of nuclear modification factor (R_{AA}) measurements on beauty flavor (open and closed mesons) from the ALICE, ATLAS, and CMS experiment at LHC. 46

2.3 Summary of azimuthal anisotropy (v_n) measurements on charm flavor (open and closed mesons) from the ALICE, ATLAS, and CMS experiment at LHC. 53

2.4 Summary of azimuthal anisotropy (v_n) measurements on beauty flavor (open and closed mesons) from the ALICE, ATLAS, and CMS experiment at LHC. 53

4.1 Detector types in the silicon tracker [90]. 86

7.1 A summary of B meson measurements in pp, pPb, and PbPb collisions in this thesis. 127

7.2 List of the data samples used with the corresponding integrated luminosities. 129

7.3 Summary of number of events generated for B meson signal MC simulations. 132

7.4 Summary table of selection criteria used for B^+ channel in different $\mathrm{p_T}$ intervals in pPb collisions. 152

7.5 Summary table of selection criteria used for B^0 channel in different p_T intervals in pPb collisions. 152
7.6 Summary table of selection criteria used for B_s^0 channel in different p_T intervals in pPb collision. 153
7.7 Summary table of selection criteria used for B^+ channel in different p_T intervals in pp collision. 153
7.8 Summary table of selection criteria used for B^+ channel in different p_T intervals in PbPb collision. 153
7.9 Summary table of selection criteria used for B_s^0 channel in different p_T intervals in pp collision. 153
7.10 Summary table of selection criteria used for B_s^0 channel in different p_T intervals in PbPb collision. 153
7.11 Extracted yields for B^+, B^0, and B_s^0 channels in pPb data. 158
7.12 Extracted yields for B^+ channel in pp and PbPb data. 158
7.13 Extracted yields for B_s^0 channel in pp and PbPb data. 158
7.14 Summary of systematic uncertainties from each factor for the B^+ channel in pPb collisions. All the values are shown in percentage. 177
7.15 Summary of systematic uncertainties from each factor for the B^0 channel in pPb collisions. All the values are shown in percentage. 177
7.16 Summary of systematic uncertainties from each factor for the B_s^0 channel in pPb collisions. All the values are shown in percentage. 177
7.17 Summary of systematic uncertainties from each factor for the B^+ channel in pp collisions. All the values are shown in percentage. 181
7.18 Summary of systematic uncertainties from each factor for the B^+ channel in PbPb collisions. All the values are shown in percentage. 182
7.19 Summary of systematic uncertainties from each factor for the B_s^0 channel in pp collisions. All the values are shown in percentage. 183
7.20 Summary of systematic uncertainties from each factor for the B_s^0 channel in PbPb collisions. All the values are shown in percentage. 184

7.21 Summary of the N_{coll}, T_{AA} and N_{part} values for different centrality bins [110]. 189

Chapter 1

Introduction

Since the discovery of protons and neutrons, scientists have been on the mission to unveil the mysterious inter-nucleon interactions. Over the past centuries, from the plum pudding model, the Yukawa potential, Quantum chromodynamics (QCD), to lattice QCD, much significant progress has been made, exploring new territories in the phase space of nuclear interaction. However, a quantitatively precise description of internuclear interactions at high energy density and high temperature remains unclear due to its complicated structure. Under extreme temperature conditions, the formation of a state consisting of deconfined quarks and gluons, the Quark-Gluon Plasma (QGP) [188, 146], is predicted by lattice QCD calculations [171]. While normal matter is made of protons and neutrons which are bound states of quarks, due to the extremely high temperature, these bound states will be decoupled in QGP, allowing them to interact with other quarks and gluons as unbound states.

Relativistic heavy ion collisions are one way, and currently the only way, to study the QGP. By colliding enormously accelerated nuclei, a droplet of QGP can be created and last for an extremely short period of time (around 10^{-23} seconds). It then cools down and produces a swarm of particles subsequently. The properties of QGP can be indirectly inferred by analyzing the responses recorded by some of the most advanced detectors scientists have ever built. Elaborate analyses have been performed by various particle experiment collaborations in the world, each focusing on different aspects of the complicated QGP properties. For example, the study of particle mo-

mentum correlations of a collision event helps to understand how the QGP evolves as a whole as it expands after the initial collision process. The momentum distribution of a collimated spray of particles, a jet, which are produced by the fragmentation and hadronization of high energy partons (which are component particles of hadrons) allows us to understand how particles interact with the QGP medium and study the so-called "jet quenching" phenomenon. By analyzing how the outgoing charged particles interact with the QGP and lose energy (by means of elastic collisions and medium-induced gluon radiations [27, 19, 101, 79, 14]), and the corresponding QGP responses, we can infer insights regarding the energy density and diffusion properties of the QGP. In this thesis we will focus on yet another approach to understand the QGP properties by using heavy quarks. More precisely speaking, we will analyze the production rates of beauty mesons (B mesons for short from now on), which are bound states of a beauty quark and a light flavor (up, down, and strange) quark, in heavy ion and proton-proton (pp) collisions to deduce the medium effects, such as the energy loss of beauty quarks, brought by the QGP system.

1.1 A brief history of nuclear physics

As far as we know, our visible universe is predominantly made of photons, electrons, protons and neutrons. Protons and neutrons (collectively as nucleons) had long been thought to be elementary particles until the 1960's when the deep inelastic scattering (DIS) experiments conducted at the Stanford Linear Accelerator Center (SLAC) revealed that protons actually have point-like objects situating at their center [28, 29] by analyzing the cross sections of electron-proton scattering at different scattering angles and incident energies. Specifically, the structure functions of the scattering cross section can be explained by a sum rule of having many point-like objects at the core of a proton. Moreover, these constituents, while bound to each other, seem to be having very small interactions with one another (the Bjorken scaling). The fact that structure functions do not depend on the absolute energy scale of the collision but on dimensionless quantities implies an independence of resolution scale and that the

constituents are effectively point-like. These constituents are referred to as partons which are essentially up, down quarks, and gluons as we now know. This discovery indirectly verified the Eightfold way or Quark model [157, 201, 202] proposed by Murray Gell-Mann and George Zweig in 1961, 7 years before the DIS experimental confirmation. The quark model suggested a theory of SU(3) flavor symmetry consisting of up, down, and strange quarks, which acted as the constituents of the various hadrons such as pions, kaons, or protons that had been discovered. It was a huge success, capable of explaining all the different meson and baryon states people had observed in experiments and most notably, the classification of the Ω^- baryon (composed of three strange quarks) with predictions of its existence, mass, and decay products before it was discovered by the Brookhaven National Laboratory (BNL) by analyzing the complicated decay chains of Ω^- baryons, from exposing a hydrogen bubble chamber with a K^- meson beam, recorded on pictures [21].

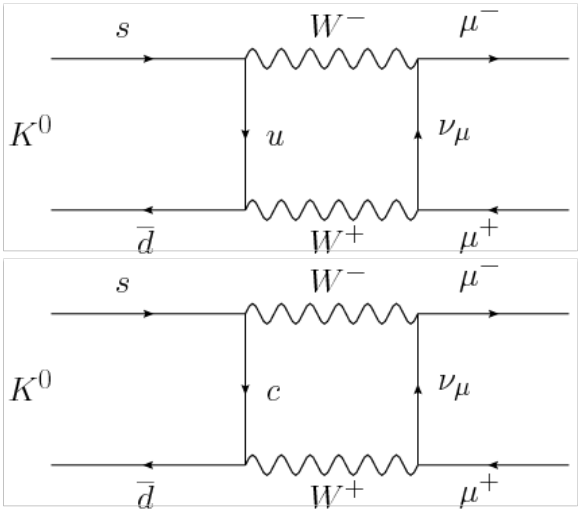

Figure 1-1: The decay of neutral kaons through the mixing between the invariant mass eigenstates and the weak interaction eigenstates of quarks [170]. The amplitudes of the two diagrams cancel with each other (ignoring the mass difference between up and charm quark), leading to a small decay rate observed in experiments.

In the early 1970's, this three-member family was extended by the "GIM mechanism" [158], which proposed a yet undiscovered charm quark. In the notion of Cabibbo angle [33], the universality of the weak interaction is preserved by having a

mixing (θ_c) between the invariant mass eigenstates and the weak interaction eigenstates. That is, the up quark is coupled (weak interaction) to a mixed state of down and strange quark, $d * \cos(\theta_c) + s * \sin(\theta_c)$, through which a flavor-changing neutral current (FCNC) that can change the flavor of a fermion without altering its electric charge also becomes possible by having a down quark coupled to a strange quark via an intermediate up quark (e.g., the left half of the upper panel in Fig. 1-1). However, experimentally, the decay of a neutral kaon which requires the existence of FCNC is found to be extremely rare. Sheldon Glashow, John Iliopoulos and Luciano Maiani proposed that this can be remedied by introducing a new quark with a corresponding coupling to the orthogonal state, $-d * \sin(\theta_c) + s * \cos(\theta_c)$, in the weak interaction. The amplitudes from the two FCNCs cancelled with each other, ignoring the mass difference between up and charm quark on the scale of W boson (which is the mediator of the weak interaction), bringing the neutral kaon decay suppressed at tree level. Three years later, Makoto Kobayashi and Toshihide Masukawa figured that for a 2 by 2 (two quark generations) unitary weak interaction matrix, one can always do an arbitrary phase transition (quantum field re-definition), making the matrix real valued which is in contradiction to the observation of CP-violation in the decay of a neutral kaon to two pions [36]. They introduced a third quark generation in realization for a unitary weak interaction matrix that contains a complex phase term. This three-generation picture is known as the CKM matrix [173] and the rest is history. A charm plus anti-charm quark meson, the J/ψ meson, was discovered, independently by two groups at BNL [17] and SLAC [18, 1] in November of 1974 (November revolution). The bottom quark was also discovered soon after in 1977 by the Fermilab [167] and finally the top quark, which came a bit late in 1995 due to its massiveness, was discovered by the CDF and D0 experiments [87, 132]. This three-generation model has since then became our understanding of QCD matter.

On the other side, scientists have also been relentlessly researching the force that governs the interactions between nucleons. Since the discovery of the neutron in 1932, people used to think the force, which binds the protons and neutrons in nuclei, came from the exchange of massive bosons (which are now known to be pions). Like the

electric Coulomb potential, it was once thought that the potential between nucleons could be described (empirically) by a spherically symmetric potential, the "Yukawa potential" [199]

$$V_{Yukawa}(r) = -g^2 \frac{e^{-\mu r}}{r} \tag{1.1}$$

where r is the distance, g is the coupling strength, and μ is the mass of the force carrier. Since then, many different empirical and phenomenological descriptions of the nuclear force have been proposed. At the same time, with the discovery of the deuteron electric quadrupole moment [172], people began to wonder about a tensorial characteristic of the nuclear force in addition to the spherically symmetric potential. Later, with the compositeness of protons being discovered, it was understood that the nuclear force we observed must result from some more fundamental structure, just like the Van der Waals force being the residual of the more fundamental electric force. This is in line with the discovery of the aforementioned Ω^- baryon, which has a spin of 3/2. Being fermions, strange quarks inside the Ω^- baryon cannot all be in parallel spin direction by Pauli exclusion principle, unless there are additional quantum numbers associated. In addition, the interactions between quarks need to be "Asymptotically free," meaning the strength of the interaction decreases when quarks scatter at higher energy (at GeV scale), to accommodate the scaling behavior observed in the DIS experiment. Since no attempts of observing a free quark have succeeded, the quarks were also believed to be confined by this (strong) interaction which later became known as color confinement. During 1964 to 1965, the concept of color was introduced by Oscar Greenberg [160], Moo-Young Han, and Yoichiro Nambu [164]. In 1973, this color symmetry was further explored by Harald Fritzsch, Heinrich Leutwyler, and Murray Gell-Mann [154]. They subsequently developed the Yang–Mills theory [198] into the theory of QCD. Earlier the same year, the asymptotic freedom characteristic of QCD was also proved/discovered by David Gross, Frank Wilczek, and David Politzer [161, 183].

Asymptotic freedom is one of the most special feature of QCD. For Yang–Mills theories [198] such as QCD, the beta function which describes the dependence of

the coupling strength g (which determines the strength of the force exerted in an interaction) on the energy scale μ (of a given physical process) can be shown to have the form

$$\beta(g) = \frac{\partial g}{\partial log(\mu)} = -\frac{g^3}{16\pi^2}\big[\frac{11}{3}C_2(G) - \frac{4}{3}n_f C(r_f) - \frac{1}{3}n_s C(r_s)\big] + O(g^5) \qquad (1.2)$$

where n_f denotes the number of Dirac spinor fields and n_s denotes the number of complex scalar fields coupled to the gauge fields. $C_2(G)$ is called the quadratic Casimir operator in the adjoint representation, $C(r_{f,s})$ is another (Casimir invariant) quantity defined through $Tr[t_r^a t_r^b] = C(r)\delta^{ab}$, and $t_r^{a,b}$'s are the generators of the fundamental representation r. In the case of the SU(N=3), i.e., QCD, where $n_f = 6,\ n_s = 0$, $C_2(G) = N = 3$, and $C(r_f) = 1/2$, one finds that as opposed to Quantum electrodynamics (QED), the beta function of strong interaction is negative. This means that as the energy scale of a physical process increases, the coupling strength will decrease and vice versa. This particular feature gives rise to the color confinement phenomenon that have been observed in experiments for decades. Intuitively, one can image pulling two quarks apart from each other. As the distance increases, the color fields between them become larger. At some point, the energy that is stored in the fields (the potential energy) becomes even larger than what's needed for the creation of a quark-antiquark pair. The original quark pair splits into two quark pairs reducing the potential energy. As a result, no free quark was observed during the process. This also explains the short range of nuclear force in spite of the fact that the strong interaction mediator, the gluon, is massless because it is energetically favorable to create new quark-antiquark pairs from the vacuum.

1.2 Quark Gluon Plasma

As we mentioned, quarks in normal matter always exist as bound states because of the color confinement. This situation changes as the temperature and density of the system increase. Because of the asymptotic freedom, as the temperature becomes

higher than the typical QCD scale $\Lambda_{QCD} \approx 200$MeV, the system undergoes a phase transition in which the quarks become deconfined and the degree of freedom (the number of independent physical parameters in the description of a physical system) greatly increases. This phase is called the Quark-Gluon Plasma (QGP).

Despite the fact that the QCD Lagrangian had been proposed some time before and been well accepted, doing calculations of observables from first principle is a formidable task for QCD because the usual perturbative techniques do not work in the energy range of interest. So far the best known procedure for conducting such calculation is by the lattice gauge theory which is formulated by calculating the path integral (usually via Monte Carlo simulation) on discretized space-time coordinates [193] and taking the continuum limit. While lattice QCD (LQCD) is extremely successful in calculating steady state properties such as the quark mass or any of QCD's thermodynamic properties (including the equation of state), calculating the dynamical properties of a system out of equilibrium is actually very difficult for LQCD to date. On the other hand, the QGP system provides a perfect alternative testing ground to understand QCD and its material properties at various different phases from an experimental and phenomenological perspective. Of course, to study the QGP we need to first create it in the laboratory. This is achieved by colliding heavy nuclei such as Pb or Au (relativistic heavy ion collisions). With a high enough kinetic energy, the energy density within the nucleus-nucleus (AA) collisions can surpass the needed value (about 1 GeV/fm^3) for a transition from normal hadronic matter to QGP phase to occur. Pictorially, the nuclei are accelerated and become highly Lorentz contracted discs (thickness equals to nucleus radius divided by Lorentz factor γ; for LHC 5 TeV collisions, γ is about 2500). As they are driven toward each other in close proximity within the collider, the (transverse) color force fields between them build up (like strings connecting the two discs). The two discs overlap, collide (mostly soft collisions with small momentum transfer), and then recede from each other, the energy stored in the color fields between them decays (breaking of these strings) into quark pairs and gluons. Because the energy density within this region is so high (≈ 10 GeV/fm^3), a QGP system is expected to form at this moment. As the discs recede further and

further, the system cools down and eventually this hot parton soup hadronizes, the energy diffuses as a swarm of particles that disperse in all directions.

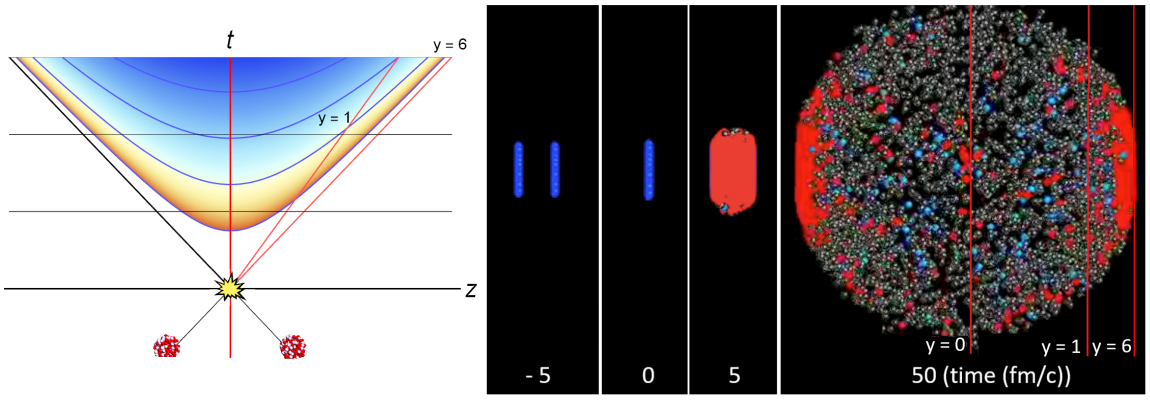

Figure 1-2: An illustration of the evolution of the Quark-Gluon Plasma (QGP) in Minkowski diagram with time (y-axis) and longitudinal direction (x-axis) coordinates (left panel). Formation of the QGP viewd in different timestamps (right panel). Blue and grey spheres are hadrons. Red regions indicate the formation of the QGP [32].

Relativistic heavy ion collisions are a great proxy to understand the otherwise complicated QCD dynamics. Studies conducted by experiments at the Relativistic Heavy Ion Collider (RHIC) and the Large Hadron Collider (LHC) [86, 135, 140, 133, 16, 153, 152] are analyzing collisions between gold (RHIC AuAu collisions) and lead (LHC PbPb collisions) ions with each other and with protons (LHC pPb collisions). The QGP system is also believed to be related to the earliest moments of the universe when the temperature was too hot for any hadron to be formed or to survive. Information about primordial matter formation, the nucleosynthesis, can be inferred by studying the QGP systems created in laboratories. In the next section, we will discuss how exactly experimentalists at modern collider experiments probe this man-made QGP system.

1.3 Hard probes

Now, we have the QGP created in the laboratory. All we need to do now is just poke this system, see how it reacts and understand its properties. This is however,

not as easy as it sounds because the QGP created in the laboratory only lasts for an extremely transient time (10^{-23} seconds). Furthermore, unlike the usual electromagnetic plasma, so far there is no way to "hold" a QGP in space and shoot a probing beam at it.

One way is to measure the remnants of the QGP. After its formation, the QGP expands, cools and eventually falls apart into a mist of hadrons that fly away. One can analyze the momenta of these final state particles to extract information regarding the bulk properties of the QGP. For example, the study of particle momentum correlations actually reveals the liquidness of the QGP. Since nuclei are composed of many nucleons, their matter content is lumpy by default. The energy distribution after the collision in the earliest moments must also be lumpy. If the QGP were to behave like an ideal gas, i.e., weakly interacting as people thought back in the days due to asymptotic freedom, the partons in the QGP would rarely scatter off each other and the azimuthal momentum distribution of final state particles would be isotropic which means the lumpiness would be washed out. However, the measured ridge structures in two particle azimuthal momentum correlations [16, 153, 152] indicate that the QGP is actually strongly interacting and is more like a thermalized liquid described by hydrodynamics. This can be understood as the initial lumpiness creating pressure gradients. These pressure gradients will induce an anisotropic flow of partons giving rise to the ridge structures in momentum correlations that have been observed. In addition, the shear viscosity of this liquid has to be low (or more precisely, the ratio between the shear viscosity and the entropy density of the system, η/s). If the shear viscosity were high, this anisotropic flow will be damped as a higher viscosity means an easier momentum exchange between fluid cells and a faster dissipation of any velocity gradient into random thermal motion. Instead, substantial anisotropies in the azimuthal distribution of final state particles were observed in heavy ion collisions, indicating a low shear viscosity. This fact also manifests itself in the Fourier coefficients of the charged particle azimuthal momentum distribution v_n (a more precise definition will be introduced later). In the presence of substantial anisotropies, these coefficients will possess positive values. One example experimental

result is shown in Fig. 1-4. Experimental data is well described by model calculations based on low shear viscosity to entropy density ratios (0 and 0.08). Interestingly, 0.08 $= 1/4\pi$ is also the universal lower bound of the η/s ratio of a plasma of infinitely strongly coupled gauge theories proposed by the AdS/CFT conjecture [179, 174].

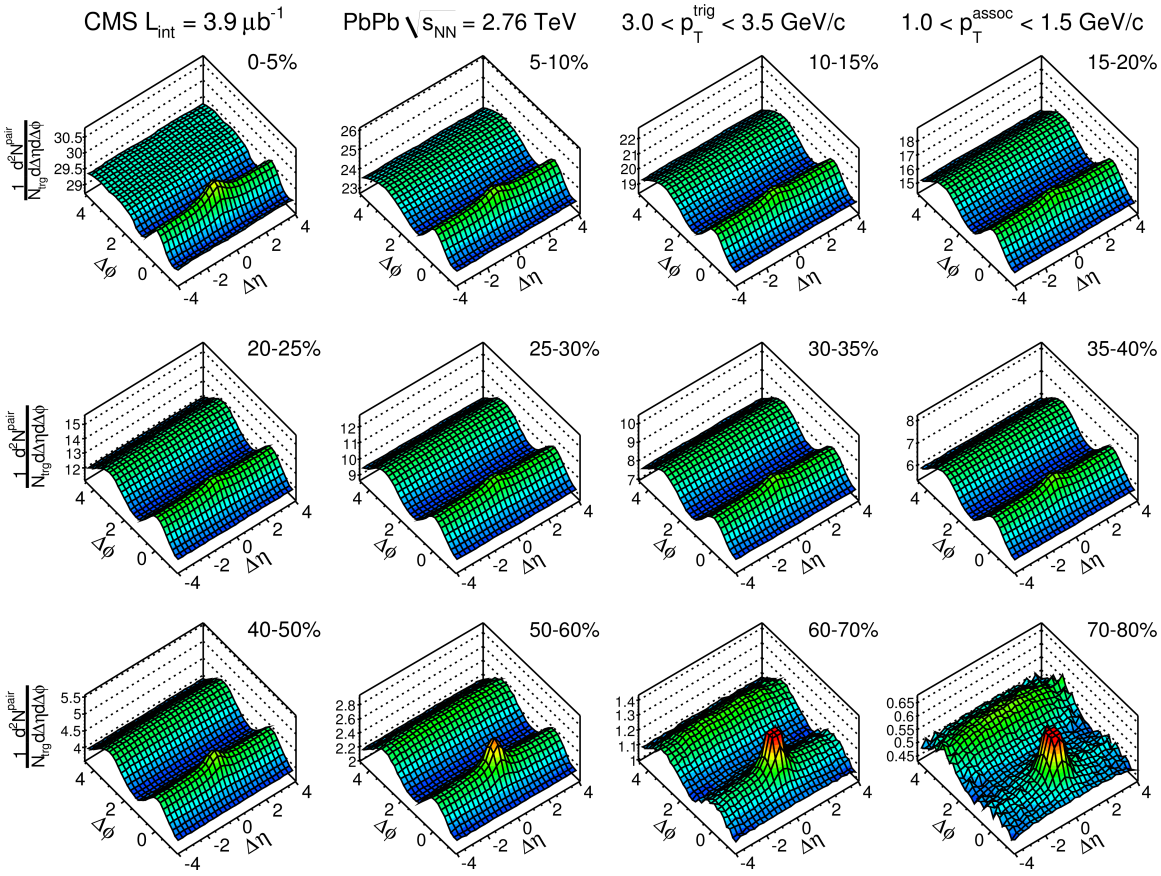

Figure 1-3: The two charged particle momentum correlations measured for different collision centralities (quantification of how "head-on" a collision is) in PbPb collisions at $\sqrt{s_{\rm NN}} = 2.76$ TeV recorded by the CMS experiment. Substantial ridge structures are observed around $\Delta\phi = 0$ across all $\Delta\eta$ values [100, 102] for more off-center collisions. $\Delta\phi$, $\Delta\eta$ are the differences in pseudo-rapidity and polar angle in the charged particle pairs respectively.

The other approach is to utilize the collision itself to provide the probes (hard probes). As the nuclei collide, by chance there are hard collisions between two partons inside (in a way similar to pp collision). In this case, particles with very large transverse momenta (tens of GeV) will be produced. These particles, produced at the earliest stage of the collision, traverse the region where the QGP is formed and ex-

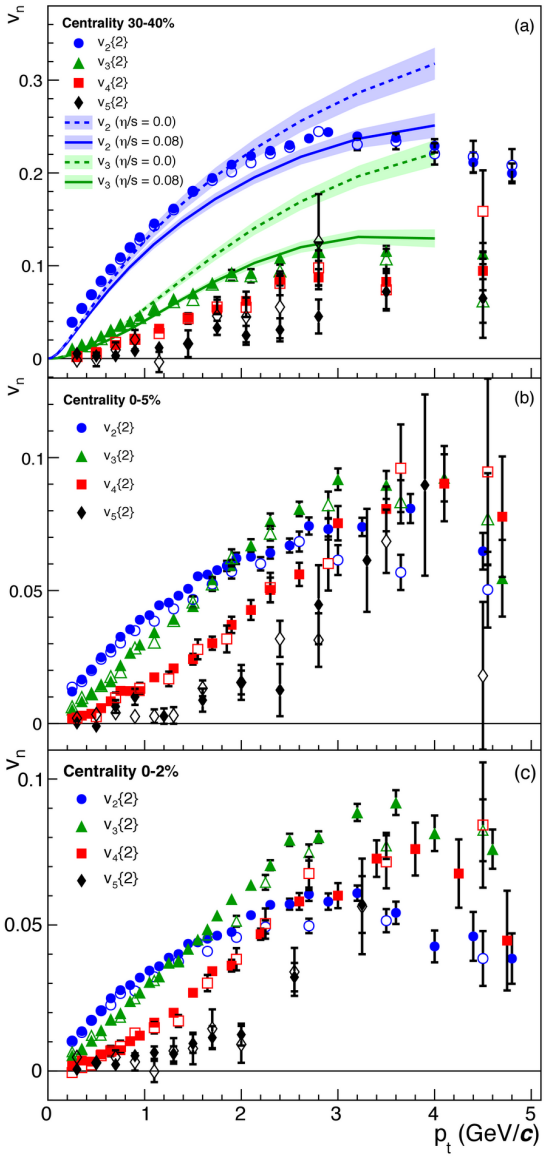

Figure 1-4: Fourier coefficients of the charged particle azimuthal distribution for different collision centralities in PbPb collisions at $\sqrt{s_{\mathrm{NN}}} = 2.76$ TeV recorded by the ALICE experiment [40, 41]. Positive values correspond to final state anisotropies.

perience the medium effect brought by the QGP. Like a charged particle penetrating through an electromagnetic plasma where its kinematics can potentially be modified, these hard probes will interact with the QGP medium and by measuring the modifications of the momentum of the probes, we can infer the fundamental properties of the QGP. An important application of this methodology is the study of jet quenching phenomena [26]. Jets are collimated sprays of particles induced by the fragmentation and hadronization of partons involved in the initial nuclei hard scatterings. Experimental results (in Fig. 1-5) from the ATLAS and CMS experiment [78, 101] both indicate a significant momentum imbalance between back to back jets by calculating the $\mathrm{A_J}$ which is defined as

$$\mathrm{A_J} = \frac{\mathrm{p_{T,1}} - \mathrm{p_{T,2}}}{\mathrm{p_{T,1}} + \mathrm{p_{T,2}}} \tag{1.3}$$

where $p_{T,1}$ and $p_{T,2}$ are the transverse momentum of the most energetic ("leading") and the second most energetic ("subleading") jet respectively. This observation can be explained by an interplay between (vacuum-like) fragmentation and fluctuations of medium induced energy loss [180, 30]. For a jet with a larger number of softer constituents (resulted from a softer fragmentation), since each constituent will interact with the medium and undergo medium-induced energy loss, a larger the number of constituents can lead to a greater medium effects experienced by the jet. In addition, for softer constituents, they are more likely to fall beyaond the reach of jet reconstruction radius (jet cone). As a result, the fluctuations of the jet-medium interaction can be amplified for jets with softer fragmentation pattern. The increase in the fraction of momentum unbalanced jets thus indicates the presence of strong interactions between the jet constituents and the medium which results in a high degree of jet quenching in the produced matter.

The ideal of measuring medium-induced modifications can also be realized by the calculation of the nuclear modification factor $R_{\mathrm{pA,AA}}$ which quantifies the particle production spectra in heavy ion collisions with respect to pp collisions. It is defined as the scaled (by the average number of binary collisions, N_{coll}) differential production

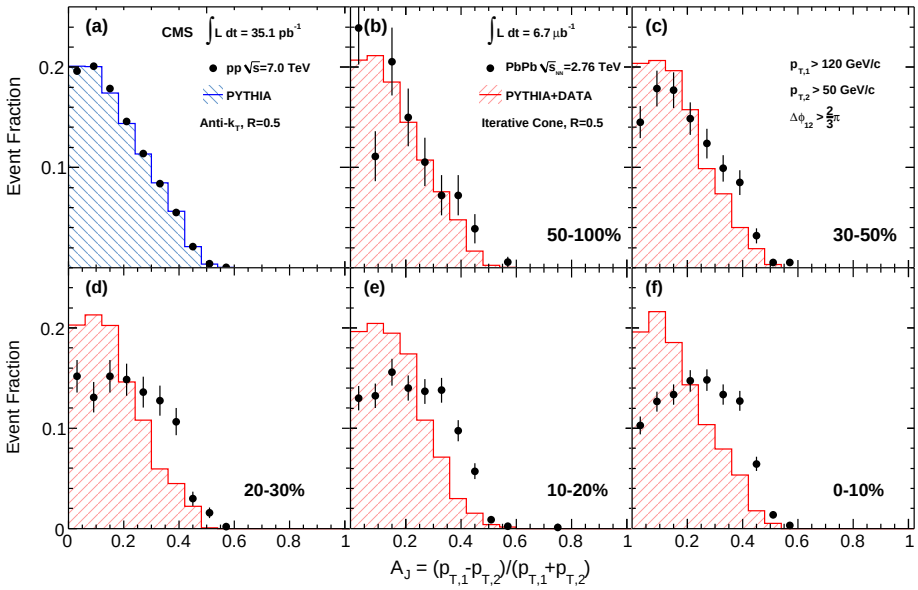

Figure 1-5: Dijet asymmetry ratio, A_J, from pp and PbPb collisions at $\sqrt{s_{NN}} = 2.76$ TeV recorded by the CMS experiment [101]. The upper left panel shows the ratio as obtained in pp collisions. The lower right panel corresponds to the ratio obtained in the most central PbPb collision events. A significant transverse momentum imbalance is observed.

yields per inelastic collision in heavy ion collisions with respect to pp collisions

$$R_{\mathrm{pA,AA}}(\mathrm{p_T, y}) = \frac{\frac{\mathrm{d^2N^{pA,AA}}}{\mathrm{dydp_T}}}{< \mathrm{N_{coll}} > \frac{\mathrm{d^2N^{pp}}}{\mathrm{dydp_T}}} \tag{1.4}$$

where $< N_{coll} >$ is the average number of binary nucleon-nucleon collisions usually computed in the Glauber model [16]. $N^{pp,pA,AA}$ is the (signal) yields per inelastic collision. For instance, in the case of pA collisions, the $< N_{coll} >$ is $A\frac{\sigma_{pp}^{inel}}{\sigma_{pA}^{inel}}$ where $\sigma_{pp,pA}^{inel}$ is the inelastic cross section of pp and pA collisions. A is the atomic mass number. Since $N^{pp,pA,AA}$ is simply the ratio between the inelastic collision and the hard process (that produces the signal) cross section, $\frac{\sigma^{hard}}{\sigma^{inel}}$, we end up with $R_{pA} = \frac{\sigma_{pA}^{hard}}{\mathrm{A}\sigma_{pp}^{hard}}$, i.e., the ratio of hard process cross sections between pA and pp collisions scaled by the atomic mass number. $R_{pA,AA}$ quantifies the relative production rates between heavy ion collisions and nucleon-nucleon collisions. In the absence of medium effects and other modifications (as is the case with W/Z bosons, which are the mediators of weak

interaction, and photons), $R_{pA,AA}$ will be positioning at unity. Measurements for the $R_{\rm AA}$ of charged hadrons from experiments at Super Proton Synchrotron (SPS), RHIC, and LHC [191, 147, 134, 137, 42, 104] are shown in Fig 1-6. The observed suppressions of production rates of charged hardrons can be attributed to energy loss of the partons as they propagate through the hot and dense QCD medium. This result also aligns with the observation of jet quenching in heavy ion collisions.

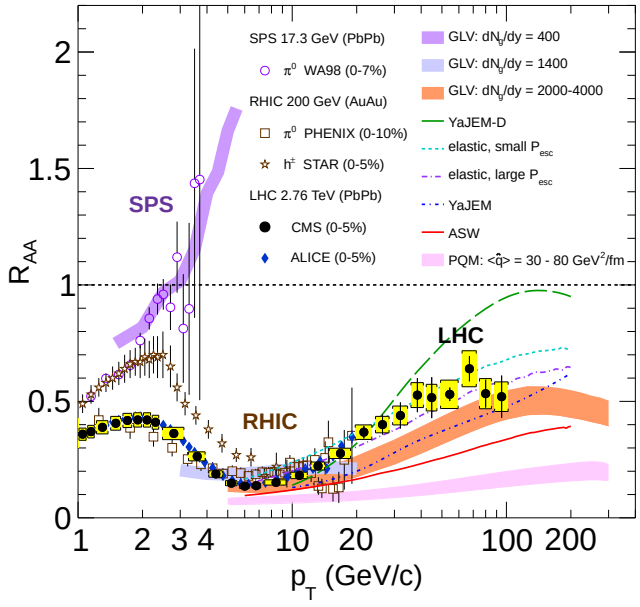

Figure 1-6: Nuclear modification factor measurements of charged hadrons from SPS [191, 147], RHIC [134, 137], and LHC [42, 104]. A less than unity value indicates a suppressed production rate in PbPb collisions with respective to pp collisions.

The unprecedented amounts of heavy ion collision data gathered by the RHIC and LHC experiments have brought us rich information about the QGP [86, 135, 140, 133, 16, 153, 152]. While some of the results matched our intuitions, others came as surprises which almost completely overturned our original expectations. In the next chapter, we will introduce the method of probing the QGP properties using heavy flavor quarks. The central parts of this thesis which are the measurements of the beauty quarks in heavy ion collisions are based on contents published in Ref. [112, 114, 122].

Chapter 2

Heavy flavor

The measurement of heavy flavor quarks (heavy quarks for short), namely the charm and beauty quarks, in heavy ion collisions is particularly interesting for several different reasons. First of all, the invariant masses of the charm and beauty quarks are higher than the QGP critical temperature, $m_{c,b} >> T_c$, thus their production is restricted to the primordial nucleon-nucleon hard collisions and thermal production is negligible for the energy range accessible to RHIC and LHC. The measured charm and beauty quarks will preserve a memory of their interaction history with the medium as opposed to light quarks and gluons which can be either generated or annihilated within the medium. Their final state spectra are norm-conserving with respect to the initial state spectra since their total numbers are conserved during the limited life time of the medium. This fact to an extent renders the nuclear modification factors easier to understand and interpret. (Note that the corresponding hadron spectra might not be norm-conversing due to the "chemistry effect", i.e., an increase in one hadron species requires decreases in other species.) Secondly, for low p_T heavy quarks, their propagation within the QGP "Browian motion" diffusive type, which can be characterized by well defined transport coefficients such as the spatial diffusion coefficient D_s [22]. This is further related to the fact that the interactions between low p_T heavy quarks and the medium are mostly elastic collisions with small momentum transfer. Next, compared to light partons which are dissolved in the medium, heavy quarks can remain good quasi-particles in a medium with large interaction strength which

makes the modeling of their propagations less complicated. They serve as identifiable tracer particles within the liquid. Additionally, the thermalization of heavy quarks is delayed relative to light partons, by a factor of m_{HQ}/T where m_{HQ} is the invariant mass of the heavy quark and T is the medium temperature [22]. Heavy quarks are not expected to be fully thermalized during the life time of the QGP. Providing this is true, measurements of the collective behavior of heavy quarks can serve as valuable tests regarding the in medium modification of quark hadronization, i.e., the coalescence mechanism. So far it is still unclear if low momentum heavy quarks can reach thermal equilibrium with the medium and participate in the collective expansion of the system [184, 14]. Lastly, the largeness of heavy quark invariant mass also affects their splitting functions, i.e., their parton branching in the medium. It has been proposed that because of the so-called "Dead cone" effect [151], quark energy loss induced by interactions with the QGP medium will depend on its invariant mass value. More in detail, medium induced energy loss can occur via collisional processes (elastic) and gluon radiations (inelastic). The Dead cone effect proposes that the radiative type energy loss follows the below formula [151]

$$dP = \frac{\alpha_s C_F}{\pi}\frac{d\omega}{\omega}\frac{k_\perp^2 dk_\perp^2}{(k_\perp^2+\omega^2\theta_0^2)^2},\ \theta_0 \equiv \frac{M}{E} \tag{2.1}$$

where ω is the energy of the radiated gluon and dP is the differential of radiated power in $d\omega dk_\perp^2$. The energy loss is inversely proportional to the invariant mass of the particle M to the fourth power when the transverse momentum of the radiated gluon ($k_\perp$) is small. In the language of experimental observables, we expect to see $R_{AA}^{\text{heavy quarks}} > R_{AA}^{\text{light quarks}}$ at low transverse momentum ($\mathrm{p_T}$) and a disappearance of this effect at high $\mathrm{p_T}$. Note that this expectation is only valid when the primordial (initial) $\mathrm{p_T}$ spectra of the quarks are identical. Comparison of energy loss between different quarks can test our understanding of the QGP properties and any deviation from this hierarchy structure can provide insights concerning the underlying mechanism of the medium-induced energy loss and hadronization.

Heavy quarks are also great probes for the so-called "Strangeness regeneration"

phenomenon. It is expected [186] that, via the gluon interaction process $gg \rightarrow q_s\overline{q_s}$, an enhancement of strangeness, with respect to hadronic matter, in a thermally and chemically equilibrated state should occur in the QGP if its temperature is above the strange quark invariant mass. The high density of strange quarks in the QGP naturally leads to the abundance of strange and multi-strange hadrons. Measurements from experiments at RHIC on the production of strange baryons and mesons provide systematic supports for this expectation [145, 144, 143, 142, 141, 139, 138, 136]. Furthermore, charm and beauty quarks, which are produced primarily in the early hard scatterings, can potentially combine with the light thermal quarks and hadronize thereafter (recombination). If recombination is a significant factor of heavy flavor hadronization in the QGP, one expects to see less suppressed D_s^+ and B_s^0 meson yields with respect to generic D and B mesons in the presence of a medium with increased strangeness content [52]. Note that this recombination with light thermal quarks would also make the final heavy flavor hadrons inherit the residual flow dynamics carried by the light quarks. In addition, there will be an interplay between the predicted enhancement of strange quark production and the aforementioned quenching mechanism. The measurement of strange-charm and -beauty mesons can reveal the underlying mechanisms of heavy flavor hadronization in heavy ion collisions.

2.1 A survey of the charm quark

In this section, we will discuss experimental results and corresponding physics significances brought by some of the most important analyses conducted by experiments at LHC. We will focus on the charm quark sector as a more thorough survey was done there, with abundant detailed differential studies available, in comparison to beauty quarks.

We briefly touched on the idea of measuring the medium modifications of hard probes (produced in the primordial hard scatterings) with respect to vacuum (pp collisions) to infer the partonic interactions (with the constituents) of the QGP. Similar concept can be employed for heavy quarks, in particular, their energy loss patterns

and suppressions (or enhancements) of production rates. Significant progress has been made by experiments at RHIC and LHC over the past decade in measuring the $R_{\rm pA}$ and $R_{\rm AA}$ of heavy quarks, pushing our understanding of the medium induced modifications a step forward. In table 2.1 and 2.2, we provide a list of heavy flavor related analyses regarding $R_{\rm pA}$ and $R_{\rm AA}$ measurements (as of January 2019) performed by the ALICE, ATLAS, and CMS experiment at LHC.

2.1.1 Medium modifications of the charm spectra

One method to indirectly measure the production of heavy quarks is to calculate the contributions of the semi-leptonic decays, e.g., $D^0 \to K^- e^- \nu_e$ or $K^- \mu^- \nu_\mu$, from heavy flavor hadrons in the inclusive lepton spectra. In these analyses, the central idea is to subtract a "cocktail" of contributions of non-heavy flavor decay leptons, such as the photonic electrons from the decay of π^0 mesons or the leptons from other vector meson (e.g., J/ψ) decays, from the inclusive lepton spectra. Lepton contributions from heavy flavor decays are actually substantial because the summation of relevant semi-leptonic decay branching ratios is of the order 10%. However, these leptons will contain contributions from both the charm quarks and the feed-down from beauty quarks, i.e., $b \to c \to e$ (μ). It is possible to separate the two contributions by exploiting the relatively long lifetime of beauty hadrons and selecting on impact parameters [63]. The $R_{\rm AA}$ of heavy flavor electrons at mid-rapidity with $\rm p_T$ down to 0.5 GeV/c in two centrality (a quantity that characterizes the degree of event activity. A smaller number indicates a stronger activity) intervals measured in PbPb collisions at $\sqrt{s_{\rm NN}} = 2.76$ TeV from the ALICE experiment [73] is shown in Fig. 2-2. The yields of electrons from heavy flavor hadron decays are found to be suppressed strongly which can be interpreted as due to the partonic energy loss in a QGP produced in the PbPb collisions. The results are compared with model calculations that include interactions between heavy quarks and the medium, as shown in the same figure. At such low $\rm p_T$ region, the nuclear modifications of the parton distribution function (nPDF) can play a significant role because of the shadowing (and anti-shadowing) effects presented in the low x region ($\rm x = 10^{-1} \approx 10^{-2}$, which is the fractional momenta

Table 2.1: Summary of nuclear modification factor ($R_{\rm AA}$) measurements on charm flavor (open and closed mesons) from the ALICE, ATLAS, and CMS experiment at LHC.

charm sector			
probe	colliding system	$\sqrt{s_{\rm NN}}$(TeV)	reference
ALICE			
Λ_c baryons	PbPb	2.76	[71]
D^0, D^+, D^{*+} mesons	PbPb	5.02	[72]
	PbPb	2.76	[10, 4, 44]
D_s^+ mesons	PbPb	2.76	[60]
D^0, D^+, D^{*+}, D_s^+ mesons	pPb	5.02	[51, 55, 59]
heavy flavor electrons	PbPb	2.76	[64, 73]
	pPb	5.02	[61]
heavy flavor muons	PbPb	2.76	[43]
	pPb	5.02	[65]
inclusive J/ψ mesons	PbPb	5.02	[66]
	PbPb	2.76	[45, 50, 9, 58]
	XeXe	5.44	[70]
	pPb	8.16	[11]
	pPb	5.02	[2, 7, 5]
ψ(2S) mesons	PbPb	2.76	[9]
	pPb	2.76	[3, 8]
Υ(1S), Υ(2S) mesons	PbPb	5.02	[77]
Υ(1S) mesons	PbPb	2.76	[53]
Υ(1S), Υ(2S) mesons	pPb	5.02	[54]
ATLAS			
heavy flavor muons	PbPb	2.76	[83]
prompt J/ψ mesons	PbPb	5.02	[84]
	pPb	5.02	[82]
Υ (1S) mesons	PbPb	5.02	[82]
CMS			
charm-tagged jet	pPb	5.02	[115]
D^0 mesons	PbPb	5.02	[126]
	PbPb	2.76	[111]
prompt J/ψ mesons	PbPb	5.02	[123]
	PbPb	2.76	[105, 117]
	pPb	5.02	[118]
ψ(2S) meson	pPb	5.02	[125]

(of individual nucleon) carried by individual partons). As we can see, the results are better described when the shadowing effects are included in a theoretical calculation

Table 2.2: Summary of nuclear modification factor ($R_{\rm AA}$) measurements on beauty flavor (open and closed mesons) from the ALICE, ATLAS, and CMS experiment at LHC.

beauty sector			
probe	colliding system	$\sqrt{s_{\rm NN}}$(TeV)	reference
ALICE			
beauty flavor electrons	PbPb (pPb)	2.76 (5.02)	[63]
non-prompt J/ψ mesons	PbPb	2.76	[6]
	pPb	5.02	[74]
ATLAS			
non-prompt J/ψ mesons	PbPb	5.02	[84]
	pPb	5.02	[82]
CMS			
beauty-tagged jets	PbPb	2.76	[109]
	pPb	5.02	[113]
non-prompt J/ψ mesons	PbPb	5.02	[123]
	PbPb	2.76	[105, 117]
	pPb	5.02	[118]
Υ(1S), Υ(2S), Υ(3S) mesons	PbPb	5.02	[130]
	PbPb	2.76	[105, 103, 119]

in both centrality intervals. We will return to nPDF effects shortly.

In Fig. 2-2, a similar result but using heavy flavor muons from the ATLAS experiment is shown [83]. An even clearer event activity dependence of suppression can be observed. The result is further compared with the $R_{\rm AA}$ of inclusive charged hadrons [80] and prompt D^0 mesons [126] (introduced shortly) measured at $\sqrt{s_{\rm NN}} =$ 5.02 TeV. As we can see, the $R_{\rm AA}$ of heavy flavor muons, which includes contributions from both charm and beauty quarks, is larger than inclusive charged hadrons. This suggests a smaller suppression of muons from heavy flavor hadron decays relative to that of light partons. However, we note that the results should not be compared directly with one another at the same $\rm p_T$ because of the changes in kinematics during the decays and the difference in the initial production spectra. Moreover, we also note that according to the central values of perturbation QCD calculations, the $\rm p_T$ spectrum of heavy flavor leptons is sensitive to charm and beauty quark energy loss at different $\rm p_T$ regions based on the decay kinematics and the $\rm p_T$ differential cross

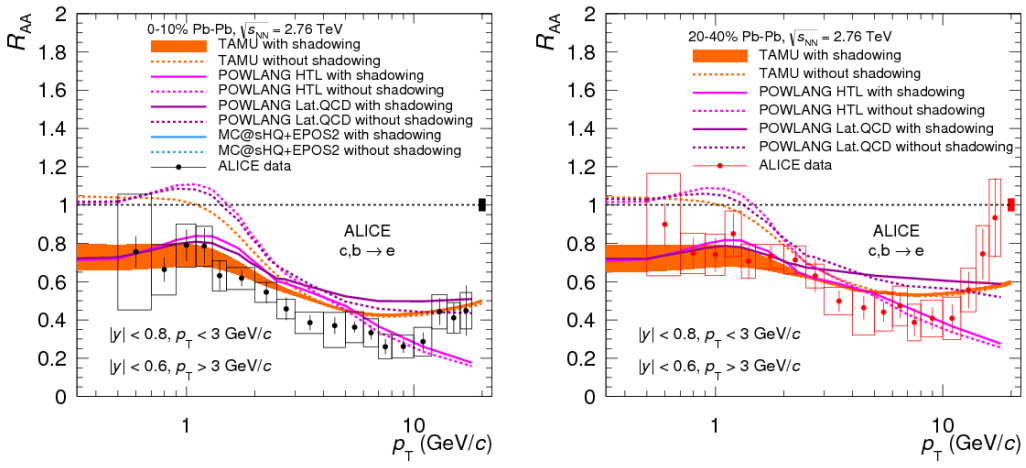

Figure 2-1: The nuclear modification factor (R_{AA}) of heavy flavor electrons at mid-rapidity down to $\mathrm{p_T}$ = 0.5 GeV/c in two centrality intervals (left: 0–10%, right: 20–40%) measured in PbPb collisions at $\sqrt{s_{\mathrm{NN}}}$ = 2.76 TeV from the ALICE experiment [73]. The results are compared with various theoretical predictions with and without the inclusion of nuclear shadowing effects.

sections of parent charm and beauty hadrons. Specifically, leptons with $\mathrm{p_T}$ below 5 GeV/c are more sensitive to charm energy loss while more than 60% of the leptons with $\mathrm{p_T}$ larger than 10 GeV/c originate from beauty quarks. The strong suppressions of muons obtained here correspond to an in-medium energy loss of both charm and beauty quarks.

The other common method employed to measure the modifications of heavy quarks is via a direct reconstruction of a given exclusive hadron decay channel. In this method, one exploits the relatively long decay length of the heavy flavor hadrons by identifying their decay vertices. The invariant mass spectrum can be reconstructed from these identified heavy flavor hadrons and their yields can be extracted accordingly. In Fig. 2-3 and Fig. 2-4, measurements from the ALICE and CMS experiments on the production yields of open charm mesons (consisting of a charm quark and a light flavor anti-quark), the D mesons, in PbPb collisions at $\sqrt{s_{\mathrm{NN}}}$ = 5.02 TeV are shown [44, 4, 10, 72, 111, 126]. In the upper panel of Fig. 2-3 which contains the R_{AA} results of the weighted sum of D^0, D^+, and D^{*+} mesons (non-strange D mesons) measured in the most central collisions, we can see a suppression that is maximal

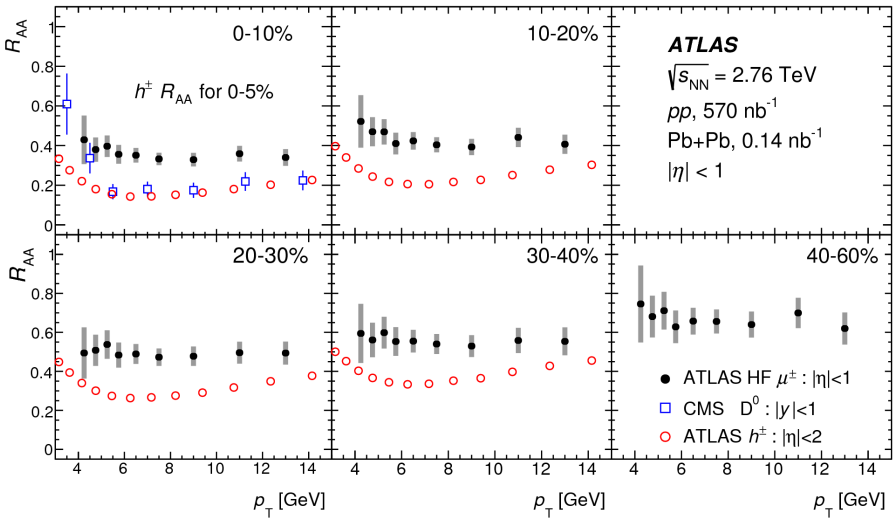

Figure 2-2: The nuclear modification factor ($R_{\rm AA}$) of heavy flavor muons at mid-rapidity with different event centrality (from 10 to 60%) measured in PbPb collisions at $\sqrt{s_{\rm NN}}$ = 2.76 TeV from the ATLAS experiment [83].

at around p_T = 6 to 10 GeV/c where a reduction of the yields by a factor of about 5 with respect to the pp reference is observed. The suppression gets smaller with decreasing p_T for p_T < 6 GeV/c, and the $R_{\rm AA}$ becomes compatible with unity in the interval of 1 < p_T < 3 GeV/c. This can be understood as the potential effects of a collective behavior from the radial flow, creating a "flow bump" centering at the low p_T region. A few different theoretical calculations were superimposed on the same panel for comparison. While most of the models provide a fair description of the data in the region of p_T < 10 GeV/c, we can notice that models without the inclusion of radiative energy loss (BAMPS el., POWLANG, and TAMU) tend to slightly deviate from data in the high p_T region where the effect of medium induced gluon radiation is expected to dominant. A comparison of D meson $R_{\rm AA}$ obtained by the ALICE and CMS experiments is also shown in the lower right panel of Fig. 2-3. The two results are compatible with each other within uncertainty.

In the lower panel of Fig. 2-4, the resulting prompt D^0 meson $R_{\rm AA}$ measured in inclusive centrality by the CMS experiment [126] is compared to the $R_{\rm AA}$ of inclusive charged hadrons [39] at the same collision energy and in the same centrality range.

We can see many similar trends between this figure and Fig. 2-2. In both figures (note the beam energy and centrality differences between the two figures), the R_{AA} of D^0 mesons is different from that of inclusive charged hadrons for $\mathrm{p_T} < 5$ GeV/c while gradually becoming comparable with each other thereafter. This is consistent with a mass dependent energy loss that occurs at around D meson $\mathrm{p_T} = 5$ GeV/c and a disappearance of this effect for higher $\mathrm{p_T}$. However, we want to stress that the differences in fragmentation functions between light partons and charm quarks (harder for charm quarks) can tamper this conclusion and complicate the comparison as proposed in Ref. [149]. Notably, results from non-prompt J/ψ mesons [123] and B^+ mesons [114] are also included in the same panel. In particular, we can readily see a higher R_{AA} of non-prompt J/ψ mesons in comparison to that of inclusive charged hadrons and D mesons. We will discuss the results related to beauty quark in later sections.

2.1.2 Heavy quark diffusion in the medium

The azimuthal anisotropy coefficient v_n is an observable complementary to R_{AA} which aims to deduce the collective behaviors of probes in the medium. Specifically, one measures the degree of anisotropy in the azimuthal momentum distribution of heavy flavor hadrons which encodes the transport properties of the medium. This is because of the collective dynamics of the expanding medium which converts the initial-state spatial anisotropy into final-state particle momentum anisotropy [68] by creating pressure gradients and is most pronounced for low $\mathrm{p_T}$ partons. On the other hand, for high $\mathrm{p_T}$ partons produced in non-central collisions, the two nuclei overlap in an approximately lenticular region, the short axis of this region lies in the reaction plane. Partons emitted in the direction of the reaction plane (in-plane) have, on average, a shorter in-medium path length than partons emitted orthogonally (out-of-plane), leading to a stronger suppression in the latter case. These effects thus cause a momentum anisotropy which can be characterized by the Fourier coefficients v_n, of the distribution of the particle azimuthal angle ϕ relative to the initial-state symmetry

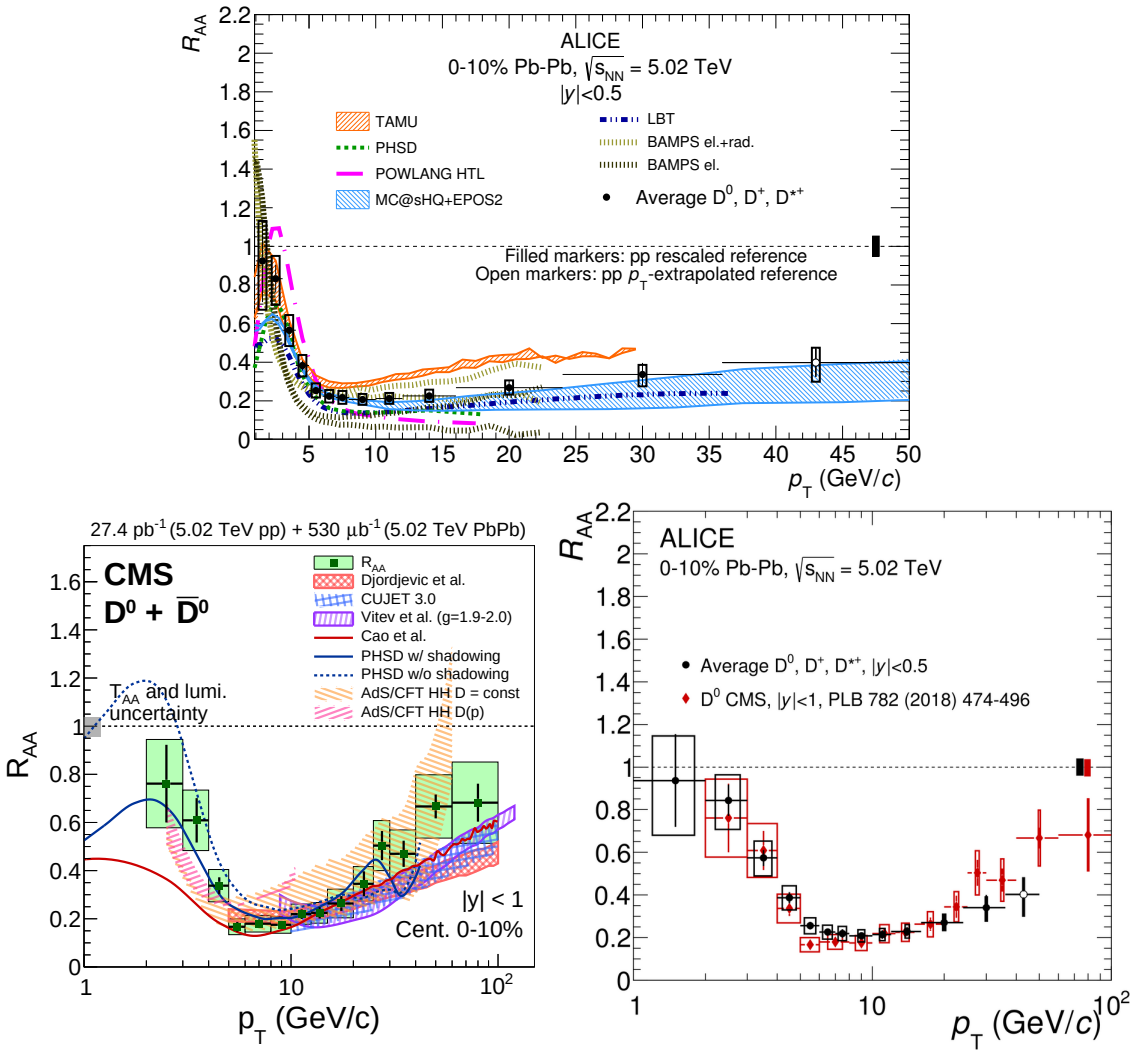

Figure 2-3: Nuclear modification factor ((R_{AA})) measurements of open charm mesons in PbPb collisions at $\sqrt{s_{\mathrm{NN}}} = 5.02$ TeV from the ALICE [72] (upper) and the CMS [126] (lower left) experiment. A comparison between the results obtained by the two experiments is shown in the lower right panel.

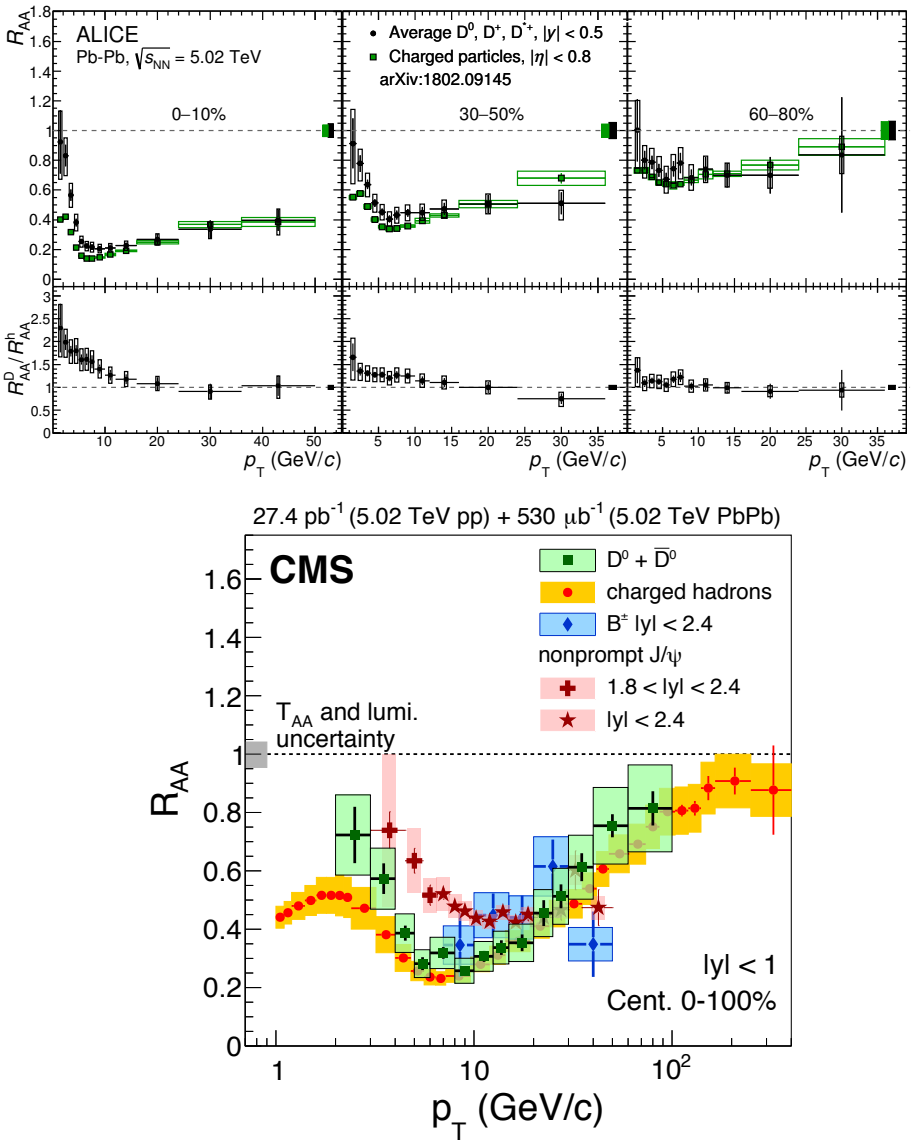

Figure 2-4: Upper: nuclear modification factor ((R_{AA})) measurements in PbPb collisions at $\sqrt{s_{\mathrm{NN}}} = 5.02$ TeV for inclusive charged particles [12] and non-strange D mesons [72] from the ALICE experiment. Lower: similar measurements for inclusive charged hadrons [39], D^0 mesons [126], non-prompt J/ψ mesons [123] (J/ψ mesons from b hadron decays), and B mesons [114].

plane angle Ψ_n (for the n-th harmonic).

$$\frac{d^2\mathrm{N}}{d\phi d\mathrm{p_T}} = \frac{d\mathrm{N}}{d\mathrm{p_T}}[1 + 2\sum_{n=1}^{\infty} v_n(\mathrm{p_T})\cos(\phi - \Psi_\mathrm{n})] \tag{2.2}$$

where Ψ_n is the initial-state spatial plane of symmetry of the n-th harmonic, defined by the geometrical distribution of the nucleons participated in the collision [49]. In non-central collisions, the largest contribution corresponds to v_2=$\left\langle\cos(2(\phi - \Psi_n))\right\rangle$, also known as the elliptic flow. While the measurements of R_{AA} are more connected with the density driven effect which is most effective during the earlier phase of the medium, the transfer of v_2 from the medium to the heavy quark is primarily in the later phases of the evolution. More in detail, the v_2 of heavy flavor hadrons is expected to provide information on the degree of thermalization of heavy quarks in the medium at low $\mathrm{p_T}$ (2 to 3 GeV/c). The participation of heavy quarks in the collective expansion is expected to give a positive v_2. For intermediate $\mathrm{p_T}$ (3 to 6 GeV/c), v_2 is expected to be sensitive to the presence of recombination processes in the hadronization of heavy quarks. At high $\mathrm{p_T}$ ($>$ 6 GeV/c), the v_2 measurement can constrain the path-length dependence of the in-medium parton energy loss, which becomes the dominant contribution to the azimuthal anisotropy and is also predicted to give a positive v_2. In table 2.3 and 2.4, we provide a list of heavy flavor azimuthal anisotropy measurements in pPb and PbPb collisions performed by the ALICE, ATLAS, and CMS experiment at LHC.

In Fig. 2-5, results of the azimuthal anisotropy coefficients, v_2 and v_3, of prompt D^0 mesons in PbPb collisions at $\sqrt{s_{\mathrm{NN}}}$ = 5.02 TeV from the CMS experiment is presented [124]. We can clearly see that the D meson v_2 and v_3 coefficients increase with $\mathrm{p_T}$ to significant positive values in the low $\mathrm{p_T}$ region, reaching a maximal value of 0.1 to 0.2 at around $\mathrm{p_T}$ = 4 GeV/c and then decreasing (slowly) thereafter. This can be interpreted as an interplay between a direct flow thermalization of charm quarks, like those of light partons, and the hadronization of the heavy quarks through the coalescence with light thermal partons which impart their flow dynamic to the heavy mesons, leading to an increase of D meson v_2 with respect to that of charm quarks

Table 2.3: Summary of azimuthal anisotropy (v_n) measurements on charm flavor (open and closed mesons) from the ALICE, ATLAS, and CMS experiment at LHC.

charm sector			
probe	colliding system	$\sqrt{s_{\rm NN}}$(TeV)	reference
ALICE			
D^0, D^+, D^{*+}, D_s^+ mesons	PbPb	5.02	[68, 69]
D^0, D^+, D^{*+} mesons	PbPb	2.76	[46, 49]
heavy flavor electrons	PbPb	2.76	[56]
	pPb	5.02	[67]
heavy flavor muons	PbPb	2.76	[57]
inclusive J/ψ mesons	PbPb	5.02	[62, 76]
	PbPb	2.76	[47]
	pPb	5.02, 8.16	[75]
ATLAS			
heavy flavor muons	PbPb	2.76	[83]
prompt J/ψ mesons	PbPb	5.02	[85]
CMS			
D^0 mesons	PbPb	5.02	[124]
	pPb	8.16	[121]
prompt J/ψ mesons	PbPb	2.76	[117]
	pPb	8.16	[127]

Table 2.4: Summary of azimuthal anisotropy (v_n) measurements on beauty flavor (open and closed mesons) from the ALICE, ATLAS, and CMS experiment at LHC.

beauty sector			
probe	colliding system	$\sqrt{s_{\rm NN}}$(TeV)	reference
ALICE			
beauty flavor electrons	PbPb (pPb)	2.76 (5.02)	[63]
non-prompt J/ψ mesons	PbPb	2.76	[6]
	pPb	5.02	[74]
ATLAS			
non-prompt J/ψ mesons	PbPb	5.02	[85]
CMS			
non-prompt D^0 mesons	PbPb	5.02	[129]
non-prompt J/ψ mesons	PbPb	2.76	[117]
	pPb	8.16	[127]

at low and intermediate p_T. A comparison of the v_2 between non-strange D mesons and D_s^+ mesons could potentially disentangle the two effects which will be discussed shortly. We also notice that the model (TAMU) which includes only collisional energy loss tends to describe the data poorer than models that also incorporate radiative energy loss. The v_2 and v_3 of the inclusive charged hadrons [120] are also superimposed for comparison. For $p_T < 6$ GeV/c, the magnitudes of D meson v_2 and v_3 coefficients are smaller than those of charged hadrons in the centrality classes 10–30% and 30–50%. Similar to inclusive charged hadrons, the D meson v_2 increases with decreasing centrality in the 0–50% centrality range, while the v_3 coefficient shows little centrality dependence. This is consistent with an increasing elliptical eccentricity with decreasing centrality and an approximately constant triangularity stemming from geometry fluctuations.

In Fig. 2-6, results of the non-strange D mesons from the ALICE experiment [69, 68] are presented. In the upper panel, a comparison of v_2 is again made between D mesons and inclusive charged hadrons. A similar trend can be observed. In the bottom panel, a few theoretical predictions are superimposed for comparison. The under-prediction of models without radiative energy loss persist, in addition, we also see that the model (BAMPS) that does not include the effects of quark hadronization via recombination seems to describe the data slightly poorer.

2.1.3 Heavy quark hadronization in the QGP

To further determine the relevance of quark hadronization via coalescence in medium, one possibility is to investigate the productions of Λ_c baryons and D_s^+ mesons. The recombination of charm quarks with light quarks in the medium can lead to an enhanced baryon-to-meson ratio at low and intermediate p_T in comparison to that expected in pp collisions. As a result, one expects to see a higher Λ_c^+ baryon over D^0 meson yield ratio in PbPb collisions with respect to pp collisions. Furthermore, in the case of charm baryon, the possible existence of light di-quark bound states in the QGP could further enhance this ratio in the coalescence model. Similarly for D_s^+ mesons, an enhanced D_s^+ meson over non-strange D meson ratio can be introduced by the

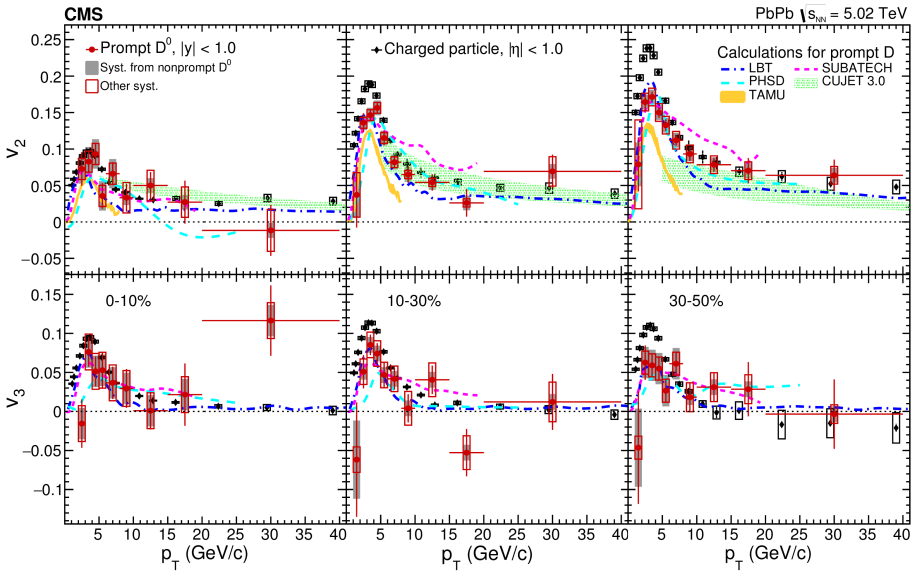

Figure 2-5: Prompt D^0 meson azimuthal anisotropy coefficients, v_2 and v_3, in PbPb collisions at $\sqrt{s_{\mathrm{NN}}} = 5.02$ TeV from the CMS experiment [124].

charm-strange quark recombinations. Thus the study of non-strange D mesons, D_s^+ mesons, and Λ_c^+ baryons could help disentangling the effects between recombination and radial flow.

This possibility, which is a marker of a deconfined medium, was indeed explored by the ALICE experiment. In Fig. 2-7, the Λ_c^+/D^0 yield ratios which were measured in pp collisions at $\sqrt{s} = 7$ TeV and in pPb and PbPb collisions at $\sqrt{s_{\mathrm{NN}}} = 5.02$ TeV are shown in the left panel [71]. A larger Λ_c^+/D^0 yield ratio in PbPb than in pp collisions, differs by about two standard deviations, can be observed clearly. This observation is qualitatively in agreement with a scenario where a significant fraction of charm quarks hadronize via coalescence with light quarks from the medium, leading to an enhanced baryon production with respect to that of mesons. In the right panel, the R_{AA} values between Λ_c^+ baryons, non-strange D, and D_s^+ mesons are shown. The measurement of D_s^+ mesons in PbPb collisions is shown in Fig. 2-8 and compared with model predictions which include the effects of hadronization via recombination. While one model (TAMU) predicts a sizable difference between non-strange D meson and D_s^+ meson R_{AA} at $\mathrm{p_T}$ around 2 GeV/c, the other model (PHSD) predicts the

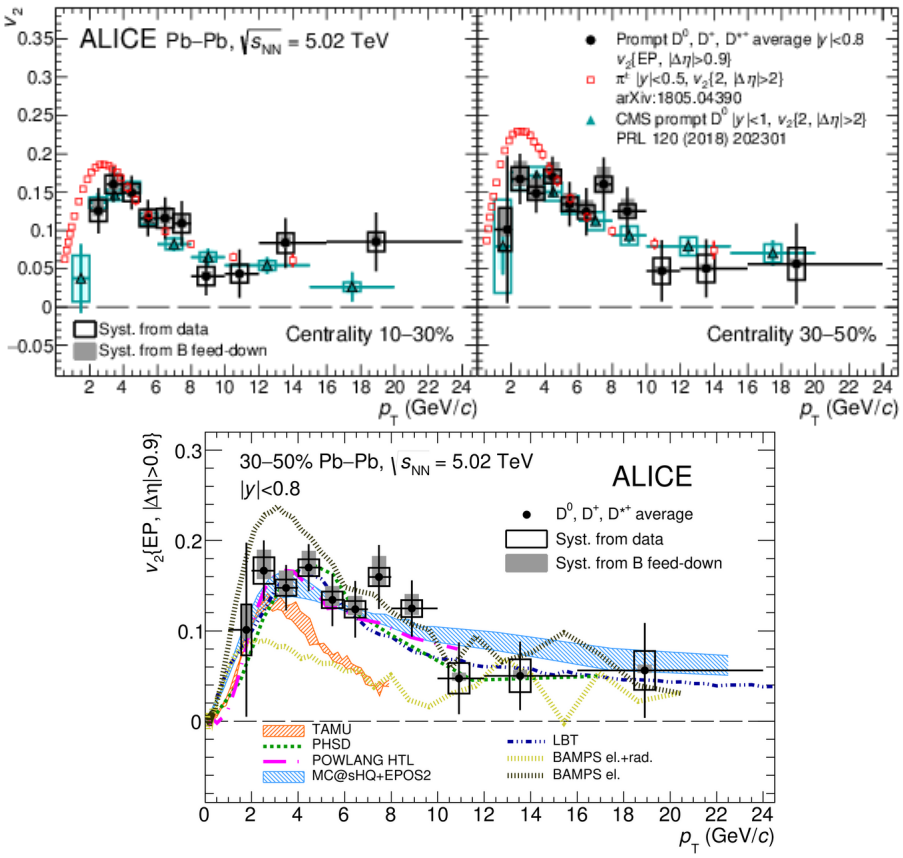

Figure 2-6: Non-strange D meson (D^0, D^+, and D^{*+}) azimuthal anisotropy coefficients, v_2, in PbPb collisions at $\sqrt{s_{\mathrm{NN}}} = 5.02$ TeV from the ALICE experiment [69, 68].

effect to be very small. Measurements extend toward lower p_T region are crucial to fully understand the hidden details.

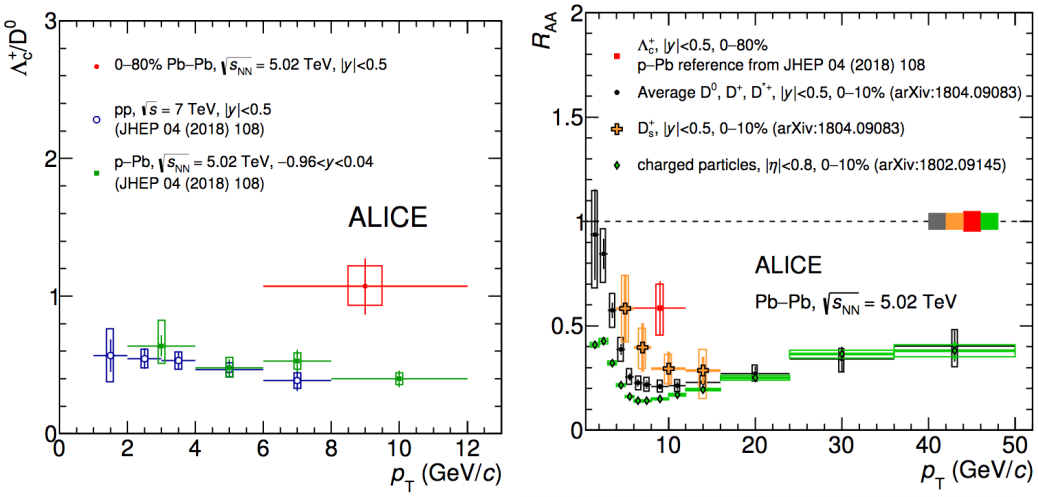

Figure 2-7: Left: the Λ_c^+/D^0 yield ratios measured in pp collisions at $\sqrt{s} = 7$ TeV and in pPb and PbPb collisions at $\sqrt{s_{\rm NN}} = 5.02$ TeV by the ALICE experiment [71]. Right: Comparison of nuclear modification factors ($R_{\rm AA}$) between inclusive charged hadrons, Λ_c^+ baryons, non-strange D mesons (D^0, D^+, and D^{*+}), and D_s^+ mesons.

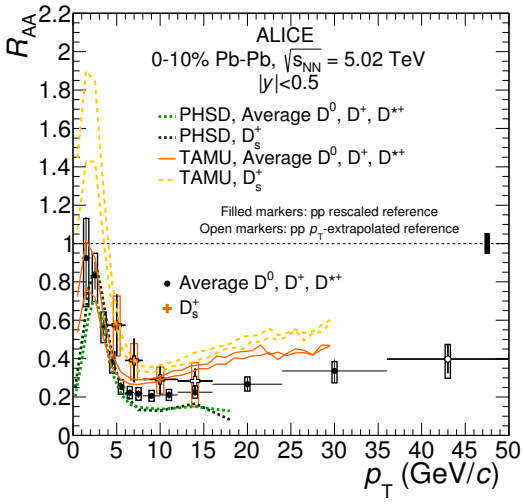

Figure 2-8: Comparison of nuclear modification factors ($R_{\rm AA}$) between non-strange D mesons (D^0, D^+, and D^{*+}) and strange-charm D_s^+ mesons from the ALICE experiment [72].

2.1.4 Cold nuclear matter effects and the surprise in pA collisions

Lastly, we finish our survey of the charm sector by briefly commenting on the initial nuclei matter effects, the cold nuclear matter (CNM) effects. These effects attribute to the modification of parton distribution function in bound nucleons with respect to free nucleons. At current LHC beam energy, the most relevant parts come from the incoherent multiple scatterings, the shadowing effect, which reduces the parton density at low x region. It is important to understand the CNM effects because, similar to the effects of the QGP, they too can alter the spectra of experimental observables such as the aforementioned nuclear modification factor. Experimentally, this can be achieved by investigating the pPb collisions where only minimal QGP is expected to be formed. Example results of the nuclear modification factors in pPb collisions (R_{pA}) from the ALICE experiments are shown in Fig. 2-9. In the left panel, non-strange D mesons R_{pA} [59] is shown and its structure can be well described by models that include the CNM effects. The modification induced by the nuclear shadowing dynamics which reduces the D meson production rate is most pronounced at low $\mathrm{p_T}$. In the right panel, heavy flavor muons R_{pA} [65] measured in the backward rapidity (forward direction is defined as the direction lead ions going toward) is shown. At the backward region, the effects from nuclear anti-shadowing which leads to an increased parton density, are expected to present.

The above results seem to suggest the suppression of production yields we observed in PbPb collisions might be originated from the presence of the QGP because the patterns of R_{AA} and v_n we measured in PbPb collisions match the expectation of the formation of a hot and dense medium and the CNM effects we observed in pPb collisions are not sufficient to explain this large suppressions in PbPb collisions. Surprisingly, indications of long-range anisotropies also appeared in pPb collisions. In Fig 2-10, v_2 measurements of heavy quarks in pPb collisions are presented. In the left panel, the v_2 of prompt D^0 mesons in pPb collisions at $\sqrt{s_{\mathrm{NN}}} = 8.16$ TeV measured by the CMS experiment [121] is shown (as red markers). Positive v_2 values

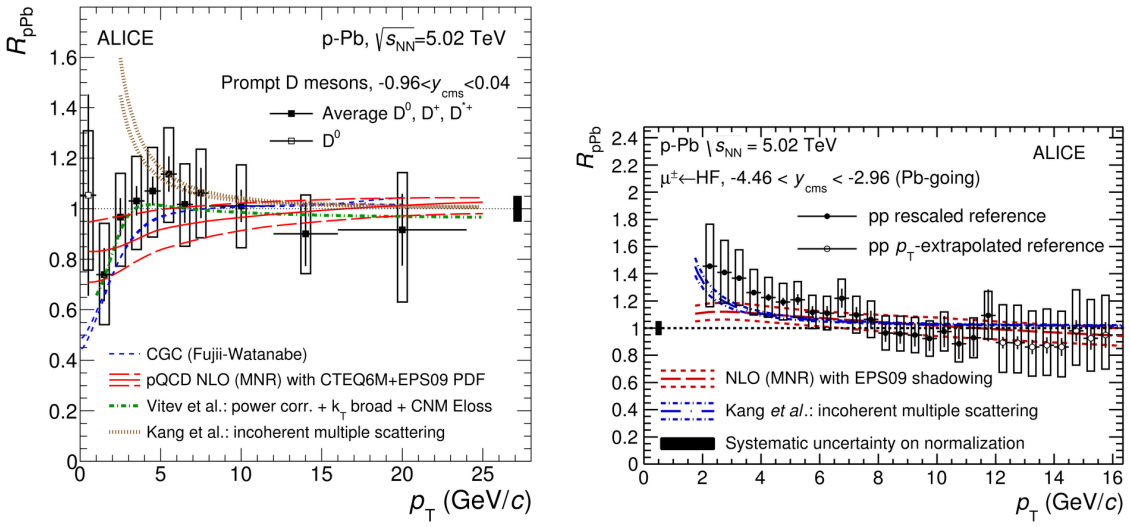

Figure 2-9: Nuclear modification factors (R_{pA}) of non-strange D mesons [59] (left) and heavy flavor muons [65] (right) measured in pPb collisions from the ALICE experiments.

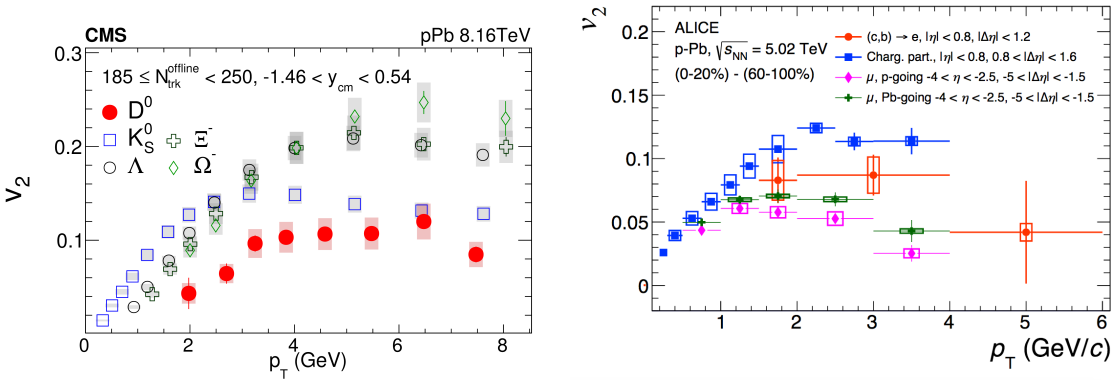

Figure 2-10: Azimuthal anisotropy coefficient, v_2, of D^0 mesons [121] (left) and heavy flavor electrons [67] (right) measured in pPb collisions from the CMS and ALICE experiments.

throughout the p_T interval between 1.5 to 8 GeV/c with a similar pattern to that in PbPb collisions are observed. In the right panel, the v_2 measurements of heavy flavor electrons in pPb collisions at $\sqrt{s_{NN}}$ = 5.02 TeV measured by the ALICE experiment [67] is shown (as red markers) together with the v_2's of inclusive charged hadrons and muons. The patterns of v_2 between different particle mass, light versus heavy quarks, of pPb collisions is very similar to that of PbPb collisions. This evidence seems to suggest a hot QGP medium has been formed at a significantly reduced collision system size while the R_{AA} results suggest otherwise. Much efforts have been made from both theoretical and experimental communities, trying to understand the delicate tensions between the R_{AA} and v_2 results by having a small QGP system that can induce a large flow while only minimally change the momentum of the probes. Other potential interpretations focusing on initial state effects, such as gluon saturation within the Colour Glass Condensate (CGC) effective theories where long range color strings/tubes (resulted from the saturation of parton phase space) connecting partons with different momentum direction are created, or the multiple scattering of partons with the spectator nucleons traveling in the longitudinal direction (comover interactions), are also being studied.

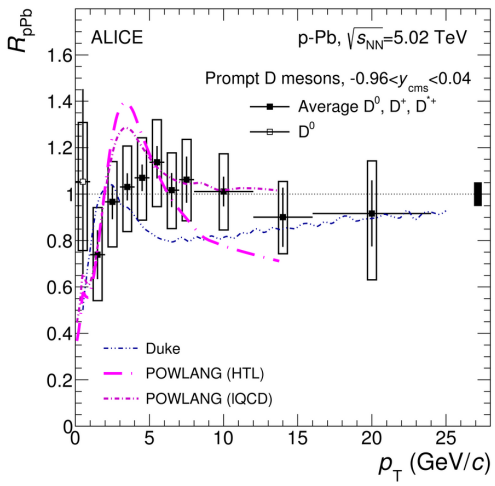

Figure 2-11: Nuclear modification factors (R_{pA}) of non-strange D mesons [59] compared with transport models that include the presence of a medium in the pPb collisions.

Toward the end of the section, we present a comparison of the non-strange D meson $R_{\rm pA}$ with predictions from two transport models that assume a QGP is formed in the pPb system (Fig. 2-11). As we can see, current precision of the measurements does not allow us to draw conclusions on the role of the CNM effects from the possible presence of a hot medium effects. The correct interpretation that can capture $R_{\rm pA}$ and v_2 simultaneously remains an open question to be further studied in future analyses.

2.2 A beautiful probe

In the previous section, we presented a survey of current charm quark measurements. We focused on selected results that brought the most significant impacts and briefly discussed the insights they represent. At the beginning of this chapter, we presented the importance and benefits of using heavy quarks as probes for the medium properties. We start this section by listing some of the advantages of using beauty quarks (versus charm quarks) to probe the medium. Firstly, in classical kinetic theory, the evolution of a density function $f(x,p)$ in the phase space is described by the "Boltzmann transport" equation [23, 184, 22].

$$\left[\frac{\partial}{\partial t}+\frac{\mathbf{p}}{E}\frac{\partial}{\partial \mathbf{x}}+\mathbf{F}\frac{\partial}{\partial \mathbf{p}}\right]f_Q(x,p)=C[f_Q(x,p)] \tag{2.3}$$

where $\mathbf{F}$ corresponds to an external force term and $C[f_Q]$ indicates the change of (local) density resulted from collisions. This equation essentially follows from Liouville's theorem. The key is the determination of the collision term which Boltzmann assumed to be (solely) coming from two body collisions

$$Cf_Q=\int d\mathbf{q}\big[w(\mathbf{p}+\mathbf{q},\mathbf{q})f_Q(x,p+q)-w(\mathbf{p},\mathbf{q})f_Q(x,p)\big] \tag{2.4}$$

where $w(p,q)$ characterizes the rate of collisions (per unit momentum phase space) which change the particle momenta from $\mathbf{p}$ to $\mathbf{p}-\mathbf{q}$, i.e., momentum transfer of $\mathbf{q}$. The first term can be understood as incoming flux where particles with original momentum $\mathbf{p}+\mathbf{q}$ end up with momentum $\mathbf{p}$ and the second term is the outgoing

flux. This rate $w(\mathbf{p},\mathbf{q})$ can be calculated by considering a heavy quark scatters off thermal partons [184, 22].

$$w(\mathbf{p},\mathbf{q}) = \frac{1}{128\pi^2}\int \frac{d^3k}{(2\pi)^3} f_{q,g}(x,p)\frac{|\mathcal{M}_{(q,g),Q}|^2}{E_p E_k E_{p-q} E_{k+q}}\delta^0(E_p + E_k - E_{p-q} - E_{k+q}) \quad (2.5)$$

where $\mathcal{M}$ is the scattering matrix element and $f_{q,g}$ is the density function of light quarks and gluons. Understanding the density function f_Q thus involves solving the above differential-integral equation. One way to simplify this task is by Taylor expanding $w(\mathbf{p}+\mathbf{q},\mathbf{q})f_Q(x,p+q)$ around q

$$w(\mathbf{p}+\mathbf{q},\mathbf{q})f_Q(x,p+q) = w(\mathbf{p},\mathbf{q})f_Q(x,p) + q_i\frac{\partial}{\partial q_i}(wf) + \frac{1}{2}q_i q_j\frac{\partial^2}{\partial q_i \partial q_j}(wf) \quad (2.6)$$

Inserting the corresponding expressions into the above Boltzmann equation yields the "Fokker-Plank" equation [184, 22].

$$\frac{\partial}{\partial t}f_Q = \frac{\partial}{\partial p^i}\Big[A_i(\mathbf{p})f_Q + \frac{\partial}{\partial p^j}[B_{ij}(\mathbf{p})f_Q]\Big] \quad (2.7)$$

where

$$A_i \equiv \int d^3q\ w(\mathbf{p},\mathbf{q})q_i \quad (2.8)$$

and

$$B_{ij} \equiv \int d^3q\ w(\mathbf{p},\mathbf{q})q_i q_j \quad (2.9)$$

which can be directly related to the so-called drag force γ and momentum diffusion coefficient D_p. The Fokker-Plank equation can be further recast to a stochastic differential equation, the Langevin equation, for simulations [22].

$$\Delta\mathbf{p}/\Delta t = -\eta_D(p)\mathbf{p} + \boldsymbol{\xi}(t) \quad (2.10)$$

where ξ is a stochastic term and η characterizes the viscous drag on the heavy quarks due to the medium. Langevin equation is more suited for numerical simulations as it provides a recipe to update the heavy quark momentum through the sum of a

deterministic friction force and a random noise term [23]. Furthermore, the heavy quark transport coefficients can be calculated via lattice QCD, allowing one to establish a link between theoretical predictions and experimental observables. However, the validity of this approximation requires a small momentum transfer q with respect to p which is most readily achievable by having a heavy quark ($M_Q >> gT$) [23]. The heaviness of beauty quarks in comparison to charm quarks can thus improve the precision of this approximation. This can be observed in Fig 2-12 where the R_{AA} and v_2 in PbPb collisions at $\sqrt{s_{\mathrm{NN}}} = 2.76$ TeV were evaluated for different heavy quarks mass in both the Boltzmann and Langevin equation [22]. We can see that for heavier quark mass, the two approaches yield closer distributions, indicating the validity of Langevin approximation [23, 22].

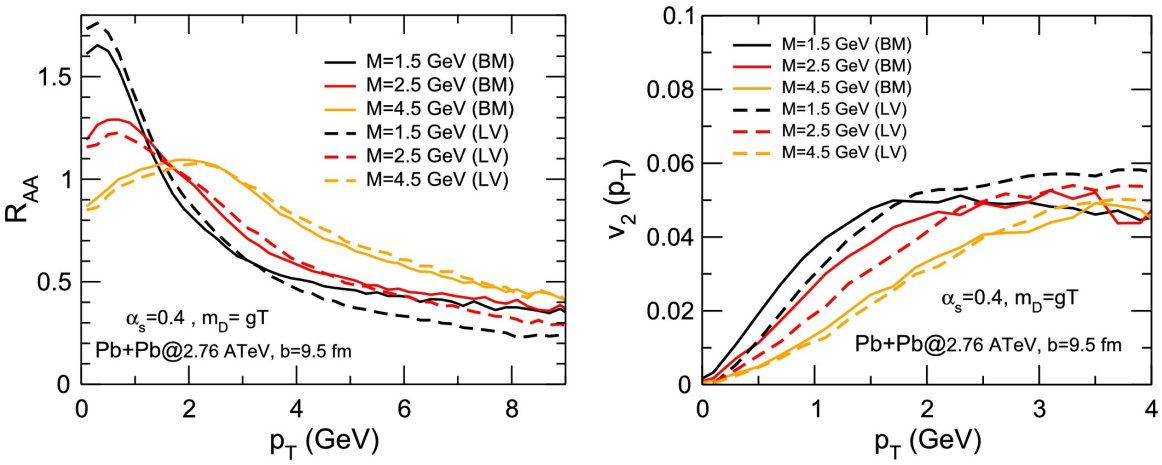

Figure 2-12: Nuclear modification factor (left panel) and elliptic flow (right panel) for heavy quarks in semi-central PbPb ($\sqrt{s_{\mathrm{NN}}} = 2.76$ TeV) collisions for different values of the heavy quark (HQ) mass, in a Boltzmann (solid lines) and in a Langevin approach (dashed lines) [22].

Secondly, lattice QCD simulation which allows one to calculate QCD quantities from first principles and has the advantage of providing non-perturbative answers, not limited to a weak-coupling regime, is one of the most powerful tools for calculating various QGP properties. However, current calculations of the heavy quark transport coefficients in lattice QCD usually involve taking the limit of an infinitely heavy quark where the expectation value of the temporal correlator of the stochastic terms

$\left\langle \vec{\xi}(t)\vec{\xi}(t')\right\rangle$ of the Langevin equation is taken over a thermal bath of gluons and light quarks plus an (infinitely) heavy quark frozen to its position. In this aspect, the heaviness of beauty quarks again enable the validity of this limit and its resulting calculations.

Lastly, we recall a point made earlier regarding utilizing the comparison between light partons and charm quarks to infer the mass dependent energy loss hierarchy. Because of the annihilation and generation of light partons by the QGP, the differences in initial spectra and fragmentation functions, and the contributions from gluon splitting, the suppression patterns observed in the inclusive charged hadron and D meson $R_{\rm AA}$ are complicated convolutions of many effects. In this case, a more pertinent comparison can be made between charm and beauty quarks. In Fig. 2-13 and Fig. 2-14 we refer calculations made in Ref. [22] for the fraction of energy loss as a function of in-medium path length (in fm). As we can see, beauty quark energy loss is substantially smaller than charm quark, especially at the lower energies. This suggests a potential difference between D and B meson $R_{\rm AA}$ might be readily visible at $\rm p_T$ around 10 GeV/c as in the lower panel of Fig. 2-4.

As readers might have noticed in the table, a much larger proportion of experimental efforts had been focusing on the charm sector. The reason is simply because of the much lower production cross section of beauty quarks compared to charm quarks which makes the corresponding measurements exceedingly challenging unless an extraordinary signal to background ratio can be obtained. One way is to indirectly measure the beauty hadrons just like the heavy flavor lepton analyses in which one only measures parts of the final state particles from beauty hadron decays. One example is to reconstruct the so-called non-prompt J/ψ mesons which are J/ψ mesons produced faraway from the collision region. These J/ψ mesons are presumably coming from beauty hadron decays. Since the decay length of a beauty hadron is hundreds of μm, non-prompt J/ψ mesons can be used to identify the presence of beauty hadrons and infer their original kinematics. Results from the ATLAS [82, 84] and CMS [117, 118, 123] experiments (Fig. 2-15) on such measurements indeed indicate substantial suppressions of non-prompt J/ψ meson production rate. In addition to

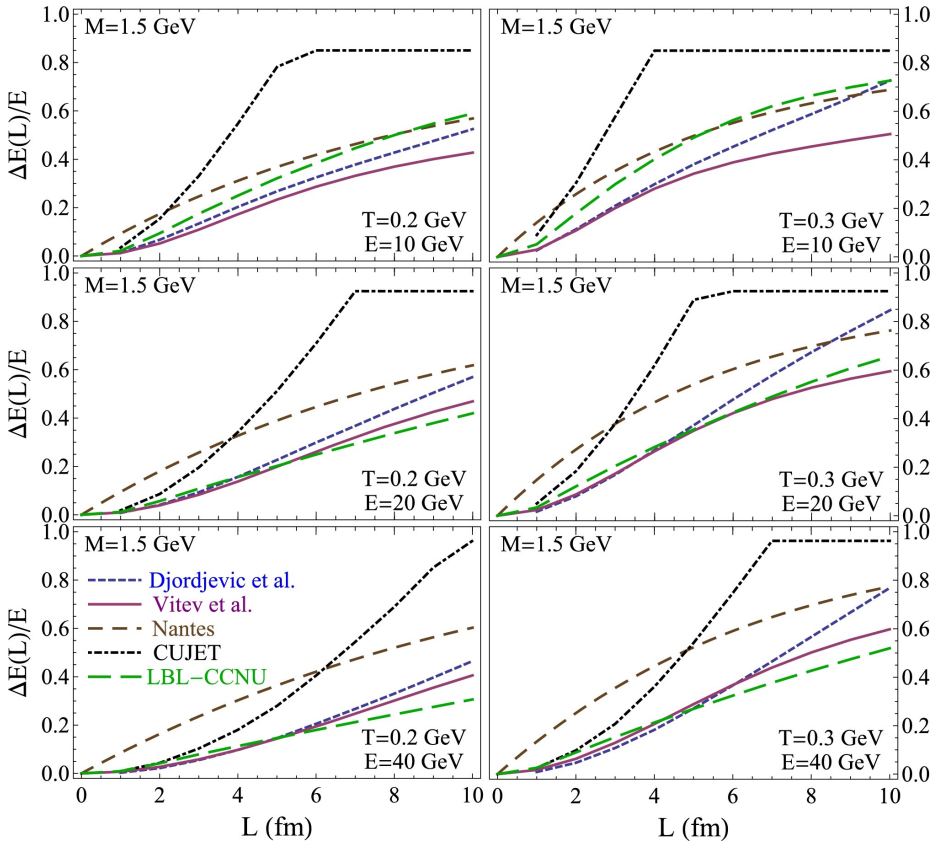

Figure 2-13: Fractional energy loss, $\Delta E/E$, of charm quarks as a function of their path length in a fixed-temperature QGP for various model calculations at two temperatures T and three initial quark energies E [22].

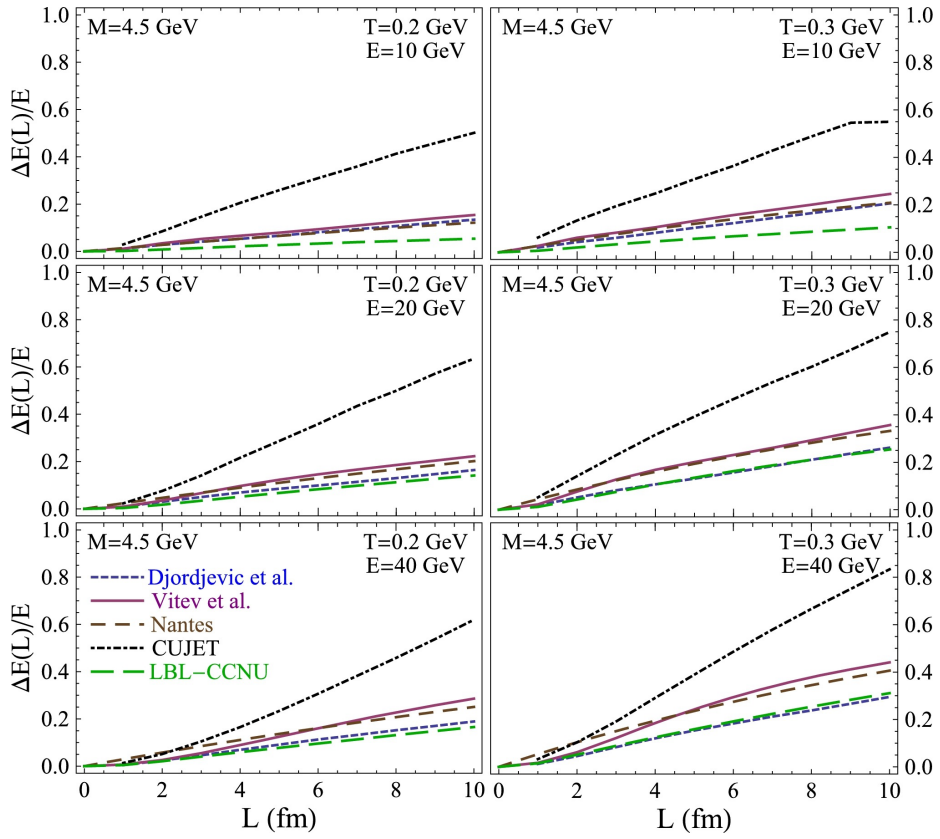

Figure 2-14: Fractional energy loss, $\Delta E/E$, of beauty quarks as a function of their path length in a fixed-temperature QGP for various model calculations at two temperatures T and three initial quark energies E [22].

that, we also see a relatively flat p_T dependence of non-prompt J/ψ R_{AA} comparing to the D meson R_{AA} shown in Fig. 2-3. Interestingly, a mild rapidity dependence which once appeared in the 2.76 TeV data, did not show up again in the 5.02 data. We would like to emphasize that the two sets of results (from 2.76 and 5.02 TeV data) are fully compatible with each other and we should always carefully scrutinize the associated uncertainties of any experimental results before expeditiously drawing a conclusion. If we flip back to Fig. 2-3 again, where this non-prompt J/ψ results were superimposed on the same panel, we can readily observe the fact that the R_{AA} of non-prompt J/ψ mesons is higher than that of D mesons through out the range of p_T between 3 to 11 GeV/c.

Similarly, the azimuthal anisotropy coefficients v_2, can be measured for non-prompt J/ψ mesons. In Fig. 2-16, results obtained by the ATLAS experiment [85] for non-prompt J/ψ mesons in PbPb collisions at $\sqrt{s_{NN}} = 5.02$ TeV are shown. We can see a positive v_2 for non-prompt J/ψ mesons, just like the D meson v_2 which is shown in Fig. 2-5 and Fig. 2-6. Moreover, if one compares the results for p_T interval between 10 to 30 GeV/c, v_2 values of D mesons and non-prompt J/ψ mesons are rather similar, both centering around 0.04. Analogous observations can be seem by comparing the v_2 values measured using heavy flavor leptons as shown in Fig. 2-17 and recalling the transition between charm and beauty quark contributions at around $p_T = 5$ GeV/c. Measurements extending to lower p_T region will be necessary before concluding on the similarity of charm and beauty quarks in-medium collective behavior and relevant underlying mechanisms.

Other approaches include measuring the D mesons and leptons (as we've already seen) from beauty hadron decays. Thus far all the efforts had been indirect measurements, which means the beauty hadrons that came from the hadronization of beauty quarks were not directly measured. The physics objects reconstructed in these measurements are evidently only indirectly linked to the original beauty quark kinematics. One will need to know the changes of kinematics between the beauty hadrons and their decay products to gain full access to the original beauty quark energies. Most importantly, since the beauty hadrons are measured collectively, i.e.,

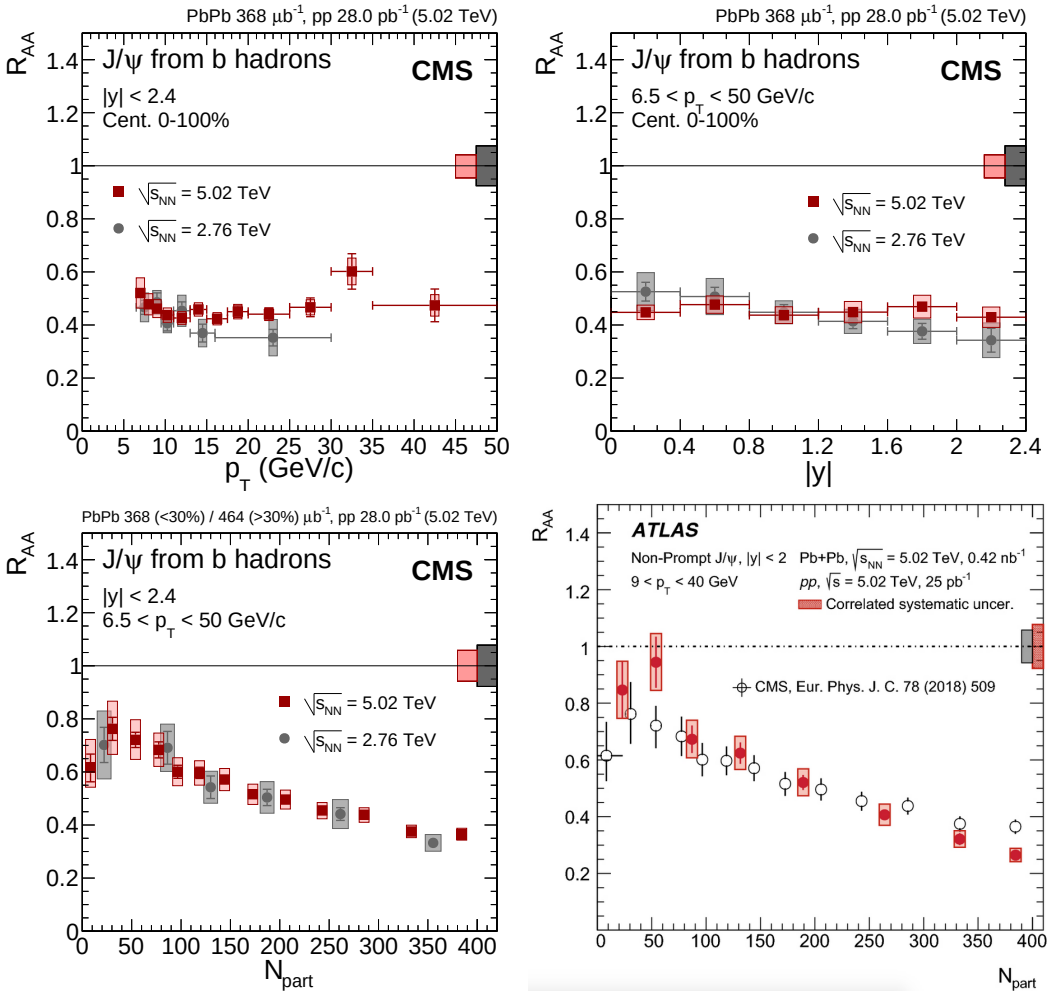

Figure 2-15: Nuclear modification factors (R_{AA}) of non-prompt J/ψ mesons as a function of $\mathrm{p_T}$ (upper left), rapidity (upper right), and centrality (lower left, larger $\mathrm{N_{part}}$ indicates more central collisions) in PbPb collisions at $\sqrt{s_{\mathrm{NN}}} = 2.76$ and 5.02 TeV measured by the the CMS [123] experiment. Similar results from the ATLAS experiment [84] (lower right) is also shown for comparison.

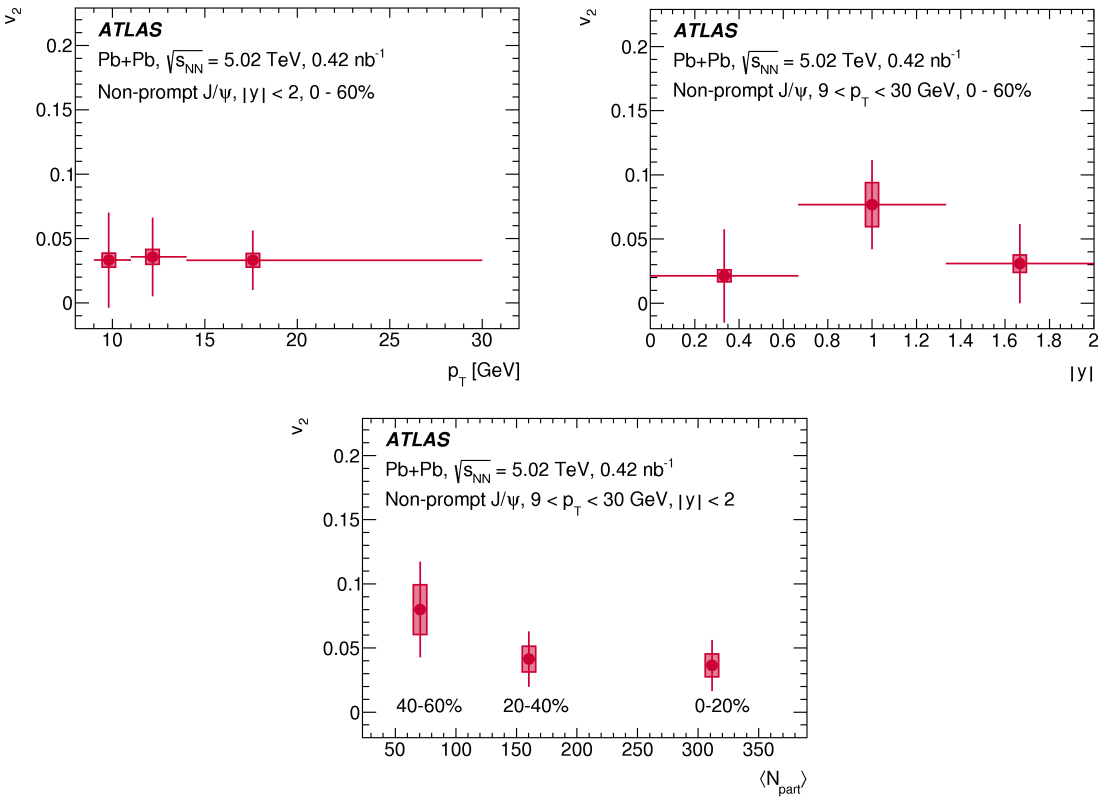

Figure 2-16: Azimuthal anisotropy coefficients v_2, of non-prompt J/ψ mesons as a function of p_T (upper left), rapidity (upper right), and centrality (lower) in PbPb collisions at $\sqrt{s_{NN}} = 5.02$ TeV measured by the ATLAS experiment [85].

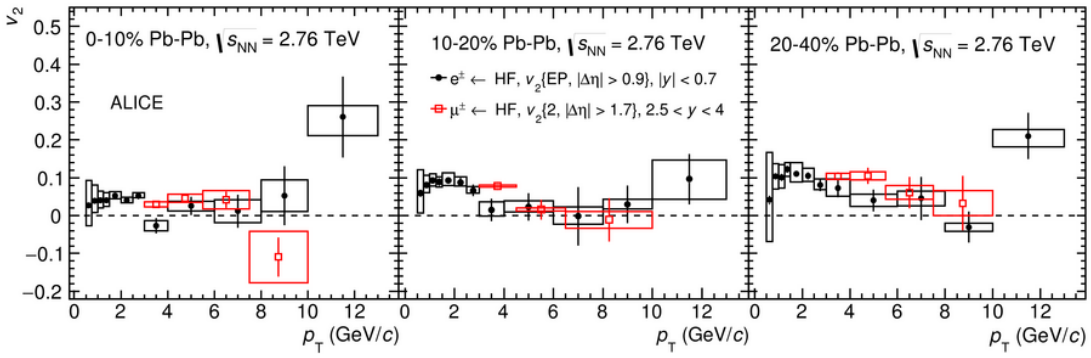

Figure 2-17: Azimuthal anisotropy coefficients v_2, of heavy flavor muons [57] and electrons [56] in PbPb collisions at $\sqrt{s_{NN}} = 2.76$ TeV measured by the ALICE experiment.

one did not distinguish between different beauty hadron species, there is no way to compare the modifications between B^+ and B_s^0 mesons and unveil the recombination and the strangeness regeneration effect.

2.3 The knowns and the known unknowns

We would like to finish this chapter by summarizing some of the lessons we have learned so far from past experiment results and insights that can be drawn for future efforts.

- We saw much evidence of significant suppression, with respect to pp collisions, of charm and beauty hadron production in both direct and indirect measurements in PbPb collisions, suggesting the presence of medium-induced energy loss.

- In addition to suppression, there were also indications of mass-dependent energy loss, especially between the R_{AA} results of light and charm hadrons at low $\mathrm{p_T}$ region.

- On the flip side, comparisons between light and charm flavor is complicated by many factors including the differences in fragmentation functions, initial spectra, and gluon splitting contributions. Furthermore, since light partons are frequently generated and annihilated by the medium, particularly at low $\mathrm{p_T}$ where the dead cone effect is most pronounced, the identity of an in-medium light parton is sketchy. We note that these caveats can potentially be eased by comparing between charm and beauty quark energy loss instead.

- Experimentally, comparisons between direct and indirect measurements can further degrade the validity of a statement because of the changes in kinematics involved in the decays.

- Positive v_2 which indicates the participation of charm quarks in the collective expansion of the medium were observed.

- The entanglement between 1) a scenario where a genuine radial flow of (fully) thermalized charm quarks was created in the QGP; and 2) the effects coming from hadronization via quark recombination where charm quarks partially inherit the flow dynamics of the corresponding light partons, needs to be addressed prior to providing more detail information. At the same time, we want to propose that measurements of other charm hadron species can potentially disentangle these effects. For example, measurements of $c\bar{c}$ meson (e.g., J/ψ meson) v_n would help to quantify the effect from direct charm flow because there is no light flavor involved in this case. The measurements of charm baryon (e.g., Λ_c baryon) v_n can put constraints on the relative strength of the two effects because of the additional light quark inside the baryon (with respect to charm mesons).

- Low $\mathrm{p_T}$ measurements of the v_2 values of B mesons are necessary before concluding that the collective behavior of charm and beauty quarks within an expanding medium originated from a common mechanism.

- The precise description of the pPb system, regarding whether a thermalized medium is indeed produced during the collisions, remains an open question.

- On the theory side, for a model to precisely describe the data, more often than not both collisional and radiative energy loss need to be incorporated in the calculation.

In this thesis, we will try to address some of the above concerns and questions by performing the first fully reconstructed beauty hadron measurements from the CMS experiment [112, 114, 122]. Specifically, we will present the calculations of the B^+, B^0, and B_s^0 open beauty meson $R_{pA,AA}$ which are the main objectives of the analyses presented in this thesis. As opposed to the indirect measurements, the full decay chains of the beauty hadron are reconstructed via the secondary vertex fitting technique (introduced in later sections). We analyzed the pp and PbPb collision (at $\sqrt{s_{\mathrm{NN}}}$ = 5.02 TeV) data recorded by the CMS experiment. In addition, we also analyzed

the pPb collision data collected at the same energy. Although the aforementioned positive D meson v_2 and experimental evidence of ridge-like structures in both pp and pPb collisions [48, 81, 106] together seem to indicate a small droplet of QGP might have been formed in pPb collisions, nevertheless since the size of this QGP is minimal, medium effects are assumed to be negligible and measurable modifications should be mostly attributed to the presence of the initial nuclei matter with a modified parton distribution function. Results from pPb collisions thus serve as baselines for comparisons with PbPb collisions. However, since each decay channel is reconstructed separately, the branching ratio of these channels, of order 10^{-5}, will greatly reduce the statistics available and is the main drawback of this approach. As a result, the precisions of the measurements presented in this thesis are inevitably lower than those of the indirect measurements. Nevertheless, our results mark the first triumph of a direct measurement of beauty quark energy loss. They unlocked a new door for us to get closer to the yet enigmatic QGP system and will serve as stepping stones for future measurements.

Finally we would like to comment on closed heavy flavor mesons (consisting of a charm (beauty) and an anti-charm (beauty) quark, also known as charmonium (bottomonium)) before proceeding, since so far we have only touched on open heavy flavor mesons. Closed heavy flavor mesons, namely the quarkonia, have long been considered as golden probes of QGP properties. Due to the nature of their production mechanism, quarkonium modification in the QCD medium is related to the so-called "Debye" screening (color screening) effect. Intuitively, this can be understood as the fact that the color force between the two quarks is screened by the presence of deconfined QCD partons. These bound states will thus be dissolved into the medium and the probability of this melting depends on the binding energy of the states. In other words, different quarkonium states will receive different amounts of modifications induced by the QGP. In fact, the foregoing recombination mechanism also participates and contributes to the (re-)formation of the charmoniums. At the LHC energy regime, on average about 30 $c\bar{c}$ pairs are produced in heavy ion collisions [200]. These pairs fall apart as described above. However, by chance a charm quark wandering in the

QCD soup can bump into an anti-charm quark (or vice versa) and re-form a bound state together. Consequently the detailed charmonium medium modification will be an interplay between the two mechanisms. A sequential melting pattern was observed experimentally by measuring the relative yields between J/ψ and Ψ(2S) mesons and between various Υ meson states. Measurements of quarkoniums can provide profound information and insights regarding the fundamental QCD properties but are unfortunately beyond the scope of this thesis.

Chapter 3

Common high energy/particle physics notions

In the following, we will briefly mention a few concepts and terminologies frequently used by the experimental high energy physics community. They will appear multiple times through out the thesis.

Transverse momentum In particle collider experiments, by definition the incoming beams only carry z direction (where the beams are coming from) momenta. A conserved quantity of particular importance is thus the transverse momentum $\mathrm{p_T}$, which is the momentum relative to the beam direction in the x-y plane.

Rapidity and pseudo-rapidity A particularly important quantity of high energy physics is rapidity y, which is defined as

$$\frac{1}{2}\ln\frac{\mathrm{E}+\mathrm{p_z c}}{\mathrm{E}-\mathrm{p_z c}} \tag{3.1}$$

It is additive under boosting which makes it very convenient. In experimental analyses, one often uses another quantity instead, the pseudo-rapidity η

$$\eta = -\ln\,\tan(\theta/2) = \frac{1}{2}\ln\frac{|\mathbf{P}|+\mathrm{p_z c}}{|\mathbf{P}|-\mathrm{p_z c}} \tag{3.2}$$

where θ is the polar angle. This is because in the relativistic limit where light particles are treated as massless, η becomes a good approximation to y.

For the pPb collision data used in this thesis, the collisions were asymmetric. Because of this asymmetry nature, LHC conducted two separate periods of pPb collision data-taking. In the first part of the data-taking (around 60% or $21\,\mathrm{nb}^{-1}$ of the pPb data), the proton beam traveled to the negative η direction (toward Léman lake) with an energy of 4 TeV while the lead beam traveled to the positive η direction (toward Jura Mountains) at 1.58 TeV. The system was boosted to the negative η direction. During the last 40% ($14\,\mathrm{nb}^{-1}$) period, the beams were swapped and the collision system was boosted to the positive η direction.

We will denote the η measured in the lab frame to be η_{lab} and the η in the center of mass frame to be η_{CM}. The relation between the 5.02 TeV pPb collision data is

$$\eta_{\mathrm{CM}} = -(\eta_{\mathrm{lab}}^{\mathrm{1st}} + 0.465) \tag{3.3}$$

for the first data-taking period and

$$\eta_{\mathrm{CM}} = (\eta_{\mathrm{lab}}^{\mathrm{2nd}} - 0.465) \tag{3.4}$$

for the second period. The number 0.465 is the value needed to convert the pseudorapidity in the lab frame to the center of mass frame. The additional negative sign in the conversion formula of the first period is to reverse the proton and lead beam direction such that a fair comparison can be made between the two data-taking periods.

Monte Carlo simulation Monte Carlo (MC) simulation plays a significant role in physics experiments. It provides a direct way to access the relation between a physics process and its corresponding detector signature. In the case of particle physics experiments, an exemplary physics process of interest is a proton-proton collision at some center of mass energy. Different generators calculate and model the physics process differently but in most cases, it involves producing a list of final state particles

resulted from the physics process of interest. PYTHIA8 [189] is one widely used generator in the high energy physics community and is the generator used for analyses presented in this thesis. Once the particle list is generated, simulations (using the GEANT4 package [13]) which model the interaction between generated particles and material comprising the detector will proceed. Responses (raw digits) of detector sensors are simulated accordingly and a "hypothetical" event is created. In most cases, we will "reconstruct" this hypothetical event as if it were true collision data using simulated detector responses. This reconstructed event can then be compared with the generated information (the particle list) and provides important information such as the acceptance or efficiency (introduced in later sections). For heavy ion collisions, additional generators are used to simulate the large number of soft particles induced by the QGP. This is done by using HIJING [192] and HYDJET [176] event generators and superimposing the particle lists on top of the PYTHIA8 generated events.

Centrality As we have qualitatively sketched above, high energy nucleus-nucleus collisions can be imagined as two colliding (Lorentz contracted) discs. Generally speaking, the centrality of a collision can be characterized by the extent of the overlap between the two discs. The closer the transverse distance between the two centroids of the discs (the impact parameter), the more central the collision. Experimentally, what can be measured to quantify this is the energy deposited in the forward direction (in the case of CMS, the responses recorded by the Hadronic Forward calorimeters at pseudo-rapidity of $3.0 < |\eta| < 5.0$). If we assumed a monotonic relation between the impact parameter and the amount of energy participated in a collision (which is a valid assumption in the case when nuclear matter is uniformly distributed in the nucleus volume although in reality, fluctuations usually exist), the closer the transverse distance, the more energy is expected to be deposited by the QGP, resulting in more high momentum final state particles to be measured. For a head-on collision, more energy is expected to be deposited by the QGP, resulting in more high momentum final state particles to be measured. Collision events can thus be categorized or

binned into different "centrality" classes according to their ranking in terms of energy deposits. For example, an event in the 0 to 10% centrality class means it is among the top 10% most central collisions.

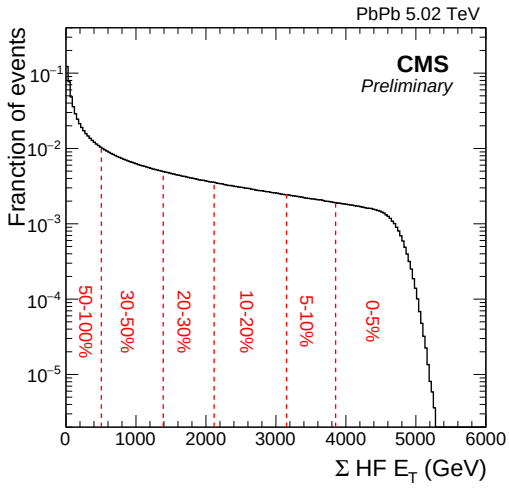

Figure 3-1: Distribution of the sum of HF E_T for a large minimum bias event sample divided into centrality classes [110].

The concept of centrality is not of crucial importance in the context of analyses presented in this thesis as all the results were measured inclusively in centrality (0 to 100%). Nevertheless it is useful to keep this concept in mind as the results from other analyses we will be comparing with were often measured in a differential centrality bin.

Chapter 4

Experimental Apparatus

The experimental data used for this thesis were collected by the Compact Muon Solenoid (CMS) experiment at the Large Hadron Collider (LHC) [31]. It is a particle accelerator experiment that is able to drive particles to an unprecedented speed and smash these particles to each other. In such a high energy collision, a QGP is expected to form. With the outstanding resolution of one of the most advanced particle detector, scientists and students from the CMS collaboration are able to study the QCD medium effect carefully. In this section we will describe the basic layout of the LHC and the CMS experiment.

4.1 The Large Hadron Collider

LHC is the world's largest particle accelerator built by the European Organization for Nuclear Research (CERN). It is designed to provide both proton and lead ion beams to study the physics of standard model and beyond. Protons are generated from the ionization of H_2 plasma enhanced by an electron beam which is used to strip hydrogen nuclei of their electrons. Electric fields along the accelerator switch between positive and negative at a frequency which is carefully tuned so that the accelerated protons are not in a continuous stream, but in closely spaced "bunches." The cylindrical bunches with a radius of 16.6 μm and a length of 7.55 cm group the protons together with a bunch spacing of 25 ns, corresponding to a bunch crossing

frequency of 40 MHz. Protons are subsequently directed and accelerated by the Linear accelerator 2 (Linac2), Proton Synchrotron Booster (PSB), Proton Synchrotron (PS), and Super Proton Synchrotron (SPS) to 50 MeV, 1.4 GeV, 25 GeV, and 450 GeV respectively before transferred to the LHC main ring. For lead ions, it is created from a source of vaporized lead. They enter Linac3 for the first acceleration and then be collected and accelerated by the Low Energy Ion Ring (LEIR), PS, and SPS.

The beams are kept in the LHC ring by superconducting magnets, with a current of 11,850 amps and cooled to 1.9 K by a liquid helium cryogenic system, which produce a magnetic field around 8.33 Tesla. Insertion magnets which squeeze the beams together allow the beams to be directed to the detector and collide with the beams from the opposite direction. During the acceleration, dipole magnets will provide a magnetic field that guides the particles along the design orbit while quadrupole magnets will confine the particles in the vicinity of the design orbit. To account for the energy losses due to synchrotron radiations, specially designed metallic chambers were installed around the ring. They provide a RF voltage of 8-16 MV/beam with carefully tuned frequency. These radio waves interact with the passing bunches and compensate for an energy loss of 7 keV per turn.

The collision data analyzed in this thesis are proton-lead (pPb) collisions collected during 2013 (Run1) and proton-proton (pp) and lead-lead (PbPb) collisions both of which collected during 2015 (Run2). Center of mass energies of these collision data were all $\sqrt{s_{\mathrm{NN}}} = 5.02$ TeV. Cumulated luminosity recorded by the CMS can be found in Fig. 4-2 and Fig. 4-3.

4.2 The Compact muon solenoid

CMS (Fig. 4-4) is a general purpose detector located at interaction point 5 (P5) of the LHC ring. It was built around a superconducting solenoid magnet with an overall length of 13 m and a diameter of 7 m which produces a magnetic field around 3.8 Tesla. For such high intensity magnetic field to work properly, a large iron "return yoke" weighting over 12000 tonnes is used to guide the field. It is able to unam-

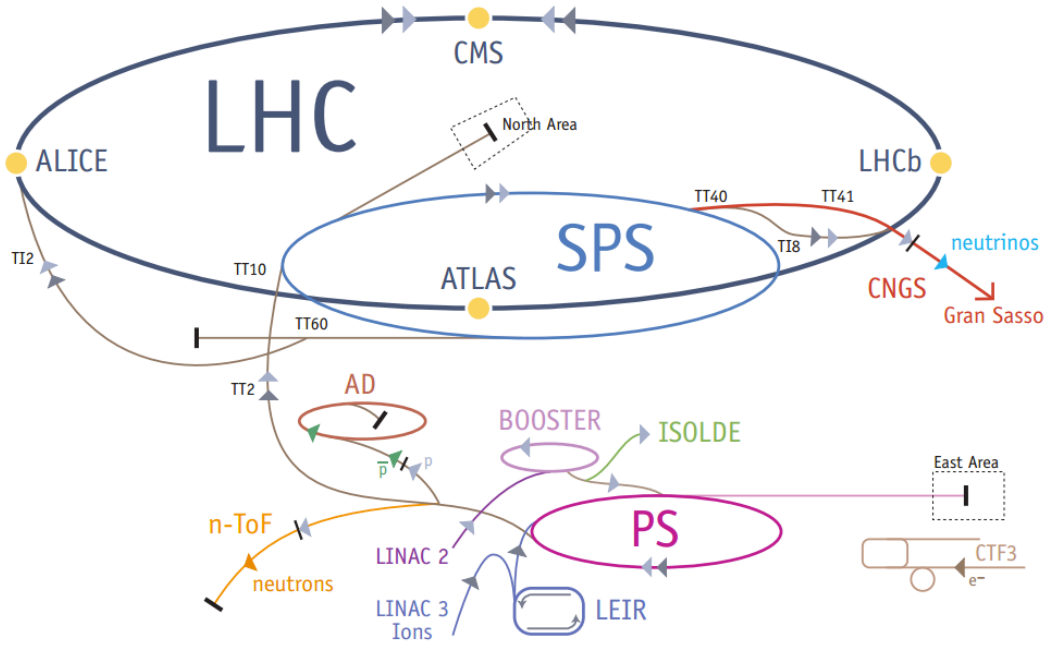

Figure 4-1: A schematics of the LHC with the beam injection sequence.

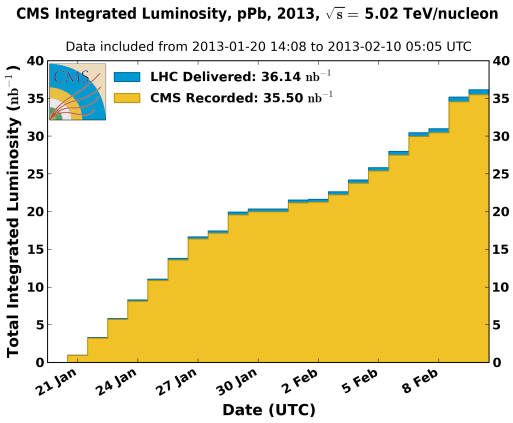

Figure 4-2: The integrated luminosity delivered by the LHC for proton-lead collisions during 2013.

biguously determine the charge sign of TeV scale particles with a momentum resolution of $\Delta p/p \approx 10\%$. Roughly speaking, CMS is composed of the silicon tracking system (tracker), the electromagnetic calorimeter (ECAL), the hadronic calorimeter (HCAL), and the muon chamber. The design of CMS is optimized to well identify muons, charged particles, electrons, and jets with an excellent momentum resolution.

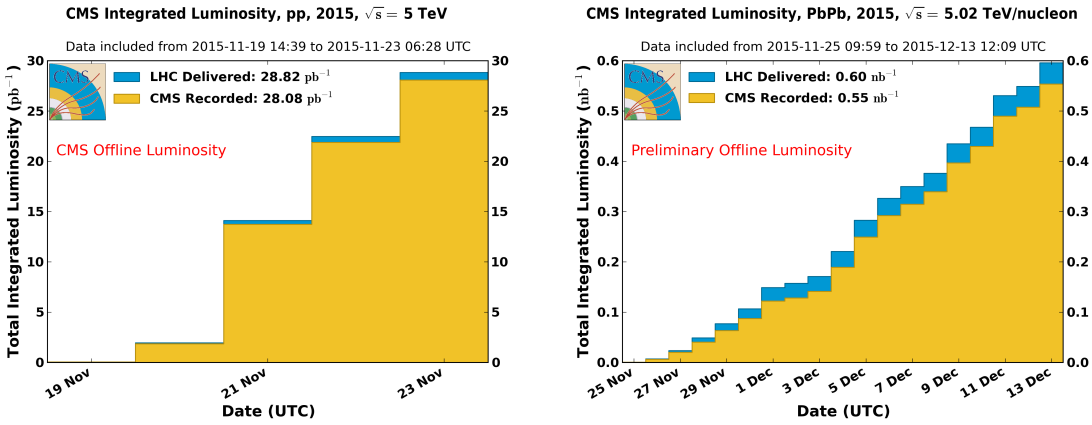

Figure 4-3: The integrated luminosity delivered by the LHC for proton-proton (left) and lead-lead (right) collisions during 2015.

Secondary vertices and impact parameters can also be precisely measured (thanks to the exceptional resolution of the CMS pixel tracker which will be described shortly) for an efficient identification of heavy flavor decays.

The coordinate system of CMS originates from the body center of pixel detector (the inner parts of the tracker) which is the closest sub-detector to the beam spot. The z-axis points along the beam direction (counter-clockwise) toward Jura mountain (located to the west of LHC in the France territory) from P5. The x and y axis then adopt the right-hand rule with x-axis pointing inward to the LHC ring center and y-axis pointing vertically upward. In spherical coordinate, the azimuthal angle ϕ is measured from the x-axis in the $x-y$ plane, while polar angle θ is measured from the z-axis. Conventionally, (sub-)detectors situated at the z direction are called "endcap" while (sub-)detectors surrounding the $x-y$ plane are referred to as "barrel."

4.2.1 Tracking System

The tracking system (tracker) as shown in Fig. 4-5, is situated at the innermost part of CMS. It provides precise measurements of the charged sign, momentum, and trajectory of charged particles. In particular, the reconstruction of the two physics objects (the charged tracks and muons which will be introduced in the next chapter) that were heavily used in this thesis rely on the responses recorded by the CMS

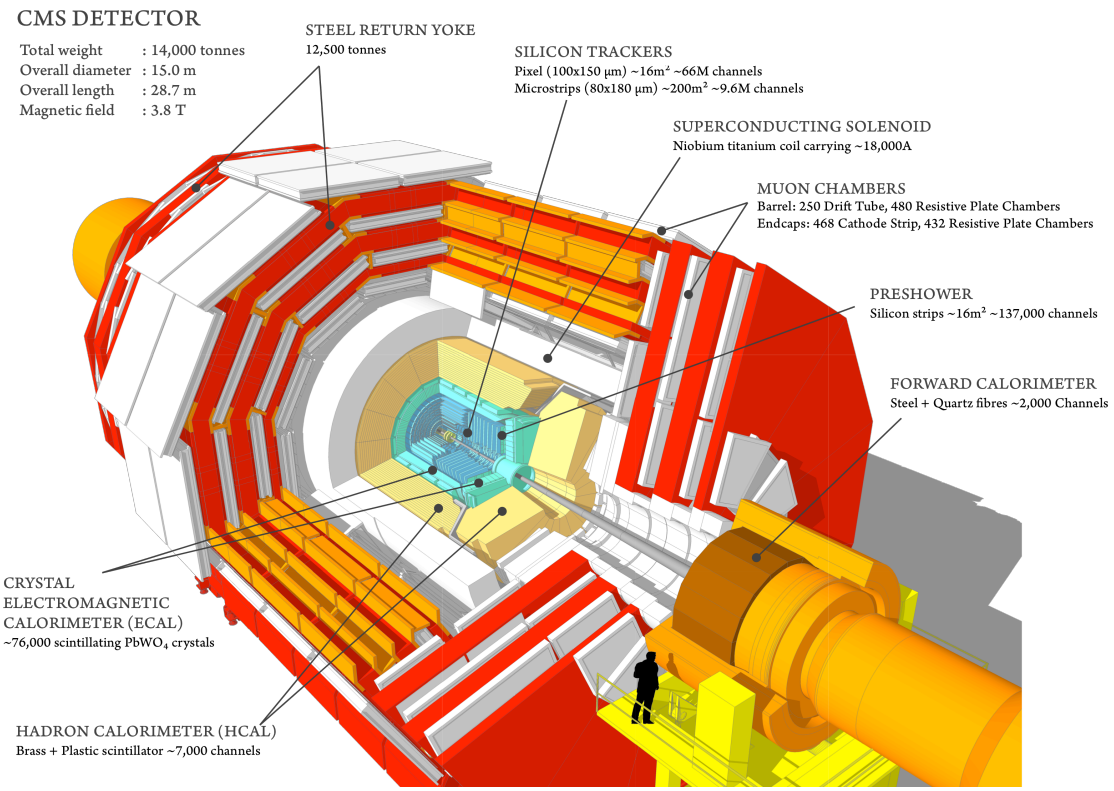

Figure 4-4: An overview of the CMS detector.

tracking system. The CMS tracking system is thus especially crucial for this thesis. When a charged particle passes through the silicon sensors of the tracking system, electrons will be liberated from the silicon atoms creating electron-hole pairs which are collected by electronic chips and recorded. The tracking system covers a $|\eta| < 2.5$ range with about 200 m^2 active area containing 1440 pixel and 15148 strip modules. It consists of two sub-systems, the pixel detector and the strip detector, both made of numerous silicon sensors.

Pixel Tracker The pixel detector is comprised of three barrel layers and two endcap disks on each side of the detector as shown in Fig. 4-6. The three barrel layers are located at 4.4, 7.3, and 10.2 cm from the origin respectively with a length of 53 cm. The endcap disks extending from 6 to 15 cm in radius are being placed at $|z| = 34.5$ and 46.5 cm. Each pixel is a 100×150 μm cell. 48 and 18 million cells cover a total area of 0.78 and 0.28 m^2 for barrel and endcap region respectively. The pixel tracker

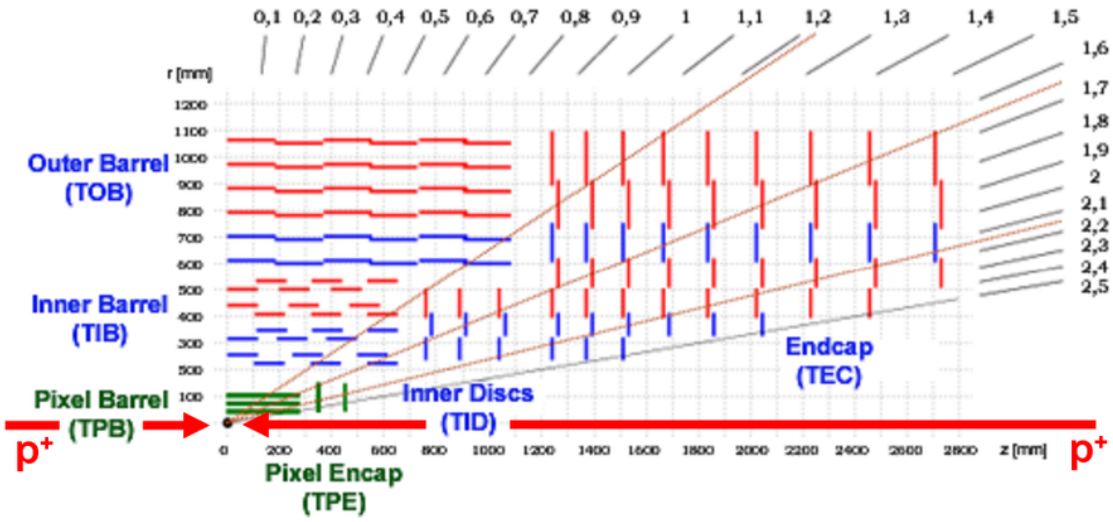

Figure 4-5: The CMS tracker layout. The outer radius is around 110 cm, and the total length in the z direction (along the beam pipe) is approximately 540 cm.

has a spatial resolution of about 10 μ in the $r-\phi$ direction (barrel) and about 20 μm in the z direction (endcap) as can be seem in Fig. 4-7.

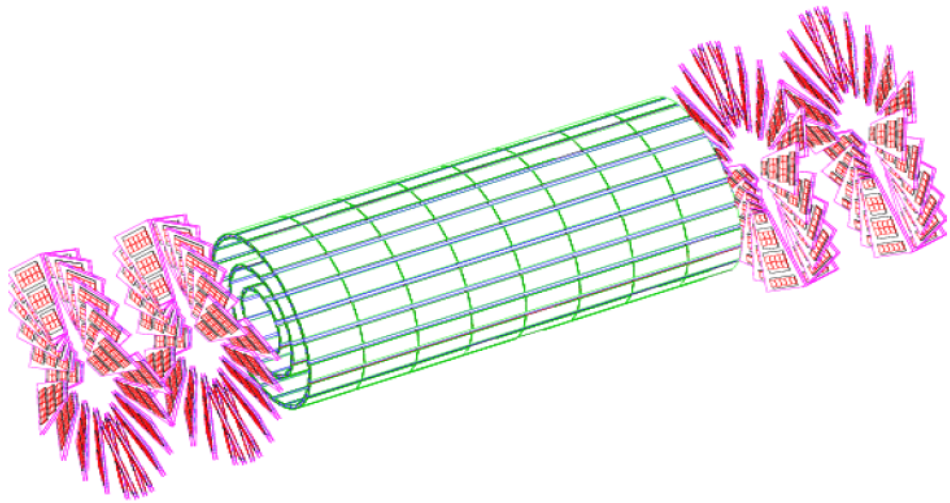

Figure 4-6: Layout of the pixel detector in the CMS tracker.

It it worth mentioning that a new pixel layer had been installed in the CMS pixel tracker during 2017. Unfortunately the analyses presented here were conducted before this installation and did not enjoy the benefits the new pixel layer provids. The reconstruction efficiency of the relevant physics objects used in this thesis is expected

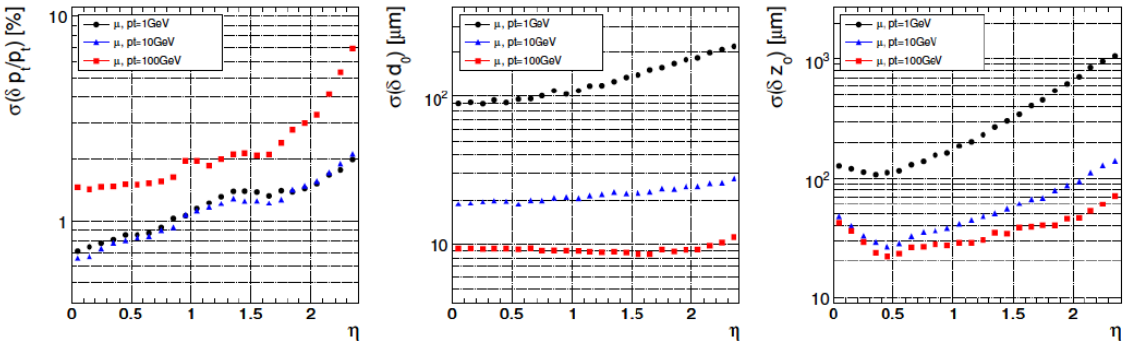

Figure 4-7: Resolutions of track p_{T} (left), d_0 (center), and z_0 (right) with muons p_{T} of 1, 10, 100 GeV/c [94].

to be greatly increased. With the much larger heavy ion collision dataset that is going to be collected in the future LHC data-taking period, the precision of B meson measurements is expected to be significantly improved.

Strip Tracker Between radial region 20 to 116 cm is the strip tracker. The strip tracker can be divided into two parts, the inner and outer strip tracker. The inner tracker consists of the Tracker Inner Barrel (TIB) and the Tracker Inner Disk (TID) systems while the outer system consists of the Tracker Outer Barrel (TOB) and the Tracker End Cap (TEC) systems. TIB has four barrel layers placing at radii 25.5, 33.9, 41.9 and 49.8 cm, stretching along beam line within $|z| < 70$ cm. TIB strip pitches are 80 μm for layer 1, 2 and 120 μm for layer 3, 4 which lead to a resolution of 23 and 35 μm respectively. TID has four disks (on both side), placing between $|z| = \pm 80$ to $|z| = \pm 90$ cm, covering an angle of $|\eta| < 2.5$. The disk spans from 20 to 50 cm in radius with strip pitches varing from 100 to 141 μm. The TIB/TID system is surrounded by the TOB/TEC system. TOB comprises four identical wheels each having 3 inner and outer cylinders. The four wheels are glued together by aluminum elements with a total length of 236 cm (plus cable). The six cylinders have radii of 60.8, 69.2, 78.0, 86.8, 96.5, and 108.0 cm, forming six detection layers with strip pitches varying from 120 to 180 μm, providing a resolution from 35 to 53 μm. The TED, comprising nine disks on each sides ($\pm z$), is located between $|z| = 124$ to

$|z| = 280$ cm. Each disk expands a radius from 22.0 to 113.5 cm with strip pitches varying between 97 to 184 μm. Detail parameters related to the strip tracker are listed in Tab. 4.1.

Table 4.1: Detector types in the silicon tracker [90].

part	No. detectors	thickness (μm)	mean pitch (μm)
TIB	2724	320	81/118
TOB	5208	500	81/183
TID	816	320	97/128/143
TEC	2512	320	96/126/128/143
TEC(2)	3888	500	143/158/183

4.2.2 Electromagnetic Calorimeter (ECAL)

The purpose of CMS ECAL is to measure the spatial positions and the energy/momentum of electrons (positrons) and photons. It is a homogeneous and hermetic detector made of lead tungstate ($PbWO_4$) scintillating crystals which has a shape roughly like a rectangle. When a electron or photon encounters the ECAL, it generates a shower of electrons, positrons and photons. The heavy nuclei of the ECAL crystals collect these particles and excite their bounded electrons to higher energy states. When the excited electrons return to lower orbits, the energy differences will be released in the form of photons (scintillations). The photodetectors or photodiodes, on the ECAL will then collect these photons and generate signal responses. Photodiodes are made of semi-conducting silicons with a strong electric field applied to them. When a scintillation photon strikes the silicon and knocks an electron out, this electron will be accelerated by the electric field and strikes nearby silicon atoms, striping their electrons off as well, which creates an avalanche of electrons. General layout of the CMS ECAL can be found in Fig. 4-8.

Lead tungstate is used as scintillating material. It has short radiation length ($X_0 = 0.89$ cm; this value can be compared with the radiation length of iron which is 1.8 cm), small Moliere radius (2.2 cm), short response time (emits 80% of light

within 25 ns), and high radiation hardness ($\sim$ 10 Mrad). The material is however highly sensitive to temperature. A cooling system to extract the heat dissipated by the read-out electronics is therefore required. During nominal operation, the ECAL is maintained at 18°C with a $\pm$0.05°C tolerance.

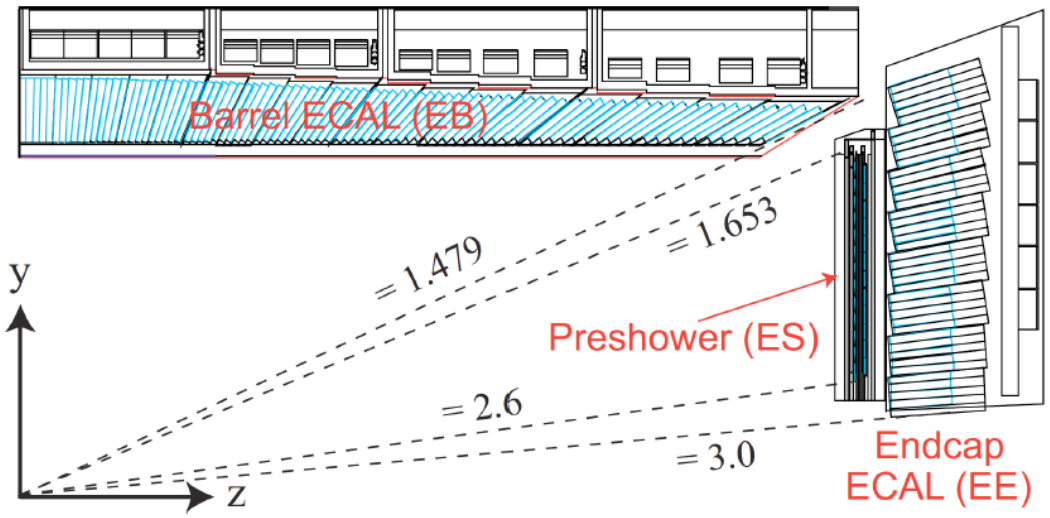

Figure 4-8: Layout of the CMS Electromagnetic Calorimeter system (ECAL).

The ECAL energy resolution can be parameterized by the following expression [90]

$$\left(\frac{\sigma}{\mathrm{E}}\right)^2 = \left(\frac{\mathrm{S}}{\sqrt{\mathrm{E}}}\right)^2 + \left(\frac{\mathrm{N}}{\mathrm{E}}\right)^2 + \mathrm{C}^2, \tag{4.1}$$

where S is a stochastic term, N is a noise term, and C is a constant term. Current beam test shows that S =0.028 $\mathrm{GeV}^{\frac{1}{2}}$, N = 0.12 GeV, and C = 0.003 GeV.

4.2.3 Hadronic Calorimeter (HCAL)

The CMS HCAL is responsible for measuring the energy of hadrons. The HCAL is also a hermetic detector which surrounds the ECAL, covering almost all solid angle except for the beam direction. It is made of sampling calorimeters which comprise alternating layers of dense absorbers and tiles of plastic scintillators. Since the HCAL is placed between the CMS magnet solenoid (R = 2.95 m) and ECAL (R = 1.77 m), it is subjected to a high intensity magnetic field with very limited space. Brass which

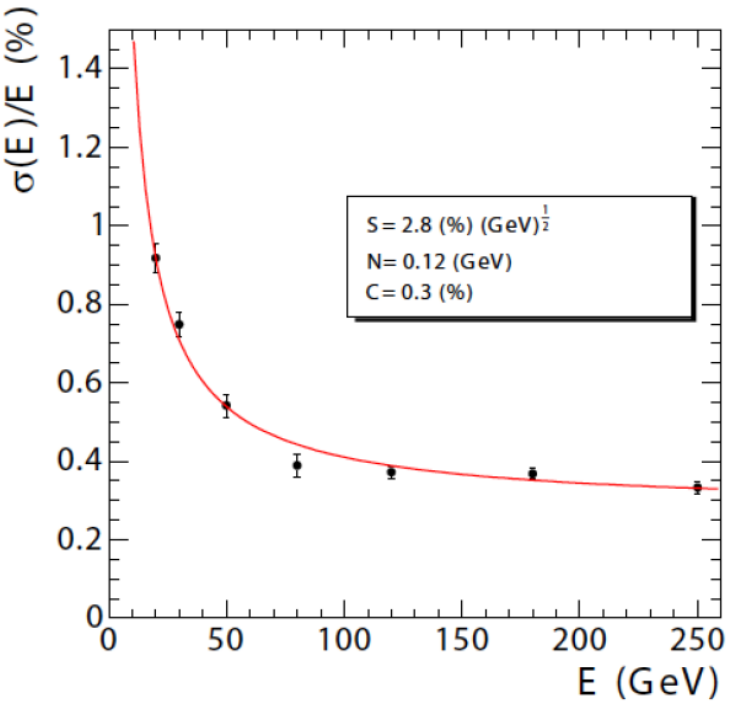

Figure 4-9: ECAL energy resolution as a function of energy measured in an electron test beam [94]. The central value of the stochastic (S), noise (N), and constant (C) terms are shown in the legend.

is a non-magnetic material with short interaction length (λ_l = 16.6 cm); this value is comparable to that of iron and lead; brass is cheaper than lead while being a non-magnetic material as opposed to iron) is thus used as absorber. When a hadronic particle passes through the absorbers, showers of secondary particles will emerge via interactions with the brass material, creating a cascade of showers. These showers will activate the scintillators to emit blue-violet light which will be transformed to green light by the embedded wavelength-shifting fibres. The photons are then transmitted to multi-channel hybrid photodiodes (HPDs) which are designed to operate under a high intensity magnetic field. These optical fibres then carry the light signals to the readout box of a "megatile" which consists of many tiles. Signals from various tiles are then added optically and form a "tower" of energy. The general layout of the HCAL can be found in Fig. 4-10.

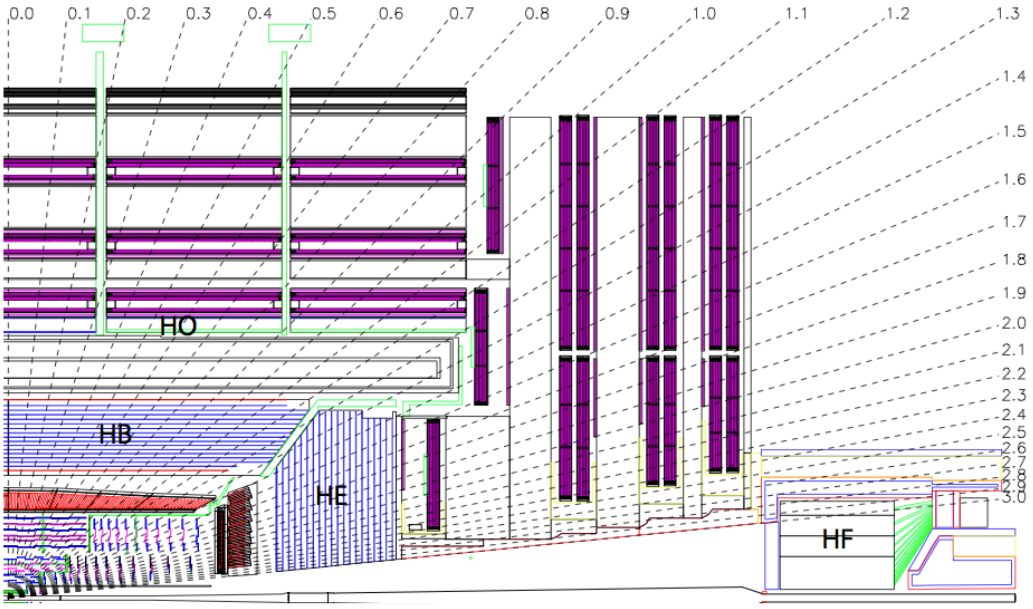

Figure 4-10: Layout of the CMS Hadronic Calorimeter (HCAL).

4.2.4 Muon System

The muon system is the outermost sub-detector of CMS with an overall coverage up to $|\eta| = 2.4$. As the name suggests, it is used for the reconstruction of muons which is one of the physics objects used in this thesis. It is a gaseous detector which can be classified into three different type of chambers, drift tubes (DT), cathode strip chambers (CSC), and resistive plate chambers (RPC). Shown in Fig. 4-11 is a layout of the muon system.

Drift Tube DTs are placed at the barrel region ($|\eta| < 1.2$) where the neutron induced background is small and the magnetic field is low. It is organized into five wheels, each hosting four stations (at radii of 4.0, 4.9, 5.9, and 7.0 m), and sandwiched between the iron yokes. In total, there are 250 DTs in the CMS muon system and each chamber consists of planes of aluminum drift tubes (shown in Fig .4-12). DTs are made of gold-plated stainless-steel wire anodes and cathode strips within an Ar/CO_2 mixed gas volume. A voltage of +3600 V is applied on the wires and -1800 V on the cathodes. When a muon passes through the gaseous, it knocks the electrons out of

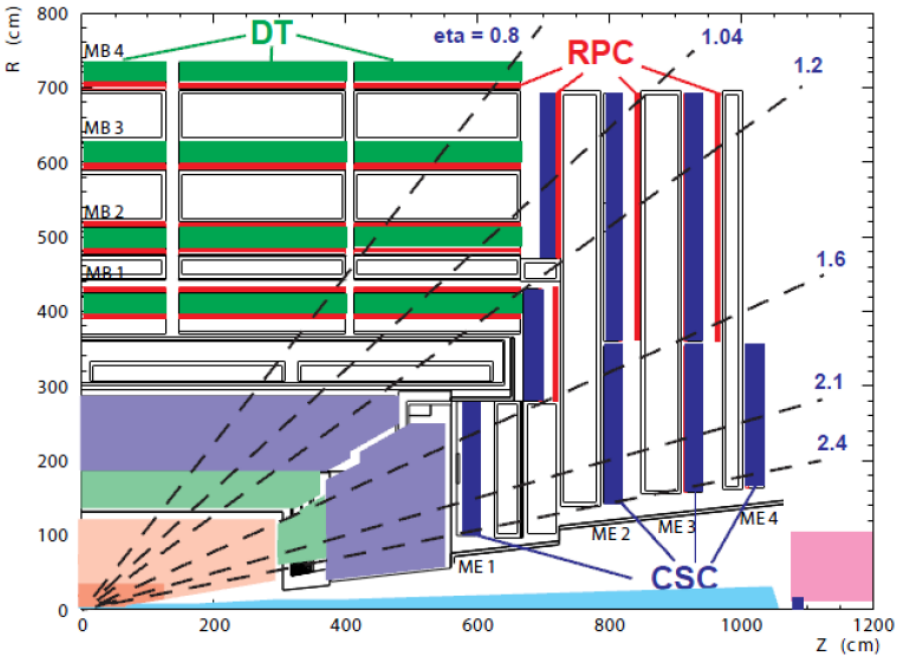

Figure 4-11: Layout of the CMS muon system.

the atoms. The electrons drift to the wires while the ions are collected by the strips. By registering the position of the wire that receives the electrons and the distance between the muon and the wire which can be known by calculating the drifting time electrons take to reach the wire, DTs can measure two position coordinates of a muon.

Cathode Strip Chamber In the endcap region ($|\eta| = 0.9$ to 2.4) where the neutron induced background rate and the magnetic field are both high, the fast response, high granularity, and radiation hard CSCs are used. The CSCs consist of 6 anode wire planes interleaved among 7 cathode panels as shown in Fig .4-13. Each CSC is composed of arrays of positively-charged anode wires crossed with negatively-charged copper cathode strips within a gas volume. It works in a very similar way as other muon chambers. When a muon passes through CSCs, it knocks electrons off the gas atoms, The anodes and cathodes then collect these electrons and ions as signals.

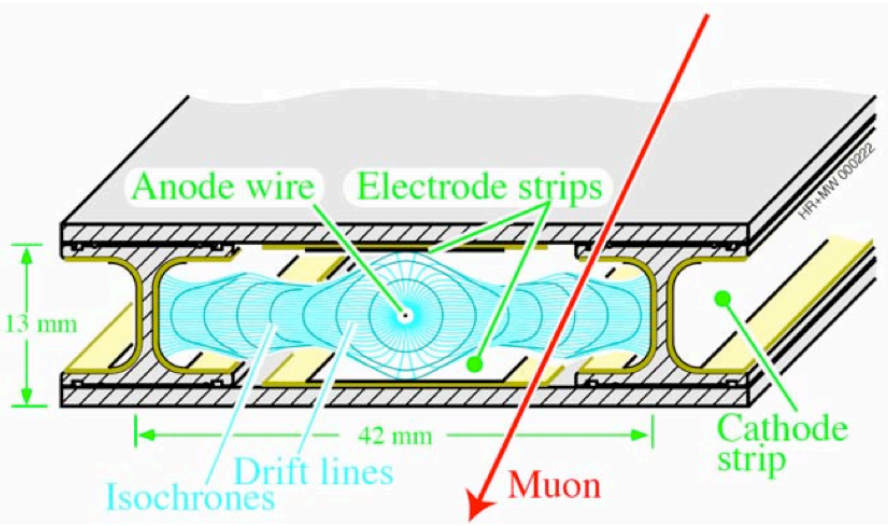

Figure 4-12: Layout of the Drift Tubes (DT).

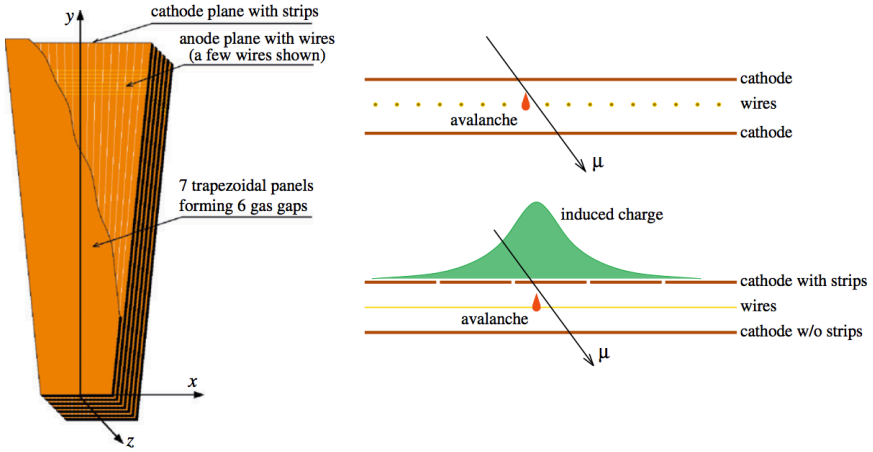

Figure 4-13: Layout of the Cathode Strip Chambers (CSC).

Resistive Plate Chamber RPCs cover up to $|\eta| < 1.6$ and are sandwiched between the DTs and CSCs. It is designed to have a time resolution shorter than 25 ns between 2 consecutive ionizing events. Therefore, a dedicated trigger system based on this fast and highly-segmented RPC is set up. A RPC consists of a positively-charged anode plate and a negatively-charged cathode plate, both made of high resistivity plastic material, and is separated by non-flammable mixture of gas (96.2% $C_2H_2F_4$, 3.5% iC_4H_{10}, and 0.3% SF_6). Since the electrodes are transparent to the electrons,

when a passing muon knocks the electrons off the gas atoms, causing an avalanche of electrons and ions, these electrons and ions will be picked up by external metallic signal strips and be used by the trigger system. A layout of RPC can be found in Fig .4-14.

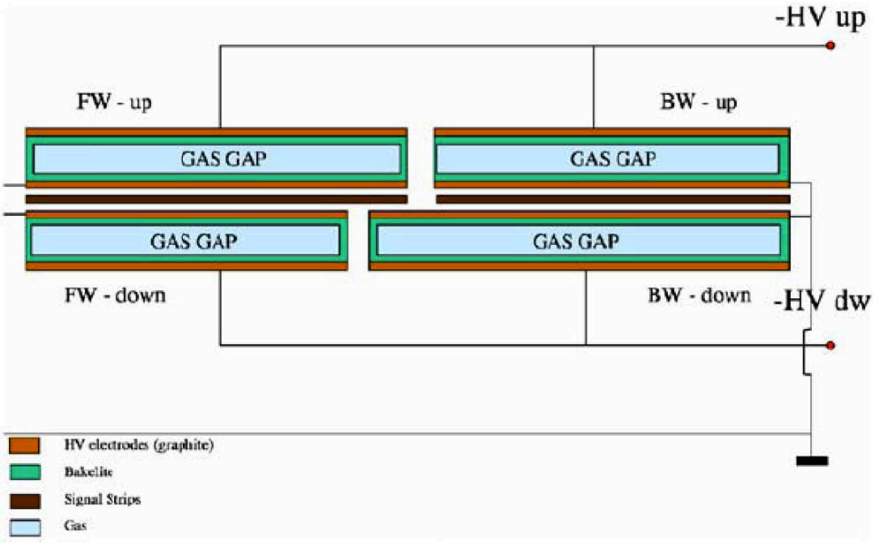

Figure 4-14: Layout of the Resistive Plate Chambers (RPC).

4.2.5 Relevant sub-detectors to this thesis

Among the sub-detectors described above, the tracking system and the muon system are the most relevant to this thesis. Specifically, the two building components (charged tracks and muons) of the B mesons measured in this thesis are reconstructed based on the responses recorded by these two sub-detectors. We will introduce the underlying algorithms used to reconstruct these two objects in the next chapter.

4.3 Trigger System

During the 2015 lead-lead collision data-taking, a maximal instantaneous luminosity of around 3 mb^{-1} per second was reached, corresponding to a collision rate of order 10 kHz. Only a relatively small fraction of these collisions contain physics processes of interest to this thesis. A trigger system is thus crucial to select events, such as events that contain muons which are the events analyzed in this thesis, for full event reconstruction and permanent storage. The CMS trigger system is divided into two levels, the Level-1 trigger and the High level trigger. A flow chart is displayed in Fig. 4-16.

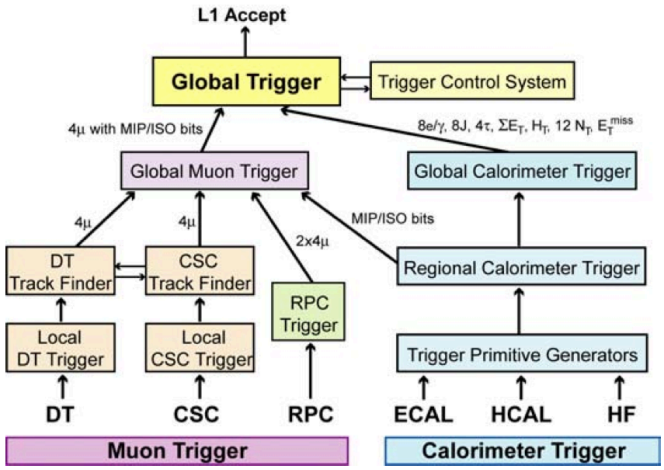

Figure 4-15: Architecture of the Level-1 Trigger.

4.3.1 Level-1 Trigger (L1)

The L1 trigger consists of custom-designed, largely programmable electronics (hardware triggers). The Level-1 triggers utilize the information collected from calorimetries and muon systems. Decisions regarding whether to accept and store a given event are made based on the quality of primitive trigger objects such as electrons, photons, muons, and jets. To ensure a high response rate, L1 triggers use only partial data (coarsely segmented) and hold the high-resolution data in pipelined memories in the front-end electronics. The architecture of L1 trigger hierarchy which is crucial

for this thesis can be found in Fig. 4-15. At the first layer, only events that triggered individual muon system sub-detectors will enter the workflow. Regional muon track reconstructions using only responses within individual sub-detectors are then performed. A global muon track finding combining information from the calorimeters and the regional muon tracks is done subsequently. And finally, the L1 triggers used in this thesis are fired. During the 2015 PbPb collision data-taking, the peak L1 rate (which happened around the end of the data-taking period when the collision rate is at its maximal) for the double muon trigger used in this thesis was around 280 Hz.

4.3.2 High Level Trigger (HLT)

Events that passed the L1 trigger are transferred to front-end readout buffers from the pipeline which is fully monitored by the Data Acquisition (DAQ) system. Each event, with a size of about 1.5 MB, is contained in hundreds of readout buffers. This partial data is collected and transmitted to an online event filter system (a processor farm with thousands of commercial processors). Events are then being further reconstructed there. Decisions for permanent storage of an event are made based on different strategies (HLT path). These events are classified into different primary datasets (PDs) according to the HLT path they passed/triggered. Offline reconstructions and physics analyses are performed on these primary datasets. A simplified flowchart can be found in Fig. 4-16.

Although the purpose of HLT is to filter out unimportant events, sometimes the signal rate is still too high for the computing system to handle. In this case, we will process and store only a fraction of all the events that have triggered the HLT path. For example, we store only 1 out of 10 events that passed the HLT path. This is called "prescale" with a rate of 10. Prescale is commonly used among various different HLT path in order to control the trigger rates. Even the same HLT path may have different prescale rates during different periods of the data-taking. For the purpose of this thesis, only events with at least one (HLT level) muon were analyzed. The corresponding double muon HLT rate (at maximal collision rate during 2015 PbPb collision data-taking) was around 35 Hz after prescale. This can be compared with

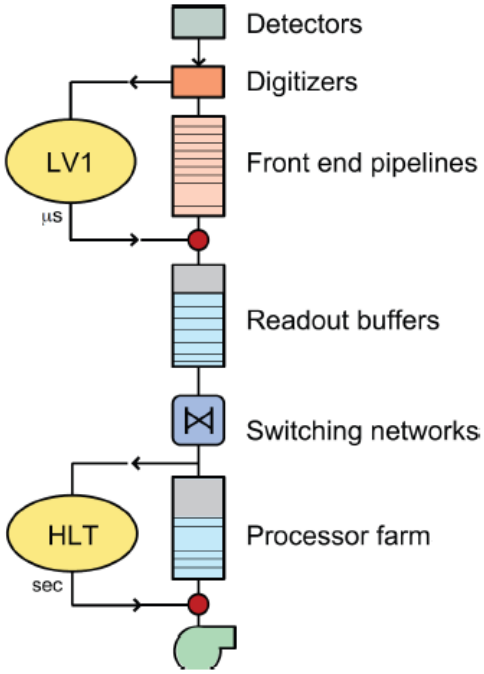

Figure 4-16: Trigger system [95].

the maximal collision rate of 20 kHz and the importance of HLT is self-evident.

Chapter 5

Physics Objects

The digital responses recorded by the CMS detector are stored for physics analyses. Different analysis objects such as particle trajectories (tracks), interaction points (primary vertices or PVs for short), or energy clusters in calorimeters are reconstructed by utilizing this information. Objects such as leptons or photons that have direct physical interpretations can also be reconstructed with more complex algorithms by aggregating these analysis objects. Three objects that were heavily used in the measurements presented in this thesis, tracks, vertices, and muons will be introduced in the following sections.

5.1 Track

The CMS tracking system is situated at the heart of the experiment and is responsible for the trajectory reconstruction of charged particles. Almost all object reconstructions rely on a good track reconstruction as a necessary ingredient. Even for a neutral particle, it is also required to be "not" associated with any tracks (as neutral particles do not leave responses in the tracking system). The superb granularity of the CMS tracking system ensures an over 99% hit recording efficiency which provides an extraordinary high track reconstruction efficiency.

A charged particle traverses the detector under the magnetic filed as a helix and is described by five parameters. One naive parameterization consists of a reference point

on the transverse plane $(0, y_0, z_0)$ and a velocity vector (v_{x0}, v_{y0}, v_{z0}). Usually one uses a more common parameterization, the so-called **perigee** parameterization [25] which is defined by the following variables

- ϵ_p: Signed transverse distance of the point of closest approach. By convention, the sign is positive if the reference point is at the left of the point of closest approach, looking along the trajectory;
- z_p: Longitudinal distance of the point of closest approach;
- θ: Polar angle of the momentum vector;
- ϕ_p: Azimuthal angle of the momentum vector at the point of closest approach;
- ρ: Signed transverse curvature, where the sign is the negative of the charge.

Many other parameterizations exist and their benefits depend on the detector designs, the collision systems, and the particle types.

Track reconstruction (tracking) is divided into the following steps [91, 92, 38].

Hit reconstruction Tracker responses/measurements are clustered as "hits." The seeding of a cluster starts from searching for a pixel (strip) response with signal over noise ratio $S/N > 6(3)$ and nearby strips with $S/N > 5(2)$. The cluster position is determined from the centroid of signal heights.

Seed generation Hits are the building elements of track trajectories which usually comprise of at least 3 hits. A hit triplet is found by starting from a single hit as "seed" and branching out. The process begins with finding an outer hit in the pixel tracker. A compatible inner hit is then searched, with beamspot constraints, to form a hit pair. A hit triplet can then be created by finding a third hit which is compatible with the hit pair within a certain search window. Hit triplets are used to reconstruct pixel tracks (as opposed to fully reconstructed tracks which include hits in the strip tracker).

Trajectory fitting By the relation between the curvature and the magnetic field, transverse momentum can be determined. Impact parameters can also be obtained by the spacial position of the hits and the momenta of the tracks [37]. With pixel tracks at hand, pixel vertices can be determined. Full trajectories can then be generated from hit triplets or hit pairs plus pixel vertices. A measurement at the next tracking layer that is compatible with the trajectory is found by extrapolating the trajectory, with the scatterings and energy losses due to interactions between detector material taken into account, in a Kalman filter approach which will be described later. In addition, a special trajectory is also created with no measured hits found on this layer so as to account for the possibility of a missing hit. The whole procedure is repeated until the outermost layer is reached and a stopping condition is satisfied.

Ambiguity resolution Same hit can be shared by several tracks. On the other hand, a particle trajectory may also be reconstructed from different seeds. Resolving this ambiguity is crucial in tracking. For example, the ambiguity resolution for tracking in pp collisions is based on the fraction of hits which are shared between two trajectories

$$f_{shared} = \frac{N_{shared}^{hits}}{min(N_1^{hits}, N_2^{hits})} \tag{5.1}$$

where N_1^{hits}, N_2^{hits} are the number of hits of the first and second track. If the fraction is larger than 0.5, the track with the least number of hits is discarded. If the number of hits are the same, the track with larger χ^2 is discarded.

5.1.1 Kalman filter

As mentioned above, the fitting of hits into a trajectory is done via the well-known **Kalman filter** [155, 156, 25, 88, 89] approach. The idea is to find the trajectory that is most compatible with the hit set in an iterative way where the estimated parameters and relevant covariance matrices are updated by the information of successive measurements with energy losses and material scatterings taken into account. In this section we will describe the basics of the Kalman filter in a more general approach.

We will follow the notations used in Ref. [155].

Consider a situation where we want to measure the physical state x_k of an object, e.g., the velocity of a vehicle in a GPS system or the trajectory parameters of a charged particle in detector. Of course, we can not directly measure a physical state. Instead, we have measurements m_k, e.g., signals from satellites or tracking detector responses, for us to infer x_k. We assume m_k is related to x_k linearly via

$$\begin{aligned} m_k &= \mathrm{H}_k x_k + \epsilon_k \\ E\big[\epsilon_k\big] &= 0,\ cov\big[\epsilon_k\big] = \mathbf{V}_k = \mathbf{G}_k^{-1} \end{aligned} \tag{5.2}$$

where ϵ_k is the measurement intrinsic uncertainty, e.g., a finite electronic resolution, associated with a measurement, parameterized by a covariance matrix $\mathbf{V}_k$ (e.g., derived from detector simulation). The k denotes the updating epoch we are currently at.

Now, the physical state itself also propagates, for example, the physical object can itself be a dynamical object such as a vehicle we are positioning or our measurements might have affected the physical state such as the interactions between charged particles and tracking pixels. Let's say, at the beginning (when k = 0), we had a measurement x_0. We then performed and obtained another measurement denoted as x_1. These two physical states are related by

$$\begin{aligned} x_k &= \mathrm{F}_{k-1} x_{k-1} + w_{k-1} \\ E\big[w_k\big] &= 0,\ cov\big[w_k\big] = \mathbf{Q}_k \end{aligned} \tag{5.3}$$

where w_{k-1} is the intrinsic uncertainty (such as the intrinsic uncertainty of a particle deflection) associated with the propagation, parameterized by a covariance matrix $\mathbf{Q}_k$.

Note that we have assumed linear relations in both cases. More often than not, the relations are nonlinear. In those cases, one usually Taylor expands the nonlinear relation to first order and obtains a linear relation.

Suppose we now have a prediction of the current state which we denote as x_k^{k-1}. We

define the difference between this prediction and the true physical state $x_{k,t}$ (subscript "t" indicates true) to be $e_k^{'} = x_k^{k-1} - x_{k,t}$ with a covariance matrix

$$E\big[e_k^{'} e_k^{'\,T}\big] = \mathrm{C}_k^{k-1}. \tag{5.4}$$

The goal is to estimate the true current state $x_{k,t}$ by combining our prediction x_k^{k-1} and the current measurement m_k. In other words, assuming the uncertainties are all Gaussian distributed, we would like to minimize the squared error (χ^2) of $e_k = x_k - x_{k,t}$ or the trace of the covariance matrix

$$\mathrm{C}_k = E\big[e_k e_k^{\,T}\big]. \tag{5.5}$$

Let's consider a general solution for the minimization problem of the form

$$\begin{aligned} x_k &= x_k^{k-1} + \mathrm{K}_k(m_k - \mathrm{H}_k x_k^{k-1}) \\ &= x_k^{k-1} + \mathrm{K}_k(\mathrm{H}_k x_{k,t} + \epsilon_k - \mathrm{H}_k x_k^{k-1}) \end{aligned} \tag{5.6}$$

If we use this expression to expand the covariance matrix C_k

$$\begin{aligned} \mathrm{C}_k &= (I - \mathrm{K}_k\mathrm{H}_k)E\big[(x_k^{k-1} - x_{k,t})(x_k^{k-1} - x_{k,t})^T\big](I - \mathrm{K}_k\mathrm{H}_k)^T + \mathrm{K}_k E\big[\epsilon_k \epsilon_k^T\big]\mathrm{K}_k^T \\ &= (I - \mathrm{K}_k\mathrm{H}_k)\mathrm{C}_k^{k-1}(I - \mathrm{K}_k\mathrm{H}_k)^T + \mathrm{K}_k\mathbf{V}_k\mathrm{K}_k^T \\ &= \mathrm{C}_k^{k-1} - \mathrm{K}_k\mathrm{H}_k\mathrm{C}_k^{k-1} - \mathrm{C}_k^{k-1}\mathrm{H}_k^T\mathrm{K}_k^T + \mathrm{K}_k(\mathrm{H}_k\mathrm{C}_k^{k-1}\mathrm{H}_k^T + \mathbf{V}_k)\mathrm{K}_k^T \end{aligned} \tag{5.7}$$

Note that the term related to $E\big[(x_k^{k-1} - x_{k,t})(\epsilon_k^T)\big]$ is zero since there is no correlation between the error of our prediction and the intrinsic uncertainty of a measurement.

Now, we take differentiation of the trace of C_k with respect to K_k to find the optimal value

$$\frac{dT[\mathrm{C}_k]}{d\mathrm{K}_k} = -2\mathrm{C}_k^{k-1}\mathrm{H}_k^{\,T} + 2\mathrm{K}_k(\mathrm{H}_k\mathrm{C}_k^{k-1}\mathrm{H}_k^T + \mathbf{V}_k) = 0 \tag{5.8}$$

Note that C_k^{k-1} is symmetry as it is a covariance matrix.

This gives the optimal value of K_k known as the **Kalman gain**

$$\mathrm{K}_k = \mathrm{C}_k^{k-1}{\mathrm{H}_k}^T(\mathrm{H}_k\mathrm{C}_k^{k-1}\mathrm{H}_k^T + \mathbf{V}_k)^{-1} \tag{5.9}$$

If we substitute K_k back to the expression of C_k, we obtain the covariance matrix of our x_k estimate

$$\mathrm{C}_k = \mathrm{C}_k^{k-1} - \mathrm{K}_k\mathrm{H}_k\mathrm{C}_k^{k-1} = (I - \mathrm{K}_k\mathrm{H}_k)\mathrm{C}_k^{k-1} \tag{5.10}$$

This finish our estimation of the true current state $x_{k,t}$. To proceed to the (k+1)-th step, we simply propagate this estimation via

$$x_{k+1}^k = \mathrm{F}_k x_k \tag{5.11}$$

So as the covariance matrix

$$\begin{aligned} e_{k+1}^{'} &= x_{k+1}^k - x_{k+1,t} \\ &= \mathrm{F}_k x_k - \mathrm{F}_k x_{k,t} - w_k \\ &= \mathrm{F}_k(\epsilon_k) - w_k \end{aligned} \tag{5.12}$$

$$\mathrm{C}_{k+1}^k = E\big[e_{k+1}^{'}{e_{k+1}^{'}}^T\big] = \mathrm{F}_k\mathrm{C}_k{\mathrm{F}_k}^T + \mathbf{Q}_k \tag{5.13}$$

Lastly, we do a little algebra to change to different expressions for K_k, x_k, and C_k. These expressions will be used in a later section. Firstly we note we can rewrite K_k

$$\begin{aligned} & \mathrm{K}_k = \mathrm{C}_k^{k-1}{\mathrm{H}_k}^T(\mathrm{H}_k\mathrm{C}_k^{k-1}\mathrm{H}_k^T + \mathbf{V}_k)^{-1} \\ \rightarrow\ & \mathrm{K}_k(\mathrm{H}_k\mathrm{C}_k^{k-1}\mathrm{H}_k^T + \mathbf{V}_k) = \mathrm{C}_k^{k-1}{\mathrm{H}_k}^T \\ \rightarrow\ & \mathrm{K}_k(\mathrm{H}_k\mathrm{C}_k^{k-1}\mathrm{H}_k^T\mathbf{G}_k + I) = \mathrm{C}_k^{k-1}{\mathrm{H}_k}^T\mathbf{G}_k \\ \rightarrow\ & \mathrm{K}_k = (\mathrm{C}_k^{k-1} - \mathrm{K}_k\mathrm{H}_k\mathrm{C}_k^{k-1}){\mathrm{H}_k}^T\mathbf{G}_k \\ \rightarrow\ & \mathrm{K}_k = \mathrm{C}_k{\mathrm{H}_k}^T\mathbf{G}_k \end{aligned} \tag{5.14}$$

Use this expression of K_k in the equation of x_k estimate

$$\begin{aligned} x_k &= x_k^{k-1} + \mathrm{K}_k(m_k - \mathrm{H}_k x_k^{k-1}) \\ &= (I - \mathrm{K}_k\mathrm{H}_k)x_k^{k-1} + \mathrm{K}_k m_k \\ &= \mathrm{C}_k(\mathrm{C}_{k+1}^k)^{-1}x_k^{k-1} + \mathrm{C}_k\mathrm{H}_k{}^T\mathbf{G}_k m_k \\ &= \mathrm{C}_k((\mathrm{C}_{k+1}^k)^{-1}x_k^{k-1} + \mathrm{H}_k{}^T\mathbf{G}_k m_k) \end{aligned} \tag{5.15}$$

The covariance matrix of estimate C_k becomes

$$\begin{aligned} &\mathrm{C}_k = (I - \mathrm{K}_k\mathrm{H}_k)\mathrm{C}_k^{k-1} \\ \rightarrow\ &\mathrm{C}_k(\mathrm{C}_k^{k-1})^{-1} = I - \mathrm{K}_k\mathrm{H}_k = I - \mathrm{C}_k\mathrm{H}_k{}^T\mathbf{G}_k\mathrm{H}_k \\ \rightarrow\ &\mathrm{C}_k((\mathrm{C}_k^{k-1})^{-1} + \mathrm{H}_k{}^T\mathbf{G}_k\mathrm{H}_k) = I \\ \rightarrow\ &\mathrm{C}_k = ((\mathrm{C}_k^{k-1})^{-1} + \mathrm{H}_k{}^T\mathbf{G}_k\mathrm{H}_k)^{-1} \end{aligned} \tag{5.16}$$

These are the basics of the well-known Kalman filter technique. In the case of tracking, the physical state x_k of interest is the track trajectory parameters (the commonly used perigee parameterization can be found in Ref. [25]). The measurement m_k will be the recorded responses or the hits at different tracker layers. The propagations and relations between physical states F_k are characterized by the details of the tracking detector design and material. The transformations between states and measurements H_k depend on both the design of the tracking detector and the parameterization of a trajectory.

5.2 Vertex

A vertex is defined to be the spatial point where a collision or interaction took place and where tracks originate from. Similar to the track fitting, we would like to find the position that is most compatible with a given set of tracks (vertexing). The process of vertexing starts from grouping tracks into clusters, based on their points of closest approaches with respect to the beam line on the z-coordinate. Vertex fitting is then performed for each cluster which determines the best estimate of the vertex

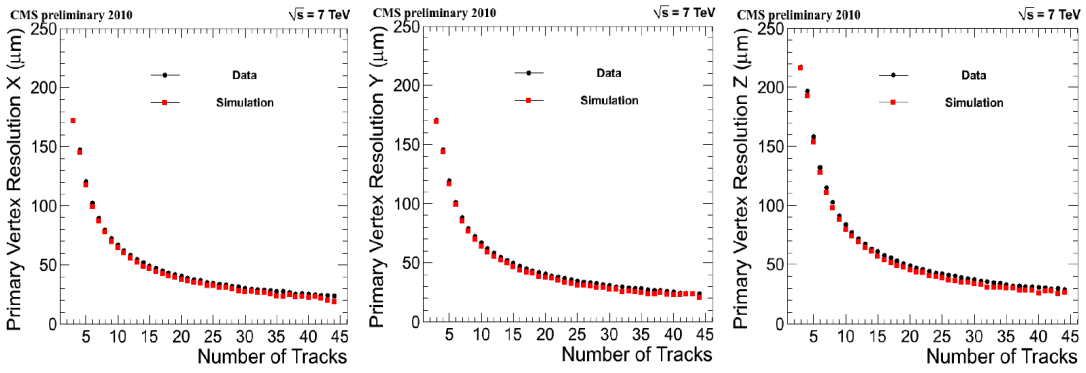

Figure 5-1: Primary vertex resolutions [99] in x (left), y (center), and z (right) as a function of the number of tracks used in the fitted vertices from simulation.

parameters including its position, covariance matrix, and track parameter updates. The Kalman filter approach (with small modifications) described in the previous section is commonly used for this purpose. Similar to tracking, a vertex is obtained by a sequential updates of the vertex parameters. It is mathematically equals to a global least-squares minimization (we will see this shortly) which is the optimal estimator when the measurements are Gaussian distributed and the fitted parameters depend linearly on those measurements. Many different robustifications of the Kalman filter exist such as the **Adaptive vertex fit** (AVF) [148, 93] which down-weights tracks according to their distances to the vertex. It is thus robust against outlying tracks, which are either mismeasured tracks or tracks from other vertices. Each track is assigned a weight between 0 and 1 based on its compatibility with their common vertex and this weight varies from one iteration to the next until the fit converges. However, for simplicity we will only present the basic version of the Kalman filter approach. The resolution of primary vertex (the spatial point where the hard scattering took place) reconstruction at CMS can be found in Fig. 5-1.

5.2.1 Vertexing using Kalman filter

The concept of vertexing is to estimate a position (vertex) given a set of track trajectories such that these tracks are most likely to be originated from. In addition, by constraining these tracks to be coming from a common position, the procedure can

in return provide better estimates of the track trajectories themself. One common method of vertexing is the Kalman filter technique described in the tracking section (we will follow the notations used in Ref. [155]). In this picture, each associated track is considered as an individual measurement and we will, at each step, utilize one track to re-estimate the vertex position. The trajectory parameters p_k will be the measurement itself. The vertex position x_k and the momentum of this track at the vertex q_k together are the physical state to be estimated (basically the "x_k" in the tracking section). The relation between state and measurement can be expressed as

$$p_k = \mathrm{H}_k x_k = \begin{bmatrix} \mathbf{A}_k & \mathbf{B}_k \end{bmatrix} \begin{bmatrix} x_k \\ q_k \end{bmatrix} + c \tag{5.17}$$

where $\mathbf{A}_k$ and $\mathbf{B_k}$ are 5 by 3 matrices and c is a constant (the 0-th order term of the Taylor expansion of $p_k = h_k(x_k, q_k)$ for some nonlinear relation h_k).

The relation between $(k-1)$-th estimate and k-th prediction is straightforward since each tracks are independent measurements, happening at the same time. For this reason, we can simply put

$$x_k^{k-1} = x_{k-1} \tag{5.18}$$

In other words, $\mathrm{F} = I$ and $\mathbf{Q}_k = 0$.

Covariance matrix for x_k will also be directly related from one another via

$$\mathrm{C}_k^{k-1} = \mathrm{C}_{k-1} \tag{5.19}$$

For the q_k^{k-1} estimate, since we do not have any prior information, we will simply assign it with the momentum of the k-th track at the current vertex position estimate or even some random values with an infinite covariance matrix

$$\mathrm{D}_k^{k-1} = (1/\delta)I,\ \delta \to 0 \tag{5.20}$$

We will see that the q_k^{k-1} dependence disappears in the expression.

Now, we use the Kalman filter formula we derived previously and substitute the corresponding expressions

$$\begin{aligned}\begin{bmatrix} x_k \\ q_k \end{bmatrix} &= \mathrm{C}_k\Big(\begin{bmatrix} (\mathrm{C}_k^{k-1})^{-1} & 0 \\ 0 & (\mathrm{D}_k^{k-1})^{-1} \end{bmatrix} \begin{bmatrix} x_k^{k-1} \\ q_k^{k-1} \end{bmatrix} + \begin{bmatrix} \mathbf{A}_k^T \\ \mathbf{B}_k^T \end{bmatrix} \mathbf{G}_k(p_k - c_k)\Big) \\ &= \mathrm{C}_k \begin{bmatrix} (\mathrm{C}_k^{k-1})^{-1} x_k^{k-1} + \mathbf{A}_k^T \mathbf{G}_k(p_k - c_k) \\ (\mathrm{D}_k^{k-1})^{-1} q_k^{k-1} + \mathbf{B}_k^T \mathbf{G}_k(p_k - c_k) \end{bmatrix}\end{aligned} \tag{5.21}$$

with the formula for C_k we derived earlier

$$\begin{aligned}\mathrm{C}_k &= \Big(\begin{bmatrix} (\mathrm{C}_k^{k-1})^{-1} & 0 \\ 0 & (\mathrm{D}_k^{k-1})^{-1} \end{bmatrix} + \begin{bmatrix} \mathbf{A}_k^T \\ \mathbf{B}_k^T \end{bmatrix} \mathbf{G}_k \begin{bmatrix} \mathbf{A}_k & \mathbf{B}_k \end{bmatrix}\Big)^{-1} \\ &= \begin{bmatrix} (\mathrm{C}_k^{k-1})^{-1} + \mathbf{A}_k^T \mathbf{G}_k \mathbf{A}_k & \mathbf{A}_k^T \mathbf{G}_k \mathbf{B}_k \\ \mathbf{B}_k^T \mathbf{G}_k \mathbf{A}_k & (\mathrm{D}_k^{k-1})^{-1} + \mathbf{B}_k^T \mathbf{G}_k \mathbf{B}_k \end{bmatrix}^{-1} \\ &= \begin{bmatrix} (\mathrm{C}_k^{k-1})^{-1} + \mathbf{A}_k^T \mathbf{G}_k^B \mathbf{A}_k)^{-1} & -\mathbf{W}_k \mathbf{B}_k^T \mathbf{G}_k \mathbf{A}_k \mathbf{C}_k \\ (-\mathbf{W}_k \mathbf{B}_k^T \mathbf{G}_k \mathbf{A}_k \mathbf{C}_k)^T & \mathbf{W}_k + \mathbf{W}_k \mathbf{B}_k^T \mathbf{G}_k \mathbf{A}_k \mathbf{C}_k \mathbf{A}_k^T \mathbf{G}_k \mathbf{B}_k \mathbf{G}_k \end{bmatrix}\end{aligned} \tag{5.22}$$

where

$$\begin{aligned}\mathbf{W}_k &= (\mathbf{B}_k^T \mathbf{G}_k \mathbf{B}_k)^{-1} \\ \mathbf{G}_k^B &= \mathbf{G}_k - \mathbf{G}_k \mathbf{B}_k \mathbf{W}_k \mathbf{B}_k^T \mathbf{G}_k\end{aligned} \tag{5.23}$$

The matrix inversion can be checked to be true by a direct matrix multiplication.

Now, one can see that $(\mathrm{D}_k^{k-1})^{-1} q_k^{k-1}$ comes in pair and since $(\mathrm{D}_k^{k-1})^{-1} = \delta I$, this term essentially vanishes. Finally, the resulted update equation for x_k and q_k (we are not really updating q_k because we are considering a new track at each step) are

$$\begin{aligned}x_k &= \mathrm{C}^k\big[(\mathrm{C}_k^{k-1})^{-1} x_{k-1} + \mathbf{A}_k^T \mathbf{G}_k^B (p_k - c_k)\big] \\ q_k &= \mathbf{W}_k \mathbf{B}_k^T \mathbf{G}_k (p_k - c_k - \mathbf{A}_k x_k)\end{aligned} \tag{5.24}$$

We can expand this recursive relation of x_k using the fact that $\mathrm{C}_k^{k-1} = \mathrm{C}^{k-1}$

$$\begin{aligned} x_k &= \mathrm{C}^k\big[(\mathrm{C}_k^{k-1})^{-1}x_{k-1} + \mathbf{A}_k^T\mathbf{G}_k^B(p_k - c_k)\big] \\ &= \mathrm{C}^k\big[\mathrm{C}_{k-1}^{k-2})^{-1}x_{k-2} + \mathbf{A}_{k-1}^T\mathbf{G}_{k-1}^B(p_{k-1} - c_{k-1}) + \mathbf{A}_k^T\mathbf{G}_k^B(p_k - c_k)\big] \\ &= \mathrm{C}^k\big[\sum_{i=0}^{k}\mathbf{A}_i^T\mathbf{G}_i^B(p_i - c_i)\big] \\ &= \mathrm{C}^k\big[\sum_{i=0}^{k}\mathbf{A}_i^T\mathbf{G}_i(1 - \mathbf{B}_k\mathbf{W}_k\mathbf{B}_k^T\mathbf{G}_k)(p_i - c_i)\big] \end{aligned} \tag{5.25}$$

given that we started with $x_0 = 0$.

Notably, this expression is exactly the same as the global method in Ref. [24] (eq.22a) in which instead of a Kalman like filtering and updating process, one directly consider the global minimal χ^2 from all the tracks. This indicates that the order in which the tracks are used in the Kalman filter method does not affect the result which is expected since the Kalman filter process essentially summarizes the knowledge of the previous state into a prediction at each iteration.

5.3 Muons

The identifications and reconstructions of muon candidates makes use of measurements in both the tracking and muon systems. It is roughly divided into three steps; regional, standalone and global reconstructions. Three different muon reconstruction algorithms, standalone (using only responses in the muon system), global (using responses in the muon system and the tracking system), and tracker (using responses in the muon system and the tracking system) muon algorithm, which are most oftenly used by CMS analyses will be introduced. Each algorithm has its own strength and the choice is entirely analysis dependent. For example, in the study of cosmic-ray muons which do not leave measurements in the tracker system, standalone muon is a better choice in this circumstance. On the other hand, for analyses focusing on low energy physics, of order several GeV's, which may not leave enough hits in the muon chambers for a standalone muon to be reconstructed, tracker muon will be a better

choice for its high reconstruction efficiency. For analyses presented in this thesis, both tracker and global muons were used. Specifically, the muons used in the thesis were required to match the criteria of the two algorithms. Standalone muon algorithm was not directly used in the reconstruction of the B mesons but served as the underlying algorithm used in the relevant HLT.

5.3.1 Regional Reconstruction

Regional reconstruction, also called local reconstruction, employs only minimum information recorded by the muon system, i.e. it is a detector level reconstruction. In the barrel region, drift time within a DT is calculated to find the hit position in a cell. A segment within the muon system can then be reconstructed which is built from a set of aligned hits. In the endcap region, inputs to the reconstruction are digits from cathode strips and anode wires.

5.3.2 Standalone Muon

Standalone reconstruction, also called Level-2 reconstruction, uses only data from muon chambers and aims to reconstruct a track in the muon system. The reconstruction starts with segments of the muon chambers obtained by the regional reconstruction. Positions, momenta, and directions associated with the segments found in the innermost chambers are used to seed the muon trajectories. From an inside out approach, Kalman filter is used to predict the position of the trajectory on the next measurement surface. Prediction and measurement are compared with each other and the vertex state vector is updated. The procedure iterates until the outermost measurement surface of the muon system is reached. An opposite direction fitting, outside in, is then employed. In the end, this muon track is extrapolated to the interaction point and a vertex constrained fit to the muon track parameters is performed.

5.3.3 Global Muon

Global muon reconstruction which is also called Level-3 reconstruction consists of extending the muon trajectories seeded from the standalone muons to the tracking system. A standalone muon trajectory is extrapolated to the tracking system with the energy losses of multiple scatterings within detector material taken into account. For each standalone muon track, a search for matched tracker tracks is performed, and the best-matched tracker track is selected. A trajectory is build based on this tracker track plus the standalone muon. A new trajectory is re-fitted which involves measurements of both the tracking system and the muon chamber. Fig. 5-2 shows the global muon reconstruction efficiency.

5.3.4 Tracker Muon

As opposed to global muon which follows an outside-in approach from the muon chamber to the tracking system, tracker muons [98] are reconstructed by an inside-out approach. All tracker tracks with p_T >0.5 GeV/c and p >2.5 GeV/c are considered to be possible muon candidates. Tracker tracks are extrapolated to the muon system. If at least one muon segment is found to be compatible with the extrapolation, the tracker track together with the segment qualified as a tracker muon.

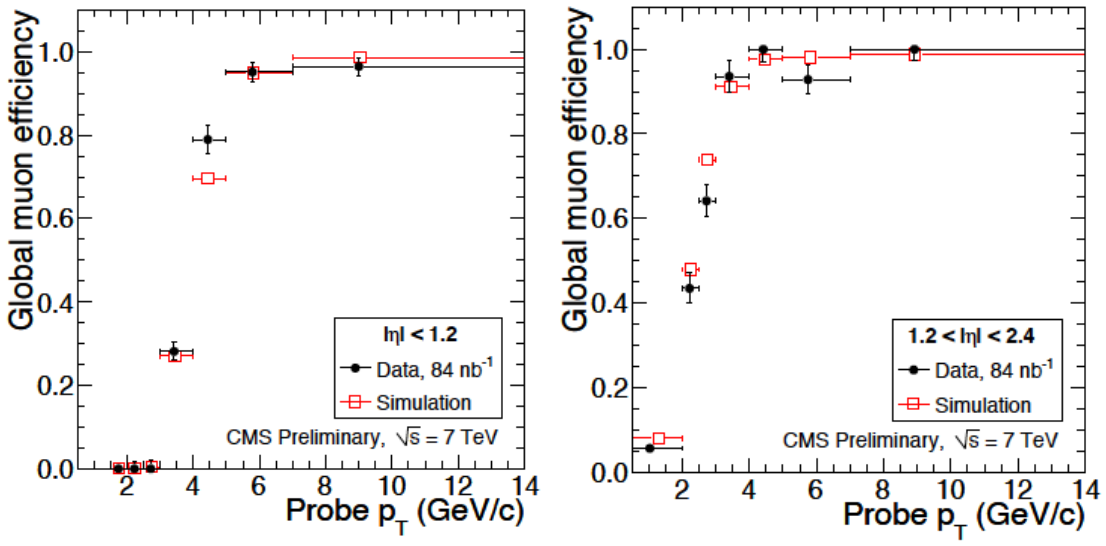

Figure 5-2: Muon reconstruction efficiencies in the barrel (left) and the endcap (right) with data compared to simulations [98].

Chapter 6

Machine learning

Machine learning (ML) is a methodology of enabling a machine to automatically learn a strategy that can satisfy or maximize some criteria from a given input data set. It is one of the most powerful technologies of the 21st century with limitless potential. It has ubiquitous influence and one can easily find applications of ML in our daily life. Some common examples include identifying pedestrians from street photos or finding patterns from past meteorology data to forecast the future weather. In these cases, the optimization criteria will be the probability or accuracy that a ML model successfully finds the signals or makes the correct predictions. In other words, a ML model is trying to find the underlying truth of a particular data set.

In most cases, a ML problem or more broadly speaking, a data science problem can be classified into two categories, supervised learning and unsupervised learning. The difference is, in a supervised learning, a (labeled) data set, where the underlying truth of each data point is known, is accessible while in an unsupervised learning, there is no such data set. The goal of an unsupervised learning is usually aiming to segment or cluster the data points. For a supervised learning, one focuses on training a model that helps to identify the desired signals and patterns. We will focus on supervised learning which is used to identify B meson signals in the analyses of this thesis.

Practically, a ML model is specified by two components, model algorithm and model parameters. For example, given a data set with information about track trajec-

tories, we would like to distinguish tracks that truly originate from charged particles. A naive model algorithm can be that we simply select tracks with trajectory fitting χ^2 below some β_1 and the number of tracker hits above some β_2. This model algorithm simply cuts a rectangle in the 2-D phase space of χ^2 vs number of hits (referred to as cut-based method hereafter) as shown in Fig. 6-1. We specify the model algorithm while the precise values of β_1 and β_2, the model parameters, are left for the machines (our computers) to learn from the data.

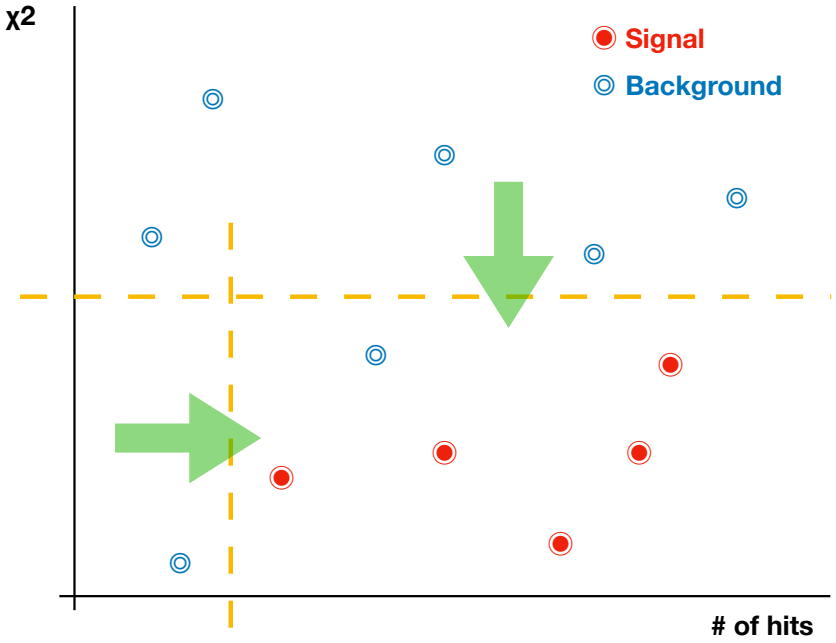

Figure 6-1: Exemplary phase space of track trajectory data with two features, fitting χ^2 (y-axis) and number of tracker hits (x-axis). Signal (true) data points are shown as red dots while background (false) data points are shown as blue dots. A rectangle is selected from the phase space, populated mostly by signal data points.

Another example model algorithm in which we try to find a straight line in the phase space ($\beta_1 x + \beta_2 y = 0$) that can separate the signal points from the background points would look like Fig. 6-2. This is similar to the well-known **Perceptron** algo-

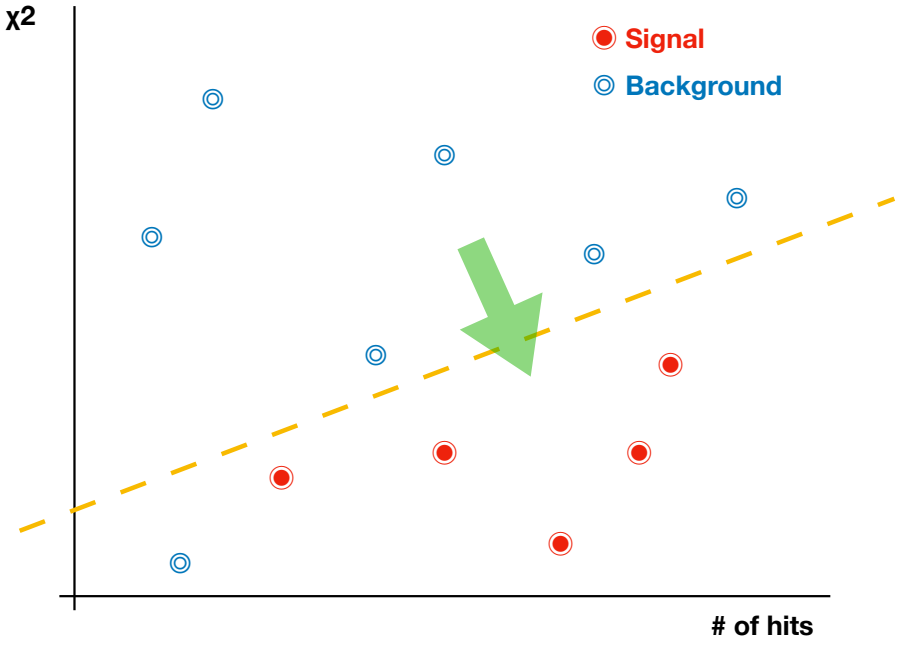

Figure 6-2: Exemplary phase space of track trajectory data with two features, fitting χ^2 (y-axis) and number of tracker hits (x-axis). Signal (true) data points are shown as red dots while background (false) data points are shown as blue dots. A straight line is drawn to separate the signal points from background points.

rithm. Again the precise value of β_1 and β_2 are left for the machines to find out.

The learning procedure in which a machine tries to search for the best β values that give the highest model accuracy using a labeled data set (training set), which is a data set with the underlying truth of each data point available like those shown in Fig. 6-1 and Fig. 6-2, is called "training." Once the training is done with the model parameters fully specified, the model can be applied to an unlabeled data set for practical usage. Complementary to training, there is usually a follow-up procedure called "testing" which is also performed on a labeled data set. During testing, the model parameters no longer change because the purpose of testing is to provide a proper estimation of the model accuracy to prevent bias or overfitting. One important thing about the

labeled set used in testing (testing set) is that it has to be non-overlapped with the training set.

6.1 Training and testing error

At the core of most ML models or algorithms is the optimization of an objective function. The objective function provides a measure for model performance. In other words, the lower (or higher depending on the definition) the objective function value, the better the model performance. For example, mean-square between predictions and true values is a very common indicator of model performance. In this case, the objective function or loss function is

$$\text{Loss} = \frac{1}{n}\sum_{i=1}^{n}(Y_i - \hat{Y}_i)^2 \tag{6.1}$$

The learning process essentially is a process of finding the model parameter values that minimize this loss function (error). The loss value associated with the training (testing) set is the training (testing) error. Testing error is also called empirical error because in the large sample limit, it approximates the true model error which is also known as generalization error.

A good and reasonable model usually has a compatible training and testing error. If the testing error is much larger than the training error, this indicates the model is overfitting. The model overfits the training set such that it artificially picks certain data points that minimize the loss function, resulting in a model that is actually far from the true underlying distribution. Consider a simple ML case in which we want to identify photos of cats and dogs. Given a training set with only two photos, a black cat and a white dog, the model will not try to unveil the underlying difference between cats and dogs but simply predict every black animal to be a cat and white animal to be a dog which is obviously incorrect. Overfitting usually happens when our ML model complexity is far beyond the number of data samples available for training. On the other hand, there is also underfitting which happens when training and testing

error are compatible but both very large. This indicates our ML algorithm simply does not have the ability to model the true underlying distribution correctly.

This property is sometimes called the bias vs variance trade-off. One way to visualize this is to plot the errors as a function of model complexity as shown in Fig. 6-3. At the beginning, both training and testing error are high. The model is underfitting the training set. This is called the high bias region as our model is biased and our prediction is not accurate enough. As the model complexity grows, the training error decreases because the model is fitting the training set with more elaborate models. After some point, our model begins to overfit the training set. Although the training error continues to decrease, the testing error actually increases. This is called the high variance region. Our model overfits the training set and even variations of the training samples are wrongly captured, resulting in a high testing error.

The ideal working point will be somewhere between the two regions where the testing error is minimized. Because, on average, testing error is a proxy to generalization error, this point will also be where the true model error is minimized. However, one should absolutely avoid repeatedly using the testing set to "tune" the model algorithm in order to have the testing error minimized, because this essentially uses the testing set for "training" and the testing error will become a biased estimation (biased toward smaller error) of the generalization error. One way to resolve this is to further retain another data set called "validation set." This set will be exclusively used for the selecting and tuning of model algorithms and complexities. In addition, a more elaborate procedure based on the same concept called **Cross validation** is very commonly used among the ML community. As opposed to having a fixed validation set, in cross validation, the validation set is a dynamical split of the training set, i.e., in each training, the validation set is different. With this, the testing set can remain untouched and used for estimation of the model accuracy.

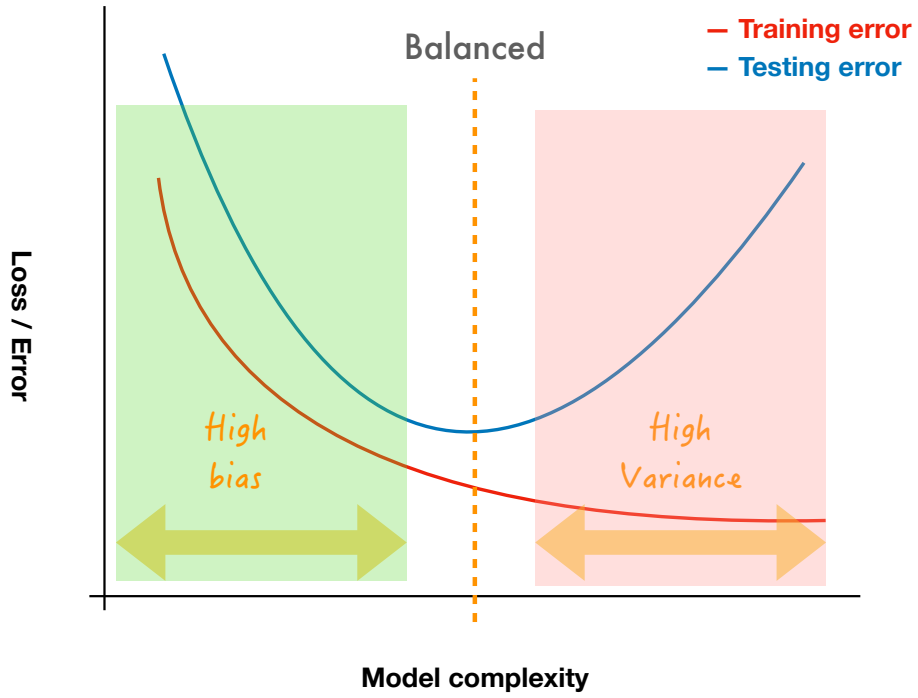

Figure 6-3: Exemplary error curve as a function of model complexity. Training and testing error are shown as blue and red curves.

6.2 Feature engineering

One of the most critical elements to construct a successful ML model, although strictly speaking not unique to the context of ML, is feature engineering. The goal of feature engineering is to construct features or variables that best serve the need of the analysis. For example, in a case where one wants to identify electrons not coming from photon conversions, ECAL measurements will be very important. However, if we just naively input all the hits ECAL recorded, it is very difficult for the machine alone to come up with a good predictive model. Instead, we can "engineer" new features that encode the size and shape of the ECAL clusters. This will greatly help the machine to identify the signal we want as we are essentially telling the machine what information to look at. Good features are very important for a successful ML model. For instance, if

we use HCAL information as features, it is almost hopeless to have a reliable model because neither types of the electrons leave any imprints in the HCAL and in this case, HCAL information will only give irrelevant and redundant features.

Theoretically, as long as one naively inputs all the information we have about the data set into the training, a ML model with a very high complexity should in principle automatically capture and create these good features for us. Using the above example, one could simply input all the ECAL hits to the training and keep our fingers crossed for the machine to discover and create the correct features itself. But in reality, what always happens is either the model is unable to do so because of the almost infinite possible ways of creating new features or the model simply overfits because the complexity is too high. For this reason, feature engineering is absolutely the first step for any successful ML model. One needs to understand the physics and the detector very well in order to use ML successfully.

6.2.1 Feature selection

We described earlier the importance of feature engineering. It helps the machine to capture important information and relations in the data. However, too many features also pose problems. First, when the number of features becomes too large, certain ML algorithms, such as decision tree, are more likely to overfit the training data. This is because while the degrees of freedom (features) of our model increases, the number of data samples stays the same. Secondly, correlations may exist among different features. For example in a B meson decay event, B meson decay length and B meson momentum are two highly correlated features. In the extreme case, adding fully correlated features can lead to unstable results, causing the model to be unable to converge and leading to computing failure. Some common techniques to resolve this include **Principle component analysis** (PCA) and **Linear discriminant analysis** (LDA) which aim to build orthogonal features from linear combinations of existing features. The last caveat of having too many features is the increase in computing time. This increase has to be compensated for by sacrificing other parts. For the model to stay within a reasonable computing time, we may have to reduce the vari-

able scanning granularity, loosen the convergent criteria, or reduce model complexity by other means. If the added features are not as useful, they simply lead to a net loss of predictive power.

It goes without saying that feature selection is as important as feature engineering or any other parts of a ML analysis. One well-known method for feature selection is the so-called **Regularization**. The idea is to add a penalization term in the loss function of the form

$$\sum_{j=1}^{m} |(\beta_j)^l| \tag{6.2}$$

where β's are model parameters and m is the number of β's. l determines how the regularization is performed, in particular, when $l = 1$, it is known as "Least absolute shrinkage and selection operator" (LASSO) regression while $l = 2$ is known as Ridge regression. LASSO regression will drive the β values of unimportant features to zero and retain only useful features, i.e., feature selection. For Ridge regression, since the penalization is quadratic, it is known for resolving the feature collinearity mentioned earlier.

However, regularization is not applicable to all ML algorithms. In this case, a more straightforward method called "forward (backward) stepwise feature selection" can be used. In the forward method, one starts the training of a ML model with only a single feature and gradually adds in more features at each step. At each step, one re-trains the model and compares its error with the model from the previous step. If no significant decrease in error is observed, this newly added feature can potentially be discarded as it is not providing enough predictive power. For the backward method, one starts with the full set of features and subtracts features at each step. Note that one has to be extremely careful as the order in which the features are added (or subtracted) matters a lot. Stepwise feature selection is the method used for the analyses presented in this thesis.

6.3 Decision tree

A decision tree is very similar to a binary tree, which is a data structure consisting of "nodes" with each node connected to two more daughter nodes or no daughter node if it is an end node. Each node represents a group of data samples. A selection of these data samples, based on a particular variable or rule, is performed and these samples are split into two groups, i.e., two daughter nodes. The same splitting proceeds on the two daughter nodes until it reaches some convergent criteria. The goal of the decision tree is such that one can make predictions, whether it's the data point's classes (for classification) or values (for regression), based on where the data points reside in the tree.

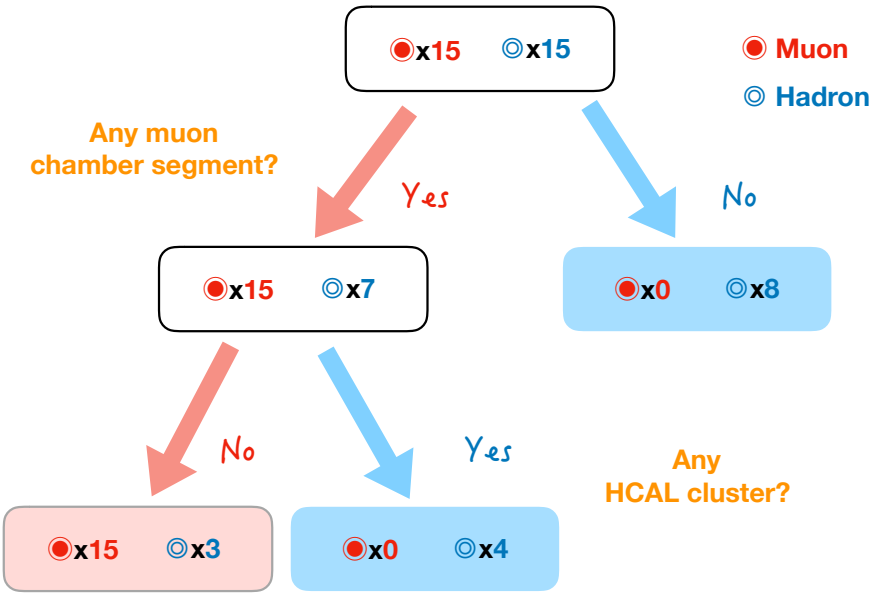

Figure 6-4: Exemplary flowchart of a shallow decision tree.

For example, let's say we start with a sample of data points each representing a track either originated from a muon or a hadron as the flowchart shows in Fig. 6-4.

At the root node we have the full data samples of our training set. We first split this node by asking if the data point has a corresponding segment in the muon chambers, and we move those data points that do to the left node and those that don't to the right node. We find that the left node is still somewhat ambiguous. We further split this node by asking if there is a corresponding cluster in the HCAL. This completes a simple decision tree training process. The predictions are made for each end node and in this example we have three end nodes. We can then use this tree to make predictions for new observations. Observations that follow this decision tree to the red end nodes will be predicted as muons while those ending up in the blue end nodes are predicted as hadrons. Note that this is an overly simplified example just for the illustration of the decision tree algorithm. In reality, more complicated ML algorithms (e.g., a deeper decision tree or the ensemble method which will be introduced shortly) are used for physics analyses.

The above decision tree example is aiming for classification purpose. Predictions are made for each end node (nodes with no further splitting) based on the majority. We certainly want each node to be as "pure", i.e., having less classes, as possible. At each node, a quantity is calculated, measuring how pure a node is. Two of the most commonly used quantities are the so-called **Gini impurity** and **Entropy**.

Gini impurity:

$$I = \sum_{i=1}^{K} p_i(1 - p_i) \tag{6.3}$$

where p_i is the fraction of sample class i at this node. Gini impurity can basically be understood as how likely one will wrongly predict a data point (since p_i is the class fraction and $1 - p_i$ is the probability of making a wrong prediction).

Entropy or Shannon entropy:

$$H = -\sum_{i=1}^{K} p_i \log p_i \tag{6.4}$$

Entropy also quantifies the purity of a node, for example, if there is only a single class in this node, the entropy will be zero. It also has a well-known property that it

corresponds to the minimal expected encoding length of the classes in this node.

The node splitting during the training of a decision tree proceeds by finding the variable and cutting value that can maximize the difference between the mother node and the weighted sum of two daughter nodes

$$Gain = I_n - \frac{n_l}{n} I_{n_l} - \frac{n_r}{n} I_{n_r} \tag{6.5}$$

where n, n_l, and n_r are the numbers of data points residing at the mother node, left daughter node, and right daughter node respectively. I_n, I_{n_l}, and I_{n_r} are the corresponding Gini impurities or entropies. The splitting of a node stops once there is no way to further improves the gain by a significant amount (the precise value is part of the model algorithm to be tuned).

Although only the classification tree is used in this thesis, nevertheless we include the criteria for a regression tree for completeness. For a regression tree, the value of a data point is predicted by the mean or median value of the node. A commonly used measure (the quantity to be minimized at each node) is the variance of a node

$$Variance = \frac{1}{n} \sum_{i=1}^{n} (x_i - \mu_x)^2 \tag{6.6}$$

The splitting seeks to reduce the variance of each node. The *Gain* in the regression tree is similar to that of classification tree shown in equation 6.5, i.e., the difference between the variance of mother node and the weighted sum of daughter nodes.

6.4 Ensemble method

As we have almost overly emphasized, one common issue of a ML model is overfitting. This problem is particularly serious for decision tree. In an extreme case where there are more variables than data points, the decision tree can simply have the same number of end nodes as data points and reach a 100% prediction accuracy (zero training error) by putting each data point at one end node. To avoid this, the depth

of the trees and the splitting criteria need to be properly constrained. But this also means the predictive power may be greatly reduced.

The ensemble method is an approach aiming to resolve this problem by training many weak models/learners and aggregating them. For example, in the context of decision tree, we train many shallow decision trees (a forest) and combine the decisions of each individual trees to make a final prediction. This is one variant of the ensemble methods known as **Bootstrap aggregating** or bagging for short. By combining results from many weak learners (trees), we reduce the possibility of overfitting while maintaining a good predictive power.

6.4.1 Boosting (adaptive)

Boosting is another variation of the ensemble methods. The idea of boosting is to apply high weights to the data points which were wrongly classified by the previous week learner. If we go back to the example we just described in Fig. 6-4, one can notice that there were three hadrons (in the lower left red end node) wrongly classified. In the case of boosting algorithm, we will increase the weights of these three data points. Let's say we double the weights of these three data points and have the remaining sample unchanged. We then train a new decision tree on this weighted sample as shown in Fig. 6-5. Since the weights of these three data points were increased, the new tree will focus more on classifying them correctly and this new tree is going to be different from the old tree. In the new tree, instead of requiring at least one muon segment in the first node splitting, it requires two in this case. Now we have two trees, suppose we have a new data sample and we what to know if it's a hadron (we denote a prediction of being a hadron as "1" and "0" for being a muon). Let's say tree number one predicts it to be a muon (prediction = 0) while tree number two predicts it as a hadron (prediction = 1). Our final prediction in this case is the average of the two predictions, i.e., 0.5. If we decide to classify any prediction above zero (the working point or cutoff) to be a hadron and any prediction below or equal to zero to be a muon., the combination of the two trees will actually have a 100% accuracy in predicting hadrons. But be awared that at the same time, the second tree

wrongly classified two muons as shown in Fig 6-5. As a result, the actual working point will entirely depend on the main objective of the given analyses (e.g., focusing on the prediction accuracy of muons or hadrons). Please note that this is an overly simplified example. Depending on the details of the specific boosting algorithm, we usually do not simply double the weights of wrongly classified data points and the final prediction might not be an average of individual trees. Below we will describe the basic idea of the so-called **Adaptive boosted decision tree** (BDT) which is the method used for the analyses in this thesis. For simplicity, we limit the discussion to only binary classifier, i.e., a prediction is either true or false, such as the binary decision tree.

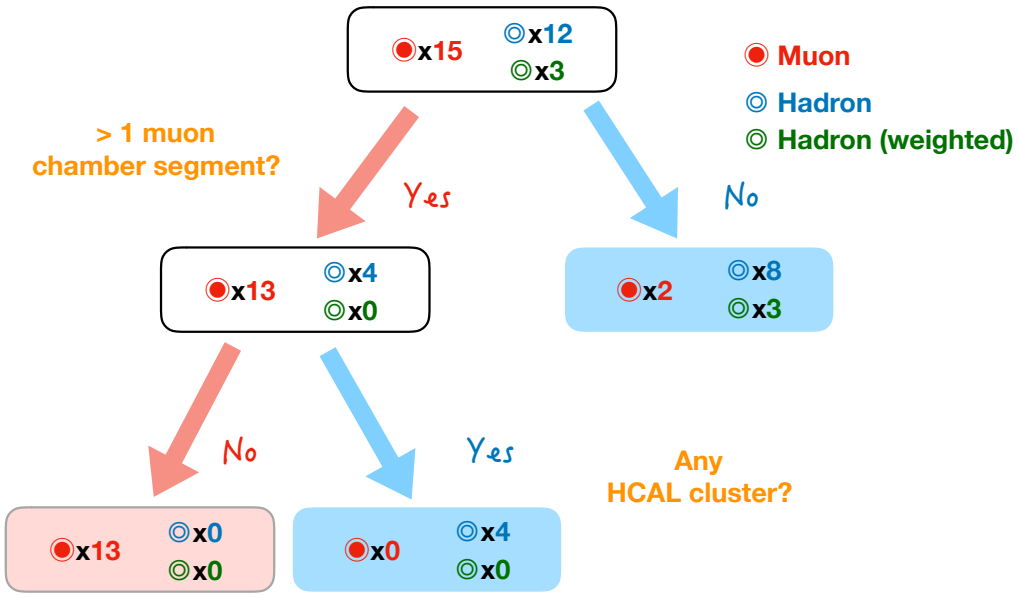

Figure 6-5: Exemplary flowchart of a second shallow decision tree. The decision of this tree will be combined with the first tree in the boosting algorithm to make the final prediction.

The boosting method consists of successive training epochs of the weak learners

(which are shallow decision trees in our case). Each epoch starts with a set of weights for every date points $\mathrm{x_i}$ which are determined by the previous training epoch. Let's say we are at the m-th training epoch and denote $h_{m-1}(\mathrm{x_i})$ to be the ensemble of weak learners from the previous m-1 training epochs. Now, we want to add a new leaner $\hat{h}_m(\mathrm{x_i}, \theta_m)$ (which is a decision tree in our case) that has a model parameter θ_m to this ensemble with some weight α_m (a coefficient). The new ensemble will then be

$$h_m(\mathrm{x_i}) = h_{m-1}(\mathrm{x_i}) + \alpha_m \hat{h}_m(\mathrm{x_i}, \theta_m) \tag{6.7}$$

and the data point weights after this epoch will be

$$W_m(i) = \exp(-y_i h_m(\mathrm{x_i})) \tag{6.8}$$

where y_i is the true class of data point i.

Note that a weight is small when our prediction matches the true class and large when the two disagree. A wrongly classified data point is thus assigned a "larger" weight such that in the next epoch, the next learner will focus more on classifying this point correctly.

Now we define the loss function to be the sum of weights

$$\begin{aligned} L(\alpha_m, \theta_m) &= \sum_{i=1}^{i=n} \exp(W_m(i)) = \sum_{i=1}^{i=n} \exp(-y_i h_m(\mathrm{x_i})) \\ &= \sum_{i=1}^{i=n} \exp(-y_i(h_{m-1}(\mathrm{x_i}) + \alpha_m \hat{h}_m(\mathrm{x_i}, \theta_m))) \\ &= \sum_{i=1}^{i=n} W_{m-1}(i) \exp(-\alpha_m y_i \hat{h}_m(\mathrm{x_i}, \theta_m))) \end{aligned} \tag{6.9}$$

Since the exponent is positive if our prediction and the true class mismatched, this expression will be smaller if more data points are correctly predicted by our current learner.

Our goal now is finding the proper value of α_m and model parameter θ_m for the new learner so as to minimize this loss function. Firstly, we note that for any value

of α, we have

$$\begin{aligned} L(\alpha_m, \theta_m) &= \sum_{i=1}^{i=n} W_{m-1}(i)\exp(-\alpha_m y_i \hat{h}_m(\mathrm{x_i}, \theta_m))) \\ &= \sum_{y_i = \hat{h}_m(\mathrm{x_i}, \theta_m)} W_{m-1}(i)\exp(-\alpha_m) + \sum_{y_i \neq \hat{h}_m(\mathrm{x_i}, \theta_m)} W_{m-1}(i)\exp(\alpha_m) \\ &= \sum_{i=1}^{i=n} W_{m-1}(i)\exp(-\alpha_m) + \sum_{y_i \neq \hat{h}_m(\mathrm{x_i}, \theta_m)} W_{m-1}(i)\big(\exp(\alpha_m) - \exp(-\alpha_m)\big) \end{aligned} \tag{6.10}$$

The first term is a pure sum of weights and is thus irrelevant to the minimization. We like to minimize the second term which can essentially be minimized by finding a learner that best classifies the data set with weight $W_{m-1}(i)$.

Next, we like to find the optimal value of α_m. This can be done via taking the derivative of L

$$\begin{aligned} &\frac{dL(\alpha_m, \theta_m)}{d\alpha_m} \\ =&\frac{\sum_{y_i = \hat{h}_m(\mathrm{x_i}, \theta_m)} W_{m-1}(i)\exp(-\alpha_m) + \sum_{y_i \neq \hat{h}_m(\mathrm{x_i}, \theta_m)} W_{m-1}(i)\exp(\alpha_m)}{d\alpha_m} = 0 \\ \rightarrow &\sum_{y_i = \hat{h}_m(\mathrm{x_i}, \theta_m)} W_{m-1}(i)\exp(-\alpha_m) = \sum_{y_i \neq \hat{h}_m(\mathrm{x_i}, \theta_m)} W_{m-1}(i)\exp(\alpha_m) \\ \rightarrow &\ \alpha_m = \frac{1}{2}\log\frac{\sum_{y_i = \hat{h}_m(\mathrm{x_i}, \theta_m)} W_{m-1}(i)}{\sum_{y_i \neq \hat{h}_m(\mathrm{x_i}, \theta_m)} W_{m-1}(i)} = \frac{1}{2}\log\frac{1-\epsilon_m}{\epsilon_m}, \end{aligned} \tag{6.11}$$

where we have defined the learner error as $\epsilon_m = \sum_{y_i \neq \hat{h}_m(\mathrm{x_i}, \theta_m)} W_{m-1}(i)$.

With this, we can update our ensemble by

$$h_m(\mathrm{x_i}) = h_{m-1}(\mathrm{x_i}) + \alpha_m \hat{h}_m(\mathrm{x_i}, \theta_m) \tag{6.12}$$

We will also need to ensure our new weights $W_m(i) = \exp(h_m(\mathrm{x_i}))$ are properly normalized

$$\begin{aligned} &W_m(i) \rightarrow c_m W_m(i) \\ &s.t.\ \sum_{i=1}^{i=n} W_m(i) = 1 \end{aligned} \tag{6.13}$$

This finishes the basics of the BDT algorithm.

To summarize our BDT algorithm:

1. Initialize weights $W_0 = \frac{1}{n}$;
2. Repeat the following three steps until converge;
3. Train a new decision tree $\hat{h}_m(\mathrm{x_i}, \theta_m)$ that minimizes the training error $\epsilon_m = \sum_{y_i \neq \hat{h}_m(\mathrm{x_i}, \theta_m)} W_{m-1}(i)$;
4. Add this new decision tree to the ensemble with $h_m(\mathrm{x_i}) = h_{m-1}(\mathrm{x_i}) + \alpha_m \hat{h}_m(\mathrm{x_i}, \theta_m)$ where $\alpha_m = \frac{1}{2} \log \frac{1-\epsilon_m}{\epsilon_m}$;
5. Update the weights $W_m(i) = W_{m-1}(i) \exp(-\alpha_m y_i \hat{h}_m(\mathrm{x_i}, \theta_m)))$ and normalize the new weights to unity;

For the BDT algorithm setting used in this thesis, 850 trees were generated/trained and each tree was limited to a maximal depth of 3 layers. In addition, we also required that each node contains at least 2.5% of the total training events.

Chapter 7

Analysis

We talked about the physics importance of measuring B meson transverse momentum spectra modifications in medium in chapter 2. In this chapter we will present the details of the analyses which are based on contents published in Ref. [112, 114, 122]. The way we measured the B mesons was via reconstructing their full decay chains. We then extracted the raw yields from the reconstructed B meson candidate mass spectra. Given the luminosity and the number of inelastic events (minimum bias events) analyzed, we can calculate its cross sections by correcting the raw yields with corresponding efficiencies. Specifically, we measured the differential cross sections $d\sigma/d\mathrm{p_T^B}$ of B^+, B^0, and B_s^0 mesons as summarized in Table 7.1

Table 7.1: A summary of B meson measurements in pp, pPb, and PbPb collisions in this thesis.

Collision system	pp	pPb	PbPb
$\sqrt{s_{\mathrm{NN}}} = 5.02$ TeV	B^+, B_s^0	B^+, B^0, B_s^0	B^+, B_s^0

The decay chains we chose to analyze are the following exclusive channels

- $B^+ \to J/\psi\ K^+ \to \mu^+\ \mu^-\ K^+$
- $B^0 \to J/\psi\ K^*(892)^0 \to \mu^+\ \mu^-\ K^+\ \pi^-$
- $B_s^0 \to J/\psi\ \phi \to \mu^+\ \mu^-\ K^+\ K^-$

with the J/ψ, $K^*(892)^0$, and ϕ mesons subsequently decay via $J/\psi \to \mu^+\mu^-$, $K^*(892)^0 \to K^+\pi^-$, and $\phi \to K^+K^-$. A schematics of the B^+ meson decay can be found in Fig. 7-1.

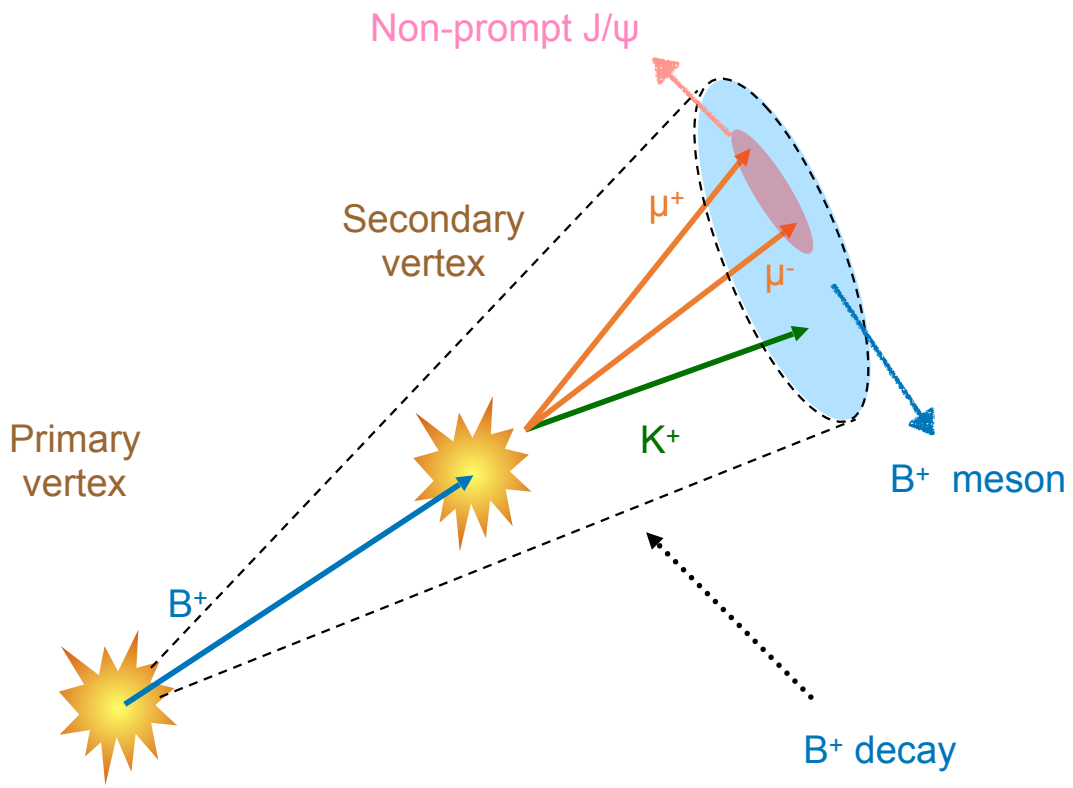

Figure 7-1: A schematics of the B^+ meson decay.

The cross sections from different collision systems can then be compared and the nuclear modification factors can be calculated. In the following, the reconstruction of the full B meson decay chains via vertex fitting, which is one of the most crucial parts of the analyses, will be described. A list of basic selection criteria applied to data that ensure the events and objects we analyzed were under control with high quality will be provided and explained. We will then present another important part of the analyses which is the training of a machine learning classification model that can provide a high signal to background ratio. Systematic and statistical uncertainties which are essential for any experimental results will also be discussed. Finally, our

results will be presented and compared with several different theoretical models.

7.1 Data samples

The data samples analyzed in the analyses were collected by the CMS experiment at a center of mass energy $\sqrt{s_{\mathrm{NN}}} = 5.02$ TeV. Chronologically, the data used for the pPb analysis was collected during 2013 while the data used for pp and PbPb analyses were collected during 2015. A summary of the corresponding luminosity of each data samples can be found in Table 7.2. Because of the asymmetry nature of pPb collisions, LHC conducted two separate periods of data-taking during the pPb data-taking. In the first part of the data-taking (around 60% or $21\,\mathrm{nb}^{-1}$ of the pPb data), the proton beam traveled to the negative η direction (toward Léman lake) with an energy of 4 TeV while the lead beam traveled to the positive η direction (toward Jura Mountains) at 1.58 TeV. The system was boosted to the negative η direction. During the last 40% ($14\,\mathrm{nb}^{-1}$) period, the beams were swapped and the collision system was boosted to the positive η direction.

Table 7.2: List of the data samples used with the corresponding integrated luminosities.

System	Luminosity
pPb	$35\,\mathrm{nb}^{-1}$
pp	$28\,\mathrm{pb}^{-1}$
PbPb	$351\,\mu\mathrm{b}^{-1}$

The triggers used in the pp and pPb data were both un-prescaled during the whole data-taking period while the PbPb trigger had different prescale values throughout the data-taking period. Events used in the pp and PbPb analyses were collected with triggers requiring the presence of two independent muon candidates in the muon detector with no muon $\mathrm{p_T}$ or muon rapidity threshold. For the pPb analysis, the corresponding trigger selected events with at least one muon with a $\mathrm{p_T}$ threshold of 3 GeV/c.

In order to extract those genuine inelastic hadronic collision events and remove

unwanted beam backgrounds and noises, several offline event selections were applied to the data set. Firstly, for every data samples, events were required to have at least one reconstructed primary vertex (PV). This PV was formed by two or more associated tracks and was required to have a distance from the nominal interaction region of less than 15 cm along the beam axis and less than 0.15 cm in the transverse plane. A beam-background filter was applied to pp events to remove the beam-gas and beam-halo events [108, 190, 182] which are essentially collisions between beam and beam gas (or beam remnants). An additional selection (for hadronic collisions) was applied to both pPb and PbPb events by requiring a coincidence of at least 3 towers in the forward hadronic calorimeter, with more than 3 GeV total energy, on both sides of the interaction point. Finally for PbPb events only, a cluster compatibility filter was applied.

Cluster compatibility: For a particle trajectory with given η and z-position of the collision vertex, the expected cluster width it can leave in the pixel modules can be calculated. This means that for a given z-position of a vertex, one can determine the number of clusters that have widths compatible with this vertex and define a cluster-to-vertex compatibility [128, 131].

7.2 Monte Carlo samples

MC simulations played a paramount role in the analyses. They provided the correction factors needed to convert B meson raw yields to cross sections. Moreover, they were also used for training ML models, estimating systematic uncertainties, and cross-checking potential biases. In this section, we will describe the types of MC simulations used in the analyses and related re-weighting procedures.

7.2.1 Signal samples

Dedicated B meson signal samples were generated in order to estimate the acceptance and selection efficiencies, to study the background components, and to evaluate sys-

tematic uncertainties. First of all, PYTHIA8 [189] generator was used to generate inclusive (all quark, anti-quark, as well as gluon initiated) QCD processes at a center of mass energy of 5.02 TeV. Several prefilters at the generation steps were applied in order to optimize the generating processes and conserve resources. Only signal events (with at least one B^+, B^0, or B_s^0 meson generated, which were forced to decay exclusively to the signal channels by means of the EVTGEN package [175]) were kept in the simulations. Final state radiations (FSR) were generated using PHOTOS [20]. Since a full heavy ion event generator is not yet available, underlying events of heavy ion collisions and the hard probes (the beauty quarks in this case) are generated separately. To simulate the underlying events in pPb and PbPb collisions, HIJING [192] and HYDJET [176] event generators were used . These generators simulated minimum bias collisions and were both tuned to reproduce the total particle multiplicities and charged-hadron spectra and to approximate the underlying event fluctuations seen in real data.

As one expects, the generated B mesons will have an exponentially falling p_T spectra as the higher the momentum of a B meson, the harder for it to be produced in a collision. High p_T B mesons are thus relatively rare comparing to low p_T B mesons in the same MC simulation. In order to increase the efficiency of high p_T B meson generations, we generated several MC simulations with same configurations but different lower bound of $\hat{p}_T$ which specifies the momentum transfer between the two colliding nucleons. The higher the $\hat{p}_T$, the more probable a high p_T B meson is generated. This procedure is done for the generation of 5.02 TeV pp and PbPb collision samples. Around fifty thousand events were generated in 5 different $\hat{p}_T$ lower bounds ([0, 5, 15, 30, 50]). On the contrary, the pPb samples were generated inclusively, i.e., $\hat{p}_T$ lower bound were equal for every samples, since the size of pPb simulated events were relatively small and the selection criteria used were looser. Five hundred thousand events were generated for each channel. A summary of number of events generated is summarized in Table. 7.3.

Table 7.3: Summary of number of events generated for B meson signal MC simulations.

System	number of events generated	$\hat{p}_T$
pPb	B^+, B^0, B_s^0; 500k events for each channel	[0]
pp	B^+, B_s^0; 50k events for each channel and $\hat{p}_T$	[0, 5, 15, 30, 50]
PbPb	B^+, B_s^0; 50k events for each channel and $\hat{p}_T$	[0, 5, 15, 30, 50]

7.2.2 J/ψ samples

In addition to the signal B meson MC simulations, we also generated other MC simulations to aid the study of background processes (in particular, the peaking background study which will be introduced in later sections). As one can imagine, the biggest background contributions are processes that can produced a J/ψ meson. These processes are classified into two categories base on the closeness between the J/ψ meson vertex and the interaction point as the following.

- The prompt J/ψ mesons: which consist of J/ψ mesons produced at the vicinity of the interaction point. They are produced either directly from the collisions or as the daughters of particles that decay promptly such as Υ mesons.

- The non-prompt J/ψ mesons: which consist of J/ψ mesons that are the daughters of b hadrons with decay channels different from those signal channels we are investigating.

Dedicated sets of prompt J/ψ and non-prompt J/ψ meson MC simulations were generated for pp, pPb, and PbPb collisions. Further discussions about these background contributions will be presented in later sections.

7.2.3 MC re-weighting

Although an ideal MC simulation should mimic real collision data perfectly. Unavoidably discrepancies between real data and simulations almost always exist. It could be that the generator simply does not generate the process correctly due to our limited knowledge of the underlying physics phenomenon or the information of

detector condition used in the simulation is not updated properly. In order to account for this discrepancy, a re-weighting procedure was applied to MC simulations. This procedure can be understood as follows: instead of using each generated event equally, we assigned a different weight to each event so that in the end, the weighted distribution (of a given variable) of the MC simulations are the same as real data. Three re-weighting procedures, each focused on a particular variable, were applied to the MC simulations. We will use the B_s^0 channel as an example in the following.

Firstly, the p_T spectrum of the simulated B_s^0 mesons was re-weighted to match the **Fixed-order next-to-leading order logarithmic approach** (FONLL) [177, 178] theoretical calculations. In Fig. 7-2, the B_s^0 meson p_T spectrum obtained in MC simulations (left panel) is compared to the FONLL calculations at 5.02 TeV (middle panel). A ratio distribution between the two is shown in the right panel of the same figure. The weight function was obtained by fitting this ratio distribution with a 2nd order polynomial.

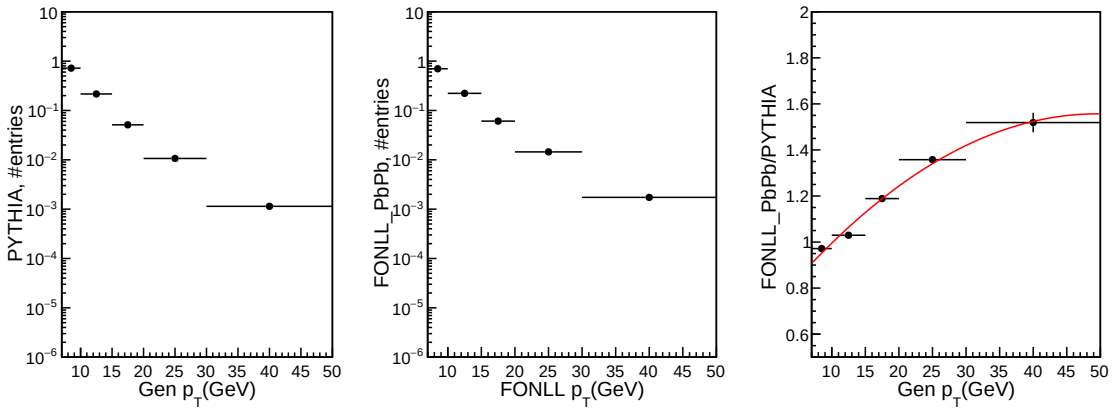

Figure 7-2: B_s^0 meson p_T spectrum obtained in PbPb MC simulations (left) compared to FONLL calculations in PbPb collisions at 5.02 TeV (middle). The ratio between the two distributions was fitted with a 2nd order polynomial function (right).

Secondly, the centrality distribution of PbPb collision simulations was re-weighted to match the real data. In the left panel of Fig. 7-3, the centrality distribution of MC simulations (red) is compared to the one in real data (black). On the right panel, again the corresponding ratio is presented. The weighting function was obtained by

fitting the ratio with the following function

$$p_1 e^{p_2(c-p_3)^{p_4}} \tag{7.1}$$

where p_1, p_2, p_3, and p_4 are the fitting parameters and c is the centrality.

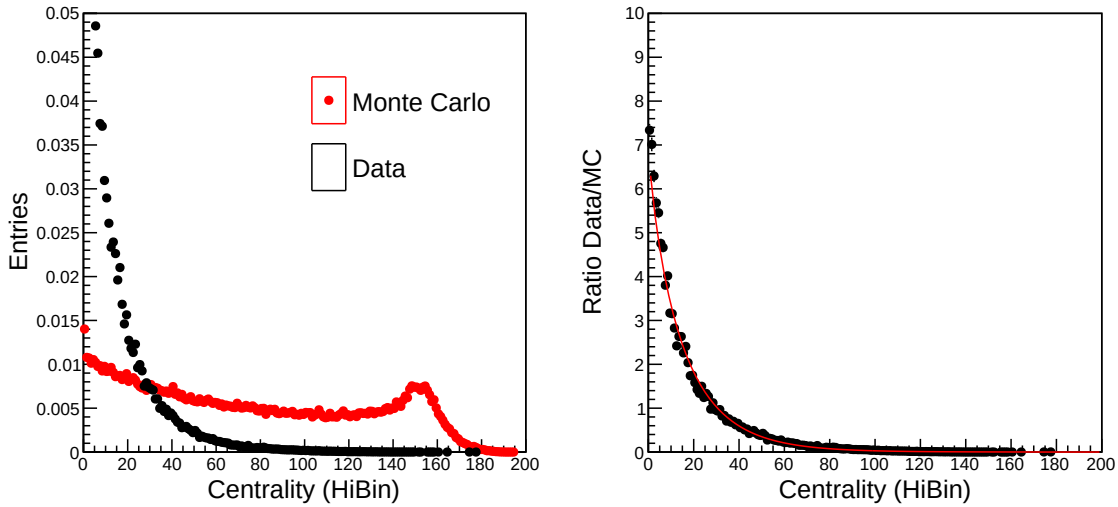

Figure 7-3: Centrality distribution of MC simulations (red) and real data (black) in PbPb collisions at 5.02 TeV (left). The ratio between the centrality distributions of real data and MC simulations was fitted with a exponential-like function (right).

Finally, the primary vertex z-position (PVz) distribution was also re-weighted. The result after the re-weighting can be found in Fig. 7-4. On the left panel, the red markers show the MC simulated PVz distribution after the weighting while the black markers are from real PbPb collision data. Note that our measurements are actually insensitive to the absolute value of the PV position because the reconstruction of a B meson relies only on the relative distance between the PV and the secondary reconstructed vertex (introduced in a later section). Our estimation of this effect is only 1.3%.

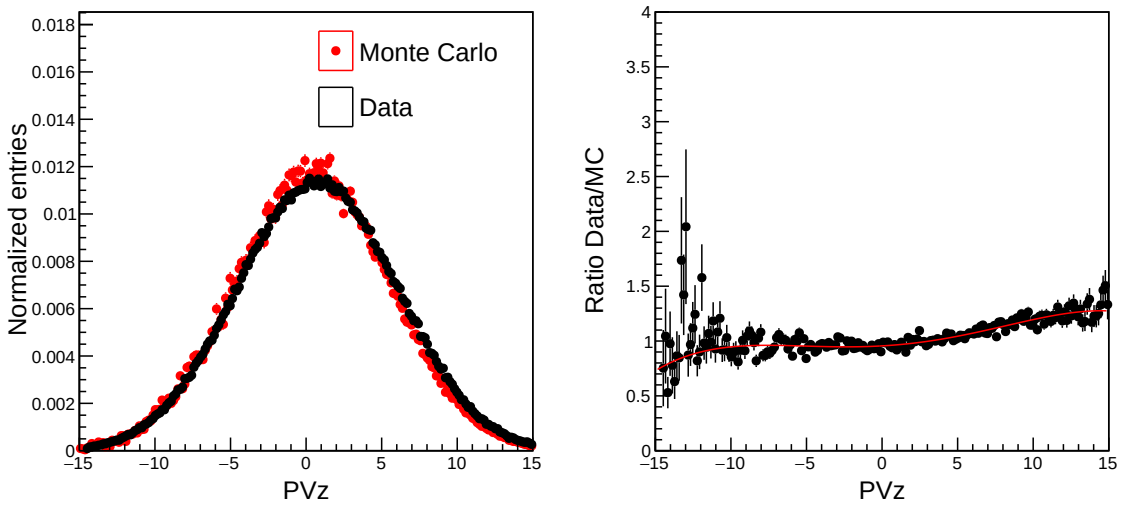

Figure 7-4: Primary vertex z position (PVz) spectrum obtained in PbPb collision simulations after the re-weighing procedure (red marker) compared to real PbPb collision data (black marker) at 5.02 TeV (left). The ratio between the MC simulations and real data distributions (right).

7.3 B meson reconstruction

The foundation of fully reconstructing B meson decay is to identify displaced tracks (tracks originated from vertices away from the PV) and their associated vertices, the secondary vertices (SV). As mentioned earlier, this is possible because B mesons have particularly long decay lengths. We will combine tracks and muons in the events and fit the combinations to obtain the SVs. In the following, the idea of this fitting procedure will be described.

7.3.1 Secondary vertex reconstruction

The core technique that enables the full reconstruction of B meson decay SV is the so-called **Kinematic vertex fitter** [185]. It is a **Least means squared** minimization (LMS) which is essentially the same as the global method in Ref. [24] with an additional constraint term $\mathrm{H}(p_i^{fit}) = 0$ where $p_i^{fit} = \mathbf{A}_i x + \mathbf{B}_i q_i + c_i$. Following the same notations we used in section 5.2, x is the vertex position, q_i is the i-th track momentum, and p_i is the trajectory parameters. In other words, x and q_i together is the physical state and p_i is the measurement. Since $\mathrm{H}(p_i)$ can be a non-linear function, we Taylor expand it at some reference point p_i^{ref} so that our constraint term becomes

$$\frac{\partial \mathrm{H}(p_i^{ref})}{\partial p_i}(\delta p_i) + \mathrm{H}(p_i^{ref}) = D_i \delta p_i + d_i = 0 \tag{7.2}$$

where $\delta p_i = (p_i^{fit} - p_i^{ref})$.

The global minimization objective function that we would like to minimize is now

$$\sum_i^n (p_i - p_i^{fit})^{\mathrm{T}} \mathrm{G}^{-1} (p_i - p_i^{fit}) + 2\lambda^T (D_i \delta p_i + d_i) \tag{7.3}$$

where G is the covariance matrix of p_i and λ is the **Lagrange multiplier**. The fitter seeks the optimal values of x and q_i to minimize this objective function. Intuitively, for a given set of track trajectories, the vertex fitter re-fits these trajectories by modifying their trajectory parameters in a way such that these trajectories will all pass a common point in the space while satisfying addition external constraints. The

re-fitted values are those that minimize the χ^2 value which is defined based on the covariance matrix between trajectory measurements. A common vertex, the SV, is produced during this process.

In the case of reconstructing the B meson decay vertex, we would like to find this vertex by fitting the pion/kaon tracks from the B meson decays with the muon tracks that come from the J/ψ meson that resulted from the same B meson. For this, we paired all possible combinations of muons and tracks within a event and find the SV for each combination. Every combinations within a single event were considered to be possible B meson candidates. Now, constraints can be incorporated by the vertex fitter we just described. In particular, we constrained these trajectories to have the PDG [162] invariant masses of a muon or a kaon/pion after the fitting. Furthermore, we also constrained the muon pairs and track pairs to have the PDG masses of a J/ψ meson and a $K^*(892)^0$ or ϕ meson. By adding these constraints, the fitter can greatly remedy the detector resolution effects and is one of the indispensable parts of the analyses.

A flowchart of the workflow we just described is shown in Fig. 7-5. Firstly, muons and tracks were required to pass several quality selection criteria which will be described in section 7.4.1 and section 7.4.2. J/ψ candidates were then reconstructed by vertexing all possible muon pairs with opposite charge signs. For the reconstructions of the B^0 and B_s^0 mesons, the intermediate $K^*(892)^0$ and ϕ resonances were reconstructed by vertexing all possible track pairs. Charged tracks within the events (passing the quality selection criteria) were assigned the kaon or pion invariant masses (depending on the channel). $K^*(892)^0$ and ϕ meson candidates were then reconstructed in the same way as the J/ψ candidates via vertexing. Finally, the B^+ candidates were built by combining the J/ψ candidates with a track assigned a kaon mass while the B^0 and B_s^0 candidates were built by combining the J/ψ candidates with the $K^*(892)^0$ or ϕ candidates. A final vertexing was performed on these candidates with constraints that ensure the masses of the muon pairs equal to PDG J/ψ meson mass and the masses of track pairs equal to PDG $K^*(892)^0$ or ϕ meson masses. Note that we have referred to the reconstructed objects as "candidates" since they

were no more than some combinations of muons and tracks and can very well be just background.

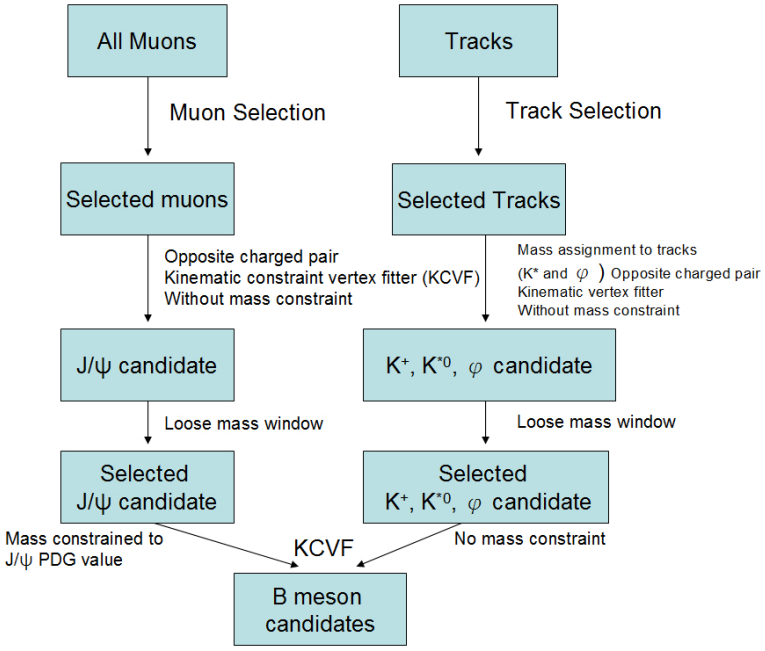

Figure 7-5: A flowchart of the B meson reconstruction workflow

7.4 Selection criteria

Different quality selection criteria were applied to muon and track objects used in the reconstruction of the B meson candidates. This is to ensure the objects we used are genuine physics objects that match our assumptions and expectations rather than fake objects from some random noise or combinatorial background. In addition, we also want to exclude candidates that were illy reconstructed as they will degrade our precision. Reconstructed J/ψ, $K^*(892)^0$, ϕ, and B mesons were also subjected to different selection criteria for the same purposes.

In the following, we will present a comprehensive list of the selection criteria used in the analyses. Some of them were based on studies performed by the CMS muon and tracking groups. Others were results of dedicated analyses done for the B meson measurements. Note that because of the difference in collision systems (e.g., pPb

vs PbPb) and detector condition (pPb data was recorded during 2013 while pp and PbPb data were recorded during 2015), the selection criteria will be slightly different between each other.

7.4.1 Muon and J/ψ selection

The muon candidates were selected according to the following criteria, developed by the CMS muon group [116].

- a Global muon (unique to 2015 data);
- a Tracker muon;
- at least one well matched segment in the muon station;
- transverse impact parameter $D_{xy} < 0.3$;
- longitudinal impact parameter $D_z < 20$ and 30 for 2015 and 2013 data respectively;
- number of pixel layer valid hits > 0;
- number of total tracker (pixel + strip layer) valid hits > 5.
- the χ^2/ndf of the muon track in tracker < 1.8 (unique to 2013 data);

These selection criteria ensure a high signal to noise ratio and the trajectory measurement uncertainties due to resolution effects are minimal.

In addition to these quality selection cuts, a phase space requirement is also required (acceptance selections). This is due to the design and positioning of the muon chambers in the CMS detector. Only muons with a minimal p_T or p threshold, as a function of its η, are able to register adequate number of hits in the muon chambers. Therefore, we exclude muons that run below these thresholds to have a better signal

to noise ratio.

2013 criteria :

$$
\begin{aligned}
&\mathrm{p}_{\mathrm{T}}^{\mu} > 3.3\mathrm{GeV/c} && \text{for } |\eta^{\mu}| < 1.3 \\
&\mathrm{p}_{\mathrm{T}}^{\mu} > 2.9\mathrm{GeV/c} && \text{for } 1.3 \leq |\eta^{\mu}| < 2.2 \\
&\mathrm{p}_{\mathrm{T}}^{\mu} > 0.8\mathrm{GeV/c} && \text{for } 2.2 \leq |\eta^{\mu}| < 2.4
\end{aligned}
$$

2015 criteria :

$$
\begin{aligned}
&\mathrm{p}_{\mathrm{T}}^{\mu} > 3.5\mathrm{GeV/c} && \text{for } |\eta^{\mu}| < 1.2 \\
&\mathrm{p}_{\mathrm{T}}^{\mu} > (5.77 - 1.8 \times |\eta^{\mu}|)\mathrm{GeV/c} && \text{for } 1.2 \leq |\eta^{\mu}| < 2.1 \\
&\mathrm{p}_{\mathrm{T}}^{\mu} > 1.8\mathrm{GeV/c} && \text{for } 2.1 \leq |\eta^{\mu}| < 2.4
\end{aligned}
\tag{7.4}
$$

These single muon selections were chosen in order to guarantee a reasonable ($\approx$ 10%) reconstruction and trigger efficiency for all the selected muons.

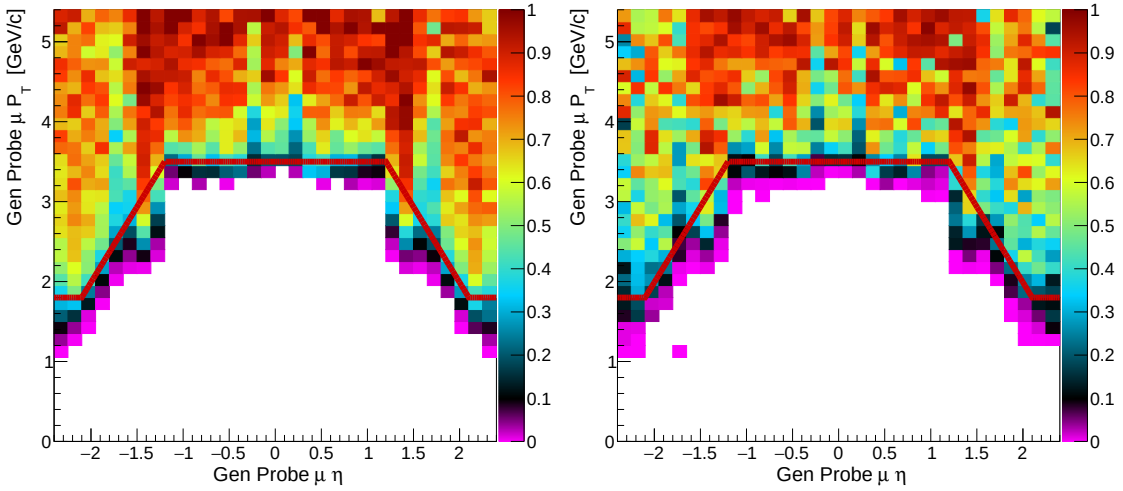

Figure 7-6: Single muon acceptance×efficiency using pp (left) and PbPb (right) reconstruction algorithms. The red line represents the 2015 single muon acceptance cuts [123].

7.4.2 Track selection

Similarly for tracks, they were selected according to the following criteria

- a **highPurity** [107] identification tag which is a ML model with variables consist of number of measurements, fitting χ^2, transverse and longitudinal distance to the PV, and other variables;
- track η <2.4;
- track p_T selection depending on the collision system and decay channel.

collision system/track p_T (GeV/c)	B^+	B^0	B_s^0
pPb	0.9	0.7	0.7
pp	0.5	—	0.0
PbPb	0.8	—	0.0

Again these selections ensure a high signal to noise ratio and reliable trajectory measurements. In particular, the track p_T thresholds also serve as a pre-selection for controlling the processing time and storage resources. This variable will be used in the ML classification model which will be discussed in a later section.

7.4.3 J/ψ meson selection

In addition to single muon quality selections, for a muon pair, the following selections were applied

- two muons have opposite charge signs;
- dimuon invariant mass value within a mass window centering around the PDG J/ψ mass;
- probability of the two muon tracks to originate from the same decay vertex > 1% (vertexing probability).

These selections enabled us to discard muon pairs that are dissimilar to the J/ψ meson assumption which are pairs resulted from uncorrelated muons within the same event.

7.4.4 $K^*(892)^0$, ϕ and B meson selection

For the B^0 and B_s^0 channels, since the intermediate resonance $K^*(892)^0$ and ϕ mesons were reconstructed, additional selection criteria were applied to these two channels. In particular, a loose $K^*(892)^0$ and ϕ invariant mass window were applied, before vertexing, in order to increase the processing speed by skipping the vertexing of unnecessary candidates. Mass window of B meson is also applied for the same reason.

- B meson candidate invariant mass value between 4.5 to 6.5 GeV/c^2.
- track pair invariant mass value within a mass window centering around the $K^*(892)^0$ or ϕ meson PDG mass;

Note that the differences between B meson masses before and after the vertexing is of order 0.2 GeV/c^2. Since we are only interested in B meson candidates with invariant mass value (after the vertexing) close to the PDG value (specifically, 5 to 6 GeV/c^2), i.e. those that match the corresponding B meson assumptions, this selection has virtually no effect on the results but greatly speed up the computing time. Note that this is a very wide interval (5 to 6 GeV/c^2) which will include B meson candidates far off the B meson resonance peak, i.e., background candidates. The reason is related to the yield extraction procedure which will be introduced in a later section. As for the intermediate meson mass windows, the observed ϕ meson mass width in signal MC simulations is less than 0.01 GeV/c^2. This selection is thus also loose enough and does not affect the real signal candidates while removing the majority of background candidates.

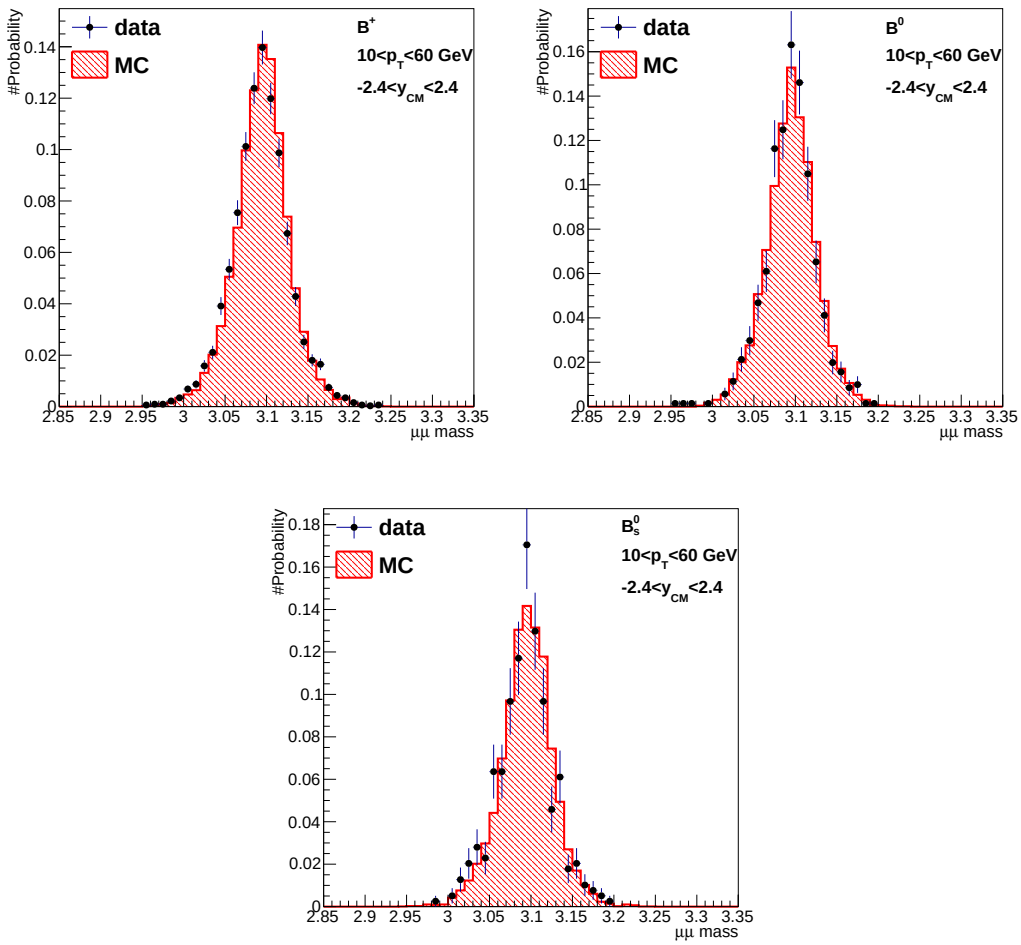

Figure 7-7: J/ψ meson invariant mass spectra from the selected B^+ (top left), B^0 (top right), and B_s^0 (bottom) meson candidates with $10 < \mathrm{p_T} < 60$ GeV/c and $|y| < 2.4$ passing the selection criteria described above in pPb collision real data and MC simulations.

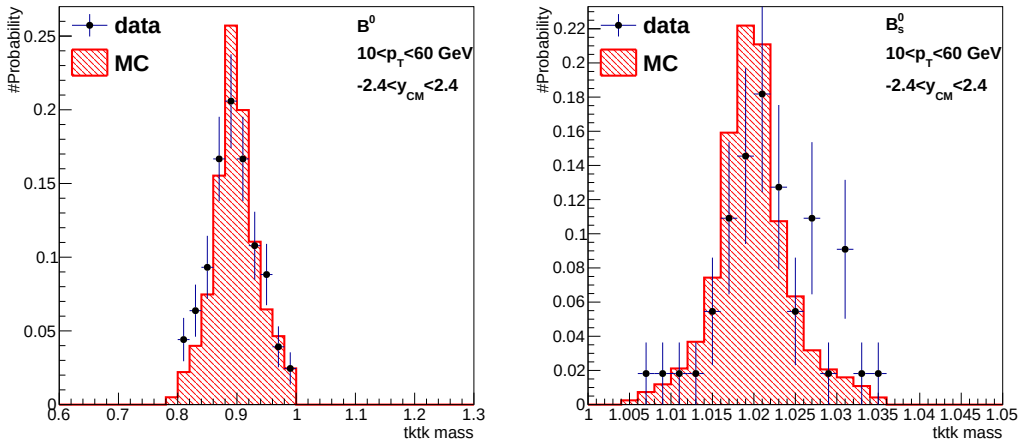

Figure 7-8: $K^*(892)^0$ (left) and ϕ meson (right) invariant mass spectra, from the selected B^0 and B_s^0 meson candidates respectively, with $10 < \mathrm{p_T} < 60$ GeV/c and $|y| < 2.4$ passing the selection criteria described above in pPb collision real data and MC simulations.

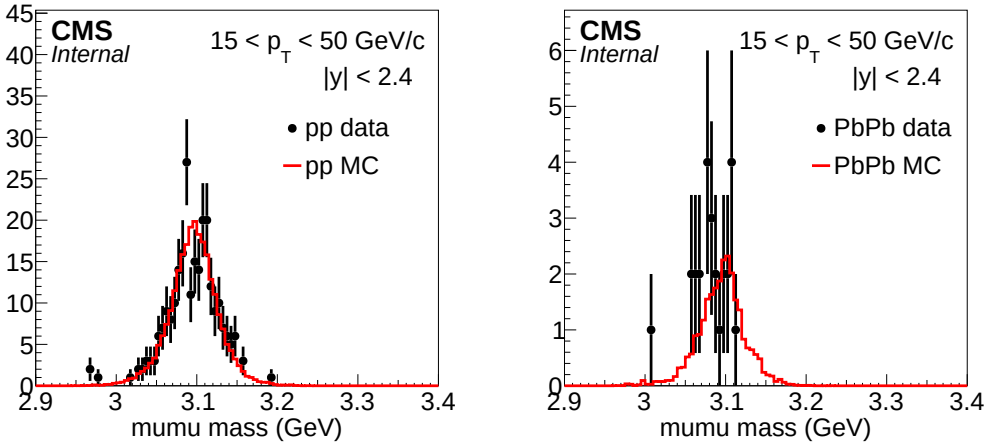

Figure 7-9: J/ψ meson invariant mass spectra from the selected B_s^0 meson candidates with $15 < \mathrm{p_T} < 50$ GeV/c and $|y| < 2.4$ passing the selection criteria described above in pp (left) and PbPb (right) collision real data and MC simulations.

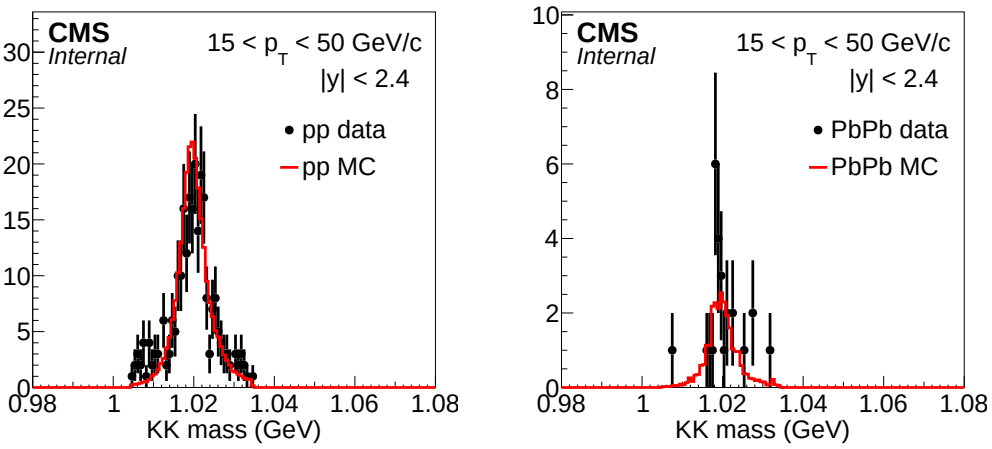

Figure 7-10: ϕ meson invariant mass spectra from the selected B_s^0 meson candidates with $15 < \mathrm{p_T} < 50$ GeV/c and $|y| < 2.4$ passing the selection criteria described above in pp (left) and PbPb (right) collision real data and MC simulations.

7.5 B meson selection optimization

In the pp collision data, a clear B meson resonance is already observable after applying the selections presented in section 7.4. However, the situation is drastically different in pPb and PbPb collisions as the number of combinatorial backgrounds (combinations of unrelated tracks and muons) is much larger. Better and tighter B meson selection criteria are necessary for measuring B mesons in pPb and PbPb collisions. On the other hand, even for the pp analysis, one would like to decrease the statistical uncertainty which is related to the performance of the yield extraction procedure (introduced in the next section). Since the performance is further related to the ratio of signal over background in the mass spectrum (the higher the ratio, the better the performance), devising good B meson selections is also very beneficial for the pp data. In this section, we will introduce a procedure that can maximally separate signal from background and reconstruct observable resonances in the pPb and PbPb data. To extract as much B meson signals from the data as possible, two things are crucial. 1) Create new features that are capable of differentiating signal from background; 2) Utilize a ML model to search for the optimal way of using these features. We will describe these two parts in what follows.

7.5.1 Feature engineering

We would like to create features that can capture the differences between signal and background B meson candidates. Firstly, for a signal B meson candidate, by definition all the muons and tracks of a given combination originated from the same vertex. Vertex fitting performance or more precisely the fitting χ^2 value naturally serves as a good feature. Secondly, as we mentioned earlier, the decay length of a B meson is comparatively long due to the smallness of off-diagonal elements of the CKM matrix. The distance between the collision PV and the SVs of B meson candidates is a useful feature. Thirdly, since we are reconstructing particles with momenta around tens of GeV/c with invariant masses around 5 GeV/c^2 while the decay daughters, the muons, pions, and kaons, all have sub-GeV invariant masses. The decay system is expected

to be boosted in the lab frame. The opening angles between daughter muons and tracks can be very small comparing to combinatorial background candidates. Next, for channels with intermediate resonances, the invariant masses of $K^*(892)^0$ and ϕ meson candidates will also be good indicators. In particular, for the B^0 channel, there are sizable background contributions (the peaking backgrounds, to be discussed in a later section) coming from the B_s^0 decay channel in which one of its kaon tracks (from ϕ meson decays) was wrongly identified as pions. Since the kaon track in this case is assigned a smaller mass value (the mass of pion), these contributions pile on the left of the signal resonance peak in the invariant mass spectrum. A selection on the absolute track pair invariant mass value can remove these background contributions. Lastly, we also want to consider other possible relations between decay daughters. The track p_T, η, as well as the distance between track vertex and PV are being used as features also. A list of features used in the ML training:

- vertex fitting probability, the fitting χ^2 value;
- 2D and 3D SV to PV distance normalized by its uncertainty;
- α_B angle: the angle between the B meson displacement (PV to SV pointing vector) and the B meson momentum direction;
- cosine θ_B angle: the cosine value of the angle between the B meson displacement vector and the B meson momentum direction in the transverse direction;
- the invariant mass of the track pair (which forms $K^*(892)^0$ or ϕ meson candidates);
- track pair invariant mass difference: the absolute difference between the invariant mass of the track pair and the corresponding PDG mass ($K^*(892)^0$ or ϕ meson);
- the transverse momentum of the pion or kaon track;
- normalized track Dxy: the normalized transverse distance between the pion or kaon track to PV;

Note that during the process of feature engineering, many other features were developed and tested. The set of features presented above are those found to be most effective after the feature selection process discussed previously in section 6. A schematics of the B^+ meson decay and the definitions of features (variables) used in selection optimization can be found in Fig. 7-11.

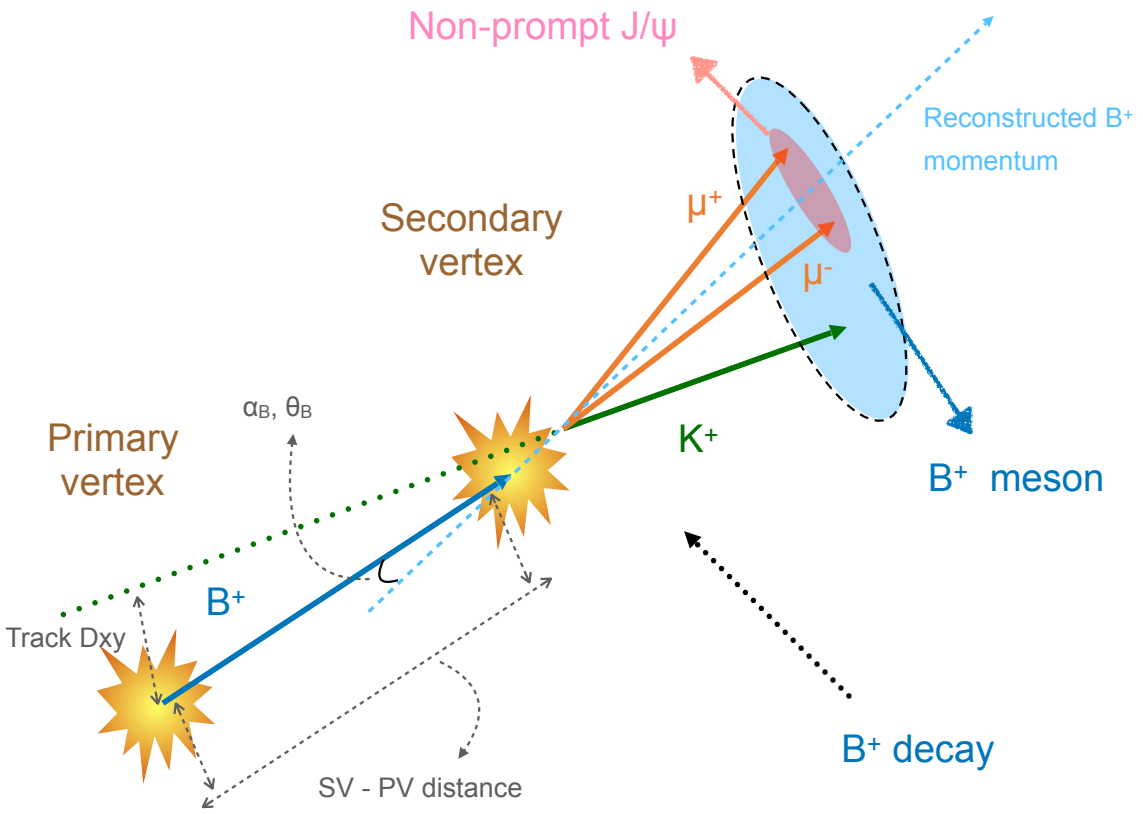

Figure 7-11: A schematics of the B^+ meson decay and the definitions of features (variables) used in selection optimization.

7.5.2 Machine learning selection criteria optimization

With the set of features we came up with in the previous section, the next thing will be finding the optimal way to utilize all these different features to distinguish signals from backgrounds in data. Conventionally, this is done by inspecting the distributions of each features between signal and background, often from simulations, to find an

optimal point where the two are maximally separated. This is done repeatedly and in the end, one comes up with a cut value for each of these features just like those in section 7.4, cutting a hyper-cube in the phase space of features.

However, this procedure is very time consuming and unless one really scanned through all possible cut values of these features, it is difficult to make sure that a global optimal point have been reached. Moreover, if these features are correlated to each other, this manual effort will never capture it. This is where the ML technique plays a critical role. By training a ML model, one can find the proper selection criteria that is optimized for this purpose automatically (ML cut optimization). The ML software used in this thesis is the **TMVA** (Toolkit for Multivariate Data Analysis with ROOT) [168].

For our analyses, reconstructed B meson signals in MC simulations were used as signals for training. Reconstructed candidates in the "sideband" ($0.2\ \mathrm{GeV/c^2} < |M_B - M_B^{PDG}| < 0.3\ \mathrm{GeV/c^2}$ where M_B is the reconstructed B meson candidate invariant mass value while M_B^{PDG} is the corresponding B meson PDG mass) of the B meson invariant mass spectrum of real data were used as backgrounds. This ML cut optimization was performed in each B meson $\mathrm{p_T}$ intervals (which is chosen such that real data statistics are evenly distributed in each bins) separately.

The goal of the optimization procedure is to maximize the statistical significance of the signal, minimize background contributions, and keep a reasonably high signal efficiency. Two ML algorithms, cut-based and BDT were used in this thesis. In the case of the cut-based method, the machines scan the model parameter space to search for the cut values that minimize the background efficiency (the probability for a background sample to pass the selection, also known as "fall-out") for a given signal efficiency (also known as "recall"). This means we will have many signal and background efficiency pairs as the output of the cut-based method. For the BDT method, the algorithm provides a BDT discriminant variable after the training. A cut on the BDT discriminant variable will thus also have a corresponding signal and background efficiency pair. The optimal working point, which is a cut value set for the cut-based method and a single BDT discriminant cut value for the BDT method,

is found by scanning these signal and background efficiency pairs and finding the pair that maximizes the statistical significance $S/\sqrt{S+B}$.

- $S = S' \times$ (signal efficiency), where S' is the number of signals in the signal region before applying optimal cuts.
- $B = B' \times$ (background efficiency), where B' is the number of backgrounds in the signal region before applying optimal cuts.

S' was calculated by the expected number of signals from the FONLL calculations multiplied by quality cut (selections presented in section 7.4) efficiency estimated from simulations. B' was estimated by a linear interpolation using the number of candidates in the sideband, i.e., (number of candidates in the sideband)*(signal region width)/(sideband region width). Signal region is defined as $|M_B - M_B^{PDG}| < 2^*\sigma$ where σ is the B meson resonance width.

Cut-based

The cut-based method provides the optimal cut value (that minimize the background efficiency) of each input feature for a given signal efficiency. We scanned through signal efficiencies and found the working point (which is really a set of cut values) where the significance ($S/\sqrt{S+B}$) is maximized. In Fig. 7-12, the cut-based method result of B^+ channel in PbPb data is presented as an example. The four panels are the distributions of the significance as a function of signal efficiency of four different B^+ meson $\mathrm{p_T}$ intervals.

Results (optimized value of each variable) of the cut-based method can be found in Tab. 7.4 to Tab. 7.8.

Boosted decision tree

The BDT method combines the predictions of individual decision tree as introduced in section 6. The output is a BDT discriminant. A higher value of the BDT discriminant corresponds to more decision trees having positive predictions, i.e., more signal-like. As a result, we can cut on the BDT discriminant distribution to pick out signals. In

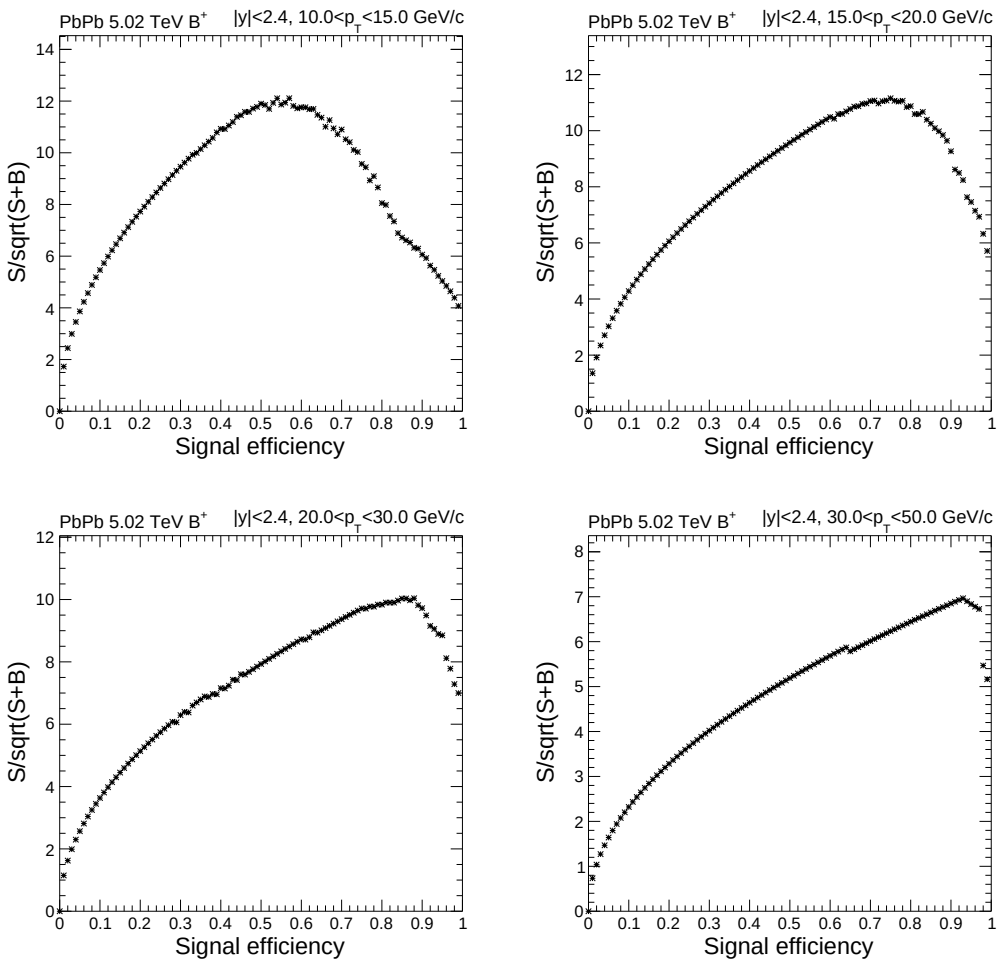

Figure 7-12: Significance, i.e., $S/\sqrt{S+B}$, as a function of signal efficiency in PbPb collisions. The four panels correspond to B^+ $\mathrm{p_T}$ 10–15 (upper left), 15–20 (upper right), 20–30 (lower left), and 30–50 (lower right) GeV/c.

Fig. 7-13, the upper two panels are the BDT discriminant distributions of testing and training sets using the B_s^0 channel with $\mathrm{p_T}$ 7-15 GeV/c in PbPb data as an example. Each BDT discriminant cut value corresponds to a signal and background efficiency. In the same Fig. 7-13, the lower left panel shows the signal efficiency as a function of background efficiency. The lower right panel shows the significance as a function of the BDT discriminant cut value. The cut value that maximizes the significance is the working point that was used in the analyses.

Results of the BDT can be found in Tab. 7.8 to Tab. 7.10.

Summary of ML results

In this section, the results of the cut optimization are summarized in different tables. For the B^+, B^0, and B_s^0 channels in pPb data, the cut-based method was used because the pPb collision events are relatively clean. The B^+ channel in pp and PbPb data also used the cut-based method except for the B^+ mesons with p_T 7–15 GeV/c in PbPb collisions where the more complicated BDT method had to be used in order to have a visible B^+ resonance in the invariant mass spectrum. Similarly, because of the high combinatorial backgrounds presented in PbPb data, the BDT method was used for the B_s^0 channel in pp and PbPb data. Tab. 7.4, 7.5, and 7.6 show the results for B^+, B^0, and B_s^0 channels respectively in pPb data. Tab. 7.7 and Tab. 7.8 are summaries of selection criteria of B^+ channel in pp and PbPb data while Tab. 7.9 and Tab. 7.10 are summaries of the B_s^0 channel.

B^+ p_T (GeV/c)	**10–60**
2D normalized SV PV distance	> 3.4
$\chi 2$ probability	> 0.013
$\cos(\theta)$	$>$ -0.35

Table 7.4: Summary table of selection criteria used for B^+ channel in different p_T intervals in pPb collisions.

B^0 p_T (GeV/c)	**10–60**
2D normalized SV PV distance	> 4.2
$\chi 2$ probability	> 0.16
$\cos(\theta)$	> 0.75
$\lvert m_{K\pi} - m(K^{0*})\rvert$	< 0.10 GeV/c^2
m_{KK}	> 1.04 GeV/c^2

Table 7.5: Summary table of selection criteria used for B^0 channel in different p_T intervals in pPb collisions.

B_s^0 p_T (GeV/c)	**10–60**
2D normalized SV PV distance	> 3.4
$\chi 2$ probability	> 0.037
$\cos(\theta)$	> 0.26
$\lvert m_{KK} - m(\phi)\rvert$	< 0.016 GeV/c^2

Table 7.6: Summary table of selection criteria used for B_s^0 channel in different $\mathrm{p_T}$ intervals in pPb collision.

B^+ p_T (GeV/c)	**7–10**	**10–15**	**15–20**	**20–30**	**30–50**
track p_T	> 0.75	> 0.88	> 0.82	> 0.84	> 1.06
$\lvert$track $\eta\rvert$	< 2.40	< 2.39	< 2.40	< 2.38	< 2.37
3D normalized SV PV distance	> 5.50	> 3.50	> 3.50	> 3.50	> 3.52
$\chi 2$ probability	> 0.032	> 0.005	> 0.008	> 0.014	> 0.015
$\cos(\theta)$	> 0.99	> 0.97	> 0.96	> 0.60	> 0.99

Table 7.7: Summary table of selection criteria used for B^+ channel in different $\mathrm{p_T}$ intervals in pp collision.

B^+ p_T (GeV/c)	**7–10**	**10–15**	**15–20**	**20–30**	**30–50**
BDT	> 0.08				
track p_T		> 1.38	> 1.70	> 2.02	> 1.94
$\lvert$track $\eta\rvert$		< 2.16	< 2.30	< 2.36	< 2.33
3D normalized SV PV distance		> 7.48	> 4.96	> 3.50	> 4.25
$\chi 2$ probability		> 0.080	> 0.052	> 0.008	> 0.017
$\cos(\theta)$		> -0.42	> -0.76	> -0.35	> 0.99

Table 7.8: Summary table of selection criteria used for B^+ channel in different $\mathrm{p_T}$ intervals in PbPb collision.

B_s^0 p_T (GeV/c)	**7–15**	**15–50**
BDT	> 0.191055	0.208973

Table 7.9: Summary table of selection criteria used for B_s^0 channel in different $\mathrm{p_T}$ intervals in pp collision.

B_s^0 p_T (GeV/c)	**7–15**	**15–50**
BDT	> 0.213755	0.254413

Table 7.10: Summary table of selection criteria used for B_s^0 channel in different $\mathrm{p_T}$ intervals in PbPb collision.

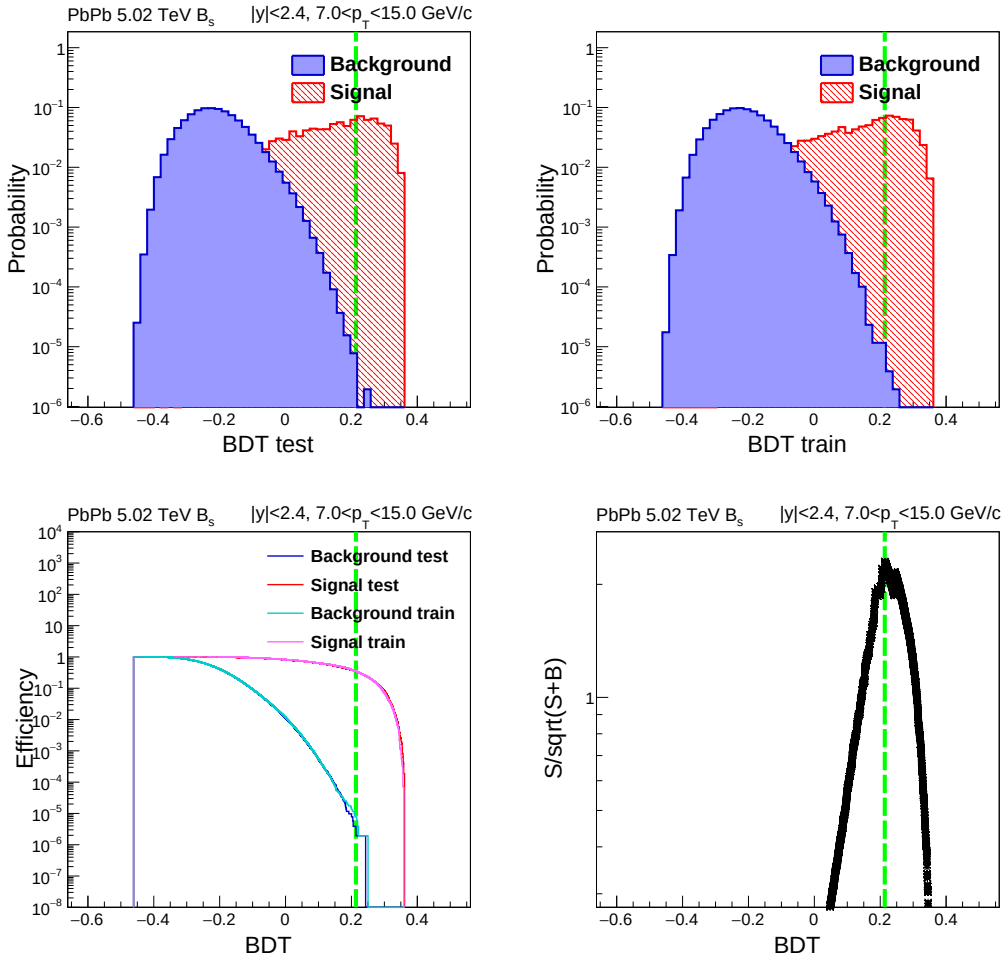

Figure 7-13: BDT discriminant distributions of signal and background from the testing and training sample (upper left and right). Efficiency as a function of BDT discriminant cut value for training and testing sample (lower left). $S/\sqrt{S+B}$ as a function of BDT discriminant cut value for B_s^0 mesons with p_T 7–15 GeV/c in PbPb collisions (lower right). The green dash line indicates the optimal BDT cut value used in the analyses

7.6 Signal Extraction

In the previous sections, we introduced the reconstruction of B meson candidates. However, not all of them are genuine B mesons. In fact in some cases, more than half of them are background candidates. By definition we can not directly distinguish signal from background candidates in real data. Nevertheless it is still possible to accurately estimate the number of background candidates in the region we are interested in (the signal-rich region). We first estimate the number of background candidates in the signal-free region (a region without signals) and propagate, e.g., linear interpolation, this number to the signal-rich region. We can then use this number to estimate the number of signals in the signal-rich by subtracting this number from the total number of candidates in this region. This procedure is called "yield extraction". Practically speaking, we used the invariant mass spectrum of B meson candidates and looked for the **Probability density function** (PDF) that can best describe this spectrum. Because the invariant mass spectrum contains both signal-free (off the B meson resonance peak) and signal-rich (around the peak) region, the PDF essentially does the interpolation for us. In the PDF, we will define both signal and background components. The shape of the background components is basically fixed by the signal-free region and this shape extends to the signal-rich region, leaving the singal components uncontaminated by background candidates. This is in fact the reason why we need to keep B meson candidates with an invariant mass value off the resonance peak as they provide the background shape for us. The PDF is found by "fitting" the invariant mass spectrum and the resulted singal components of the PDF are integrated to estimate the number of signals presented in the invariant mass spectrum. This yield extraction procedure was executed in each B meson p_T-interval.

Generally speaking, a PDF is defined by a function, e.g., a Gaussian function, with several undetermined parameters such as the mean and width of a Gaussian. The fitting procedure searches for the parameter values that best describe the spectrum. Conventionally, there are three fitting methods, the binned least-square (or χ^2), binned likelihood, and unbinned likelihood method. The binned least-square

method fits the spectrum by finding the PDF parameter θ that minimizes the χ^2 between measurements and predictions

$$\underset{\theta}{\text{argmin}} \quad = \quad \sum_{b=1}^{\#\ of\ bins} \left(\frac{n_b - f(x_b;\theta)}{\sqrt{n_b}}\right)^2 \tag{7.5}$$

where n_b is the number of data points in the histogram bin b. $f(x_b;\theta)$ is PDF predicted number of data points at the b-th bin center.

The binned likelihood method minimizes the product of the "likelihood" (the probability of having a certain number of data points dwelling in a given bin) of each bin. Each bin is assumed to have a Poisson distribution with mean value modeled by the PDF value $f(x_b;\theta)$ evaluated at the bin center.

$$\underset{\theta}{\text{argmin}} \quad = \quad \sum_{b=1}^{\#\ of\ bins} -\log \text{Poisson}(n_b; f(x_b;\theta)) \tag{7.6}$$

Unbinned likelihood method is very similar to the binned case except one directly computes the product of likelihood of each data point.

$$\underset{\theta}{\text{argmin}} \quad = \quad \sum_{i=1}^{\#\ of\ samples} -\log f(x(i);\theta) \tag{7.7}$$

$x(i)$ is the invariant mass value (x-position) of sample i.

For the measurements presented in this thesis, the three methods were all tested and the results were found to be compatible with negligible differences.

The PDF we used to model the B meson invariant mass spectrum contained three different components that were modeled individually by three different functions. The three functions were summed together to form the complete PDF for the fitting.

- *B meson signals.* The B meson signals were modeled by a **double Gaussian** function with a same mean but different widths. i.e., $p_a \times$Gaussian function$(\mu, \sigma_1)+$ $(1-p_a) \times$ Gaussian funtion(μ, σ_2), where p_a is the relative amplitude of the two Gaussian functions. This is more preferable than a single Gaussian or a Breit-Wigner function as it was shown to better describe the signal shapes in MC

simulations.

- *Combinatorial backgrounds.* Also called prompt J/ψ backgrounds. they were modeled by a **1st or 2nd-order polynomial** function. As we have mentioned, they resulted from prompt J/ψ mesons, which were produced either directly from the hard scatterings or as the daughters of particles that decay promptly to J/ψ mesons, combining with unrelated tracks within the event.

- *Peaking backgrounds.* Also called non-prompt J/ψ backgrounds. This contribution is modeled by a function derived from MC studies with the overall shape fixed by the studies (introduced in section 7.7). Only the amplitude parameter was a free parameter during the invariant mass spectrum fitting. They resulted from J/ψ mesons from b hadron decays other than the three signal channels. For example, $B_s^0 \to J/\psi\ \phi \to \mu^+\ \mu^-\ K^+\ K^-$ can fall into the decay reconstruction of $B^+ \to J/\psi\ K^+$ with one kaon track mis-identified as pion and the other kaon track ignored. Similarly for $B^+ \to J/\psi\ K^*(892)^+$ that are partially reconstructed as $B^+ \to J/\psi\ K^+$. These contributions can form peaking structures outside the signal region.

The invariant mass range considered for the fitting was between 5 to 6 GeV/c^2. Note that this range encompasses background-only regions (off signal resonance peak) which is consistent with our requirement of signal-free regions.

The fitting procedure proceeded with the following two steps:

1. A fit was performed with only a double Gaussian function to the invariant mass spectra of genuine B meson signals from MC simulations. This step determined the widths and the relative proportion of the double Gaussian function.

2. A fit was performed to real data invariant mass spectra with the complete fit function described above. The widths and the relative proportion of the double Gaussian were set to the values estimated in the previous step. Parameters of the combinatorial background components, the amplitude of the peaking

background components, and the mean of the double Gaussian function were free parameters in this fit to real data.

The invariant mass spectra fitting results for the pPb (B^+, B^0, B_s^0), pp (B^+, B_s^0), and PbPb (B^+, B_s^0) collisions are presented below.

The fitted PDFs describe the real data invariant mass spectra very well as can be seem in the figures. Summary tables of extracted yields can be found in Tab. 7.11 to 7.13.

p_T (GeV/c)	10–15	15–20	20–25	25–30	30–60
B^+ yields	337±24	192±16	68±9	30±6	43±7

p_T (GeV/c)	10–15	15–20	20–60
B^0 yields	75±11	47±8	65±9

p_T (GeV/c)	10–60
B_s^0 yields	41±8

Table 7.11: Extracted yields for B^+, B^0, and B_s^0 channels in pPb data.

p_T (GeV/c)	7–10	10–15	15–20	20–30	30–50
B^+ pp yields	390±24	981±37	611±27	416±21	125±11
B^+ PbPb yields	18±5.4	61±9.5	50±8.0	60±8.3	12±3.6

Table 7.12: Extracted yields for B^+ channel in pp and PbPb data.

p_T (GeV/c)	7–15	15–50
B_s^0 pp yields	93±11	79±10
B_s^0 PbPb yields	9.0±3.4	11±3

Table 7.13: Extracted yields for B_s^0 channel in pp and PbPb data.

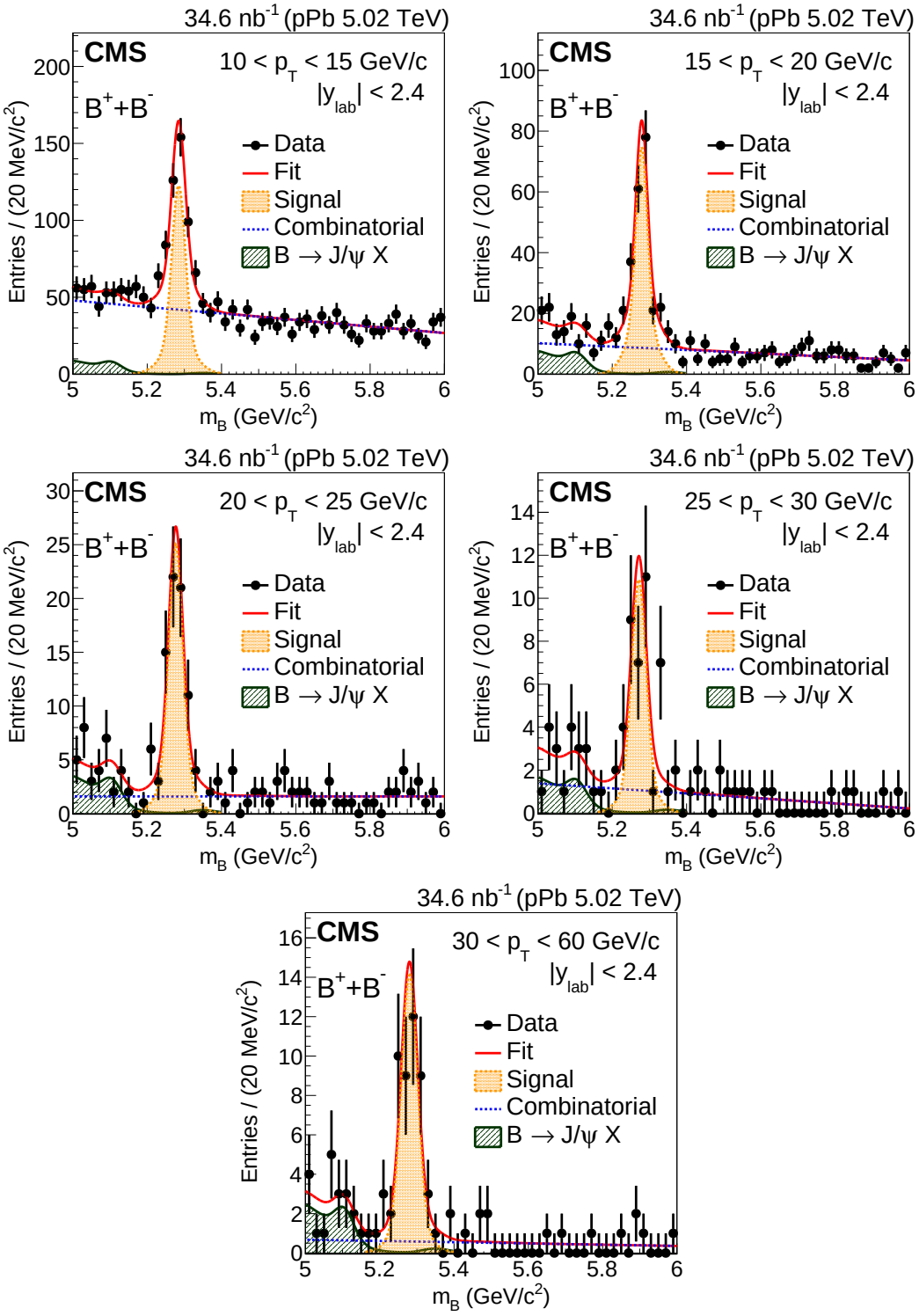

Figure 7-14: Invariant mass spectra of B^+ candidates in pPb collisions measured in $|y_{lab}| < 2.4$ and in the p_T range of 10–15 (upper left), 15–20 (upper right), 20–25 (middle left), 25–30 (middle right), and 30–60 GeV/c (bottom).

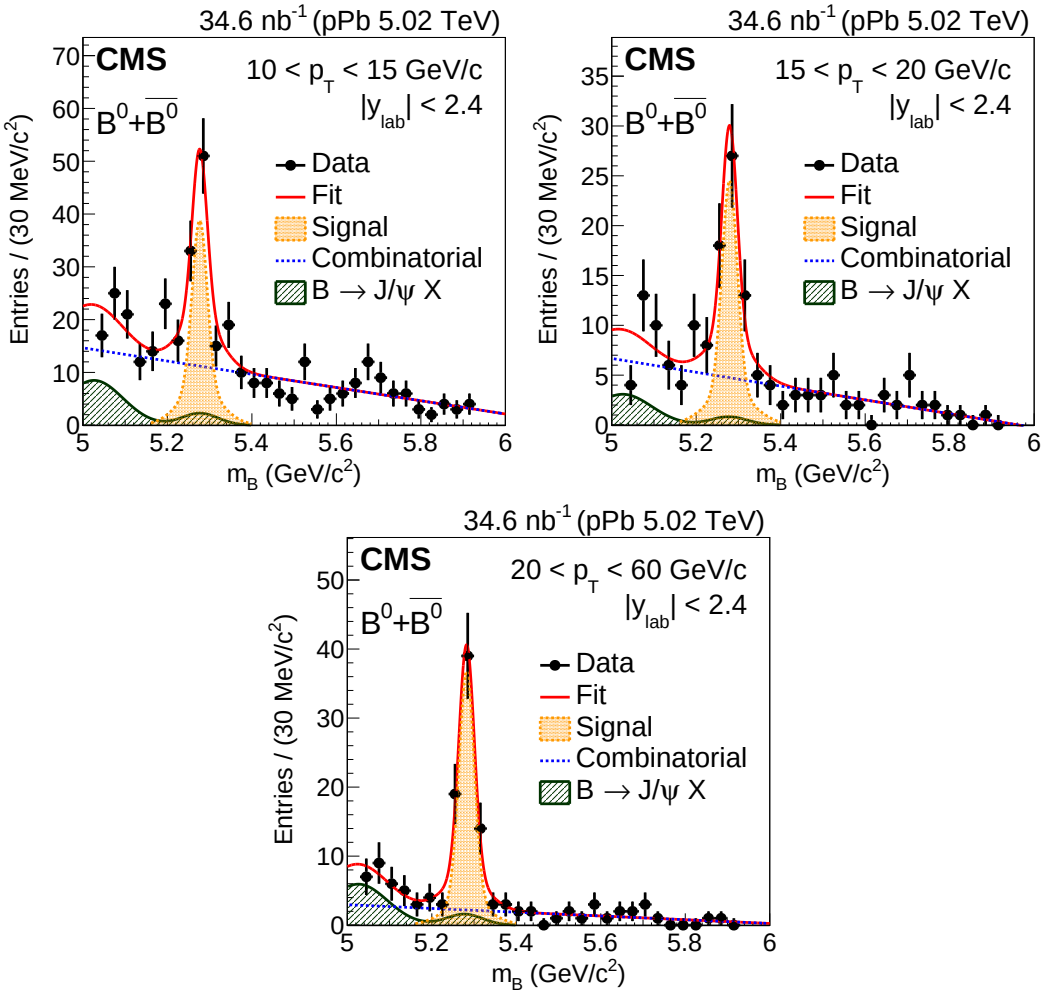

Figure 7-15: Invariant mass spectra of B^0 candidates in pPb collisions measured in $|y_{lab}| < 2.4$ and in the p_T range of 10–15 (upper left), 15–20 (upper right), and 20–60 GeV/c (bottom).

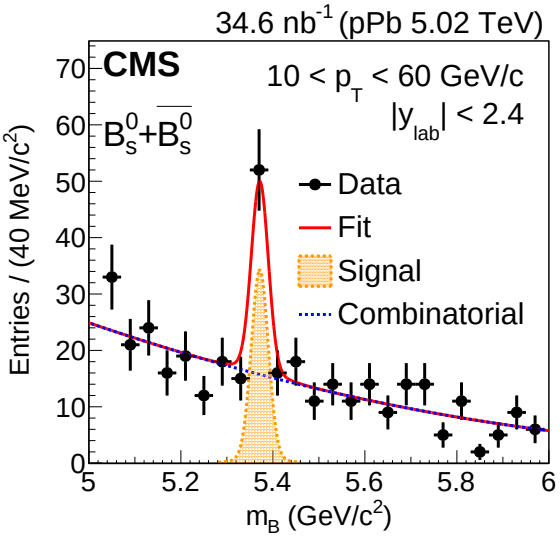

Figure 7-16: Invariant mass spectra of B_s^0 candidates in pPb collisions measured in $|y_{lab}| < 2.4$ and in the p_T range of 10–60 GeV/c.

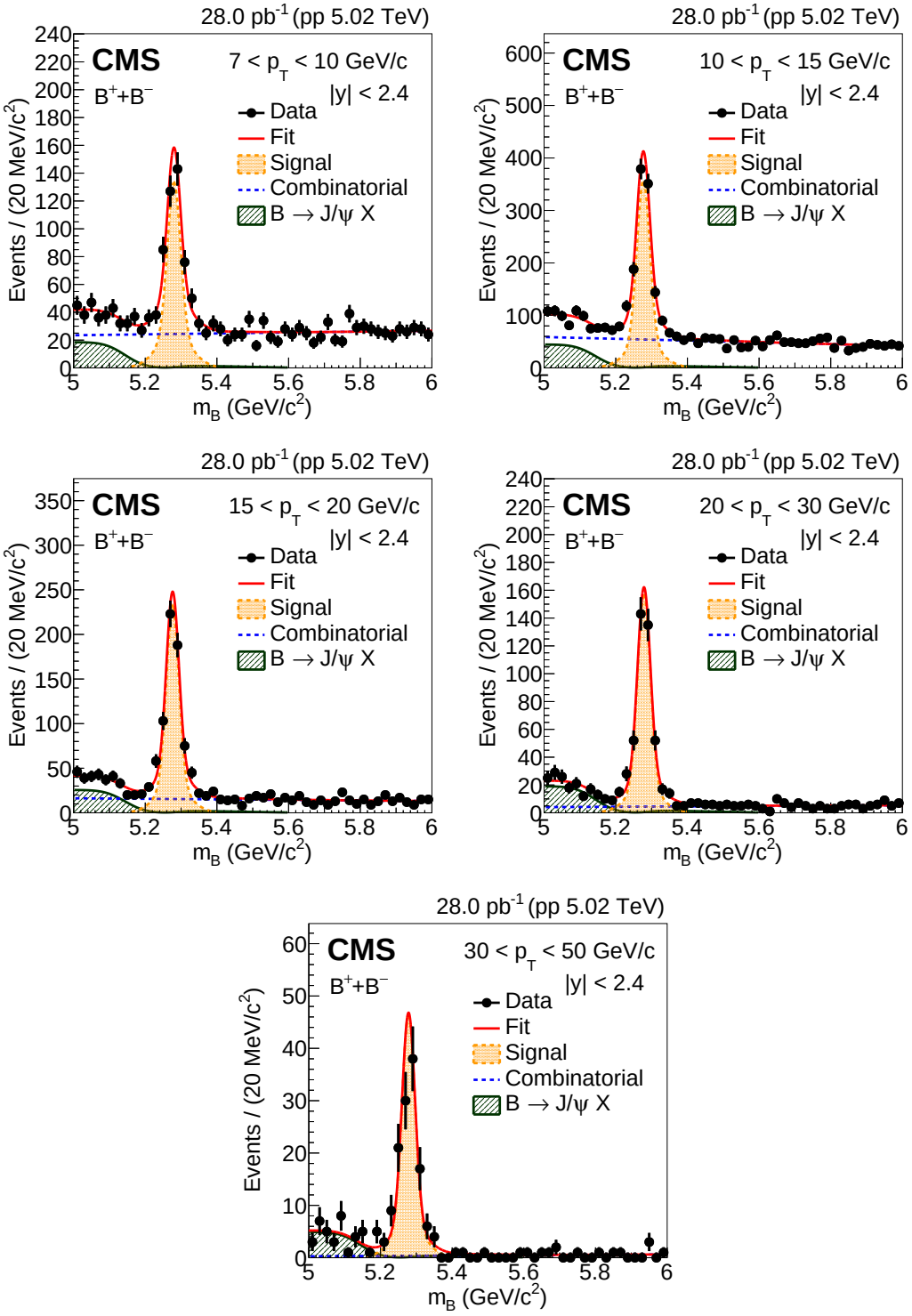

Figure 7-17: Invariant mass spectra of B^+ candidates in pp collisions measured in $|y| < 2.4$ and in the p_T range of 7–10 (upper left), 10–15 (upper right), 15–20 (middle left), 20–30 (middle right), and 30–50 GeV/c (bottom).

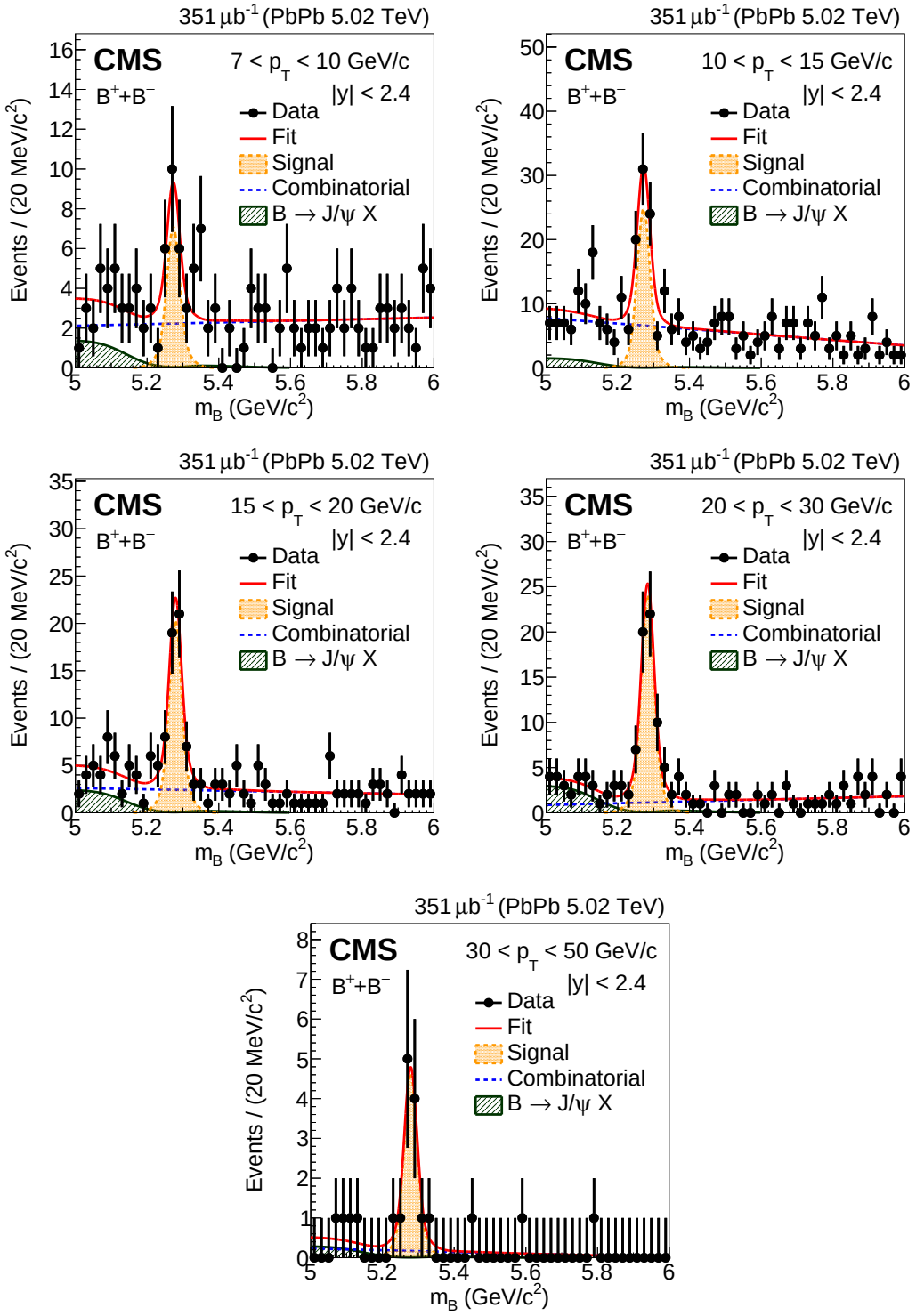

Figure 7-18: Invariant mass spectra of B^+ candidates in PbPb collisions measured in $|y| < 2.4$ and in the p_T range of 7–10 (upper left), 10–15 (upper right), 15–20 (middle left), 20–30 (middle right), and 30–50 GeV/c (bottom).

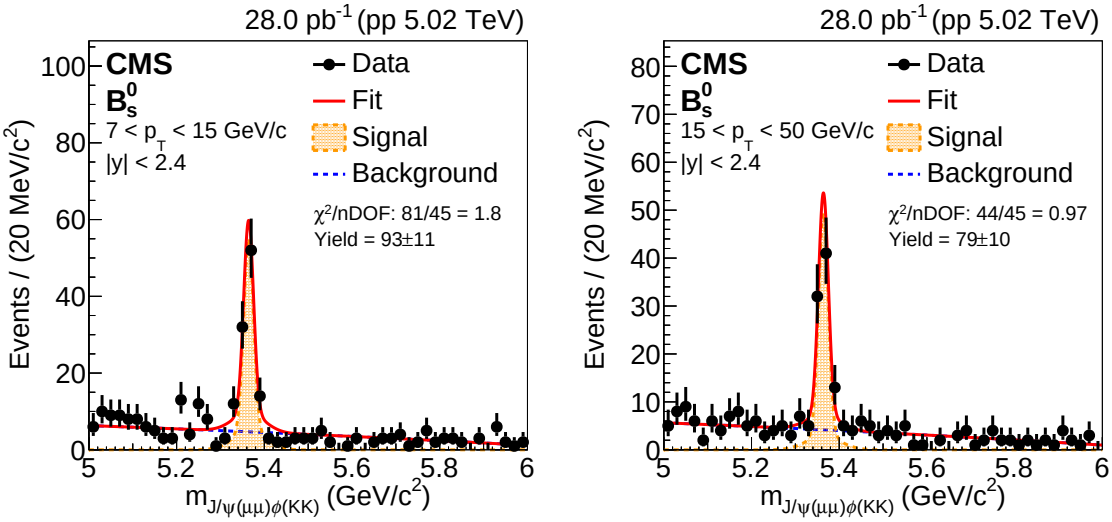

Figure 7-19: Invariant mass spectra of B_s^0 candidates in pp collisions measured in $|y| < 2.4$ and in the p_T range of 7–15 (left) and 15–50 GeV/c (right).

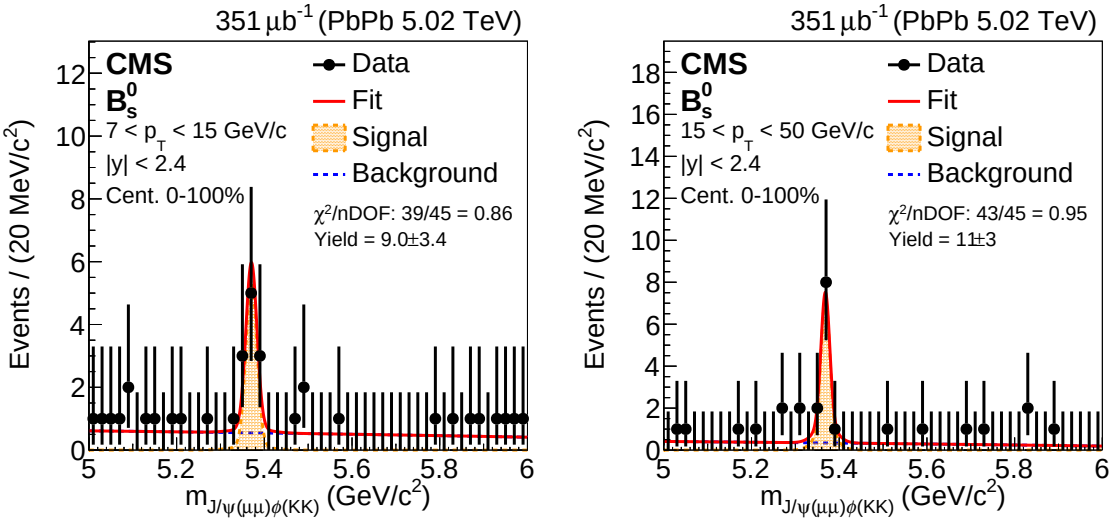

Figure 7-20: Invariant mass spectra of B_s^0 candidates in PbPb collisions measured in $|y| < 2.4$ and in the p_T range of 7–15 (left) and 15–50 GeV/c (right).

7.7 Peaking background

We mentioned briefly about the origin of the so-called peaking backgrounds or non-prompt J/ψ backgrounds. The production of J/ψ mesons mainly occurs in the following two ways: 1) the prompt J/ψ mesons produced directly from the nucleon-nucleon collisions or indirectly via the decays of heavier charmonium states; 2) the non-prompt J/ψ mesons from the decays of b hadrons. While prompt J/ψ backgrounds can be easily vetoed by selections on the J/ψ meson decay length or the opening angles between the J/ψ mesons and tracks, non-prompt J/ψ backgrounds are more difficult since the J/ψ mesons reconstructed in our signal channels were precisely the same type. Instead of trying to remove them, we can estimate their contributions. This is because the non-prompt J/ψ backgrounds coming from other b hadron decays (other than the signal channels) will form peaking structures within the invariant mass spectra. For example, $B_s^0 \to J/\psi\ \phi \to \mu^+\ \mu^-\ K^+\ K^-$ can be wrongly reconstructed as $B^+ \to J/\psi\ K^+$ with one kaon track mis-identified as a pion and the other kaon track missed. Since the mis-identified track was assigned a invariant mass value smaller than what it suppose to be and the other other track was completed not counted, the reconstructed B meson candidate will have a invariant mass value smaller than its original value. Eventually, B meson candidates mis-reconstructed in the same way piled up on the left of the B meson resonance peak, forming peaking structures in the invariant mass spectrum

In order to prevent potential biases on the yield extraction procedure, these peaking background structures need to be properly estimated and subtracted. To determine these components, we processed the inclusive non-prompt J/ψ MC simulations with the nominal workflow. We then classified each reconstructed B^+, B^0, or B_s^0 meson candidate according to their generation level information and identified those coming from genuine B^+, B^0, or B_s^0 meson decays and those resulted from non-prompt J/ψ backgrounds. In the cases where the non-prompt background contributions were non-negligible, these contributions were modeled by a dedicated PDF (consisted of many individual components). For example, for the B^+ channel, we found the major

non-prompt background contributions were the following

- 4-body B^+ meson decay channels with intermediate resonant decays, e.g., $B^+ \to J/\psi\ K^*(892)^+$. In this case, kaons emerge from $K^*(892)^+$ decays were wrongly identified as coming from genuine $B^+ \to J/\psi\ K$ decays.
- 4-body B^0 meson decay channels such as $B^0 \to J/\psi\ K^*(892)^0$. Similar to the above, kaons were wrongly identified.
- $B^+ \to J/\psi\ \pi$ decays in which the pions were mis-identified as kaons.

The resulted B^+ invariant mass spectra for these peaking background contributions are shown in Fig. 7-21 for pp and PbPb collisions obtained from inclusive non-prompt J/ψ MC simulations. It is clear that these sources create peaking structures in the region M_{inv} <5.2 GeV/c^2. These structures were found to be well modeled by a PDF consisted of an Error function and several Gaussian functions. As described in detail in section 7.6, the shape of this PDF was used as a template in the yield extraction procedure.

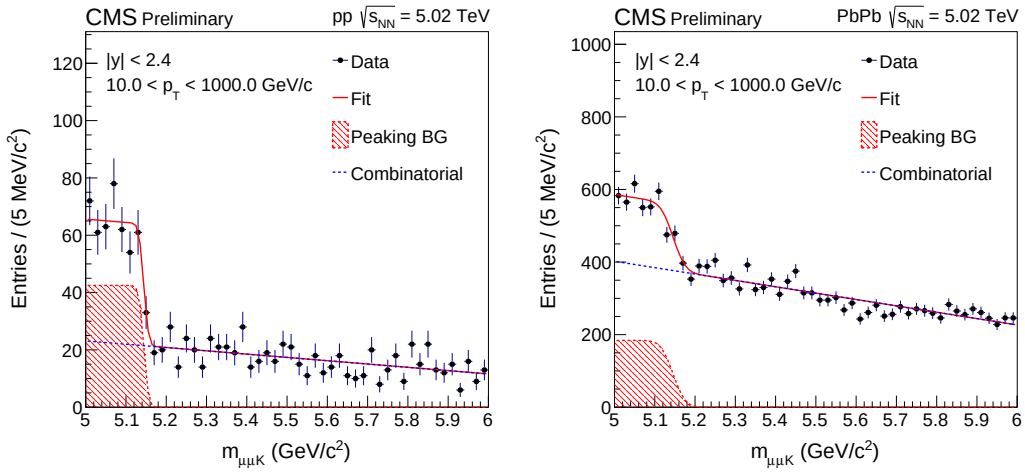

Figure 7-21: B^+ candidate invariant mass spectra obtained in non-prompt J/ψ MC simulations after vetoing the contribution of genuine $B^+ \to J/\psi\ K^+ \to \mu^+\ \mu^-\ K^+$ signal candidates for pp (left) and PbPb (right) collisions.

On the other hand, for the B_s^0 channel, the peaking background contributions were found to be negligible due to the narrow ϕ meson natural width which allowed us to

impose a tight track-pair invariant mass window and removed a large fraction of non-prompt J/ψ background contributions which do not have intermediate ϕ resonances. This can be seen in Fig. 7-22 where we plot the B_s^0 signals (blue) and non-prompt J/ψ backgrounds (red) together.

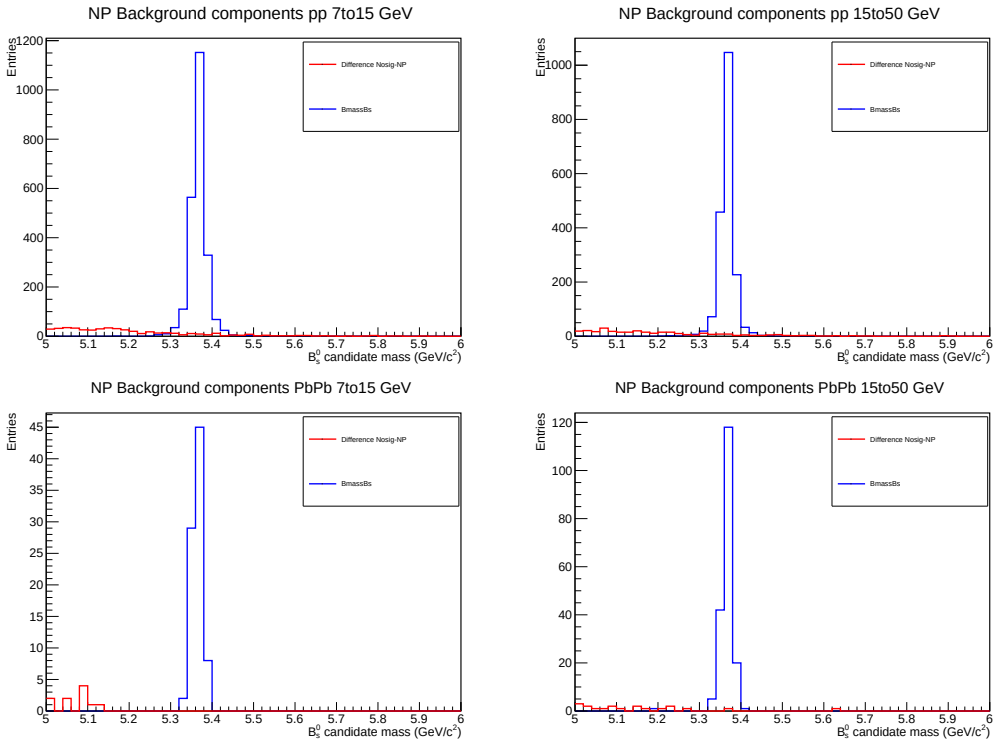

Figure 7-22: Comparison of signal (blue) and non-prompt (red) background contributions in B_s^0 channel in pp (top) and PbPb (bottom) collisions for B_s^0 mesons with p_T in 7–15 (left) and 15–50 GeV/c (right) intervals.

The non-prompt J/ψ background contributions for the B_s^0 channel was thus not included in the yield extraction fit.

7.8 Systematic uncertainties

As in every experimental result, our measurements of B mesons were affected by various sources of systematic uncertainties. Some of them might be due to the resolution of the detector and/or a change of detector condition over time. Others could be related to our limited knowledge of the different underlying physics processes. In the following, we will introduce the various systematic uncertainties that can affect our results and the methods used to estimate these effects.

7.8.1 Luminosity

An uncertainty in integrated luminosity ($\mathcal{L}$) will directly affect our measurements because the calculation of cross section depends on it.

$$\sigma^B = \frac{N^B}{\mathcal{L}} \tag{7.8}$$

where σ^B is the cross section of the B meson and N^B is the total number of B mesons produced in a given dataset. The estimation of the luminosity uncertainty in pp collisions was based on the Van der Meer (VdM) scans [96]. In PbPb collisions, the uncertainty is associated with the number of minimum-bias events used to normalize the corrected B meson yields. It was calculated by considering the uncertainty on the minimum-bias event selection efficiency [110].

7.8.2 Branching ratio

Same as luminosity, uncertainties on $B^+ \to J/\psi\, K^+ \to \mu^+\, \mu^-\, K^+$, $B^0 \to J/\psi\, K^*(892)^0 \to \mu^+\, \mu^-\, K^+\, \pi^-$, $B_s^0 \to J/\psi\, \phi \to \mu^+\, \mu^-\, K^+\, K^-$ decay branching ratios enter the cross section calculation linearly. The values were obtained from PDG. Uncertainties from each sub-channel, e.g., $J/\psi \to \mu^+\mu^-$, were added in quadrature.

7.8.3 B meson p_T shape

In section 7.2.3, we mentioned the procedure of re-weighting the B meson p_T shape in MC simulations. Although it had been shown by previous studies that FONLL better describes the heavy flavor meson spectra in real data than PYTHIA. Nevertheless this re-weighting could potentially introduce a bias and a systematic uncertainty was thus quoted to cover this possibility. It was evaluated by comparing the reconstruction and selection efficiency calculated using the unweighted (PYTHIA description) MC simulations and then compared to the FONLL weighted samples. The difference in efficiency was quoted as a systematic uncertainty.

7.8.4 Tracking efficiency

Track reconstruction efficiency is one of the correction factors used to convert the B meson raw extracted yields to the B meson differential cross sections (which we denote as ϵ in the calculation formula to be introduced in the next section). Since this value was estimated from MC simulations, a potential discrepancy between MC simulations and real data can bias the results. A systematic uncertainty was assigned to cover the discrepancy by comparing the track reconstruction efficiencies in MC simulations and real data. It was evaluated based on the studies done in the D meson analysis [126] which followed the procedure proposed in Ref. [97]. The strategy was to reconstruct the $D^*(2010)^+$ mesons in both 3 prongs decays $D^*(2010)^+ \rightarrow D^0\pi^+ \rightarrow K^-\pi^+\pi^+$ and 5 prongs decays $D^*(2010)^+ \rightarrow D^0\pi^+ \rightarrow K^-\pi^+\pi^+\pi^-\pi^+$ channels. By using the $D^*(2010)^+$ resonances, we can identify and compare the one pion and three pions decay of the D^0 mesons which differs by two pion tracks. After correcting for selection efficiency which was obtained from MC simulations, the ratio

$$\mathcal{R} = \frac{N_{K3\pi}}{N_{K\pi}} \cdot \frac{\epsilon_{K\pi}}{\epsilon_{K3\pi}} \tag{7.9}$$

divided by the ratio of PDG branching function (BF)

$$\mathcal{R}(PDG) = \frac{\mathrm{BF_{K3\pi}}}{\mathrm{BF_{K\pi}}} \tag{7.10}$$

will be proportional to the square of the ratio of pion tracking efficiency between real data and MC simulations. The relative tracking efficiency for pions in real data and MC simulations can be estimated by

$$\frac{\epsilon(data)}{\epsilon(MC)} = \sqrt{\frac{\mathcal{R}}{\mathcal{R}(PDG)}} \tag{7.11}$$

The study was performed using 5.02 TeV pp collision data. In PbPb data, a similar study was not feasible due to the larger combinatorial backgrounds. The estimation was obtained by additional comparisons between track quality variables before track selections between pp and PbPb collisions and between MC simulations.

7.8.5 Muon efficiency

Similar to track reconstruction efficiency, discrepancy regarding muon selection and identification between MC simulations and real data can induce systematic uncertainties. The efficiency of a single muon in real data was measured via the so-called "Tag and Probe" (TnP) technique [116]. The idea is to reconstruct a known resonance (e.g., J/ψ, Υ, or Z boson) built on two objects (which are two muons in our case). The two objects are subjected to different level of selection criteria which will be called the "tag" and the "probe". The "tag" is the object that passes a set of very tight selection criteria designed to ensure the required particle type is selected which in our case is a muon (of course the method is applicable to any object). The "probe" which is usually selected with very loose selection criteria will be the object we utilize to examine the efficiency of some specific selection criteria. It is further selected by paring with tags such that the invariant mass of the combination is consistent with the resonance we assumed. Based on this, three invariant mass distributions, resulted from different combinations, can be formed which are, "all pairs", "failed pairs" and "passed pairs", according to whether the probe passes or fails the criteria for which the efficiency is being measured. The peaks are fitted and the yields of "all probes", "failed probes" and "passing probes" are extracted. By combining the 3 yields, the efficiency can be calculated accordingly. Usually, this procedure is done in different kinematic (p_T and

η) regions of the probe. By comparing the efficiencies obtained with TnP between real data and MC simulations, the discrepancy can be estimated. Depending on the specific need of a analysis and the degree of the discrepancy, this value can be applied as a scaling factor to the MC simulations or be quoted as a systematic uncertainty (or both). Note that since there are two muons involved in our analyses, the single muon scaling factor was translated to B meson scaling factor by weighting a B meson candidate with the two corresponding muon scaling factors. Same in the case when quoting as a systematic uncertainty. This is a widely used technique for validating and testing the efficiency measured with MC simulations. Single muon trigger, identification, and tracking efficiencies were measured and applied in our analyses.

7.8.6 Selection efficiency

The systematic uncertainty of selection criteria is related to the discrepancy of variable distributions between MC simulations and real data. For instance, if the secondary vertex distribution of the B mesons were very different, the correction factors obtained from MC simulations will be incorrect and biased values to be used for cross section calculations in real data. This concern can be partially addressed by a side-by-side comparison of variable distributions between MC simulations and real data. The B meson variable distributions can be easily obtained for MC simulations, which have generator truth. For real data, they have to be extracted in the same way as the nominal procedure described in section 7.6. In the case where the lack of statistics in real data prohibits us from extracting yields in sufficient bins, e.g., B_s^0 channel in PbPb collisions, no proper comparison can be made between MC simulations and real data. As a result, two different methods for estimating related systematic uncertainties were used in our analyses.

The first approach was varying the cut value in steps and comparing the extracted yields to the nominal results. All the variables that were used as parts of the selection criteria were considered and they were varied one at a time. We then calculated the

following double ratio

$$Ratio(Data/MC)(i) = \frac{\epsilon_i^{Data}}{\epsilon_i^{MC}} = \frac{\frac{Yield^i_{Data}(cut\ default)}{Yield^i_{Data}(cut\ varied)}}{\frac{Yield^i_{MC}(cut\ default)}{Yield^i_{MC}(cut\ varied)}} \tag{7.12}$$

where "default" denotes the yields extracted using the nominal cut value of a given cut variable i and "varied" denotes the yields extracted with a varied cut value. The yields were extracted by fitting as in the nominal analysis workflow. The (relative) selection efficiency ϵ for each cut variable i (for both real data and MC simulations) is the ratio of extracted yields between a varied cut value and the default cut value. In the absence of any difference between real data and MC simulated efficiency, the ratio of the efficiencies is expected to be unity. Therefore we considered the difference between the $Ratio(Data/MC)(i)$ and unity as the systematic uncertainty. The maximal difference (with respect to unity) among all the scanned cut values was quoted as the systematic uncertainty associated with the cut variation of variable i. This was done for every variables used and the values derived were summed in quadrature. We quoted this sum as the total systematic of cut variation. Example results conducted on the B^+ channel in pp and PbPb collisions are shown in Fig. 7-23 and Fig. 7-24.

Note that the range in which we varied the cut value can affect the result. In practice, we varied the cut value until the difference (with respect to unity) was saturated. Also, since we varied each variable separately, correlations between the variables will not be considered. However, since we summed the maximal difference of each variable in the end, this procedure will only overestimate the systematic uncertainty associated with the selection efficiency.

The second method focused on the analyses that were obtained with the BDT method, specifically the B_s^0 channel in pp and PbPb collisions. These analyses usually have particularly low real data statistics which is exactly the reason why the cut optimizations were done using the BDT method. The cut scanning method mentioned above will be highly fluctuated because of this lack of statistics. Instead, to estimate the systematic uncertainty associated with our choice of using the BDT method, we trained the cut-base method in these analyses and compared the extracted and effi-

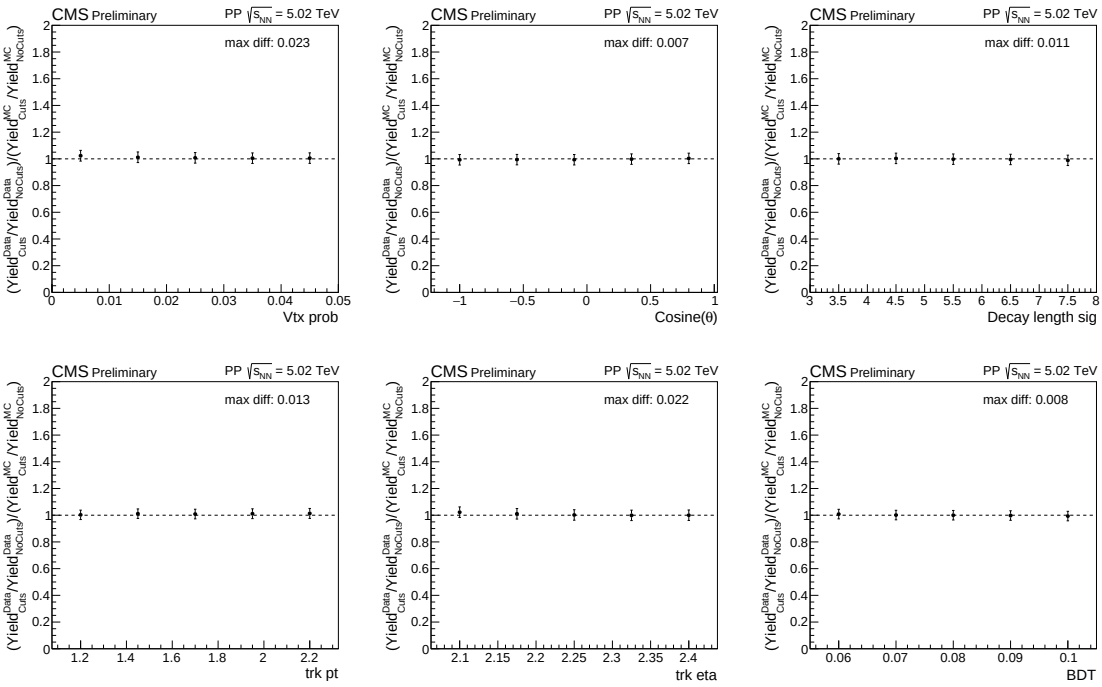

Figure 7-23: Double ratio of the cut variations for B meson vertex fitting probability (upper left), cosine(θ) angel (upper middle), decay length (upper right), track p_T (lower left), track η (lower middle), and BDT discriminant value (lower right) of B^+ channel in pp collisions.

ciency corrected yields between the original BDT method and this cut-base method. The difference between the two method was quoted as systematic uncertainty. The resulted pp mass spectra and cross sections can be found in Fig. 7-25.

Unfortunately this procedure could not be practiced in PbPb collisions as the cut-base method was unable to extract a visible resonance peak as in pp collisions. And if we wanted to use the results we obtained in pp collisions, we would need to assume the differences we obtained in pp collisions is applicable to PbPb collisions. For this reason, we checked the B_s^0 variable distributions in MC simulations between pp and PbPb samples. It turned out the distributions for signal B_s^0 mesons between pp and PbPb MC simulations were very similar. In this case, the BDT discriminant values from a BDT method trained in PbPb collisions for signal B_s^0 mesons should be very close between in pp and PbPb MC samples. We thus applied the BDT discriminant which was trained in PbPb collisions to pp collision samples. We then

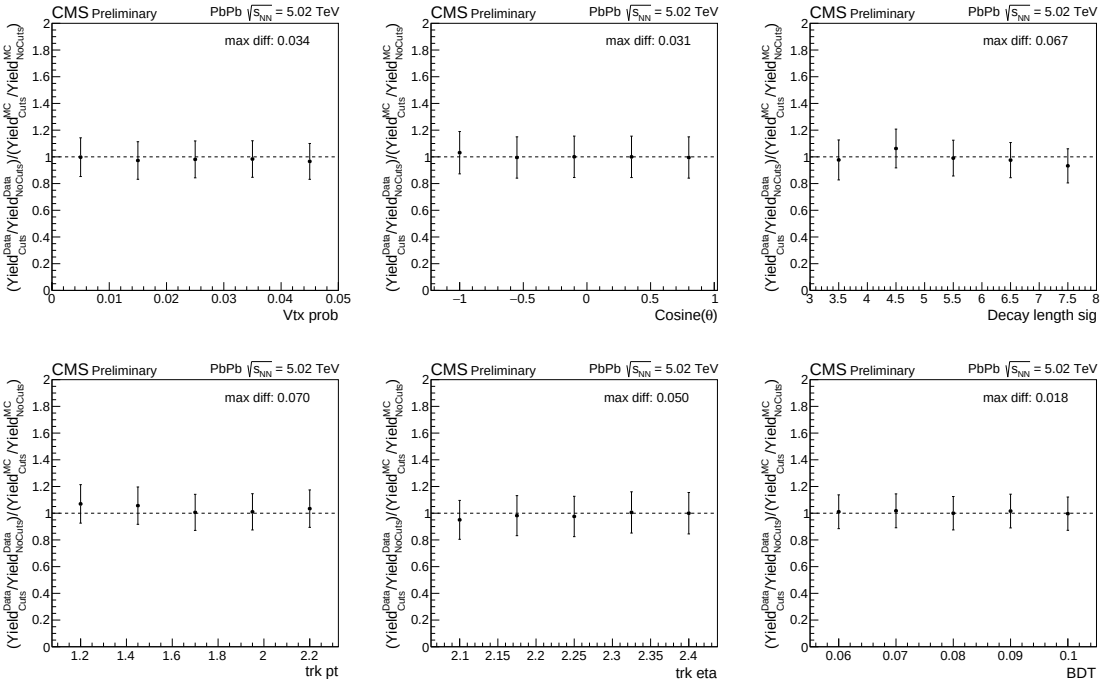

Figure 7-24: Double ratio of the cut variations for B meson vertex fitting probability (upper left), cosine(θ) angel (upper middle), decay length (upper right), track p_T (lower left), track η (lower middle), and BDT discriminant value (lower right) of B^+ channel in PbPb collisions.

took the difference in corrected yields between the pp trained BDT method and the PbPb trained BDT method as systematic uncertainty for the PbPb analyses. The resulting pp mass spectra and cross sections can be found in Fig. 7-26.

7.8.7 Acceptance correction

There are also systematic uncertainties related to the acceptance due to MC simulation's inability to fully reproduce real detector condition. To this end, systematic uncertainty for acceptance was estimated in the following way (using B_s^0 channel as an example).

- Obtain the ratios of normalized and uncorrected yields between real data and MC simulations as a function of p_T and rapidity as shown in Fig. 7-27.

- Generate 10 thousand toy ratios using Gaussian distribution in which the mean

and width of the Gaussian are the ratio itself and the error of the ratio that were obtained from the previous step.

- Use linear or 2nd-order polynomial function to fit these ratios. Fitted parameters are stored for the next step. Example of fitting are shown in Fig. 7-27.

- For each toy ratio, weight the MC simulations according to the fitted functions obtained in the previous step.

- Get the distributions of the acceptances from each weighted MC sample as shown in Fig. 7-28.

- From each distribution, calculate the corresponding minimum, maximum, mean and standard deviation values. These values are quoted as the acceptance systematic uncertainties.

7.8.8 Yield extraction

Recall that in section 7.6, we used a 2nd-order polynomial function to model combinatorial backgrounds and a double Gaussian function to model B meson signals. This choice of functions could directly affect the number of extracted yields and induced systematic uncertainties. We estimated this effect by changing the PDF to other functions and computed the yield deviations with respect to the nominal PDF. The signal and background function were varied separately and examined one at a time.

For the background function, in the case of the B_s^0 channel where the default PDF is a linear function, the background function was changed to a 2nd-order polynomial, 3rd-order polynomial, and exponential function. Fig. 7-29 shows the invariant mass spectrum fits of the B_s^0 channel in pp collisions with the use of default linear, 2nd-order polynomial, 3rd-order polynomial, and exponential function as background function respectively. We quoted the systematic uncertainty associated with background function by calculating the maximal extracted yield difference (compared with the nominal setting) among all background function variations.

For the signal function where the default setting is a double Gaussian function, we checked the effect by changing the signal function to a single Gaussian or a triple Gaussian function. Furthermore, recall that in the fitting procedure, the width parameters of the double Gaussian function were fixed to the values obtained by fitting on MC simulations. To account for potential discrepancy between real data and MC simulations on this, we checked the extracted yield variations by increasing and decreasing the width value by its one standard deviation value ($\sigma(1+\alpha) \rightarrow \sigma(1+\alpha \pm \epsilon_\alpha)$) where ϵ_α is the error of the fitted α value. In addition to this, because the mean value of the double Gaussian function in the nominal procedure was a floating parameter, we also checked the effect of fixing the mean to the value estimated by MC simulations. Fig. 7-30 shows the fits results of the B_s^0 channel in pp collisions. Again we quoted the systematic uncertainty associated with signal function by calculating the maximal yield difference (compared with the nominal setting) among all signal function variations.

The final systematic uncertainty associated with PDF variation is calculated by a quadratic sum of the signal and background variation systematic uncertainties.

7.8.9 Summary table

The various systematic uncertainty sources described above were assumed to be independent to each other and added in quadrature. These comprised the total systematic uncertainty of the cross section. In the nuclear modification factor calculations, the pp and pPb (PbPb) total systematic uncertainties were further added in quadrature except for the branching ratio uncertainties which are fully correlated between pp and pPb (PbPb) collisions. In the tables below, Tab. 7.14 to 7.16 show the summaries of various systematic uncertainty values for the B^+, B^0, and B_s^0 channels in pPb collisions. Tab. 7.17 and 7.18 (Tab. 7.19 and 7.20) show the summaries of the B^+ (B_s^0) channel in pp and PbPb collisions.

Table 7.14: Summary of systematic uncertainties from each factor for the B^+ channel in pPb collisions. All the values are shown in percentage.

Factors	(10,15)	(15,20)	(20,25)	(25,30)	(30,60)
B meson p_T shape	0.6	0.6	0.6	0.6	0.6
Tracking efficiency	3.9	3.9	3.9	3.9	3.9
Muon efficiency	6.9	5.0	5.0	4.5	6.5
Selection efficiency	4.0	4.0	4.0	4.0	4.0
Acceptance correction	0.4	0.2	1.0	0.7	0.9
Yield extraction	11.7	11.7	11.7	11.7	11.7
Luminosity	3.5	3.5	3.5	3.5	3.5
Branching fractions	3.1	3.1	3.1	3.1	3.1

Table 7.15: Summary of systematic uncertainties from each factor for the B^0 channel in pPb collisions. All the values are shown in percentage.

Factors	(10,15)	(15,20)	(20,60)
B meson p_T shape	0.6	0.6	0.6
Tracking efficiency	7.8	7.8	7.8
Muon efficiency	7.3	6.0	5.4
Selection efficiency	11	11	11
Acceptance correction	0.3	0.3	1.7
Yield extraction	10.0	10.0	10.0
Luminosity	3.5	3.5	3.5
Branching fractions	4.6	4.6	4.6

Table 7.16: Summary of systematic uncertainties from each factor for the B_s^0 channel in pPb collisions. All the values are shown in percentage.

Factors	(10,60)
B meson p_T shape	0.6
Tracking efficiency	7.8
Muon efficiency	6.5
Selection efficiency	11
Acceptance correction	5.6
Yield extraction	14.6
Luminosity	3.5
Branching fractions	8.5

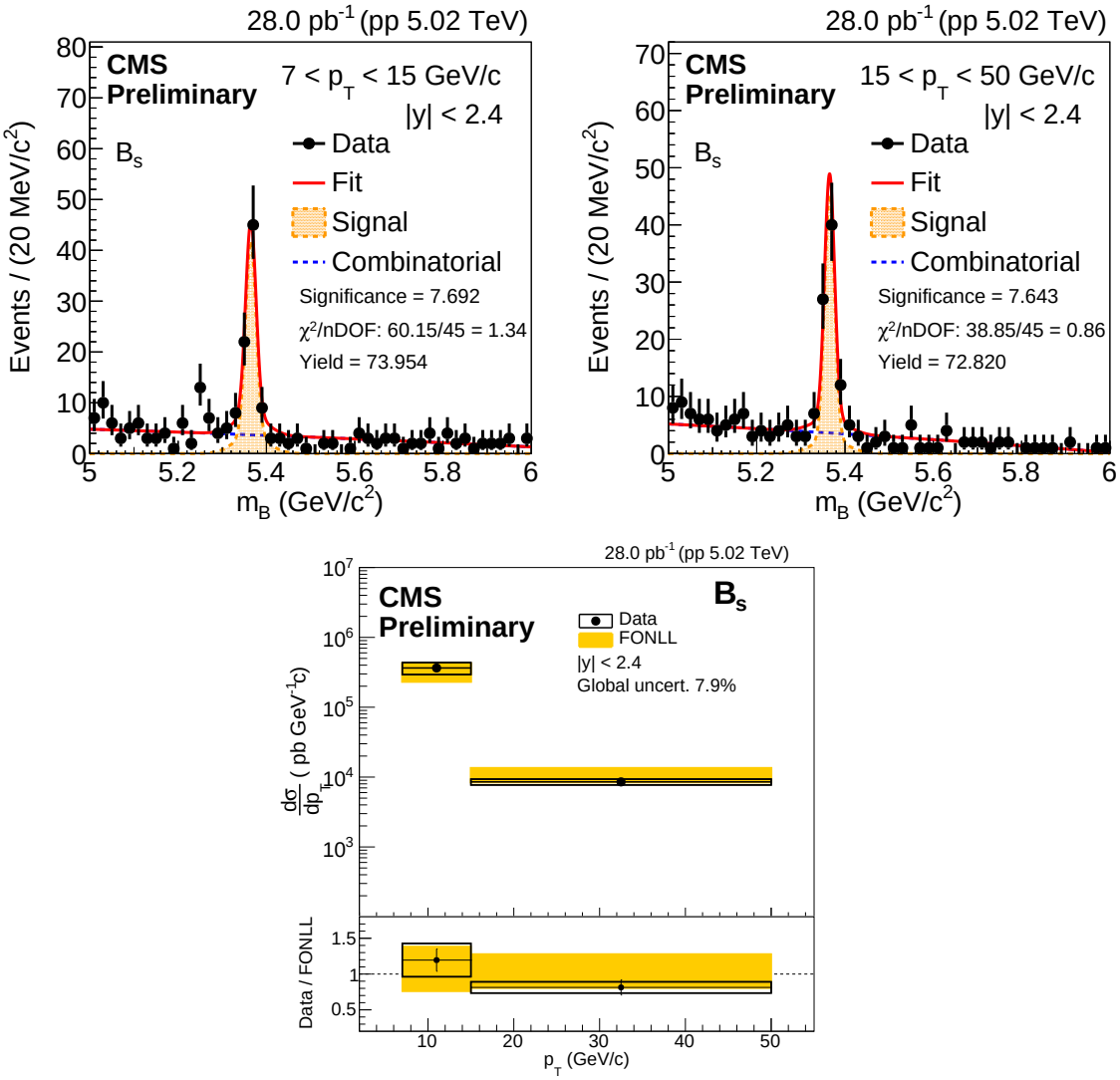

Figure 7-25: B_s^0 invariant mass spectra (top) and the corresponding cross sections (bottom) using a cut-base method in pp collisions.

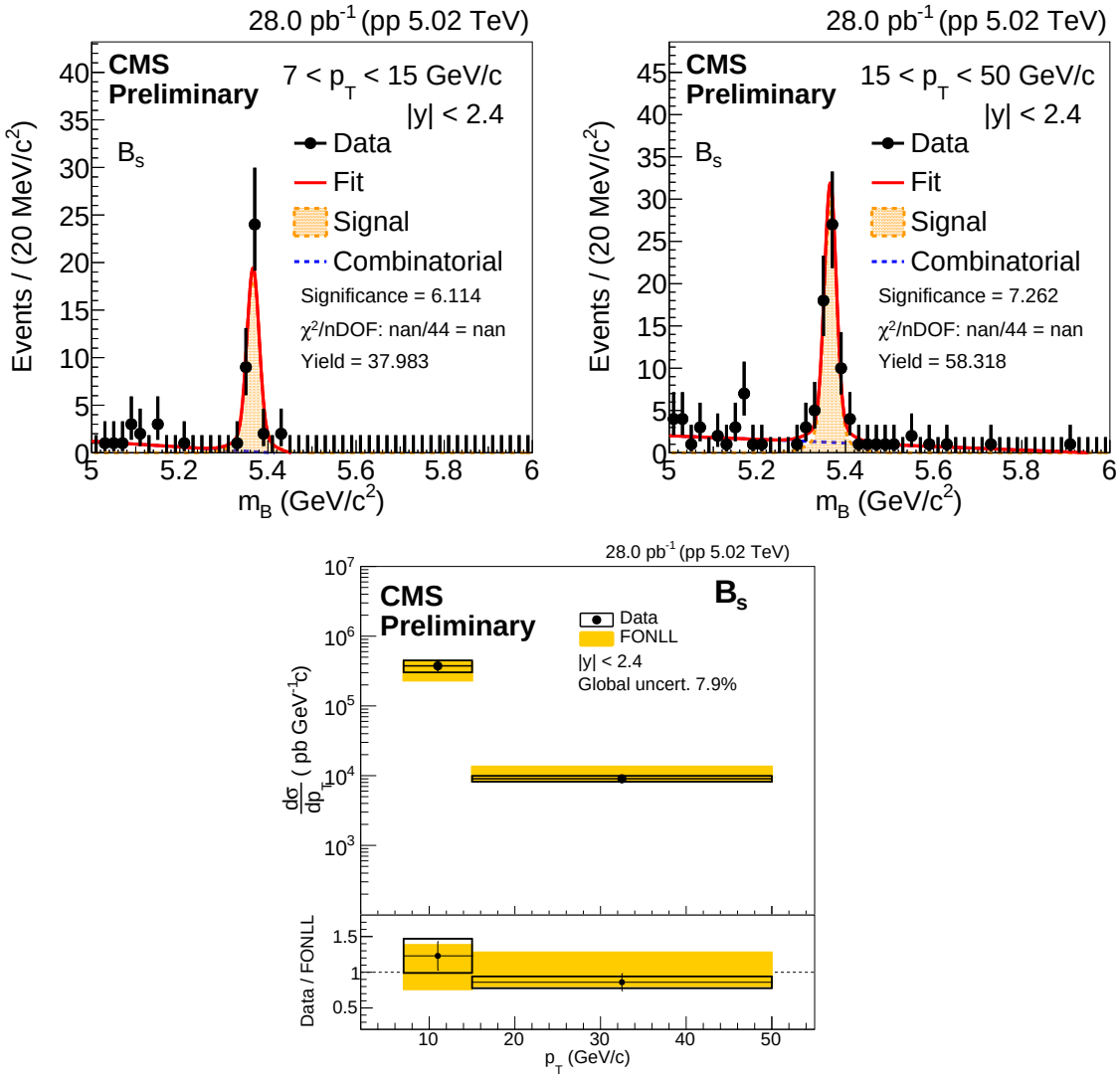

Figure 7-26: B_s^0 invariant mass spectra (top) and the corresponding cross sections (bottom) using the PbPb trained BDT discriminant in pp data.

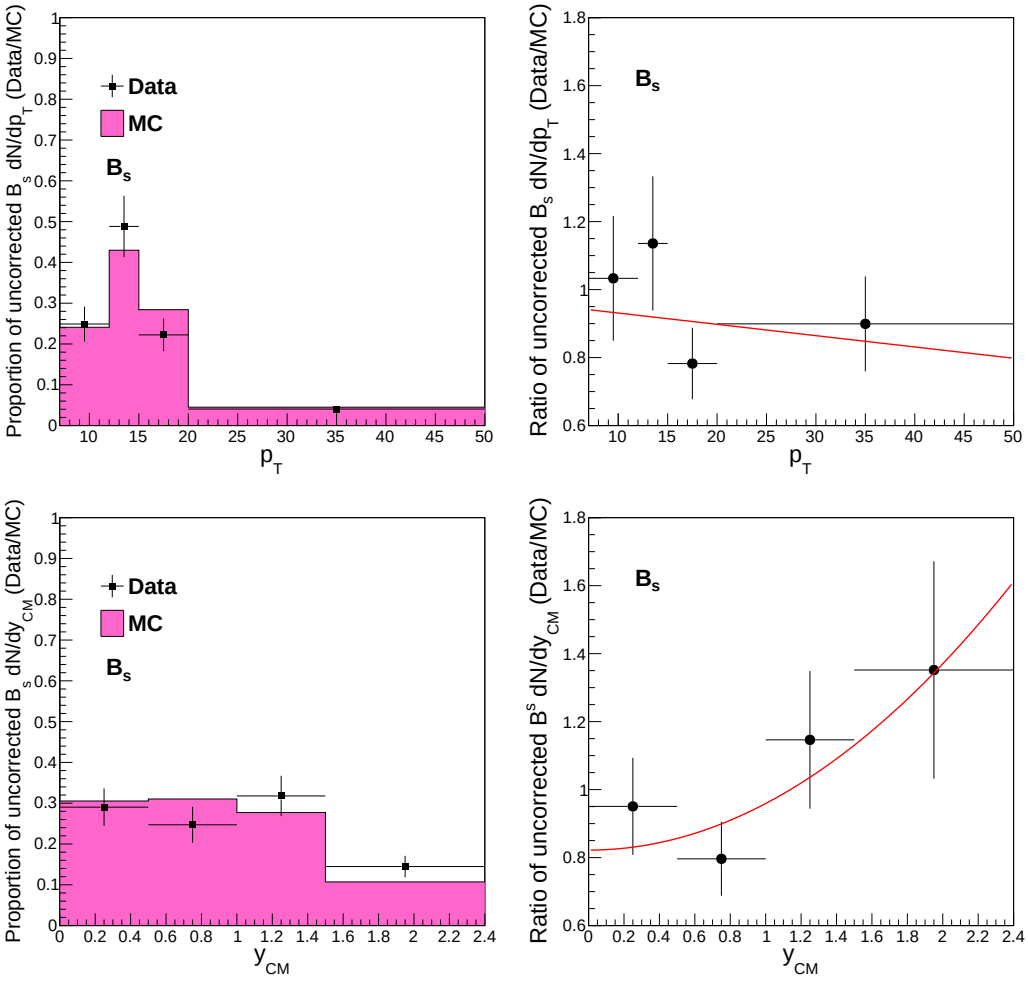

Figure 7-27: Normalized and uncorrected yields between real data and MC simulations (left) and ratios (right) with p_T (top) and rapidity (bottom) binning of the B_s^0 channel in pp collisions.

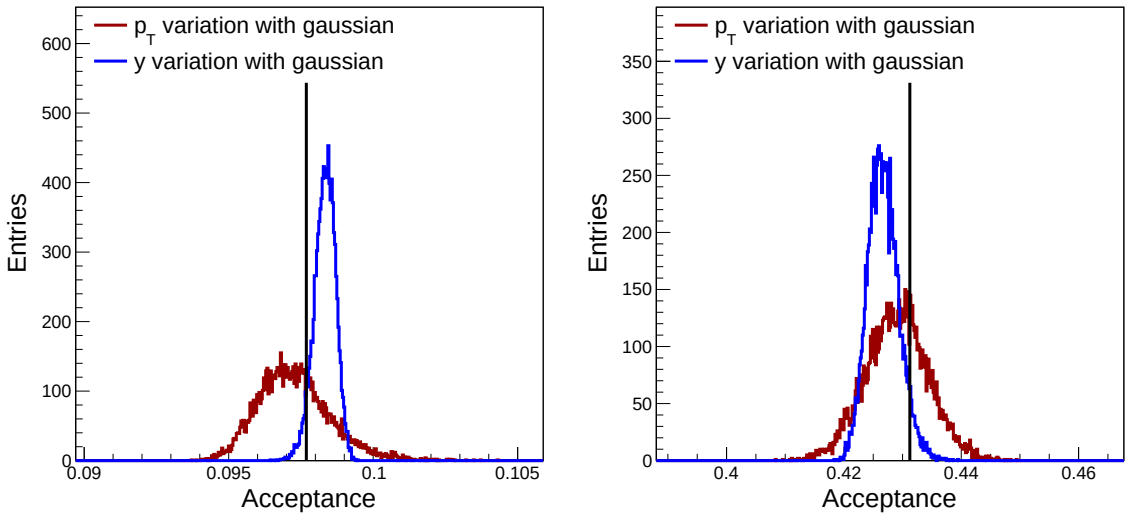

Figure 7-28: Variated acceptance distributions from toys obtained by p_T (red) and rapidity (blue) yield ratios for the B_s^0 channel in pp collisions. B_s^0 mesons with p_T 7 to 15 GeV/c (left) and 15 to 50 GeV/c (right). The black line in the middle is the nominal acceptance value in the analysis.

Table 7.17: Summary of systematic uncertainties from each factor for the B^+ channel in pp collisions. All the values are shown in percentage.

Factors	(7,10)	(10,15)	(15,20)	(20,30))	(30,50))
B meson p_T shape	2	1	1	1	1
Tracking efficiency	4	4	4	4	4
Muon efficiency	5.5	3.8	3.2	3.0	2.8
Selection efficiency	3.8	3.8	3.8	3.8	3.8
Acceptance correction	0.1	0.1	0.2	0.3	0.4
Yield extraction	2.9	2.9	2.9	2.9	2.9
Luminosity	2	2	2	2	2
Branching fractions	3.07	3.07	3.07	3.07	3.07

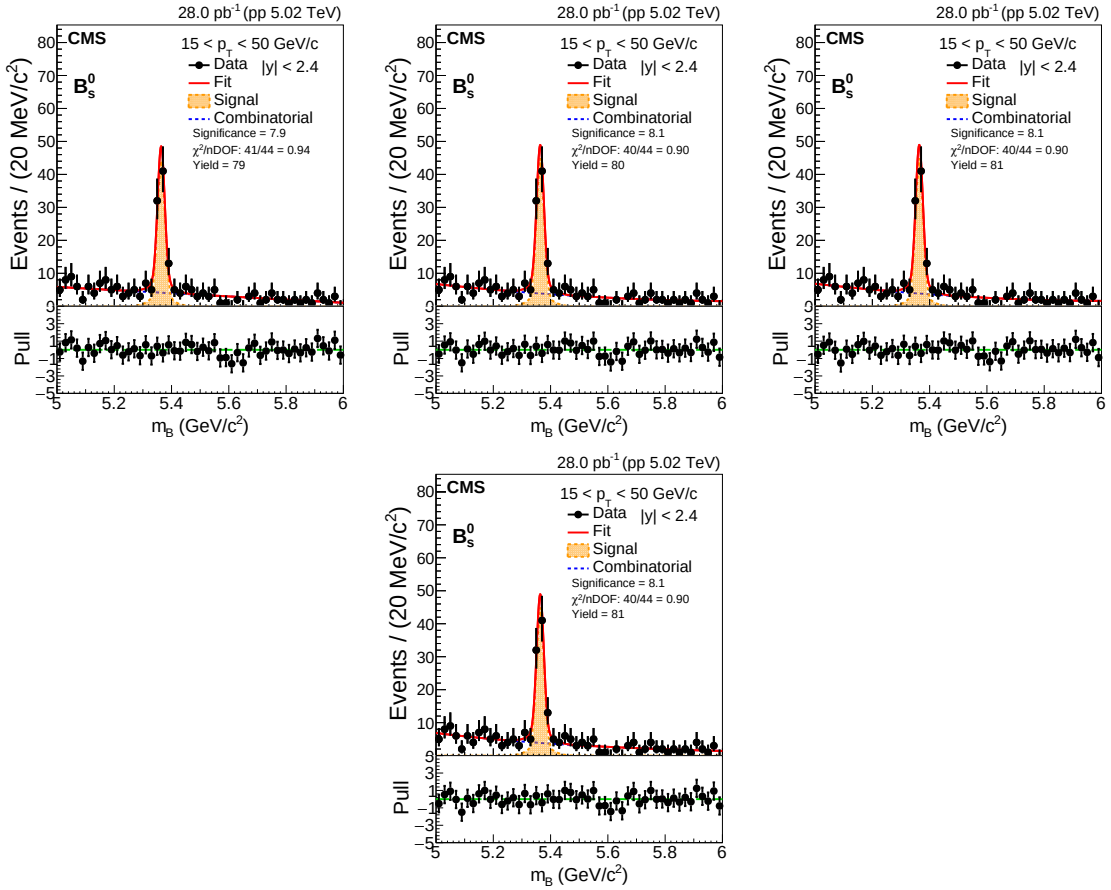

Figure 7-29: Invariant mass fit of the B_s^0 channel for B_s^0 mesons with p_T $15 < p_T < 50$ GeV/c in 5.02 TeV pp collisions. The background function variations from left to right are default linear, 2nd-order polynomial, 3rd-order polynomial, and exponential function.

Table 7.18: Summary of systematic uncertainties from each factor for the B^+ channel in PbPb collisions. All the values are shown in percentage.

Factors	(7,10)	(10,15)	(15,20)	(20,30))	(30,50))
Tracking efficiency	6	6	6	6	6
Muon efficiency	6.3	4.7	3.9	3.6	3.4
B selection efficiency	12.0	12.0	12.0	12.0	12.0
B meson p_T shape	2	1	1	1	1
Acceptance correction	0.1	0.1	0.2	0.3	0.4
Yield extraction	2.6	2.6	2.6	2.6	2.6
Luminosity	2	2	2	2	2
T_{AA}	+2.8 -3.4	+2.8 -3.4	+2.8 -3.4	+2.8 -3.4	+2.8 -3.4
Branching fractions	3.07	3.07	3.07	3.07	3.07

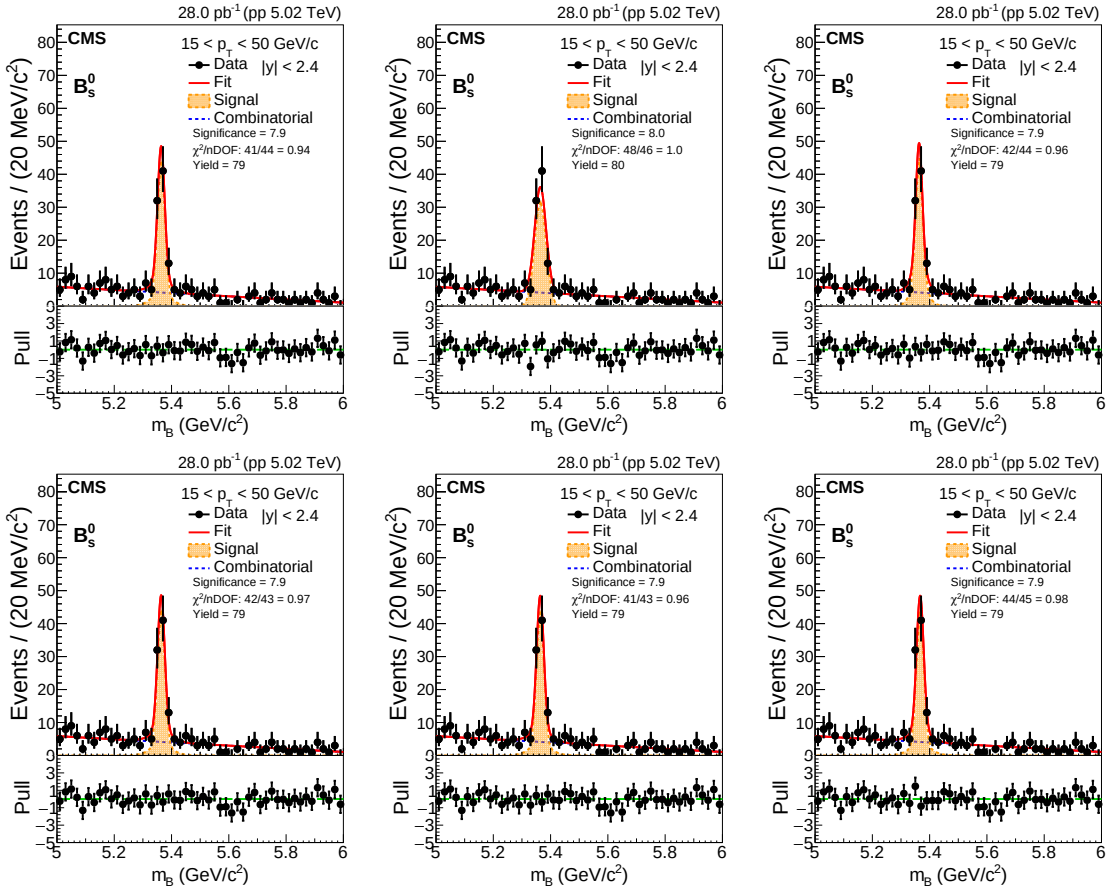

Figure 7-30: Invariant mass fit of the B_s^0 channel for B_s^0 mesons with p_T $15 < p_T < 50$ GeV/c in 5.02 TeV pp collisions. The signal function variations from left to right are default double Gaussian, single Gaussian, triple Gaussian, width decreased, width increased, and mean fixed by MC simulations.

Table 7.19: Summary of systematic uncertainties from each factor for the B_s^0 channel in pp collisions. All the values are shown in percentage.

Factors	(7,15)	(15,50)
B meson p_T shape	6.5%	2.3%
Tracking efficiency	8%	8%
Muon efficiency	4.4%	3.1%
Selection efficiency	15%	2.6%
Acceptance correction	1.7%	1.8%
Yield extraction	4.2%	1.7%
Luminosity	2.3%	2.3%
Branching fractions	7.6%	7.6%

Table 7.20: Summary of systematic uncertainties from each factor for the B_s^0 channel in PbPb collisions. All the values are shown in percentage.

Factors	(7,15)	(15,50)
B meson p_T shape	7.9%	3.8%
Tracking efficiency	12%	12%
Muon efficiency	5.1%	3.8%
Selection efficiency	19%	8.6%
Acceptance correction	1.7%	1.7%
Yield extraction	9.7%	3.6%
N_{MB}events	2%	2%
T_{AA}	+2.8 -3.4%	+2.8 -3.4%
Branching fractions	7.6%	7.6%

7.9 FONLL

The extracted yields obtained in section 7.6 were corrected for the reconstruction and selection efficiency and translated to B meson cross sections (introduced in the following section). To ensure the reliability of our results, we compared our pp cross sections with the FONLL calculations [177, 178]. For this calculation, the CTEQ6.6 parton distribution functions (PDFs) were considered. The central values were calculated by considering m_c=1.5 GeV and m_b=4.5 GeV, and the renormalization and factorization scales μ_R=μ_F=μ_0=$\sqrt{m^2 + p_T^2}$. The uncertainty band was evaluated by varying the perturbative parameters in the range 4.5< m_b <5 GeV/c^2, 1.3< m_c <1.7 GeV/c^2, μ_F, and μ_R independently in the range $0.5 < \mu_F/m_T < 2$ and $0.5 < \mu_R/m_T < 2$ with the constraint of $0.5 < \mu_F/\mu_R < 2$. We used the FONLL to calculate the cross section of a generic admixture of B mesons and baryons in pp collisions within rapidity range y <2.4 and rebinned the resulted spectrum according to the p_T intervals adopted in the analyses. The p_T-differential cross sections of B^+, B^0, and B_s^0 mesons were derived by scaling the FONLL results of the generic B meson and baryon admixture with the PDG measured fragmentation function (FF), the fraction in which b quarks hadronize to a specific type of b hadrons, as the following

- $\mathrm{BR}(b \to B^+) = (40.5 \pm 0.6)\%$
- $\mathrm{BR}(b \to B^0) = (40.5 \pm 0.6)\%$
- $\mathrm{BR}(b \to B_s^0) = (10.1 \pm 0.4)\%$

In Fig. 7-31, the FONLL p_T-differential cross sections of B^+ and B_s^0 mesons are presented. The blue curves represent the unbinned FONLL result with its total uncertainty. The black points represent the rebinned results for the B^+ and B_s^0 mesons while the red points represent the rebinned results scaled by the corresponding FF value.

Our resulted pp cross sections were found to be compatible with the FONLL predictions. This ensures the correctness of our workflow and the reliability of our measurements in the pPb and PbPb counterparts.

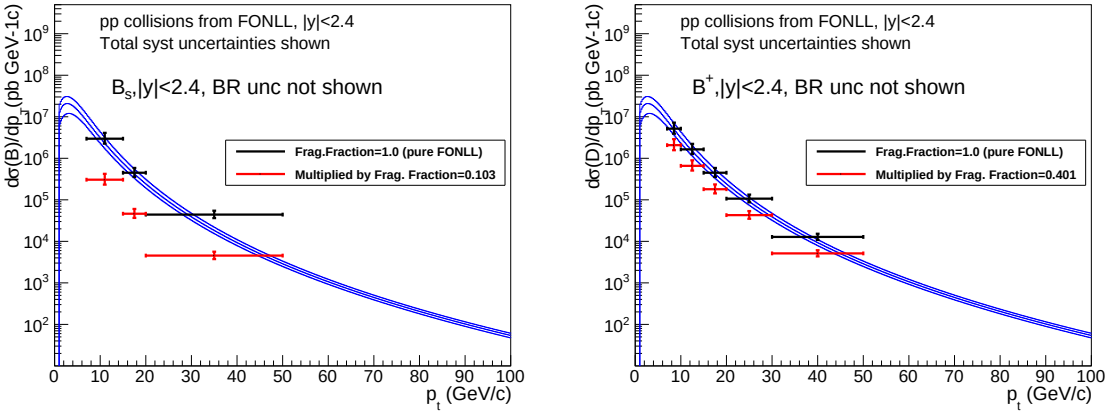

Figure 7-31: FONLL calculation for the p_T-differential cross sections of the B^+ (left) and B_s^0 (right) mesons in pp collisions at $\sqrt{s} = 5.02$ TeV. The black points represent the rebinned FONLL results and the red points represent the rebinned results scaled by the corresponding fragmentation function value.

7.10 Cross section

The p_T-differential cross section is defined as

$$\left.\frac{d\sigma^B_{pp}}{dp_T}\right|_{|y|<2.4} = \frac{1}{2}\frac{1}{\mathcal{B}\,\mathcal{L}}\frac{1}{\Delta p_T}\left.\frac{N^B_{pp}(p_T)}{\alpha_{pp}(p_T)\,\epsilon_{pp}(p_T)}\right|_{|y|<2.4}, \tag{7.13}$$

where Δp_T is the width of the p_T interval, $\mathcal{B}$ is the branching ratio of the decay chain, and $\mathcal{L}$ is the integrated luminosity. $\alpha_{pp}(p_T)$ and $\epsilon_{pp}(p_T)$ represent the acceptance and reconstruction plus selection efficiency corrections while $N^B_{pp}(p_T)$ is the yields extracted in each p_T interval. The factor $1/2$ accounts for the fact that the yields were measured for particles and antiparticles, but the cross section was given for particles only. In Fig. 7-32, the p_T-differential cross sections of B^+ and B^0_s mesons in the rapidity region $|y| < 2.4$ in pp collisions at $\sqrt{s} = 5.02$ TeV are presented. The boxes around the data points represent the total systematic uncertainties. The FONLL predictions introduced earlier were superimposed for comparison. The ratios of our measurements over the FONLL calculations are also shown. Our results are compatible with the central values of FONLL.

We also calculated the pPb collision equivalent cross sections using the extracted yields from pPb data. The calculation was based on the same formula as in Eq. 7.13. FONLL predictions were obtained as in pp collisions and then multiplied by lead atomic mass number. The resulting cross sections are shown in Fig. 7-33.

A similar quantity, the scaled p_T-differential yields dN/dp_T in PbPb collisions, which is defined as

$$\left.\frac{1}{T_{AA}}\frac{dN^B_{PbPb}}{dp_T}\right|_{|y|<2.4} = \frac{1}{2}\frac{1}{\mathcal{B}\,N_{MB}\,T_{AA}}\frac{1}{\Delta p_T}\left.\frac{N^B_{PbPb}(p_T)}{\alpha_{PbPb}(p_T)\,\epsilon_{PbPb}(p_T)}\right|_{|y|<2.4}. \tag{7.14}$$

where T_{AA} is the nuclear overlap function (from Ref. [110]). Detailed values can be found in Table 7.21. N_{events} is the number of minimum-bias events which is calculated by scaling the number of total PbPb collision events by the ratio between the minimum-bias trigger and the muon trigger efficiency. Shown in Fig. 7-34 are the

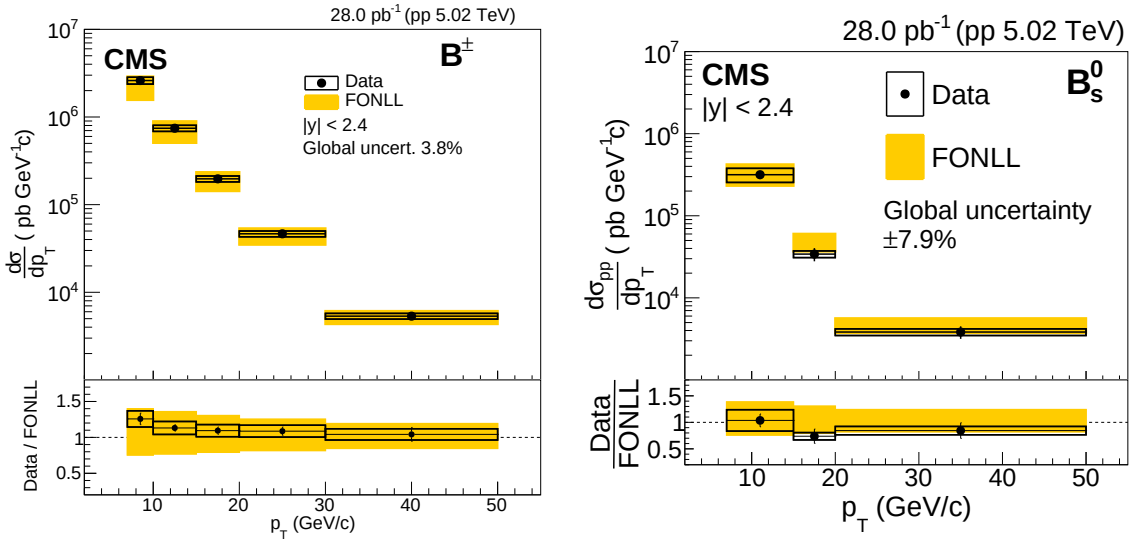

Figure 7-32: The p_T-differential cross sections of the B^+ (left) and B_s^0 (right) mesons in pp collisions at $\sqrt{s} = 5.02$ TeV in p_T intervals from 7 to 50 GeV/c. The vertical bars (boxes) correspond to statistical (systematic) uncertainties. The global systematic uncertainty, listed in the legend and not included in the point-to-point uncertainties, comprises the uncertainties in the integrated luminosity measurement and in the branching ratios. The pp cross section is compared to FONLL calculations [34] represented by the colored yellow boxes with the heights indicating the theoretical uncertainties.

PbPb scaled p_T-differential yields calculated as in equation 7.14.

Centrality	$< N_{coll} >$	$< T_{AA} >$	$< N_{part} >$
0 - 100%	$392.5 + 26.9(7.2\%) - 28.1(6.8\%)$	$5.607 + 0.155(2.8\%) - 0.191(3.4\%)$	$114.0 + 2.6(2.3\%) - 2.6(2.3\%)$
0 - 10%	$1626 + 115(7.1\%) - 121(7.5\%)$	$23.22 + 0.43(1.9\%) - 0.69(3.0\%)$	$358.8 + 2.4(0.7\%) - 2.6(0.7\%)$
10 - 20%	$1005 + 69(6.8\%) - 73(7.2\%)$	$14.35 + 0.33(2.3\%) - 0.45(3.2\%)$	$264.2 + 3.6(1.4\%) - 3.8(1.4\%)$
20 - 30%	$606.2 + 43.5(6.8\%) - 41.2(7.2\%)$	$8.66 + 0.29(3.3\%) - 0.33(3.8\%)$	$189.2 + 4.0(2.1\%) - 4.1(2.1\%)$
30 - 40%	$348.5 + 24.8(7.1\%) - 25.6(7.3\%)$	$4.978 + 0.236(4.7\%) - 0.242(4.9\%)$	$131.4 + 4.0(3.0\%) - 4.0(3.0\%)$
40 - 50%	$186.2 + 15.1(8.1\%) - 15.2(8.1\%)$	$2.66 + 0.180(6.8\%) - 0.176(6.6\%)$	$86.95 + 3.7(4.3\%) - 4.3(6.8\%)$
50 - 100%	$30.76 + 3.5(11.4\%) - 2.4(7.8\%))$	$0.4395 + 0.049(11.2\%) - 0.032(7.3\%)$	$21.87 + 1.8(8.2\%) - 1.0(4.5\%)$
10 - 30%	$805.4 + 54.7(6.8\%) - 57.9(7.2\%)$	$11.51 + 0.304(2.6\%) - 0.388(3.4\%)$	$226.7 + 3.7(1.7\%) - 3.9(1.7\%)$
30 - 100%	$98.36 + 8.0(8.1\%) - 6.4(6.4\%)$	$1.405 + 0.094(6.7\%) - 0.061(4.4\%)$	$46.81 + 2.4(11.8\%) - 1.2(10.7\%)$
0 - 20%	$1315 + 92(7.0\%) - 97(7.4\%)$	$18.79 + 0.37(1.9\%) - 0.56(3.0\%)$	$311.5 + 2.9(0.9\%) - 3.1(1.0\%)$
20 - 40%	$477.3 + 32.8(6.9\%) - 34.3(7.2\%)$	$6.82 + 0.26(3.8\%) - 0.28(4.2\%)$	$160.3 + 4.0(2.5\%) - 4.0(2.5\%)$
40 - 100%	$55.67 + 5.4(9.5\%) - 4.0(7.0\%)$	$0.810 + 0.071(8.8\%) - 0.046(5.7\%)$	$32.71 + 2.1(6.4\%) - 1.1(3.5\%)$
0 - 5%	$1819 + 130(7.1\%) - 137(7.5\%))$	$25.98 + 0.47(1.8\%) - 0.77(2.9\%)$	$384.3 + 1.8(0.5\%) - 2.0(0.5\%)$
5 - 10%	$1432 + 100(7.0\%) - 106(7.4\%)$	$20.46 + 0.38(1.9\%) - 0.60(3.0\%)$	$333.3 + 3.0(0.9\%) - 3.2(1.0\%)$
10 - 15%	$1127 + 78(6.9\%) - 82(7.3\%)$	$16.11 + 0.35(2.2\%) - 0.50(3.1\%)$	$285.4 + 3.5(1.2\%) - 3.7(1.3\%)$
15 - 20%	$882 + 60(6.8\%) - 64(7.3\%)$	$12.6 + 0.32(2.5\%) - 0.43(3.4\%)$	$242.9 + 3.8(1.6\%) - 3.9(1.6\%)$
20 - 25%	$685.9 + 46.7(6.8\%) - 49.8(7.3\%)$	$9.799 + 0.311(3.2\%) - 0.374(3.8\%)$	$205.7 + 3.9(1.9\%) - 4.1(2.0\%)$
25 - 30%	$526.5 + 36.7(7.0\%) - 38.2(7.3\%)$	$7.522 + 0.294(3.9\%) - 0.316(4.2\%)$	$172.7 + 4.0(2.3\%) - 4.0(2.3\%)$
30 - 35%	$399.4 + 28.8(7.2\%) - 29.5(7.4\%)$	$5.706 + 0.265(4.6\%) - 0.270(4.7\%)$	$144.1 + 4.0(2.3\%) - 4.0(2.3\%)$
35 - 40%	$297.6 + 22.0(7.4\%) - 22.9(7.7\%)$	$4.251 + 0.230(5.4\%) - 0.236(5.6\%)$	$118.7 + 4.0(2.3\%) - 4.0(2.3\%)$
40 - 45%	$217.2 + 16.9(7.8\%) - 17.1(7.9\%)$	$3.103 + 0.192(6.2\%) - 0.190(6.1\%)$	$96.51 + 3.8(3.9\%) - 3.8(3.9\%)$
45 - 50%	$155.2 + 13.(8.4\%) - 13.0(8.4\%)$	$2.217 + 0.162(7.3\%) - 0.157(7.1\%)$	$77.39 + 3.7(4.7\%) - 3.6(4.6\%)$
50 - 60%	$90.72 + 8.9(9.8\%) - 8.7(9.6\%)$	$1.296 + 0.120(9.2\%) - 0.115(8.8\%)$	$53.86 + 3.2(6.0\%) - 3.1(5.8\%)$
60 - 70%	$40.1 + 5.0(12.4\%) - 4.6(11.5\%)$	$0.5729 + 0.071(12.4\%) - 0.064(11.2\%)$	$30.57 + 2.6(8.5\%) - 2.4(8.0\%)$
70 - 100%	$7.663 + 1.2(15.9\%) - 0.7(9.7\%)$	$0.1095 + 0.018(16.4\%) - 0.011(10.2\%)$	$8.297 + 1.0(12.2\%) - 0.6(6.8\%)$

Table 7.21: Summary of the $N_{\rm coll}$, $T_{\rm AA}$ and $N_{\rm part}$ values for different centrality bins [110].

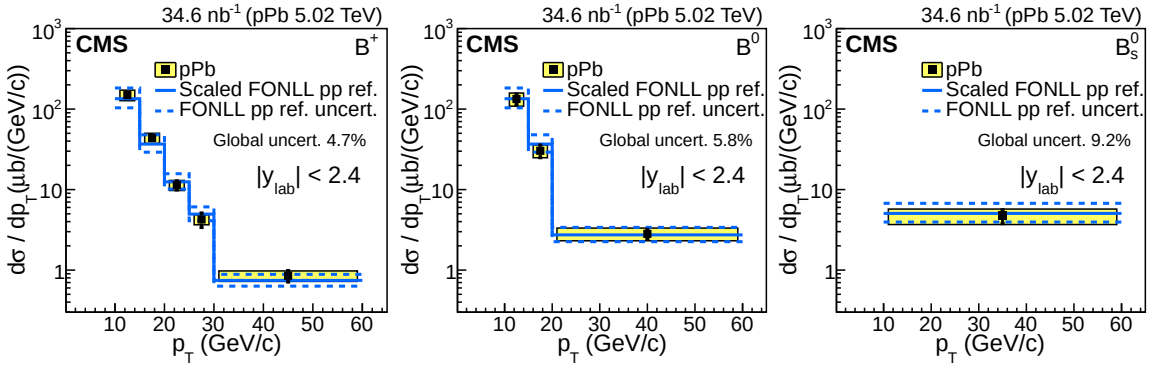

Figure 7-33: The p_T-differential cross sections of the B^+ (left), B^0 (center), and B_s^0 (right) mesons measured in pPb collisions at $\sqrt{s_{NN}} = 5.02$ TeV. Vertical bars (boxes) correspond to statistical (systematic) uncertainties. The global systematic uncertainty, listed in each panel and not included in the data points, comprises the uncertainties in the integrated luminosity measurement and in the branching ratios. Results are compared to FONLL calculations [177, 178], scaled by the number of binary NN collisions, represented by a continuous histogram. The dashed histograms represent the theoretical uncertainties of the FONLL reference.

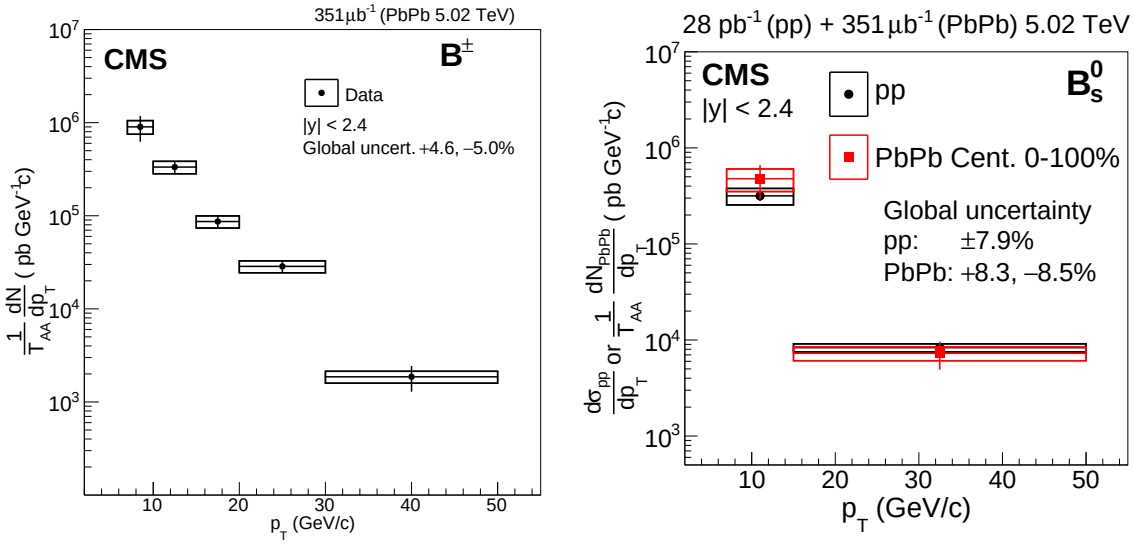

Figure 7-34: The p_T-differential corrected yields of the B^+ (left) and B_s^0 (right) mesons scaled by nuclear overlapping function (T_{AA}) in PbPb collisions at $\sqrt{s_{NN}} = 5.02$ TeV in B meson p_T intervals from 7 to 50 GeV/c. The vertical bars (boxes) correspond to statistical (systematic) uncertainties. The global systematic uncertainty comprises the uncertainties in T_{AA}, number of minimum-bias events, and branching ratios.

7.11 Nuclear modification factor

The pPb nuclear modification factor $R_{\mathrm{pA}}^{\mathrm{FONLL}}$ of B mesons is defined as

$$R_{\mathrm{pA}}^{\mathrm{FONLL}} = \frac{(\frac{\mathrm{d}\sigma}{\mathrm{dp_T}})_{\mathrm{pPb}}}{\mathrm{A}\,(\frac{\mathrm{d}\sigma}{\mathrm{dp_T}})_{\mathrm{pp}}^{\mathrm{FONLL}}} \tag{7.15}$$

where A=208 is the atomic mass number of the lead nucleus, $(\frac{d\sigma}{dp_T})_{pPb}$ is the p_T-differential cross section measured in pPb collisions at $\sqrt{s_{\mathrm{NN}}} = 5.02$ TeV and $(\frac{\mathrm{d}\sigma}{\mathrm{dp_T}})_{\mathrm{pp}}^{\mathrm{FONLL}}$ is the FONLL pp reference. Note that the measurements of pPb data were conducted before the pp data at the same collision energy was available. The pp reference was thus obtained from FONLL prediction. In Fig. 7-35, the nuclear modification factors $R_{\mathrm{pA}}^{\mathrm{FONLL}}$ of the B^+ (top left), B^0 (top right), and B_s^0 (bottom) mesons measured in pPb collisions are presented. The measurements are well compatible with unity in the full p_T range.

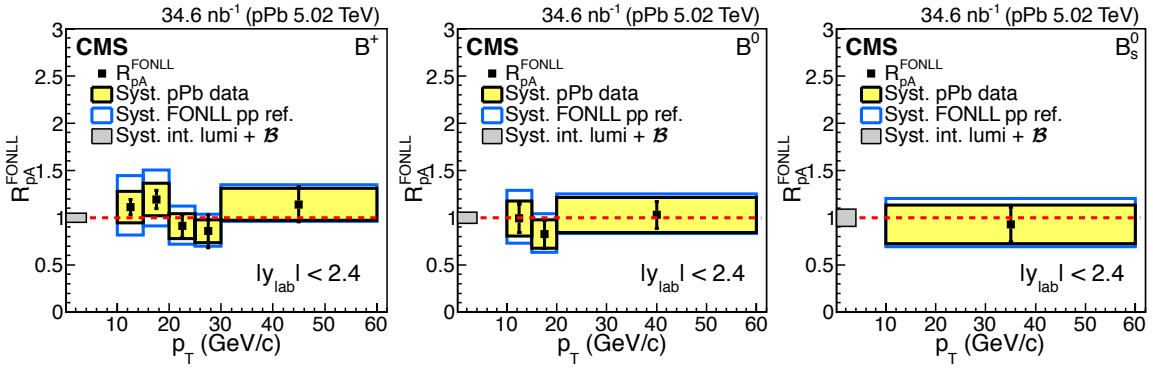

Figure 7-35: The nuclear modification factors $R_{\mathrm{pA}}^{\mathrm{FONLL}}$ of the B (left), B^0 (center), B_s^0 (right) mesons measured in pPb collisions at $\sqrt{s_{\mathrm{NN}}} = 5.02$ TeV. The statistical and systematic uncertainties on the pPb data are shown as bars and yellow boxes around the data points respectively. The systematic uncertainties from the FONLL predictions are plotted separately as open blue boxes. The global systematic uncertainties are shown as full gray boxes at unity and are not included in the data points.

For the PbPb collisions, the nuclear modification factor $\mathrm{R_{AA}}$ is defined as

$$R_{\mathrm{AA}}(\mathrm{p_T}) = \frac{1}{\mathrm{T_{AA}}} \frac{\mathrm{dN_{PbPb}^B}}{\mathrm{dp_T}} \Big/ \frac{\mathrm{d}\sigma_{\mathrm{pp}}^{\mathrm{B}}}{\mathrm{dp_T}}. \tag{7.16}$$

In Fig. 7-36, the R_{AA} of the B^+ and B_s^0 mesons in the centrality range 0-100% are shown.

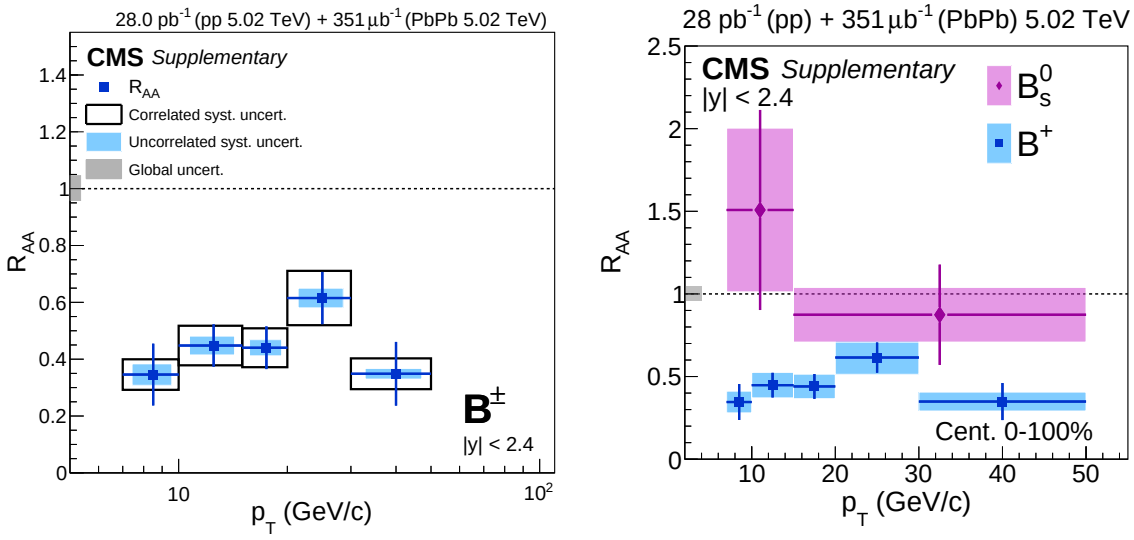

Figure 7-36: The nuclear modification factor R_{AA} of the B^+ (left) and B_s^0 (right) mesons measured in PbPb collisions at $\sqrt{s_{\mathrm{NN}}} = 5.02$ TeV from 7 to 50 GeV/c. The vertical bars (boxes) correspond to statistical (systematic) uncertainties. The global systematic uncertainty, represented by colored boxes at $R_{\mathrm{AA}} = 1$, comprises the uncertainties in the integrated luminosity measurement and the T_{AA} value.

If one compared the R_{AA} between B_s^0 mesons to the B^+ mesons as shown in the right panel of Fig. 7-36, one can see an indication of an enhancement for the B_s^0 mesons, which would be the expectation in the presence of a contribution from beauty recombination with strange quarks in heavy ion collisions. However, these values are compatible with unity and their large uncertainties do not exclude a significant suppression.

7.11.1 Comparison with theoretical predictions and discussions

In this section, we will compare the results of our R_{AA} measurements in PbPb collisions with a few different theoretical predictions. Firstly, the B^+ meson R_{AA} in PbPb collisions is compared as shown in Fig. 7-37.

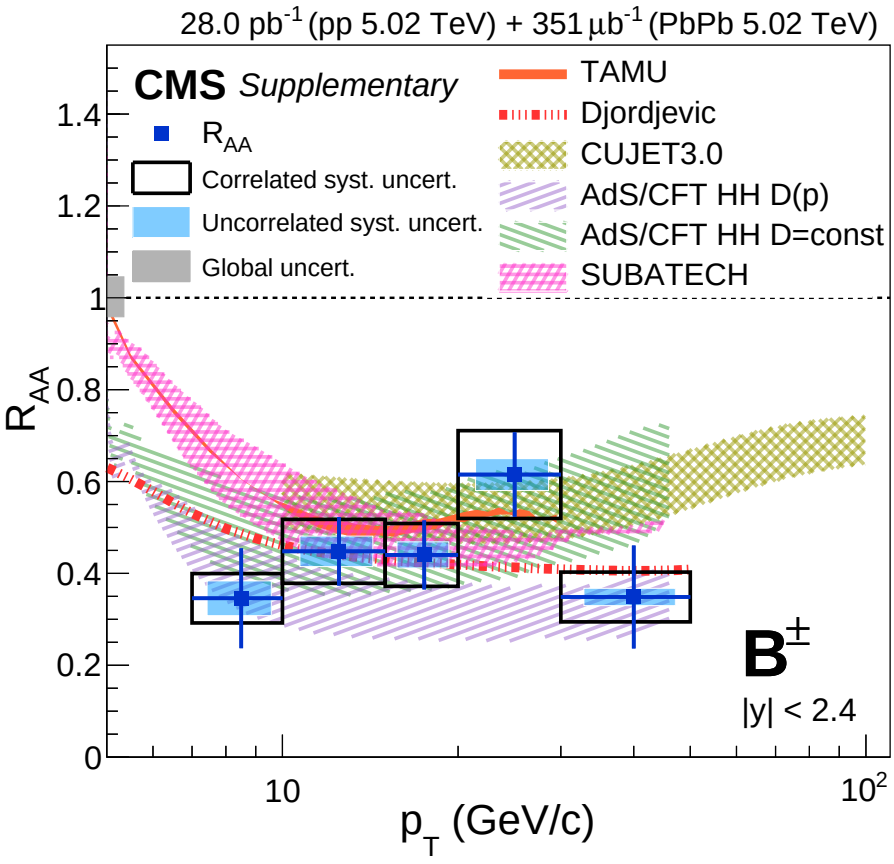

Figure 7-37: The p_T dependence of the nuclear modification factor R_{AA} of the B^+ mesons measured in PbPb collisions at $\sqrt{s_{NN}} = 5.02$ TeV. Five theoretical calculations are shown for comparison: TAMU [165, 166], Djordjevic [150], CUJET3.0 [197, 196, 195], AdS/CFT HH [169, 163], and MC@sHQ+EPOS2 [181, 159]. The line width of the theoretical calculation from Ref. [165, 166] represents the size of its statistical uncertainty.

Specifically, the p_T dependence of the B^+ meson R_{AA} is compared to the predictions of: a) two perturbative QCD based models that include both collisional and radiative energy loss (Djordjevic [150], CUJET3.0 [197, 196, 195]); b) a transport model based on a Langevin equation that includes collisional energy loss and heavy quark diffusion in the medium (TAMU [165, 166]); c) a model based on the anti-de-Sitter/conformal field theory correspondence that includes thermal fluctuations in the energy loss for heavy quarks in a strongly-coupled plasma (AdS/CFT HH [169, 163].) and d) a model with Monte Carlo propagation of heavy quarks coupled to a fluid dynamical evolution of a strongly interacting medium (MC@sHQ+EPOS2 [181, 159]).

The AdS/CFT HH calculation is provided for two settings of the diffusion coefficient D of the heavy quark propagation through the medium: either dependent on or independent of the quark momentum. These theoretical calculations differ in several aspects, e.g., the modeling of the PbPb medium (hydrodynamically [197, 166, 159] or via a Glauber model [150]) and of the energy loss sources (partonic only [197, 166, 159] or also hadronic [166]), the set of the (nuclear) parton distribution functions used for the initial heavy-quark p_T distributions, etc. Given the current statistical and systematic uncertainties, all these theoretical predictions are roughly compatible with the measurements presented. However, while the present results can not help to resolve the disagreements between different models because of the large uncertainties, including those of the theoretical calculations, they can already be used to optimize parameter settings in such models (e.g., the parton-medium coupling parameters in the AdS/CFT model).

Next, in Fig. 7-38, the B_s^0 meson R_{AA} in PbPb collisions is compared with two different theoretical predictions. The difference between the two models below $p_T \sim 15$ GeV/c reflects the contribution from the recombination processes, which are included in the TAMU but not in the CUJET3.0 model. The results measured for $p_T > 7$ and < 15 GeV/c have the power to disentangle the two models, albeit after an increase in precision, which can be achieved with a bigger data sample.

To further quantify the significance of a possible enhancement of the B_s^0 mesons over the B^+ mesons in PbPb collisions with respect to pp collisions, the ratio between the B_s^0 and the B^+ meson R_{AA} was calculated with systematic uncertainty sources that are common to both measurements cancelled. The result is shown in Fig. 7-39.

The B^+ meson R_{AA} with a wider p_T binning (15–50 GeV/c) was obtained by a B^+ meson yield weighted average of the results from the three p_T bins (15–20, 20–30 and 30–50 GeV/c) presented in the B^+ meson analysis. Assuming a Gaussian distribution with mean and width equal to that of the R_{AA} ratio and its uncertainty (including statistical and systematic components added in quadrature), the hypothesis of the ratio values being consistent with unity (no enhancement) is tested with a χ^2 test. The resulted p-values are 18% and 28% for 7–15 and 15–50 GeV/c respectively. This

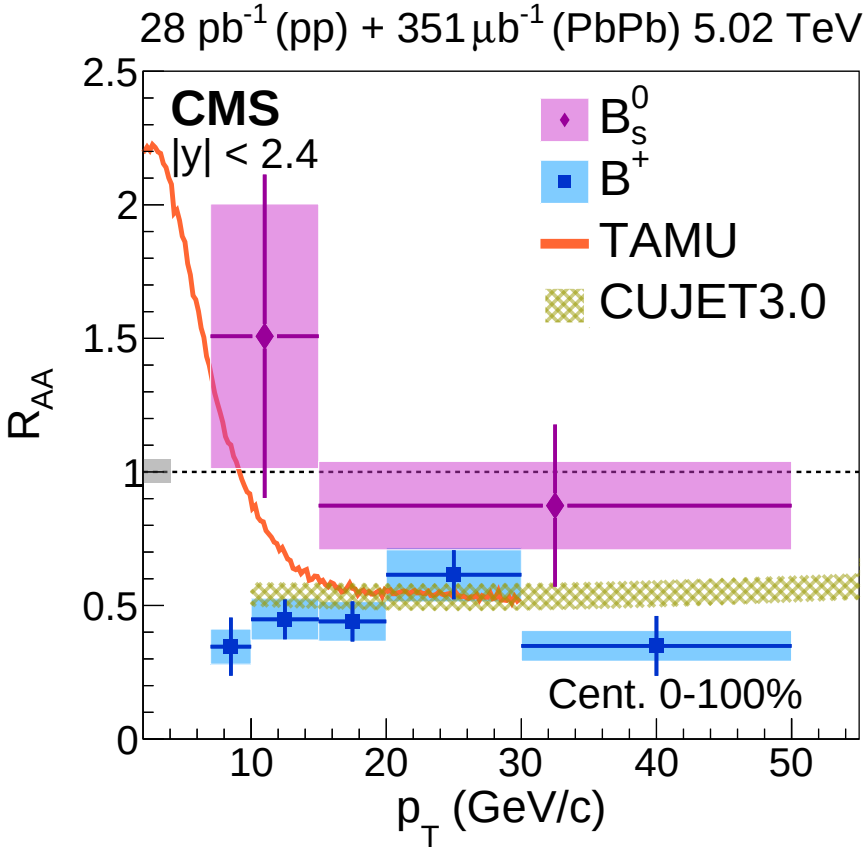

Figure 7-38: The p_T dependence of the nuclear modification factor R_{AA} of the B_s^0 mesons measured in PbPb collisions at $\sqrt{s_{NN}} = 5.02$ TeV. Two theoretical calculations are also shown for comparison: TAMU [165, 166] and CUJET3.0 [197, 196, 195]. The line width of the theoretical calculation from Refs. [165, 166] represents the size of its statistical uncertainty.

shows that, with a p-value cutoff of 5%, the scenario of no enhancement cannot be rejected.

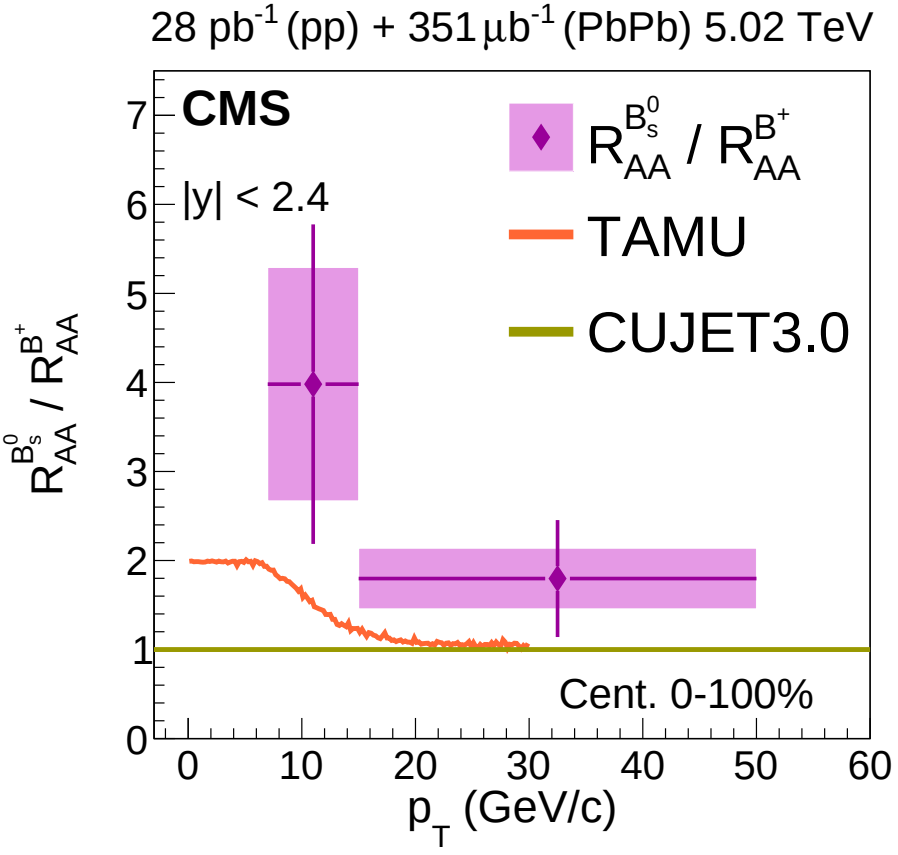

Figure 7-39: Nuclear modification factor R_{AA} ratio between the B_s^0 and B^+ mesons measured in PbPb collisions at $\sqrt{s_{\mathrm{NN}}} = 5.02$ TeV for B meson $\mathrm{p_T}$ between 7 to 50 GeV/c. Two theoretical calculations are also shown for comparison: TAMU [165, 166], and CUJET3.0 [197, 196, 195].

Chapter 8

Conclusions

We have presented the first measurements of fully reconstructed beauty mesons in heavy ion collisions. It was the synergy between the precise displaced vertex reconstruction enabled by the high resolution CMS tracking system and the use of advanced ML algorithm that makes the analyses which were previously regarded as impossible to be realized. Specifically, the B^+ and B_s^0 meson exclusive decay channels (via $B^+ \to J/\psi\ K^+ \to \mu^+\ \mu^-\ K^+$ and $B_s^0 \to J/\psi\ \phi \to \mu^+\ \mu^-\ K^+\ K^-$) were reconstructed separately using the pp and PbPb collision data (at $\sqrt{s_{\rm NN}} = 5.02$ TeV) collected by the CMS experiment. Both cross sections and nuclear modification factors were calculated for B mesons with $\rm p_T$ between 7 to 50 GeV/c and a rapidity range of $|y| < 2.4$. The framework were tested by comparing the pp results with the FONLL theoretical predictions and a good agreement was observed between the two spectra.

From the nuclear modification factors ($R_{\rm AA}$) of the B^+ mesons, a strong suppression by about a factor of two was observed. We also compared our experimental results with five different theoretical calculations. The results were found to be roughly compatible with theoretical calculations incorporating beauty quark diffusion and energy loss in a QGP system.

This result can be compared with other heavy flavor measurements from the CMS collaborations. Specifically, it was compared to the $R_{\rm AA}$ of inclusive charged hadrons [39], D mesons [126], and non-prompt J/ψ mesons [123] as shown in Fig. 8-1. Firstly, we can see the $R_{\rm AA}$ values are compatible between B^+ and non-prompt J/ψ

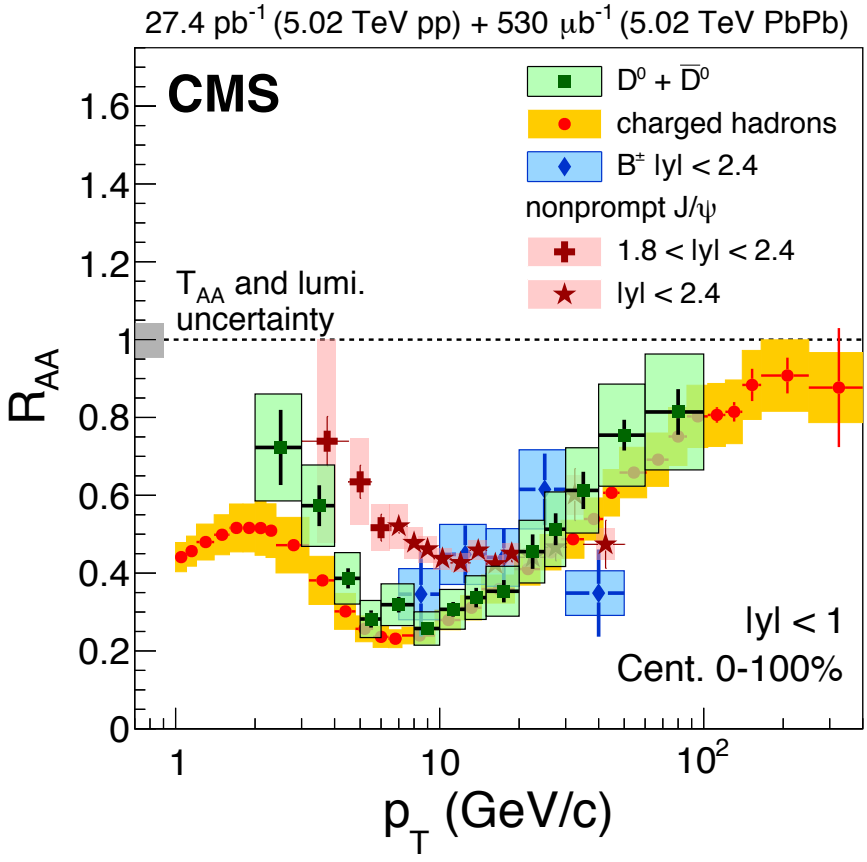

Figure 8-1: Nuclear modification factors (R_{AA}) measured in PbPb collisions at $\sqrt{s_{\mathrm{NN}}} = 5.02$ TeV for inclusive charged hadrons [39], D mesons [126], non-prompt J/ψ mesons [123] (J/ψ mesons from B hadron decay), and B mesons [114] in different $\mathrm{p_T}$ intervals and rapidity ranges.

mesons within uncertainties in the p_T 10 to 50 GeV/c interval. However, one has to keep in mind that there is a change of kinematics ($\approx$ 2 GeV/c shift) between the original beauty hadrons and its non-prompt J/ψ meson daughters as we mentioned before. Moreover, the rapidity range of the two measurements were different although current results from Ref. [123] does not indicate any rapidity dependence for the non-prompt J/ψ meson R_{AA}. Secondly, at low p_T (below 10 GeV), a sizable difference in R_{AA} values between inclusive charged hadrons, D mesons and non-prompt J/ψ mesons can be observed. This hierarchy structure can be explained by the aforementioned mass dependence of the radiative energy loss. But beside this, by coalescing with light quarks in the medium, beauty baryon (which has a lower inclusive branching ratio to J/ψ mesons) fraction may be enhanced, leading to a suppressed non-prompt J/ψ meson production. The observation of a much higher Λ_c/D^0 yield ratio in AA collisions with respect to pp collisions obtained by both experiments at RHIC [194] and at LHC [71] suggests a similar scenario in the charm sector. Unfortunately the current B^+ meson measurements were not yet able to extend the coverage to such low p_T to disentangle these different effects. Finally we also see the disappearance of this effect at higher p_T, matching the expectation of the dead cone effect. However, there are also numbers of other effects that may alter this suppression pattern. This includes the difference in primordial spectral shapes and the fragmentation functions, which are harder for heavy quarks than for light quarks. Also, since gluon splitting process dominates the light quark production, the suppression in the inclusive charged hadron R_{AA} is also sensitive to the color-charge dependence of parton energy loss [15, 149].

For the B_s^0 meson, a mild indication of an enhancement of the B_s^0 meson yields (with B^+ meson yields as baseline) in PbPb collisions with respect to pp collisions was seen, although given the current precision, the scenario of no enhancement can not be rejected either. Nevertheless this analysis demonstrated the unique capability of performing a fully reconstructed B_s^0 meson measurement in PbPb collisions with the CMS detector.

We also studied the B^+, B^0, and B_s^0 decay channels using pPb collision data at

the same beam energy for B meson with p_T in the 10 to 60 GeV/c interval. We found that the R_{pA} were all consistent with unity within the p_T and rapidity ranges studied. The CNM effects that could be presented in the initial nuclei, including nuclear shadowing (anti-shadowing) and EMC effect, did not significantly alter the production spectra within the current uncertainties. No obvious effect of a deconfined medium was found in the pPb system implying that the suppressions measured in PbPb collisions were not due to initial-state effects.

Finally, we would like to go back and echo on the several questions and concerns that were raised earlier in section 2.3. As opposed to inclusive charged hadrons and non-prompt J/ψ mesons, the R_{AA} of B^+ and D^0 mesons are now a much more apples-to-apples comparison, free of the complications brought by the medium effects and the changes of kinematics (although there are still differences in initial hard spectra and fragmentation functions). Unfortunately the p_T extent of the current analysis is still too high to make any qualitative conclusion, we do however, see the R_{AA} of B^+ mesons being compatible with that of non-prompt J/ψ mesons (with a few GeV/c p_T shift for J/ψ meson to account for the kinematics changes). We saw an indication of an enhanced B_s^0 meson production in PbPb collisions with respective to that in pp collisions, indicating the relevance of quark recombinations. The ratio of this enhancement can potentially provide important constraints on the strength of coalescence contributions in medium, allowing models to more precisely disentangle different effects of the heavy flavor collective behaviors.

Although the current results still struggled with the lack of statistics, the maneuver presented here lays the groundwork for future analyses. The measurements of exclusive B mesons give for the first time an unambiguous access to the b hadron quark-flavor content, and represent the first attempt to understand the interactions of beauty and light quarks with each other and with the medium they traverse before hadronization. With the almost 5 times statistics collected by the new LHC 2018 heavy ion data (and $\approx$ 30 times statistics to be collected in the future High Luminosity-LHC upgrade), the PbPb results presented here can be greatly improved. In particular, the still ambiguous enhancement of the B_s^0 meson over B^+ meson R_{AA}

ratio in PbPb collisions is expected to provide more stringent constraints on the relevance of recombination and unambiguous information about the mechanism of beauty hadronization in heavy ion collisions. If this enhancement of B_s^0 meson production persist in the high statistic data, a precise measurement of the B_s^0 meson R_{AA} will essentially be a stringent test on the relevance of coalescence mechanism of the B^+ mesons since the production of the B_s^0 and B^+ mesons are correlated to each other via the chemical effect. Tensions between different theoretical calculations can be narrowed down and model parameters will be improved. More precise measurements of the B^+ meson R_{AA} and future results on the angular correlations of B^+ mesons with other hadrons will allow one to draw a firmer conclusion on the relevance of collisional and radiative processes in the b quark energy loss [187, 35]. Potential measurements of other D and B hadron species will considerably help sorting out the complicated light quark coalesce contributions from other effects. Hopefully, hard works from devoted scientists around the globe will come to a harvesting time, bringing us one step closer to the intricate yet breathtaking QGP landscape in the near future.

Bibliography

[1] Abrams et al. Discovery of a Second Narrow Resonance in e^+e^- Annihilation. *Phys. Rev. Lett.*, 33:1453–1455, Dec 1974. URL: https://link.aps.org/doi/10.1103/PhysRevLett.33.1453, doi:10.1103/PhysRevLett.33.1453.

[2] ALICE collaboration. J/ψ production and nuclear effects in pPb collisions at $\sqrt{s_{\rm NN}}$ = 5.02 TeV. *Journal of High Energy Physics*, 2014(2):73, Feb 2014. URL: https://doi.org/10.1007/JHEP02(2014)073, doi:10.1007/JHEP02(2014)073.

[3] ALICE collaboration. Suppression of ψ(2S) production in pPb collisions at $\sqrt{s_{\rm NN}}$ = 5.02 TeV. *Journal of High Energy Physics*, 2014(12):73, Dec 2014. URL: https://doi.org/10.1007/JHEP12(2014)073, doi:10.1007/JHEP12(2014)073.

[4] ALICE collaboration. Centrality dependence of high-$p_{\rm T}$ D meson suppression in Pb-Pb collisions at $\sqrt{s_{\rm NN}}$ = 2.76 TeV. *Journal of High Energy Physics*, 2015(11):205, Nov 2015. URL: https://doi.org/10.1007/JHEP11(2015)205, doi:10.1007/JHEP11(2015)205.

[5] ALICE collaboration. Centrality dependence of inclusive J/ψ production in pPb collisions at $\sqrt{s_{\rm NN}}$ = 5.02 TeV. *Journal of High Energy Physics*, 2015(11):127, Nov 2015. URL: https://doi.org/10.1007/JHEP11(2015)127, doi:10.1007/JHEP11(2015)127.

[6] ALICE collaboration. Inclusive, prompt and non-prompt J/ψ production at mid-rapidity in Pb-Pb collisions at $\sqrt{s_{\rm NN}}$ = 2.76 TeV. *Journal of High Energy Physics*, 2015(7):51, Jul 2015. URL: https://doi.org/10.1007/JHEP07(2015)051, doi:10.1007/JHEP07(2015)051.

[7] ALICE collaboration. Rapidity and transverse-momentum dependence of the inclusive J/ψ nuclear modification factor in pPb collisions at $\sqrt{s_{\rm NN}}$ = 5.02 TeV. *Journal of High Energy Physics*, 2015(6):55, Jun 2015. URL: https://doi.org/10.1007/JHEP06(2015)055, doi:10.1007/JHEP06(2015)055.

[8] ALICE collaboration. Centrality dependence of ψ(2S) suppression in pPb collisions at $\sqrt{s_{\rm NN}}$ = 5.02 TeV. *Journal of High Energy Physics*, 2016(6):50, Jun 2016. URL: https://doi.org/10.1007/JHEP06(2016)050, doi:10.1007/JHEP06(2016)050.

[9] ALICE collaboration. Differential studies of inclusive J/ψ and ψ(2S) production at forward rapidity in Pb-Pb collisions at $\sqrt{s_{\rm NN}}$ = 2.76 TeV. *Journal of High Energy Physics*, 2016(5):179, May 2016. URL: https://doi.org/10.1007/JHEP05(2016)179, doi:10.1007/JHEP05(2016)179.

[10] ALICE collaboration. Transverse momentum dependence of D-meson production in Pb-Pb collisions at $\sqrt{s_{\rm NN}}$ = 2.76 TeV. *Journal of High Energy Physics*, 2016(3):81, Mar 2016. URL: https://doi.org/10.1007/JHEP03(2016)081, doi:10.1007/JHEP03(2016)081.

[11] ALICE collaboration. Inclusive J/ψ production at forward and backward rapidity in pPb collisions at $\sqrt{s_{\rm NN}}$ = 8.16 TeV. *Journal of High Energy Physics*, 2018(7):160, Jul 2018. URL: https://doi.org/10.1007/JHEP07(2018)160, doi:10.1007/JHEP07(2018)160.

[12] ALICE collaboration. Transverse momentum spectra and nuclear modification factors of charged particles in pp, pPb and PbPb collisions at the LHC. *Journal of High Energy Physics*, 2018(11):13, Nov 2018. URL: https://doi.org/10.1007/JHEP11(2018)013, doi:10.1007/JHEP11(2018)013.

[13] J. Allison et al. Recent developments in Geant4. *Nucl. Instrum. Meth. A*, 835:186, 2016. doi:10.1016/j.nima.2016.06.125.

[14] Andronic et al. Heavy-flavour and quarkonium production in the LHC era: from proton-proton to heavy-ion collisions. *Eur. Phys. J. C*, 76:107, 2016. arXiv:1506.03981, doi:10.1140/epjc/s10052-015-3819-5.

[15] Néstor Armesto, Andrea Dainese, Carlos A. Salgado, and Urs Achim Wiedemann. Testing the color charge and mass dependence of parton energy loss with heavy-to-light ratios at BNL RHIC and CERN LHC. *Phys. Rev. D*, 71:054027, Mar 2005. URL: https://link.aps.org/doi/10.1103/PhysRevD.71.054027, doi:10.1103/PhysRevD.71.054027.

[16] Néstor Armesto and Enrico Scomparin. Heavy-ion collisions at the Large Hadron Collider: A review of the results from Run 1. *The European Physical Journal Plus*, 131(3):52, Mar 2016. URL: https://doi.org/10.1140/epjp/i2016-16052-4, doi:10.1140/epjp/i2016-16052-4.

[17] Aubert et al. Experimental Observation of a Heavy Particle *J*. *Phys. Rev. Lett.*, 33:1404–1406, Dec 1974. URL: https://link.aps.org/doi/10.1103/PhysRevLett.33.1404, doi:10.1103/PhysRevLett.33.1404.

[18] Augustin et al. Discovery of a Narrow Resonance in e^+e^- Annihilation. *Phys. Rev. Lett.*, 33:1406–1408, Dec 1974. URL: https://link.aps.org/doi/10.1103/PhysRevLett.33.1406, doi:10.1103/PhysRevLett.33.1406.

[19] R. Baier, D. Schiff, and B. G. Zakharov. Energy loss in perturbative QCD. *Ann. Rev. Nucl. Part. Sci.*, 50:37, 2000. arXiv:hep-ph/0002198, doi:10.1146/annurev.nucl.50.1.37.

[20] Elisabetta Barberio, Bob van Eijk, and Zbigniew Was. PHOTOS: A Universal Monte Carlo for QED radiative corrections in decays. *Comput.Phys.Commun.*, 66:115–128, 1991. doi:10.1016/0010-4655(91)90012-A.

[21] Barnes et al. Observation of a Hyperon with Strangeness Minus Three. *Phys. Rev. Lett.*, 12:204–206, Feb 1964. URL: https://link.aps.org/doi/10.1103/PhysRevLett.12.204, doi:10.1103/PhysRevLett.12.204.

[22] A. Beraudo et al. Extraction of Heavy-Flavor Transport Coefficients in QCD Matter. *Nucl. Phys.*, A979:21–86, 2018. arXiv:1803.03824, doi:10.1016/j.nuclphysa.2018.09.002.

[23] Andrea Beraudo. Dynamics of heavy flavor quarks in high energy nuclear collisions. *Nuclear Physics A*, 931:145 – 154, 2014. QUARK MATTER 2014. URL: http://www.sciencedirect.com/science/article/pii/S0375947414002395, doi:https://doi.org/10.1016/j.nuclphysa.2014.07.038.

[24] P. Billoir, R. Frühwirth, and M. Regler. Track element merging strategy and vertex fitting in complex modular detectors. *Nuclear Instruments and Methods in Physics Research Section A: Accelerators, Spectrometers, Detectors and Associated Equipment*, 241(1):115 – 131, 1985. URL: http://www.sciencedirect.com/science/article/pii/0168900285905236, doi:https://doi.org/10.1016/0168-9002(85)90523-6.

[25] P. Billoir and S. Qian. Fast vertex fitting with a local parametrization of tracks. *Nuclear Instruments and Methods in Physics Research Section A: Accelerators, Spectrometers, Detectors and Associated Equipment*, 311(1):139 – 150, 1992. URL: http://www.sciencedirect.com/science/article/pii/0168900292908593, doi:https://doi.org/10.1016/0168-9002(92)90859-3.

[26] J. D. Bjorken. Energy Loss of Energetic Partons in Quark - Gluon Plasma: Possible Extinction of High p(t) Jets in Hadron - Hadron Collisions. 1982.

[27] J. D. Bjorken. Energy loss of energetic partons in quark-gluon plasma: possible extinction of high p_T jets in hadron-hadron collisions. Fermilab PUB 82-059-THY, 1982. URL: http://lss.fnal.gov/archive/1982/pub/Pub-82-059-T.pdf.

[28] Bloom et al. High-Energy Inelastic $e - p$ Scattering at 6° and 10°. *Phys. Rev. Lett.*, 23:930–934, Oct 1969. URL: https://link.aps.org/doi/10.1103/PhysRevLett.23.930, doi:10.1103/PhysRevLett.23.930.

[29] Breidenbach et al. Observed Behavior of Highly Inelastic Electron-Proton Scattering. *Phys. Rev. Lett.*, 23:935–939, Oct 1969. URL: https://link.aps.org/doi/10.1103/PhysRevLett.23.935, doi:10.1103/PhysRevLett.23.935.

[30] Jasmine Brewer, Andrey Sadofyev, and Wilke van der Schee. Jet shape modifications in holographic dijet systems. 2018. arXiv:1809.10695.

[31] Bruning et al. LHC design report. Vol. I: The LHC main ring. CERN-2004-003-V-1.

[32] Wit Busza, Krishna Rajagopal, and Wilke van der Schee. Heavy Ion Collisions: The Big Picture and the Big Questions. *Annual Review of Nuclear and Particle Science*, 68(1):339–376, 2018. URL: https://doi.org/10.1146/annurev-nucl-101917-020852, arXiv:https://doi.org/10.1146/annurev-nucl-101917-020852, doi:10.1146/annurev-nucl-101917-020852.

[33] Nicola Cabibbo. Unitary Symmetry and Leptonic Decays. *Phys. Rev. Lett.*, 10:531–533, Jun 1963. URL: https://link.aps.org/doi/10.1103/PhysRevLett.10.531, doi:10.1103/PhysRevLett.10.531.

[34] M. Cacciari, S. Frixione, N. Houdeau, M. L. Mangano, P Nason, and G. Ridolfi. Theoretical predictions for charm and bottom production at the LHC. *JHEP*, 10:137, 2012. arXiv:1205.6344, doi:10.1007/JHEP10(2012)137.

[35] Shanshan Cao, Guang-You Qin, and Steffen A. Bass. Heavy flavor dynamics in QGP and hadron gas. *Nuclear Physics A*, 931:569 – 574, 2014. QUARK MATTER 2014. URL: http://www.sciencedirect.com/science/article/pii/S0375947414003807, doi:https://doi.org/10.1016/j.nuclphysa.2014.09.011.

[36] J. H. Christenson, J. W. Cronin, V. L. Fitch, and R. Turlay. Evidence for the 2π Decay of the K_2^0 Meson. *Phys. Rev. Lett.*, 13:138–140, Jul 1964. URL: https://link.aps.org/doi/10.1103/PhysRevLett.13.138, doi:10.1103/PhysRevLett.13.138.

[37] CMS Collaboration. Track-Parameter Evaluation and Primary-Vertex Finding with the Pixel Detector. Technical Report CMS-NOTE-2003-026, CERN, Geneva, Sep 2003.

[38] CMS Collaboration. CMS Tracking Performance Results from early LHC Operation. 2010. arXiv:1007.1988, doi:10.1140/epjc/s10052-010-1491-3.

[39] CMS collaboration. Charged-particle nuclear modification factors in PbPb and pPb collisions at $\sqrt{s_{\mathrm{NN}}} = 5.02$ TeV. *Journal of High Energy Physics*, 2017(4):39, Apr 2017. URL: https://doi.org/10.1007/JHEP04(2017)039, doi:10.1007/JHEP04(2017)039.

[40] ALICE collaboration. Elliptic flow of charged particles in Pb-Pb collisions at 2.76 TeV. *Phys. Rev. Lett.*, 105:252302, 2010. arXiv:1011.3914, doi:10.1103/PhysRevLett.105.252302.

[41] ALICE collaboration. Higher harmonic anisotropic flow measurements of charged particles in Pb-Pb collisions at $\sqrt{s_{\rm NN}}$=2.76 TeV. *Phys. Rev. Lett.*, 107:032301, 2011. arXiv:1105.3865, doi:10.1103/PhysRevLett.107.032301.

[42] ALICE collaboration. Suppression of charged particle production at large transverse momentum in central Pb–Pb collisions at $\sqrt{s_{\rm NN}}$=2.76 TeV. *Physics Letters B*, 696(1):30 – 39, 2011. URL: http://www.sciencedirect.com/science/article/pii/S0370269310013973, doi:https://doi.org/10.1016/j.physletb.2010.12.020.

[43] ALICE collaboration. Production of Muons from Heavy Flavor Decays at Forward Rapidity in pp and PbPb Collisions at $\sqrt{s_{\rm NN}}$ = 2.76 TeV. *Phys. Rev. Lett.*, 109:112301, Sep 2012. URL: https://link.aps.org/doi/10.1103/PhysRevLett.109.112301, doi:10.1103/PhysRevLett.109.112301.

[44] ALICE collaboration. Suppression of high transverse momentum D mesons in central Pb-Pb collisions at $\sqrt{s_{\rm NN}}$ = 2.76 TeV. *Journal of High Energy Physics*, 2012(9):112, Sep 2012. URL: https://doi.org/10.1007/JHEP09(2012)112, doi:10.1007/JHEP09(2012)112.

[45] ALICE collaboration. J/ψ Suppression at Forward Rapidity in PbPb Collisions at $\sqrt{s_{\rm NN}}$ = 2.76 TeV. *Phys. Rev. Lett.*, 109:072301, Aug 2012. URL: https://link.aps.org/doi/10.1103/PhysRevLett.109.072301, doi:10.1103/PhysRevLett.109.072301.

[46] ALICE collaboration. D meson elliptic flow in non-central Pb-Pb collisions at $\sqrt{s_{\rm NN}}$ = 2.76 TeV. *Phys. Rev. Lett.*, 111:102301, 2013. arXiv:1305.2707, doi:10.1103/PhysRevLett.111.102301.

[47] ALICE collaboration. J/ψ Elliptic Flow in PbPb Collisions at $\sqrt{s_{\rm NN}}$ = 2.76 TeV. *Phys. Rev. Lett.*, 111:162301, 2013. arXiv:1303.5880, doi:10.1103/PhysRevLett.111.162301.

[48] ALICE collaboration. Long-range angular correlations on the near and away side in p-Pb collisions at $\sqrt{s_{\rm NN}}$ = 5.02 TeV. *Phys. Lett.*, B719:29–41, 2013. arXiv:1212.2001, doi:10.1016/j.physletb.2013.01.012.

[49] ALICE collaboration. Azimuthal anisotropy of D meson production in Pb-Pb collisions at $\sqrt{s_{\rm NN}}$ = 2.76 TeV. *Phys. Rev.*, C90(3):034904, 2014. arXiv:1405.2001, doi:10.1103/PhysRevC.90.034904.

[50] ALICE collaboration. Centrality, rapidity and transverse momentum dependence of J/ψ suppression in Pb–Pb collisions at $\sqrt{s_{\rm NN}}$ = 2.76 TeV. *Physics Letters B*, 734:314 – 327, 2014. URL: http://www.sciencedirect.com/science/article/pii/S0370269314003748, doi:https://doi.org/10.1016/j.physletb.2014.05.064.

[51] ALICE collaboration. Measurement of Prompt D-Meson Production in $p-$Pb Collisions at $\sqrt{s_{\rm NN}}$ = 5.02 TeV. *Phys. Rev. Lett.*, 113:232301, Dec 2014. URL: https://link.aps.org/doi/10.1103/PhysRevLett.113.232301, doi:10.1103/PhysRevLett.113.232301.

[52] ALICE collaboration. Multi-strange baryon production at mid-rapidity in Pb-Pb collisions at $\sqrt{s_{\rm NN}}$ = 2.76 TeV. *Phys. Lett. B*, 728:216, 2014. [Erratum: 10.1016/j.physletb.2014.05.052]. arXiv:1307.5543, doi:10.1016/j.physletb.2013.11.048.

[53] ALICE collaboration. Suppression of Υ (1S) at forward rapidity in Pb–Pb collisions at $\sqrt{s_{\rm NN}}$ = 2.76 TeV. *Physics Letters B*, 738:361 – 372, 2014. URL: http://www.sciencedirect.com/science/article/pii/S0370269314007242, doi:https://doi.org/10.1016/j.physletb.2014.10.001.

[54] ALICE collaboration. Production of inclusive Υ (1S) and Υ (2S) in p–Pb collisions at $\sqrt{s_{\rm NN}}$ = 5.02 TeV. *Physics Letters B*, 740:105 – 117, 2015. URL: http://www.sciencedirect.com/science/article/pii/S0370269314008430, doi:https://doi.org/10.1016/j.physletb.2014.11.041.

[55] ALICE collaboration. D-meson production in p-Pb collisions at $\sqrt{s_{NN}}$ = 5.02 TeV and in pp collisions at $\sqrt{s}$ = 7 TeV. *Phys. Rev. C*, 94:054908, Nov 2016. URL: https://link.aps.org/doi/10.1103/PhysRevC.94.054908, doi:10.1103/PhysRevC.94.054908.

[56] ALICE collaboration. Elliptic flow of electrons from heavy-flavour hadron decays at mid-rapidity in Pb-Pb collisions at $\sqrt{\rm s_{NN}}$ = 2.76 TeV. *JHEP*, 09:028, 2016. arXiv:1606.00321, doi:10.1007/JHEP09(2016)028.

[57] ALICE collaboration. Elliptic flow of muons from heavy-flavour hadron decays at forward rapidity in Pb–Pb collisions at $\sqrt{s_{\rm NN}}$ = 2.76 TeV. *Phys. Lett.*, B753:41–56, 2016. arXiv:1507.03134, doi:10.1016/j.physletb.2015.11.059.

[58] ALICE collaboration. Measurement of an Excess in the Yield of J/ψ at Very Low $\rm p_T$ in PbPb Collisions at $\sqrt{s_{\rm NN}}$ = 2.76 TeV. *Phys. Rev. Lett.*, 116:222301, Jun 2016. URL: https://link.aps.org/doi/10.1103/PhysRevLett.116.222301, doi:10.1103/PhysRevLett.116.222301.

[59] ALICE collaboration. Measurement of D-meson production versus multiplicity in pPb collisions at $\sqrt{s_{\rm NN}}$ = 5.02 TeV. *Journal of High Energy Physics*, 2016(8):78, Aug 2016. URL: https://doi.org/10.1007/JHEP08(2016)078, doi:10.1007/JHEP08(2016)078.

[60] ALICE collaboration. Measurement of D_s^+ production and nuclear modification factor in Pb-Pb collisions at $\sqrt{s_{NN}} = 2.76$ TeV. *JHEP*, 03:082, 2016. arXiv:1509.07287, doi:10.1007/JHEP03(2016)082.

[61] ALICE collaboration. Measurement of electrons from heavy-flavour hadron decays in pPb collisions at $\sqrt{s_{NN}} = 5.02$ TeV. *Physics Letters B*, 754:81 – 93, 2016. URL: http://www.sciencedirect.com/science/article/pii/S0370269315010151, doi:https://doi.org/10.1016/j.physletb.2015.12.067.

[62] ALICE collaboration. J/ψ elliptic flow in Pb-Pb collisions at $\sqrt{s_{NN}} = 5.02$ TeV. *Phys. Rev. Lett.*, 119(24):242301, 2017. arXiv:1709.05260, doi:10.1103/PhysRevLett.119.242301.

[63] ALICE collaboration. Measurement of electrons from beauty-hadron decays in pPb collisions at $\sqrt{s_{NN}} = 5.02$ TeV and Pb-Pb collisions at $\sqrt{s_{NN}} = 2.76$ TeV. *Journal of High Energy Physics*, 2017(7):52, Jul 2017. URL: https://doi.org/10.1007/JHEP07(2017)052, doi:10.1007/JHEP07(2017)052.

[64] ALICE collaboration. Measurement of the production of high-p_T electrons from heavy-flavour hadron decays in PbPb collisions at $\sqrt{s_{NN}} = 2.76$ TeV. *Physics Letters B*, 771:467 – 481, 2017. URL: http://www.sciencedirect.com/science/article/pii/S0370269317304239, doi:https://doi.org/10.1016/j.physletb.2017.05.060.

[65] ALICE collaboration. Production of muons from heavy-flavour hadron decays in pPb collisions at $\sqrt{s_{NN}} = 5.02$ TeV. *Physics Letters B*, 770:459 – 472, 2017. URL: http://www.sciencedirect.com/science/article/pii/S037026931730237X, doi:https://doi.org/10.1016/j.physletb.2017.03.049.

[66] ALICE collaboration. *J/ψ* suppression at forward rapidity in Pb–Pb collisions at $\sqrt{s_{NN}} = 5.02$ TeV. *Physics Letters B*, 766:212 – 224, 2017. URL: http://www.sciencedirect.com/science/article/pii/S0370269317300102, doi:https://doi.org/10.1016/j.physletb.2016.12.064.

[67] ALICE collaboration. Azimuthal anisotropy of heavy-flavour decay electrons in pPb collisions at $\sqrt{s_{NN}} = 5.02$ TeV. 2018. arXiv:1805.04367.

[68] ALICE collaboration. *D*-meson azimuthal anisotropy in midcentral Pb-Pb collisions at $\sqrt{\mathbf{s}_{NN}} = \mathbf{5.02}$ TeV. *Phys. Rev. Lett.*, 120(10):102301, 2018. arXiv:1707.01005, doi:10.1103/PhysRevLett.120.102301.

[69] ALICE collaboration. Event-shape engineering for the D-meson elliptic flow in mid-central Pb-Pb collisions at $\sqrt{s_{NN}} = 5.02$ TeV. 2018. arXiv:1809.09371.

[70] ALICE collaboration. Inclusive *J/ψ* production in Xe–Xe collisions at $\sqrt{s_{NN}} = 5.44$ TeV. *Physics Letters B*, 785:419 – 428, 2018. URL: http://

www.sciencedirect.com/science/article/pii/S0370269318306622, doi:https://doi.org/10.1016/j.physletb.2018.08.047.

[71] ALICE collaboration. Λ_c^+ production in Pb-Pb collisions at $\sqrt{s_{\rm NN}} = 5.02$ TeV. *Submitted to: Phys. Lett.*, 2018. arXiv:1809.10922.

[72] ALICE collaboration. Measurement of D^0, D^+, D^{*+} and D_s^+ production in Pb-Pb collisions at $\sqrt{s_{\rm NN}} = 5.02$ TeV. *JHEP*, 10:174, 2018. arXiv:1804.09083, doi:10.1007/JHEP10(2018)174.

[73] ALICE collaboration. Measurements of low-$p_{\rm T}$ electrons from semileptonic heavy-flavour hadron decays at mid-rapidity in pp and Pb-Pb collisions at $\sqrt{s_{\rm NN}} = 2.76$ TeV. *Journal of High Energy Physics*, 2018(10):61, Oct 2018. URL: https://doi.org/10.1007/JHEP10(2018)061, doi:10.1007/JHEP10(2018)061.

[74] ALICE collaboration. Prompt and non-prompt J/ψ production and nuclear modification at mid-rapidity in pPb collisions at $\sqrt{s_{\rm NN}} = 5.02$ TeV. *The European Physical Journal C*, 78(6):466, Jun 2018. URL: https://doi.org/10.1140/epjc/s10052-018-5881-2, doi:10.1140/epjc/s10052-018-5881-2.

[75] ALICE collaboration. Search for collectivity with azimuthal J/ψ-hadron correlations in high multiplicity pPb collisions at $\sqrt{s_{\rm NN}} = 5.02$ and 8.16 TeV. *Phys. Lett.*, B780:7–20, 2018. arXiv:1709.06807, doi:10.1016/j.physletb.2018.02.039.

[76] ALICE collaboration. Study of J/ψ azimuthal anisotropy at forward rapidity in PbPb collisions at $\sqrt{s_{\rm NN}} = 5.02$ TeV. *Submitted to: JHEP*, 2018. arXiv:1811.12727.

[77] ALICE collaboration. Υ suppression at forward rapidity in Pb–Pb collisions at $\sqrt{s_{\rm NN}} = 5.02$ TeV. *Physics Letters B*, 790:89 – 101, 2019. URL: http://www.sciencedirect.com/science/article/pii/S0370269318309973, doi:https://doi.org/10.1016/j.physletb.2018.11.067.

[78] ATLAS collaboration. Observation of a Centrality-Dependent Dijet Asymmetry in Lead-Lead Collisions at $\sqrt{s_{\rm NN}} = 2.76$ TeV with the ATLAS Detector at the LHC. *Phys. Rev. Lett.*, 105:252303, Dec 2010. URL: https://link.aps.org/doi/10.1103/PhysRevLett.105.252303, doi:10.1103/PhysRevLett.105.252303.

[79] ATLAS collaboration. Observation of a Centrality-Dependent Dijet Asymmetry in Lead-Lead Collisions at $\sqrt{s_{\rm NN}} = 2.76$ TeV with the ATLAS Detector at the LHC. *Phys. Rev. Lett.*, 105:252303, 2010. arXiv:1011.6182, doi:10.1103/PhysRevLett.105.252303.

[80] ATLAS collaboration. Measurement of charged-particle spectra in Pb+Pb collisions at $\sqrt{s_{\rm NN}} = 2.76$ TeV with the ATLAS detector at the LHC. *JHEP*, 09:050, 2015. arXiv:1504.04337, doi:10.1007/JHEP09(2015)050.

[81] ATLAS collaboration. Measurements of long-range azimuthal anisotropies and associated Fourier coefficients for pp collisions at $\sqrt{s} = 5.02$ and 13 TeV and p+Pb collisions at $\sqrt{s_{\mathrm{NN}}} = 5.02$ TeV with the ATLAS detector. *Phys. Rev.*, C96(2):024908, 2017. arXiv:1609.06213, doi:10.1103/PhysRevC.96.024908.

[82] ATLAS collaboration. Measurement of quarkonium production in proton–lead and proton–proton collisions at 5.02 TeV with the ATLAS detector. *Eur. Phys. J.*, C78(3):171, 2018. arXiv:1709.03089, doi:10.1140/epjc/s10052-018-5624-4.

[83] ATLAS collaboration. Measurement of the suppression and azimuthal anisotropy of muons from heavy-flavor decays in Pb+Pb collisions at $\sqrt{s_{\mathrm{NN}}} =$ 2.76 TeV with the ATLAS detector. *Phys. Rev.*, C98(4):044905, 2018. arXiv:1805.05220, doi:10.1103/PhysRevC.98.044905.

[84] ATLAS collaboration. Prompt and non-prompt J/ψ and $\psi(2S)$ suppression at high transverse momentum in 5.02 TeV Pb+Pb collisions with the ATLAS experiment. *Eur. Phys. J.*, C78(9):762, 2018. arXiv:1805.04077, doi:10.1140/epjc/s10052-018-6219-9.

[85] ATLAS collaboration. Prompt and non-prompt J/ψ elliptic flow in Pb+Pb collisions at $\sqrt{s_{\mathrm{NN}}} = 5.02$ TeV with the ATLAS detector. *Eur. Phys. J.*, C78(9):784, 2018. arXiv:1807.05198, doi:10.1140/epjc/s10052-018-6243-9.

[86] BRAHMS collaboration. Quark–gluon plasma and color glass condensate at RHIC? The perspective from the BRAHMS experiment. *Nuclear Physics A*, 757(1):1 – 27, 2005. First Three Years of Operation of RHIC. URL: http://www.sciencedirect.com/science/article/pii/S0375947405002770, doi:https://doi.org/10.1016/j.nuclphysa.2005.02.130.

[87] CDF Collaboration. Observation of Top Quark Production in $\overline{p}p$ Collisions with the Collider Detector at Fermilab. *Phys. Rev. Lett.*, 74:2626–2631, Apr 1995. URL: https://link.aps.org/doi/10.1103/PhysRevLett.74.2626, doi:10.1103/PhysRevLett.74.2626.

[88] CMS collaboration. Effective Vertex Fitting. Technical Report CMS-NOTE-1997-051, CERN, Geneva, Jun 1997. URL: https://cds.cern.ch/record/687531.

[89] CMS collaboration. Vertex Fitting with the Kalman Filter Formalism in the ORCA Reconstruction Program. Feb 2003. URL: https://cds.cern.ch/record/1364622.

[90] CMS Collaboration. *CMS Physics: Technical Design Report Volume 1: Detector Performance and Software*. Technical Design Report CMS. CERN, Geneva, 2006. There is an error on cover due to a technical problem for some items.

[91] CMS collaboration. Track Reconstruction in the CMS tracker. *CMS Note*, CMS-NOTE-2006-041, 2006. URL: http://cdsweb.cern.ch/record/934067.

[92] CMS collaboration. Track reconstruction, primary vertex finding and seed generation with the Pixel Detector. *CMS Note*, CMS-NOTE-2006-026, 2006.

[93] CMS collaboration. Adaptive Vertex Fitting. Technical Report CMS-NOTE-2007-008, CERN, Geneva, Mar 2007.

[94] CMS Collaboration. The CMS experiment at the CERN LHC. *Journal of Instrumentation*, 3(08):S08004, 2008. URL: http://stacks.iop.org/1748-0221/3/i=08/a=S08004.

[95] CMS collaboration. Commissioning of the CMS High-Level Trigger with Cosmic Rays. *JINST*, 5:T03005, 2010. arXiv:0911.4889, doi:10.1088/1748-0221/5/03/T03005.

[96] CMS collaboration. Measurement of CMS Luminosity. *CMS PAS*, CMS-PAS-EWK-10-004, 2010.

[97] CMS collaboration. Measurement of Tracking Efficiency. Technical Report CMS-PAS-TRK-10-002, CERN, Geneva, 2010. URL: https://cds.cern.ch/record/1279139.

[98] CMS collaboration. Performance of muon identification in pp collisions at $\sqrt{s} =$ 7 TeV. Technical Report CMS-PAS-MUO-10-002, CERN, 2010. Geneva, 2010.

[99] CMS collaboration. Tracking and Primary Vertex Results in First 7 TeV Collisions. *CMS Physics Analysis Summary*, CMS-PAS-TRK-10-005, 2010.

[100] CMS collaboration. Long-range and short-range dihadron angular correlations in central PbPb collisions at a nucleon-nucleon center of mass energy of 2.76 TeV. *JHEP*, 07:076, 2011. arXiv:1105.2438, doi:10.1007/JHEP07(2011)076.

[101] CMS collaboration. Observation and studies of jet quenching in PbPb collisions at $\sqrt{s_{\mathrm{NN}}} = 2.76$ TeV. *Phys. Rev. C*, 84:024906, Aug 2011. URL: https://link.aps.org/doi/10.1103/PhysRevC.84.024906, doi:10.1103/PhysRevC.84.024906.

[102] CMS collaboration. Centrality dependence of dihadron correlations and azimuthal anisotropy harmonics in PbPb collisions at $\sqrt{s_{\mathrm{NN}}} = 2.76$ TeV. *Eur. Phys. J.*, C72:2012, 2012. arXiv:1201.3158, doi:10.1140/epjc/s10052-012-2012-3.

[103] CMS collaboration. Observation of sequential Upsilon suppression in PbPb collisions. *Phys. Rev. Lett.*, 109:222301, 2012. [Erratum: Phys. Rev. Lett.120,no.19,199903(2018)]. arXiv:1208.2826, doi:10.1103/PhysRevLett.109.222301,10.1103/PhysRevLett.120.199903.

[104] CMS collaboration. Study of high-p_T charged particle suppression in PbPb compared to pp collisions at $\sqrt{s_{NN}}$ = 2.76 TeV. *The European Physical Journal C*, 72(3):1945, Mar 2012. URL: https://doi.org/10.1140/epjc/s10052-012-1945-x, doi:10.1140/epjc/s10052-012-1945-x.

[105] CMS collaboration. Suppression of non-prompt J/ψ, prompt J/ψ, and Y(1S) in PbPb collisions at $\sqrt{s_{NN}}$ = 2.76 TeV. *JHEP*, 05:063, 2012. arXiv:1201.5069, doi:10.1007/JHEP05(2012)063.

[106] CMS collaboration. Multiplicity and transverse momentum dependence of two- and four-particle correlations in pPb and PbPb collisions. *Phys. Lett.*, B724:213–240, 2013. arXiv:1305.0609, doi:10.1016/j.physletb.2013.06.028.

[107] CMS Collaboration. Description and performance of track and primary-vertex reconstruction with the CMS tracker. *Journal of Instrumentation*, 9(10):P10009, 2014. URL: http://stacks.iop.org/1748-0221/9/i=10/a=P10009.

[108] CMS collaboration. Electronics and Calibration system for the CMS Beam Halo Monitor. Technical Report CMS-CR-2014-110, CERN, Geneva, Jun 2014. URL: http://cds.cern.ch/record/2105519.

[109] CMS collaboration. Evidence of b-Jet Quenching in PbPb Collisions at $\sqrt{s_{NN}}$ = 2.76TeV. *Phys. Rev. Lett.*, 113:132301, Sep 2014. URL: https://link.aps.org/doi/10.1103/PhysRevLett.113.132301, doi:10.1103/PhysRevLett.113.132301.

[110] CMS collaboration. Centrality and Event Plane reconstruction for PbPb collisions at 5 TeV in 2015. CMS Note 2015/080, CERN, 2015. URL: http://cms.cern.ch/iCMS/user/noteinfo?cmsnoteid=CMS%20AN-2015/080.

[111] CMS collaboration. Nuclear Modification Factor of prompt D^0 in PbPb Collisions at $\sqrt{s_{NN}}$ = 2.76 TeV. Technical Report CMS-PAS-HIN-15-005, CERN, Geneva, 2015. URL: http://cds.cern.ch/record/2055466.

[112] CMS collaboration. Study of B Meson Production in p+Pb Collisions at $\sqrt{s_{NN}}$ = 5.02 TeV Using Exclusive Hadronic Decays. *Phys. Rev. Lett.*, 116:032301, 2016. arXiv:1508.06678, doi:10.1103/PhysRevLett.116.032301.

[113] CMS collaboration. Transverse momentum spectra of inclusive b jets in pPb collisions at $\sqrt{s_{NN}}$=5.02 TeV. *Physics Letters B*, 754:59 – 80, 2016. URL: http://www.sciencedirect.com/science/article/pii/S0370269316000149, doi:https://doi.org/10.1016/j.physletb.2016.01.010.

[114] CMS collaboration. Measurement of the $B^{\pm}$ Meson Nuclear Modification Factor in Pb-Pb Collisions at $\sqrt{s_{NN}}$ = 5.02 TeV. *Phys. Rev. Lett.*, 119:152301, 2017. arXiv:1705.04727, doi:10.1103/PhysRevLett.119.152301.

[115] CMS collaboration. Measurements of the charm jet cross section and nuclear modification factor in pPb collisions at $\sqrt{s_{\mathrm{NN}}} = 5.02$ TeV. *Phys. Lett.*, B772:306–329, 2017. arXiv:1612.08972, doi:10.1016/j.physletb.2017.06.053.

[116] CMS collaboration. Relative Modification of Prompt $\psi(2S)$ and J/ψ Yields from pp to PbPb Collisions at $\sqrt{s_{\mathrm{NN}}} = 5.02$ TeV. *Phys. Rev. Lett.*, 118:162301, Apr 2017. URL: https://link.aps.org/doi/10.1103/PhysRevLett.118.162301, doi:10.1103/PhysRevLett.118.162301.

[117] CMS collaboration. Suppression and azimuthal anisotropy of prompt and nonprompt J/ψ production in PbPb collisions at $\sqrt{s_{\mathrm{NN}}} = 2.76$ TeV. *The European Physical Journal C*, 77(4):252, Apr 2017. URL: https://doi.org/10.1140/epjc/s10052-017-4781-1, doi:10.1140/epjc/s10052-017-4781-1.

[118] CMS collaboration. Suppression and azimuthal anisotropy of prompt and nonprompt J/ψ production in PbPb collisions at $\sqrt{s_{\mathrm{NN}}} = 2.76$ TeV. *The European Physical Journal C*, 77(4):252, Apr 2017. URL: https://doi.org/10.1140/epjc/s10052-017-4781-1, doi:10.1140/epjc/s10052-017-4781-1.

[119] CMS collaboration. Suppression of $\Upsilon(1S), \Upsilon(2S)$ and $\Upsilon(3S)$ production in PbPb collisions at $\sqrt{s_{\mathrm{NN}}} = 2.76$ TeV. *Phys. Lett.*, B770:357–379, 2017. arXiv:1611.01510, doi:10.1016/j.physletb.2017.04.031.

[120] CMS collaboration. Azimuthal anisotropy of charged particles with transverse momentum up to 100 GeV/ c in PbPb collisions at $\sqrt{s_{\mathrm{NN}}}$=5.02 TeV. *Phys. Lett.*, B776:195–216, 2018. arXiv:1702.00630, doi:10.1016/j.physletb.2017.11.041.

[121] CMS collaboration. Elliptic flow of charm and strange hadrons in high-multiplicity pPb collisions at $\sqrt{s_{\mathrm{NN}}} = 8.16$ TeV. *Phys. Rev. Lett.*, 121(8):082301, 2018. arXiv:1804.09767, doi:10.1103/PhysRevLett.121.082301.

[122] CMS collaboration. Measurement of $\mathrm{B}_{\mathrm{s}}^{0}$ meson production in pp and PbPb collisions at $\sqrt{s_{\mathrm{NN}}} = 5.02$ TeV. *Submitted to: Phys. Lett. B.*, 2018. arXiv:1810.03022.

[123] CMS collaboration. Measurement of prompt and nonprompt charmonium suppression in PbPb collisions at 5.02 TeV. *The European Physical Journal C*, 78(6):509, Jun 2018. URL: https://doi.org/10.1140/epjc/s10052-018-5950-6, doi:10.1140/epjc/s10052-018-5950-6.

[124] CMS collaboration. Measurement of prompt D^0 meson azimuthal anisotropy in Pb-Pb collisions at $\sqrt{s_{\mathrm{NN}}} = 5.02$ TeV. *Phys. Rev. Lett.*, 120(20):202301, 2018. arXiv:1708.03497, doi:10.1103/PhysRevLett.120.202301.

[125] CMS collaboration. Measurement of prompt ψ(2S) production cross sections in proton-lead and proton-proton collisions at $\sqrt{s_{\mathrm{NN}}} = 5.02$ TeV. 2018. arXiv:1805.02248.

[126] CMS collaboration. Nuclear modification factor of D^0 mesons in PbPb collisions at $\sqrt{s_{\mathrm{NN}}} = 5.02$ TeV. *Physics Letters B*, 782:474 – 496, 2018. URL: http://www.sciencedirect.com/science/article/pii/S0370269318304386, doi:https://doi.org/10.1016/j.physletb.2018.05.074.

[127] CMS collaboration. Observation of prompt J/ψ meson elliptic flow in high-multiplicity pPb collisions at $\sqrt{s_{\mathrm{NN}}} = 8.16$ TeV. *Submitted to: Phys. Lett.*, 2018. arXiv:1810.01473.

[128] CMS collaboration. Pseudorapidity distributions of charged hadrons in proton-lead collisions at $\sqrt{s_{\mathrm{NN}}} = 5.02$ and 8.16 TeV. *JHEP*, 01:045, 2018. arXiv:1710.09355, doi:10.1007/JHEP01(2018)045.

[129] CMS collaboration. Studies of beauty suppression via nonprompt D^0 mesons in PbPb collisions at $\sqrt{s_{\mathrm{NN}}} = 5.02$ TeV. *Submitted to: Phys. Rev. Lett.*, 2018. arXiv:1810.11102.

[130] CMS collaboration. Measurement of nuclear modification factors of Υ(1S), Υ(2S), and Υ(3S) mesons in PbPb collisions at $\sqrt{s_{\mathrm{NN}}} = 5.02$ TeV. *Phys. Lett.*, B790:270–293, 2019. arXiv:1805.09215, doi:10.1016/j.physletb.2019.01.006.

[131] CMS collaboration. Pseudorapidity distributions of charged hadrons in xenon-xenon collisions at $\sqrt{s_{\mathrm{NN}}} = 5.44$ TeV. 2019. arXiv:1902.03603.

[132] D0 Collaboration. Search for High Mass Top Quark Production in $p\overline{p}$ Collisions at $\sqrt{s} = 1.8$ TeV. *Phys. Rev. Lett.*, 74:2422–2426, Mar 1995. URL: https://link.aps.org/doi/10.1103/PhysRevLett.74.2422, doi:10.1103/PhysRevLett.74.2422.

[133] PHENIX collaboration. Formation of dense partonic matter in relativistic nucleus–nucleus collisions at RHIC: Experimental evaluation by the PHENIX Collaboration. *Nuclear Physics A*, 757(1):184 – 283, 2005. First Three Years of Operation of RHIC. URL: http://www.sciencedirect.com/science/article/pii/S0375947405005300, doi:https://doi.org/10.1016/j.nuclphysa.2005.03.086.

[134] PHENIX Collaboration. Suppression Pattern of Neutral Pions at High Transverse Momentum in Au + Au Collisions at $\sqrt{s_{\mathrm{NN}}} = 200$ GeV and Constraints on Medium Transport Coefficients. *Phys. Rev. Lett.*, 101:232301, Dec 2008. URL: https://link.aps.org/doi/10.1103/PhysRevLett.101.232301, doi:10.1103/PhysRevLett.101.232301.

[135] PHOBOS collaboration. The PHOBOS perspective on discoveries at RHIC. *Nuclear Physics A*, 757(1):28 – 101, 2005. First Three Years of Operation of RHIC. URL: http://www.sciencedirect.com/science/article/pii/S0375947405005282, doi:https://doi.org/10.1016/j.nuclphysa.2005.03.084.

[136] STAR collaboration. $K^{\star}(892)^0$ production in relativistic heavy ion collisions at $\sqrt{s_{\rm NN}}$ = 130 GeV. *Phys. Rev. C*, 66:061901, 2002. arXiv:nucl-ex/0205015, doi:10.1103/PhysRevC.66.061901.

[137] STAR Collaboration. Transverse-Momentum and Collision-Energy Dependence of High-p_T Hadron Suppression in Au + Au Collisions at Ultrarelativistic Energies. *Phys. Rev. Lett.*, 91:172302, Oct 2003. URL: https://link.aps.org/doi/10.1103/PhysRevLett.91.172302, doi:10.1103/PhysRevLett.91.172302.

[138] STAR collaboration. Kaon production and kaon to pion ratio in Au+Au collisions at $\sqrt{s_{\rm NN}}$ = 130 GeV. *Phys. Lett. B*, 595:143, 2004. arXiv:nucl-ex/0206008, doi:10.1016/j.physletb.2004.06.044.

[139] STAR collaboration. Multistrange baryon production in Au-Au collisions at $\sqrt{s_{\rm NN}}$ = 130 GeV. *Phys. Rev. Lett.*, 92:182301, 2004. arXiv:nucl-ex/0307024, doi:10.1103/PhysRevLett.92.182301.

[140] STAR collaboration. Experimental and theoretical challenges in the search for the quark–gluon plasma: The STAR Collaboration's critical assessment of the evidence from RHIC collisions. *Nuclear Physics A*, 757(1):102 – 183, 2005. First Three Years of Operation of RHIC. URL: http://www.sciencedirect.com/science/article/pii/S0375947405005294, doi:https://doi.org/10.1016/j.nuclphysa.2005.03.085.

[141] STAR collaboration. Scaling Properties of Hyperon Production in Au+Au Collisions at $\sqrt{s_{\rm NN}}$ = 200 GeV. *Phys. Rev. Lett.*, 98:062301, 2007. arXiv:nucl-ex/0606014, doi:10.1103/PhysRevLett.98.062301.

[142] STAR collaboration. Enhanced strange baryon production in Au+Au collisions compared to p+p at $\sqrt{s_{\rm NN}}$ = 200 GeV. *Phys. Rev. C*, 77:044908, 2008. URL: https://link.aps.org/doi/10.1103/PhysRevC.77.044908, doi:10.1103/PhysRevC.77.044908.

[143] STAR collaboration. Energy and system size dependence of ϕ meson production in Cu+Cu and Au+Au collisions. *Phys. Lett. B*, 673:183, 2009. arXiv:0810.4979, doi:10.1016/j.physletb.2009.02.037.

[144] STAR collaboration. Strange and multi-strange particle production in Au+Au collisions at $\sqrt{s_{\rm NN}}$ = 62.4 GeV. *Phys. Rev. C*, 83:024901, 2011. arXiv:1010.0142, doi:10.1103/PhysRevC.83.024901.

[145] STAR collaboration. Strangeness enhancement in Cu+Cu and Au+Au collisions at $\sqrt{s_{\rm NN}}$ = 200 GeV. *Phys. Rev. Lett.*, 108:072301, 2012. arXiv:1107.2955, doi:10.1103/PhysRevLett.108.072301.

[146] J. C. Collins and M. J. Perry. Superdense matter: neutrons or asymptotically free quarks? *Phys. Rev. Lett.*, 34:1353, 1975. doi:10.1103/PhysRevLett.34.1353.

[147] David d'Enterria. Indications of suppressed high p_T hadron production in nucleus–nucleus collisions at CERN-SPS. *Physics Letters B*, 596(1):32 – 43, 2004. URL: http://www.sciencedirect.com/science/article/pii/S0370269304009372, doi:https://doi.org/10.1016/j.physletb.2004.06.071.

[148] J. D'Hondt, P. Vanlaer, R. Fruhwirth, and W.Waltenberger. Sensitivity of robust vertex fitting algorithms. *IEEE Trans. Nucl. Sci.*, 51:2037–2044, 2004. doi:10.1109/TNS.2004.832296.

[149] Magdalena Djordjevic. Heavy Flavor Puzzle at LHC: A Serendipitous Interplay of Jet Suppression and Fragmentation. *Phys. Rev. Lett.*, 112:042302, Jan 2014. URL: https://link.aps.org/doi/10.1103/PhysRevLett.112.042302, doi:10.1103/PhysRevLett.112.042302.

[150] Magdalena Djordjevic, Bojana Blagojevic, and Lidija Zivkovic. Lower vs. high momentum mass tomography in Quark-Gluon Plasma. 2016. arXiv:1601.07852.

[151] Yuri L. Dokshitzer and D. E. Kharzeev. Heavy quark colorimetry of QCD matter. *Phys. Lett.*, B519:199–206, 2001. arXiv:hep-ph/0106202, doi:10.1016/S0370-2693(01)01130-3.

[152] Panagiota Foka and Małgorzata Anna Janik. An overview of experimental results from ultra-relativistic heavy-ion collisions at the CERN LHC: Bulk properties and dynamical evolution. *Reviews in Physics*, 1:154 – 171, 2016. URL: http://www.sciencedirect.com/science/article/pii/S2405428316300156, doi:https://doi.org/10.1016/j.revip.2016.11.002.

[153] Panagiota Foka and Małgorzata Anna Janik. An overview of experimental results from ultra-relativistic heavy-ion collisions at the CERN LHC: Hard probes. *Reviews in Physics*, 1:172 – 194, 2016. URL: http://www.sciencedirect.com/science/article/pii/S2405428316300144, doi:https://doi.org/10.1016/j.revip.2016.11.001.

[154] H. Fritzsch, M. Gell-Mann, and H. Leutwyler. Advantages of the color octet gluon picture. *Physics Letters B*, 47(4):365 – 368, 1973. URL: http://www.sciencedirect.com/science/article/pii/0370269373906254, doi:https://doi.org/10.1016/0370-2693(73)90625-4.

[155] R. Frühwirth. Application of Kalman filtering to track and vertex fitting. *Nuclear Instruments and Methods in Physics Research Section A: Accelerators, Spectrometers, Detectors and Associated Equipment*, 262(2):444 – 450, 1987. URL: http://www.sciencedirect.com/science/article/pii/0168900287908874, doi:https://doi.org/10.1016/0168-9002(87)90887-4.

[156] R. Frühwirth, P. Kubinec, W. Mitaroff, and M. Regler. Vertex reconstruction and track bundling at the LEP collider using robust algorithms. *Computer Physics Communications*, 96(2):189 – 208, 1996. URL: http://www.sciencedirect.com/science/article/pii/0010465596000409, doi:https://doi.org/10.1016/0010-4655(96)00040-9.

[157] M. Gell-Mann. A schematic model of baryons and mesons. *Physics Letters*, 8(3):214 – 215, 1964. URL: http://www.sciencedirect.com/science/article/pii/S0031916364920013, doi:https://doi.org/10.1016/S0031-9163(64)92001-3.

[158] S. L. Glashow, J. Iliopoulos, and L. Maiani. Weak Interactions with Lepton-Hadron Symmetry. *Phys. Rev. D*, 2:1285–1292, Oct 1970. URL: https://link.aps.org/doi/10.1103/PhysRevD.2.1285, doi:10.1103/PhysRevD.2.1285.

[159] P.B. Gossiaux, J. Aichelin, Th. Gousset, M. Nahrgang, V. Ozvenchuk, and K. Werner. Gluon radiation by heavy quarks at intermediate energies and consequences for the mass hierarchy of energy loss. *Nuclear Physics A*, 931:581 – 585, 2014. QUARK MATTER 2014. URL: http://www.sciencedirect.com/science/article/pii/S037594741400356X, doi:https://doi.org/10.1016/j.nuclphysa.2014.08.096.

[160] O. W. Greenberg. Spin and Unitary-Spin Independence in a Paraquark Model of Baryons and Mesons. *Phys. Rev. Lett.*, 13:598–602, Nov 1964. URL: https://link.aps.org/doi/10.1103/PhysRevLett.13.598, doi:10.1103/PhysRevLett.13.598.

[161] David J. Gross and Frank Wilczek. Ultraviolet Behavior of Non-Abelian Gauge Theories. *Phys. Rev. Lett.*, 30:1343–1346, Jun 1973. URL: https://link.aps.org/doi/10.1103/PhysRevLett.30.1343, doi:10.1103/PhysRevLett.30.1343.

[162] Particle Data Group. Review of Particle Physics.

[163] R. Hambrock and W. A. Horowitz. AdS/CFT predictions for azimuthal and momentum correlations of $b\bar{b}$ pairs in heavy ion collisions. 2017. URL: https://inspirehep.net/record/1518153/files/arXiv:1703.05845.pdf, arXiv:1703.05845.

[164] M. Y. Han and Y. Nambu. Three-Triplet Model with Double SU(3) Symmetry. *Phys. Rev.*, 139:B1006–B1010, Aug 1965. URL: https://link.aps.org/doi/10.1103/PhysRev.139.B1006, doi:10.1103/PhysRev.139.B1006.

[165] Min He, Rainer J. Fries, and Ralf Rapp. Heavy-quark diffusion and hadronization in quark-gluon plasma. *Phys. Rev. C*, 86:014903, 2012. arXiv:1106.6006, doi:10.1103/PhysRevC.86.014903.

[166] Min He, Rainer J. Fries, and Ralf Rapp. Heavy flavor at the large hadron collider in a strong coupling approach. *Phys. Lett. B*, 735:445, 2014. arXiv:1401.3817, doi:10.1016/j.physletb.2014.05.050.

[167] Herb et al. Observation of a Dimuon Resonance at 9.5 GeV in 400-GeV Proton-Nucleus Collisions. *Phys. Rev. Lett.*, 39:252–255, Aug 1977. URL: https://link.aps.org/doi/10.1103/PhysRevLett.39.252, doi:10.1103/PhysRevLett.39.252.

[168] Andreas Hoecker, Peter Speckmayer, Joerg Stelzer, Jan Therhaag, Eckhard von Toerne, and Helge Voss. TMVA: Toolkit for Multivariate Data Analysis. *PoS*, ACAT:040, 2007. arXiv:physics/0703039.

[169] W. A. Horowitz. Fluctuating heavy quark energy loss in a strongly coupled quark-gluon plasma. *Phys. Rev. D*, 91:085019, 2015. arXiv:1501.04693, doi:10.1103/PhysRevD.91.085019.

[170] J. Iliopoulos. Glashow-Iliopoulos-Maiani mechanism. *Scholarpedia*, 5(5):7125, 2010. revision #137391. doi:10.4249/scholarpedia.7125.

[171] F. Karsch and E. Laermann. Thermodynamics and in-medium hadron properties from lattice QCD. In *Quark-Gluon Plasma III, R. Hwa (ed.),* 2003, 2003. arXiv:hep-lat/0305025.

[172] J. M. B. Kellogg, I. I. Rabi, N. F. Ramsey, and J. R. Zacharias. An Electrical Quadrupole Moment of the Deuteron. *Phys. Rev.*, 55:318–319, Feb 1939. URL: https://link.aps.org/doi/10.1103/PhysRev.55.318, doi:10.1103/PhysRev.55.318.

[173] Makoto Kobayashi and Toshihide Maskawa. CP-Violation in the Renormalizable Theory of Weak Interaction. *Progress of Theoretical Physics*, 49(2):652–657, 1973. URL: http://dx.doi.org/10.1143/PTP.49.652, arXiv:/oup/backfile/content_public/journal/ptp/49/2/10.1143/ptp.49.652/2/49-2-652.pdf, doi:10.1143/PTP.49.652.

[174] P. K. Kovtun, D. T. Son, and A. O. Starinets. Viscosity in Strongly Interacting Quantum Field Theories from Black Hole Physics. *Phys. Rev. Lett.*, 94:111601, Mar 2005. URL: https://link.aps.org/doi/10.1103/PhysRevLett.94.111601, doi:10.1103/PhysRevLett.94.111601.

[175] D.J. Lange. The EvtGen particle decay simulation package. *Nucl. Instrum. Meth.*, A462:152–155, 2001. doi:10.1016/S0168-9002(01)00089-4.

[176] I. P. Lokhtin and A. M. Snigirev. A model of jet quenching in ultrarelativistic heavy ion collisions and high-p_T hadron spectra at RHIC. *Eur. Phys. J.*, C45:211, 2006. arXiv:hep-ph/0506189, doi:10.1140/epjc/s2005-02426-3.

[177] M. Cacciari, M. Greco, P. Nason. The p_T spectrum in heavy-flavour hadroproduction. *JHEP 007,*, 9805, 1998. URL: http://arxiv.org/abs/hep-ph/9803400.

[178] M. Cacciari, S. Frixione, P. Nason. The p_T spectrum in heavy-flavor photoproduction. *JHEP 006,*, 0103, 20018. URL: http://arxiv.org/abs/hep-ph/0102134.

[179] Juan Maldacena. The Large-N Limit of Superconformal Field Theories and Supergravity. *International Journal of Theoretical Physics*, 38(4):1113–1133, Apr 1999. URL: https://doi.org/10.1023/A:1026654312961, doi:10.1023/A:1026654312961.

[180] José Guilherme Milhano and Korinna Christine Zapp. Origins of the di-jet asymmetry in heavy ion collisions. *Eur. Phys. J.*, C76(5):288, 2016. arXiv:1512.08107, doi:10.1140/epjc/s10052-016-4130-9.

[181] Marlene Nahrgang, Jörg Aichelin, Pol Bernard Gossiaux, and Klaus Werner. Azimuthal correlations of heavy quarks in Pb + Pb collisions at $\sqrt{s} = 2.76$ TeV at the CERN Large Hadron Collider. *Phys. Rev. C*, 90:024907, Aug 2014. URL: https://link.aps.org/doi/10.1103/PhysRevC.90.024907, doi:10.1103/PhysRevC.90.024907.

[182] Stella Orfanelli. *An Innovative Beam Halo Monitor system for the CMS experiment at the LHC: Design, Commissioning and First Beam Results*. PhD thesis, CERN, 2016-02-11.

[183] H. David Politzer. Reliable Perturbative Results for Strong Interactions? *Phys. Rev. Lett.*, 30:1346–1349, Jun 1973. URL: https://link.aps.org/doi/10.1103/PhysRevLett.30.1346, doi:10.1103/PhysRevLett.30.1346.

[184] Francesco Prino and Ralf Rapp. Open heavy flavor in QCD matter and in nuclear collisions. *Journal of Physics G: Nuclear and Particle Physics*, 43(9):093002, aug 2016. URL: https://doi.org/10.1088%2F0954-3899%2F43%2F9%2F093002, doi:10.1088/0954-3899/43/9/093002.

[185] Kirill Prokofiev and T. Speer. A kinematic and a decay chain reconstruction library. In *Computing in high energy physics and nuclear physics. Proceedings, Conference, CHEP'04, Interlaken, Switzerland, September 27-October 1, 2004*, pages 411–414, 2005. URL: http://doc.cern.ch/yellowrep/2005/2005-002/p411.pdf.

[186] Johann Rafelski and Berndt Müller. Strangeness Production in the Quark - Gluon Plasma. *Phys. Rev. Lett.*, 48:1066, 1982. [Erratum: 10.1103/PhysRevLett.56.2334]. doi:10.1103/PhysRevLett.48.1066.

[187] Martin Rohrmoser, Pol Bernard Gossiaux, Thierry Gousset, and Jörg Aichelin. Constraining in-medium heavy-quark energy-loss mechanisms via angular

correlations between heavy and light mesons. *J. Phys. Conf. Ser.*, 779:012032, 2017. arXiv:1611.01854, doi:10.1088/1742-6596/779/1/012032.

[188] É. V. Shuryak. Theory of hadronic plasma. *Sov. Phys. JETP*, 47:212, 1978. URL: http://www.jetp.ac.ru/cgi-bin/e/index/e/47/2/p212?a=list.

[189] T. Sjöstrand, S. Mrenna, and P. Skands. PYTHIA 6.4 physics and manual. *JHEP*, 05:026, 2006. arXiv:hep-ph/0603175, doi:10.1088/1126-6708/2006/05/026.

[190] Nicolo Tosi. *The new Beam Halo Monitor for the CMS experiment at the LHC*. PhD thesis, Bologna U., 2015. URL: http://www.infn.it/thesis/thesis_dettaglio.php?tid=10006.

[191] WA98 Collaboration. Transverse mass distributions of neutral pions from ^{208}Pb-induced reactions at 158·A GeV. *The European Physical Journal C - Particles and Fields*, 23(2):225–236, Mar 2002. URL: https://doi.org/10.1007/s100520100886, doi:10.1007/s100520100886.

[192] Xin-Nian Wang and Miklos Gyulassy. HIJING: A Monte Carlo model for multiple jet production in pp, pA, and AA collisions. *Phys. Rev. D*, 44:3501, 1991. doi:10.1103/PhysRevD.44.3501.

[193] Kenneth G. Wilson. Confinement of quarks. *Phys. Rev. D*, 10:2445–2459, Oct 1974. URL: https://link.aps.org/doi/10.1103/PhysRevD.10.2445, doi:10.1103/PhysRevD.10.2445.

[194] Guannan Xie. Λ_c Production in Au+Au Collisions at $\sqrt{s_{\rm NN}}$ = 200 GeV measured by the STAR experiment. *Nuclear Physics A*, 967:928 – 931, 2017. The 26th International Conference on Ultra-relativistic Nucleus-Nucleus Collisions: Quark Matter 2017. URL: http://www.sciencedirect.com/science/article/pii/S0375947417302658, doi:https://doi.org/10.1016/j.nuclphysa.2017.06.004.

[195] Jiechen Xu, Alessandro Buzzatti, and Miklos Gyulassy. Azimuthal jet flavor tomography with CUJET2.0 of nuclear collisions at RHIC and LHC. *JHEP*, 08:063, 2014. arXiv:1402.2956, doi:10.1007/JHEP08(2014)063.

[196] Jiechen Xu, Jinfeng Liao, and Miklos Gyulassy. Consistency of Perfect Fluidity and Jet Quenching in semi-Quark-Gluon Monopole Plasmas. *Chin. Phys. Lett.*, 32:092501, 2015. arXiv:1411.3673, doi:10.1088/0256-307X/32/9/092501.

[197] Jiechen Xu, Jinfeng Liao, and Miklos Gyulassy. Bridging soft-hard transport properties of quark-gluon plasmas with CUJET3.0. *JHEP*, 02:169, 2016. arXiv:1508.00552, doi:10.1007/JHEP02(2016)169.

[198] C. N. Yang and R. L. Mills. Conservation of Isotopic Spin and Isotopic Gauge Invariance. *Phys. Rev.*, 96:191–195, Oct 1954. URL: https://link.aps.org/doi/10.1103/PhysRev.96.191, doi:10.1103/PhysRev.96.191.

[199] Hideki YUKAWA. On the Interaction of Elementary Particles. I. *Proceedings of the Physico-Mathematical Society of Japan. 3rd Series*, 17:48–57, 1935. doi:10.11429/ppmsj1919.17.0_48.

[200] Ben-Wei Zhang, Che Ming Ko, and Wei Liu. Thermal charm production in a quark-gluon plasma in Pb-Pb collisions at $\sqrt{s_{\rm NN}} = 5.5$ TeV. *Phys. Rev. C*, 77:024901, Feb 2008. URL: https://link.aps.org/doi/10.1103/PhysRevC.77.024901, doi:10.1103/PhysRevC.77.024901.

[201] G Zweig. An SU_3 model for strong interaction symmetry and its breaking; Version 1. Technical Report CERN-TH-401, CERN, Geneva, Jan 1964. URL: http://cds.cern.ch/record/352337.

[202] G Zweig. An SU_3 model for strong interaction symmetry and its breaking; Version 2. (CERN-TH-412):80 p, Feb 1964. URL: http://cds.cern.ch/record/570209.